UNIVERSITY OF CALIFORNIA
SANTA CRUZ

Synthesis, Surface Modification and Photophysical Properties of Plasmonic Metal, Metal Oxide Nanoparticles, and Semiconductor Quantum Dots

A dissertation submitted in partial satisfaction
of the requirements for the degree of

DOCTOR OF PHILOSOPHY

in

CHEMISTRY

by

Sara Bonabi Naghadeh

June 2019

The Dissertation of Sara Bonabi Naghadeh is approved:

_____
Professor Jin Zhang, Chair

_____
Professor Scott Oliver

_____
Professor Yat Li

_____
Lori G Kletzer
Vice Provost and Dean of Graduate Studies

TABLE OF CONTENTS

LIST OF FIGURES

LIST OF TABLES

Abstract

Synthesis, Surface Modification, and Photophysical Properties of Plasmonic Metal, Metal oxide Nanoparticles, and Semiconductor Quantum Dots

Sara Bonabi Naghadeh

Nanomaterials including metals, metal oxide, and semiconductors have been studied as powerful tools for various applications including photovoltaic, photocatalyst, biomedical therapeutics, sensing, energy storage, wastewater treatment and so many more. Based on the specific application, these nanomaterials can be tuned and optimized to achieve their best performance. These modifications can be in the form of altering size, shape, crystal structure, surface passivation, surface morphology, and doping. In this dissertation, the effect of size and surface modification on optical, photophysical and photocatalytic properties of perovskite nanocrystals, CdS based nanocomposites, and hollow gold nanoparticles are investigated.

In chapter 1, a comprehensive literature review was done on photophysical properties and improved stability of organic-inorganic perovskite nanomaterials by surface passivation. In this chapter, it is discussed how by changing the capping ligand and surface passivation strategies, the size, shape and crystal structure of these nanomaterials were controlled to produce high quality nanostructured and bulk film perovskites. The degradation mechanism and surface passivation approaches to address the instability issue toward environmental factors were also highlighted. This

information emphasizes the importance of defect passivation and surface modification in achieving high performance in photovoltaic applications.

In chapter 2, a new surface passivation strategy was developed using peptide molecules with amine and carboxylic functional groups to synthesize methylammonium lead bromide ($CH_3NH_3PbBr_3$) perovskite nanocrystals (PNCs) with excellent optical properties. It was demonstrated in this work that well-passivated PNCs can only be obtained when both amino and carboxylic groups were involved, and this is attributed to the protonation reaction between $–NH_2$ and –COOH. In addition to their improved optical properties, using peptide as capping ligand resulted in increasing the product yield up to ~44%. This is due to the polar nature of peptides, which cause aggregation and precipitation of peptide-passivated PNCs from nonpolar toluene solvent. PNCs size was also controlled by adjusting the concentration of the peptide, resulting in tunable optical properties due to the quantum confinement effect. Furthermore, generality and versatility of this strategy were shown by passivating different types of PNCs such as $CsPbBr_3$.

In chapter 3, three differently sized (3.1, 5.7, and 9.3 nm) methylammonium lead bromide ($CH_3NH_3PbBr_3$) perovskite nanocrystals (PNCs) were synthesized using (3-Aminopropyl) triethoxysilane (APTES) and oleic acid (OA) as capping ligands. The size dependence of charge carrier dynamics was studied to decipher the radiative and non-radiative components. These PNCs showed size-dependent absorption and photoluminescence (PL), with the middle-sized PNCs exhibiting the highest PL quantum yield (~91%). The effect of size on the exciton/charge carrier dynamic of

PNCs was studied using transient absorption spectroscopy (TA) and time resolved photoluminescence (TRPL). The middle-sized PNCs (PNC_{35_APTES}) showed slower early time recombination compared to that of the larger and smaller PNCs, suggesting optimized passivation of surface trap states. However, the radiative lifetime was found to decrease with decreasing PNC size, which seems to be primarily determined by the PNC core, while the non-radiative lifetime is longest for the middle-sized PNCs, which is strongly influenced by the presence of bandgap states that depend on surface passivation. A kinetic model is proposed to explain the observed dynamics results, including the size dependence. This study demonstrates the competing effect between size and surface properties in determining the dynamics and optical properties of PNCs.

In chapter 4, the same three differently sized methylammonium lead bromide ($CH_3NH_3PbBr_3$) perovskite nanocrystals (PNCs) were studied using UV-Vis, photoluminescence (PL), temperature dependent PL, temperature dependent time resolved PL (TRPL), cryo-XRD, and cryo-EM to investigate crystal phase stability of the PNCs as a function of size at different temperatures ranging from 20 K to 300 K. The preliminary results showed spectral blue shift of the PL peak by decreasing the temperature, which is the opposite of what was observed for large and middle-sized particles. The lifetime of the smaller PNCs also decreased by increasing the temperature. These results can be possibly due to crystal phase transition in the small particles. Future work is suggested to further investigate the phase transition possibility using cryo-XRD at slow scanning rate and temperature dependent Raman spectroscopy.

In chapter 5, different compositions of CdS nanowires with MoS_2, NiS, NiS_2, Ni_3S_2, and $NiCo_2S_4$ nanoparticles composites were synthesized and the photocatalytic activities of them in hydrogen evolution reaction (HER) was investigated. These hierarchical structures provide high activation potentials for HER and suppresses the photo corrosion of CdS. The results indicated there is an optimal amount of nanoparticles decorated on the CdS surface for optimized performance. This optimum nanoparticle ratio will provide uniform coverage of the CdS surface resulting in efficient charge transfer. While the higher ratios form aggregate structures, which act as carrier trap states. To gain deeper insight into the mechanism behind the enhanced performance, ultrafast transient absorption (TA) techniques was used to probe the charge carrier dynamics of these CdS-based heterostructures. At the for each nanocomposite, mechanism of charge transfer between components were proposed.

In chapter 6, the effect of targeting on photothermal therapy (PTT) efficiency of hollow gold nanoparticles (HGNs) was investigated. HGNs are class of plasmonic nanomaterials which showed great potential for biomedical applications and specifically PTT. These HGNs can be easily modified on the surface and be conjugated to various targeting ligands including antibody, peptide and other small molecules such as folate. In this chapter, HGNs with an average outer diameter of 40 nm were synthesized and conjugated to anti_EGFR antibody and GE-11 peptide, which both target EGF receptors on cancer cells. The conjugated HGNs were characterized using UV-Vis, photoluminescence (PL), Inductively coupled plasma-optical emission spectrometry (ICP_OES), bicinchoninic acid assay (BCA), fluorescence microscopy,

and confocal microscopy. The preliminary results showed significantly higher cell death with peptide conjugated HGNs (91%) compared to antibody-conjugated HGNs (54%). Different hypotheses were discussed as possible explanation for this enhanced PTT efficiency including possible particle internalization, better binding to receptors due to small ligand size, and most importantly closer proximity of HGNs to the cell surface resulting in more efficient heath transfer.

DEDICATION

To my love and my amazing husband, Maziar

To my parents Mansour and Azam

To my brother Saeid

ACKNOWLEDGEMENTS

I would like to thank my advisor, Jin Z. Zhang for giving me the opportunity to join his research group and learn under his supervision. His support, guidance and encouragement, made this journey possible for me. I would also like to thank my dissertation committee, Scott Oliver and Yat Li for their support and guidance during these last 5 years.

I also thank my past labmates, Sarah Lindley and Staci Adams for patiently training me on instruments, synthesis and helping me get started in the lab. I appreciate their guidance and thoughtful advices through this journey. I want to thank my current lab mates, A' Lester Allen, Evan Vickers, Vivien Cherrette, and Melissa Guarino-Hotz for their support and making the lab more fun with their energy. I am grateful for all the undergraduate students, Alexis Yup, Zachary Schwartz, and Amanda Brewer who helped me immensely during these years.

I want to thank many visiting scholars in our lab, Hongmei Wang, Binbin Luo, Ke Xu, Longshi Rao, Ghada Abdelmageed, Yi-Hsuan Chiu, and Ying-Chih Pu who gave me the opportunity to learn from them and work with them on many collaboration projects.

I am also grateful for having my amazing cohort, Will Hollingsworth, Carmen Segura, Michael Roders, Ana Kareh, Yi Peng, and Tinayi Kou for being so supportive. We went through this process together and we overcame every challenge together.

I would also like to thank my parents Mansour and Azam, and my brother, Saeid for always and unconditionally supporting me even from thousands of miles away.

They were always there to listen to me during stressful times and assured me that everything is going to be alright.

Most of all I want to sincerely thank my amazing husband, Maziar, which none of these would be possible without his love, support, and patience.

The text of this dissertation includes reprints of the following previously published material:

Chapter 1: S. Bonabi Naghadeh, B. Luo, G. Abdelmageed, Y. Pu, C. Zhang, J. Zhang. "Photophysical Properties and Improved Stability of Organic-inorganic Perovskite by Surface Passivation". *The Journal of Physical Chemistry C*, 122, 28 (2018): 15799-15818.

Chapter 2: B. Luo*, **S. Bonabi Naghadeh***, A. Allen, X. Li and J. Zhang, "Peptide-passivated Lead Halide Perovskite Nanocrystals Based on Synergistic Effect between Amino and Carboxylic Functional Groups". *Advanced Functional Materials,* 27, 6 (2017): 1604018.

Chapter 3: S. Bonabi Naghadeh, B. Luo, Z. Schwartz, W. Holingsworth, S. Lindley, A. Brewer, A. Ayzner, J. Zhang. "Size Dependence of Charge Carrier Dynamic in Organometal Halide Perovskite Nanocrystals: Deciphering the Radiative vs Non-radiative Components". *The Journal of Physical Chemistry C*, 123, 7 (2019): 4610-4619.

Chapter 4: S. Bonabi Naghadeh, *et al.* "Size-dependent Crystalline Phase Stability of Hybrid Perovskite Nanocrystals at Different Temperatures". *To be Submitted*

S. Sarang, **S. Bonabi Naghadeh**, P. Kumar, E. Betady, V. Tung, M. Scheibner, J. Zhang, S. Ghosh, "Stabilization of Cubic Crystalline Phase in Hybrid Perovskite Quantum Dots via Surface Energy Manipulation". *The journal of physical chemistry letters* 8, 21 (2017): 5378-5384.

Chapter 5: H. Wang*, **S. Bonabi Naghadeh***, C. Li, V. L. Cherrette, P. Fang, K. Xu, J. Z. Zhang. "Enhanced Photoelectrochemical and Photocatalytic Properties of CdS

Nanowires Decorated with Ni_3S_2 Nanoparticles under Visible Light Irradiation" *Journal of The Electrochemical Society* 166, 5, (2019): H3146-H3153

H. Wang*****, **S. Bonabi Naghadeh***, C. Li, L. Ying, J. Z. Zhang. "Enhanced photoelectrochemical and photocatalytic activities of CdS nanowires by surface modification with MoS_2 nanosheets". *Science China Materials* 61, 6, (2018): 839-850

*C. Li, S. Du, H. Wang**, S. Bonabi Naghadeh**, A. C. Allen, X. Lin, G. Li, Y. Liu, H. Xu, C. He, J. Z. Zhang, P. Fang."* Enhanced visible-light-driven photocatalytic hydrogen evolution activity of $NiCo_2S_4$/CdS hetero-nanowires". *Submitted to Chemical Engineering Journal (2019)*

C. Li, H. Wang, **S. Bonabi Naghadeh**, J. Z. Zhang, P. Fang. "Visible light driven hydrogen evolution by photocatalytic reforming of lignin and lactic acid using one-dimensional NiS/CdS nanostructures". *Applied Catalysis B: Environmental* 227, (2018): 229-239

C. Li*****, **S. Bonabi Naghadeh***, H. Wang, K. Xu, Z. Lu, and J. Z. Zhang. "Enhanced Photocatalytic Hydrogen Evolution over 1D CdS by Loading NiS_2 as Cocatalyst under Visible Light Irradiation" *To be submitted.*

Chapter 6: S. Bonabi Naghadeh, *et al*. "Effect of Targeting Ligand on Photothermal Therapy Efficiency using Hollow Gold Nanoparticles" *To be submitted.*

Chapter One

1 Photophysical Properties and Improved Stability of Organic-inorganic Perovskite by Surface Passivation

1.1 Abstract

Organic-Inorganic perovskite materials in form of nanocrystals and thin films have received enormous attention recently because of their unique optoelectronic properties such as high absorption coefficient, narrow and tunable emission bandwidth, high photoluminescence (PL) quantum yield, long exciton lifetime, and balanced charge transport properties. These properties have found applications in a number of important fields, including photovoltaic (PV) solar cells, light emitting diodes (LEDs), photodetectors, sensors, and lasers. However, the stability of the materials and devices are strongly affected by several factors such as water moisture, light, oxygen, temperature, solvent, and other materials in contact such as metal oxides used in devices. Defects, particularly those related to surface states, play a critical role in the stability as well as performance of the perovskites. Various surface modification and defect passivation strategies have been developed to enhance stability and improve performance. In this chapter, we review some recent progress in the development of synthetic approaches to produce high quality nanostructured and bulk film perovskites with controlled properties and functionalities. we also highlight the degradation

mechanism and surface passivation approaches to address the issue of instability. To help gain deeper fundamental insight into mechanisms behind degradation and surface passivation, relevant properties, including structural, optical, electronic, and dynamic, are discussed and illustrated with proposed models.

1.2 Introduction

Because of the ever-increasing energy demands and environmental impact of our current major sources of energy such as fossil fuels, research in renewable energy is crucial to achieving environmental sustainability. Solar power is arguably the cleanest and most abundant source of energy and can be harvested and converted into electricity using photovoltaic (PV) cells. The first generation of solar cells was based on silicon crystals as the predominant semiconductor for PV technology.[1] However, high cost and multi-step manufacturing processes requiring high temperature (>1000°C) limit their large scale applications, and it is therefore important to develop alternatives.[2]

Organic-inorganic metal halide (OMH) perovskites are an interesting class of materials with interesting properties and promising applications and have drawn significant attention in recent years. “Perovskite” generally refers to a broad group of materials with the same structure as $CaTiO_3$, first discovered in 19th century.[3] The general formula for perovskite is ABX_3 with A and B being large and small cations, respectively and X as anion. Hybrid organic-inorganic perovskites are a subclass of the perovskite family with inorganic cations including cesium (Cs^+), rubidium (Rb^+) and organic components such as methylammonium (MA:$CH_3NH_3^+$) and formamidinium

($FA:CH(NH_2)_2^+$) in the A site, which offer opportunities to tune the properties and functionalities of the perovskites.[4] The X site can also be varied from a single halide (Cl^-, Br^-, I^-) or mixed halides to other molecules such as borohydride (BH_4^-), azide (N_3^-), and cyanide (CN^-).[5-6] Furthermore, perovskites can be doped with other elements to rationally alter their electronic and optical properties. The flexibility in composition variation, in conjunction with easy and low cost processing, tunable bandgap, large absorption coefficient, long exciton lifetime, and large charge carrier mobility,[7-9] makes them outstanding candidates for various applications, such as PV solar cells, light emitting diodes (LEDs), photodetectors, sensors, lasers and photoelectrochemical cells.[10-14]

The first PV cell based on OMH perovskite as visible light sensitizer was reported in 2009 with power conversion efficiency (PCE) of ~3.8%.[15] Since then, significant progress has been made in terms of both understanding the fundamental properties of the materials and improving the solar cell structure for higher efficiency. The PCE was increased to 9.7% with nanostructuring techniques such as depositing $MAPbI_3$ nanocrystals (NCs) on crystalline TiO_2 surface.[7] In 2013, Liu *et al.* reported ~15% PCE with $MAPbI_3$ as the sole light absorber only by modifying device structure to planar heterojunction under simulated sunlight condition.[16] This achievement proved the great potential of OMH perovskites to perform as both light absorber and active layer. In 2015, Yang *et al*. achieved PCE exceeding 20% with high quality $FAPbI_3$ films.[8] Most recently, the PCE was pushed to over 25% in a tandem configuration with silicon[17], which is comparable to their commercialized counterparts. The narrow

emission bandwidth, high photoluminescence (PL) quantum yield (QY), and broadband color tunability of the perovskite NCs or quantum dots (QDs) also makes them promising for other applications such as light emitting diode (LED) devices besides PV applications.[12, 18-19]

Despite the great promise for various applications, there are still some issues that limit large scale applications of these OMH perovskites. The most important issue is likely their instability toward environmental factors such as UV light, humidity, oxygen, solvent, temperature, and other materials in contact in devices.[20-23] Another potential issue is the toxic lead in the material, which promoted active search for replacement.[24] Studies have shown that the material instability is at least partly related to surface properties of the materials, especially defects.[25-26] Therefore, due to their large surface to volume (S/V) ratio, perovskite nanocrystals (PNCs) or perovskite QDs (PQDs) have been used as good model systems to study the issue of instability and for developing strategies for stabilization.[22] Accordingly, different approaches have been reported on surface modification and passivation, including the use of molecular capping ligands, metal oxide shells, and organic polymers.[27-29] There has also been significant effort in exploring the use of other metals to replace Pb, *e.g.* Sn, Ge, Sb, and Bi, which all have shown PV performance inferior to Pb to date.[24, 30]

In this chapter, we review recent progress in the development of different synthesis approaches to produce high quality OMH perovskites and to control their structural and photophysical properties. A major emphasis is given on approaches involving surface passivation or capping ligands used to enhance their functionalities

and improve their stability towards different environmental factors such as water moisture, oxygen, light, solvent and other materials in contact. New fundamental insights into the issue of stability and related surface passivation are provided based on detailed characterizations of the perovskites using a combination of structural, optical and ultrafast dynamics studies.

1.3 Synthesis and Structural and Optical Properties of Perovskites

Controlling the structure is very important for semiconductor nanocrystals, since their shape and size can significantly affect their chemical and physical properties. In recent years, different strategies have been developed to control the PNC structure, mainly by varying experimental conditions. Even though there are significant differences in optical and electronic properties of PNCs and bulk material, such as faster charge transport and higher PL quantum yield in bulk versus higher surface-to-volume ratio, easier processability and functionalization in PNCs, various capping ligands with different molecular structure has been used to control nucleation and growth of PNCs as well as perovskite bulk films. The surface ligands also serve to passivate surface defects and improve stability and properties such as PL of the perovskites. In the following, we discuss different surface passivation approaches for PNCs and bulk films.

1.3.1 Synthesis and Ligand Optimization for Organic-inorganic PNCs

The colloidal organic-inorganic $MAPbBr_3$ PNCs was pioneered by Schmidt *et al*., who employed straight alkyl ammonium bromide as capping ligands to stabilize $MAPbBr_3$ via a solvent induced precipitation method.[31] These capping ligands help to terminate the growth process, resulting in $MAPbBr_3$ PNCs with 20% PL QY. A year later, the same group reported improved PL QY up to ~83% using the same capping ligands just by optimizing the ratio of octylammonium bromide:MABr:$PbBr_2$ (Figure 1a).[32] The large enhancement of PL QY was attributed to the passivation of uncoordinated bromide and lead ions by octylammonium and octadecene, thereby reducing nonradiative recombination. Actually, it was later demonstrated that octadecene can be effectively removed, indicating the weak interaction between octadecene and PNCs.[33] It was also found that some rectangular NCs coexist in the products (Figure 1a), which were later shown to be 2D $MAPbBr_3$ perovskite nanoplatelets (PNPs) with different layers (Figure 1b).[34] Alkyl ammonium salt, such as octylammonium bromide, functions as a soft-template, which induces the formation of both spherical-like NCs and NPs.

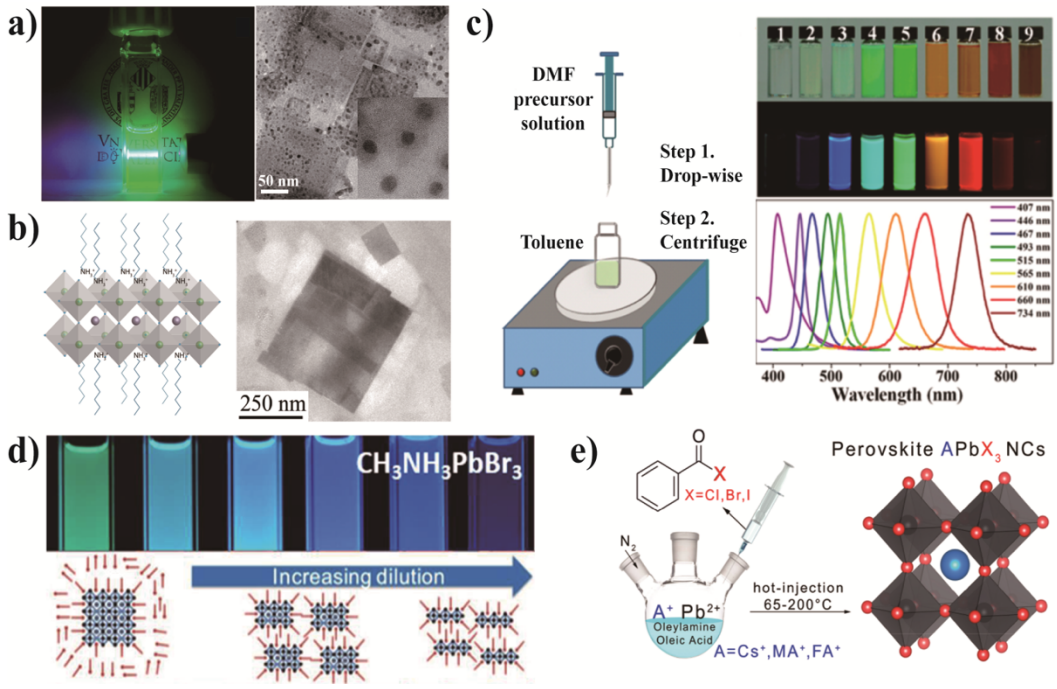

Figure 1-1-a) Image of the $MAPbBr_3$ PNCs dispersed in toluene under UV-laser pointer excitation (left) and TEM image of $MAPbBr_3$ PNCs (right). (b) Schematic illustration of 2D PNPs (left) and TEM image of purified $MAPbBr_3$ NPs. c) Schematic illustration of LARP technique (left), pictures of $MAPbX_3$ PNCs under room light and UV light and PL emission spectra of $MAPbX_3$ PNCs. d) Photograph of $MAPbBr_3$ PNCs suspensions with different dilutions under UV light. e) Scheme of colloidal synthesis of lead halide PNCs using benzoyl halides as halide precursors.

Uniform $MAPbX_3$ PNCs with high PL QY (~70%) was developed by Zhang *et al.* via a ligand-assisted reprecipitation (LARP) approach, in which N,N-dimethylformamide (DMF) and toluene were regarded as solvent and anti-solvent, respectively (Figure 1c).[18] Unlike single alkyl ammonium bromide, both octylamine and oleic acid were utilized as capping ligand, resulting in well-passivated PNCs with good dispersibility. The strong PL stems from increased exciton binding energy, small sized particles, and proper surface passivation. Moreover, the emission of $MAPbX_3$ PNCs can be tuned through the entire visible range by varying the halogen ratio (Figure

1c).[18]Although the product yield of PNCs is low, this approach is simple and produces PNCs with excellent optical properties. As another example, $MAPbX_3$ PNPs with layer-dependent optical properties were produced using the LARP method and by varying the ratio between octylammonium and MA.[35] Li *et al.* extended this method to the synthesis of all-inorganic $CsPbX_3$ PNCs[36]. It should be noted that $MAPbX_3$ PNCs produced this way without purification tend to suffer from agglomeration, decomposition, or further structural change. Even simple dilution can induce transformation from PNCs to PNPs due to excess amine and osmotic swelling (Figure 1d).[37] Also, capping ligands binding to the PNCs are highly dynamic,[33] and, therefore, the PNCs can degrade or change because of the loss of ligands during purification.

As a common method for synthesizing all-inorganic $CsPbX_3$, hot-injection is also versatile for making hybrid $MAPbX_3$ PNCs.[38-40] For instance, $MAPbX_3$ PNCs with 15-50% PL QY were obtained by Vybornyi *et al*. via hot-injection method.[38] Although no polar solvent was involved, the $MAPbX_3$ PNCs still decomposed or aggregated in weeks, similar to $MAPbX_3$ PNCs prepared via an emulsion method.[41] This shows that organic-inorganic hybrid $MAPbX_3$ perovskites are much more labile than that of all inorganic $CsPbX_3$ due to the lower formation energy of $MAPbX_3$ and volatile constituents like CH_3NH_2 and HX.[41] As ternary compounds, $MAPbX_3$ and $CsPbX_3$ are usually prepared with two precursors such as MABr/CsBr/Cs oleate+$PbBr_2$, which limits the variation of composition to some degree. On the basis of the method proposed by Wei *et al.*,[42] Imran *et al*. demonstrated an alternative "three-precursors approach" (Figure 1e) in which $CH_3NH_3^+$ and Pb^{2+} were dissolved in fatty acid followed by the

injection of a benzoyl halide precursor.[39] $MAPbX_3$ PNCs with fine morphology, controllable size distribution and excellent photonic properties were obtained due to the high boiling point of benzoyl halide and controllable release of the halide ions. More importantly, this strategy can be extended to the synthesis of $CsPbX_3$ and $FAPbX_3$ PNCs with minor modification. In addition, several other techniques have shown good potential for fast and large-scale synthesis and structural control, *e.g.* template method,[43-44] ultrasound,[45-46] pulsed laser irradiation,[47] ligand-mediated transport[48] and electrospray.[49]

Given the chemical instability of $MAPbX_3$, $FAPbX_3$ has recently attracted considerable attention due to its high thermal stability, broad color tunability and long lived hot carriers.[50-57] Perumal *et al.* synthesized $FAPbX_3$ PNCs via the LARP method using common oleic acid and octylamine ligands. However, the obtained $FAPbBr_3$ PNCs show a wide size distribution (1-30 nm). Similar broad size distribution was found by Kovalenko *et al.* using synthesis conditions adopted from that for $CsPbBr_3$ PNCs.[53] The broad distribution is attributed to deprotonation of FA^+ caused by oleylamine. By substituting unprotonated oleylamine with oleylammonium bromide, monodisperse $FAPbBr_3$ PNCs with 5% standard size deviation were obtained using a hot-injection method, in which the average size could be tuned from 5 to 50 nm via altering the amount of oleylammonium bromide and reaction temperature.[53] Later, $FAPbI_3$ PNCs with high QYs (>70%) and dispersibility were synthesized by the same group.[58] In striking contrast with the limited chemical durability of $MAPbI_3$ and phase transformation of $CsPbI_3$, $FAPbI_3$ PNCs with nearly cubic structure exhibit much better

stability for several months. Furthermore, by using a droplet-based microfluidic platform, the Kovalenko's group studied the $FAPbX_3$ PNCs growth conditions, shape evolution, and halide ion segregation.[59-60] In related studies, Wang *et al*. demonstrated the controlled synthesis of FA^+-Cs^+ double cation perovskite nanowires and nanosheets by introducing bis(2-ethylhexyl)-amine for morphological modulation.[61] The synthesis of $FAPbX_3$ PNCs via LARP method at room temperature has also been reported.[56, 62] Overall, due to the larger ionic radius and higher tolerance factor, compared to MA^+ and Cs^+, FA^+-based lead halide perovskites show some advantages in terms of thermal stability and wide tunability over the red-infrared regions.

1.3.2 Size and Structural Control

For inorganic semiconductor nanocrystals (NCs), their optical and electronic properties depend strongly on size, especially when the size is smaller than the Bohr exciton radius, due to quantum confinement effect,[35] and, to a lesser degree, on shape. Size and shape can thus be used to alter their properties and functionalities for different applications. Structural control can usually be achieved by varying the experimental conditions to alter the nucleation and growth processes of the NCs.

For PNCs, while the synthesis is often relatively simple using templating strategies,[43] the removal of templates used for structural control remains a challenge. The template approach is also ineffective for continuous size control of PNCs with respect to that of liquid-phase synthesis. For hybrid organic-inorganic $MAPbX_3$ PNCs, LARP strategy affords advantages including large-scale synthesis, open environment,

and room temperature.[18] $MAPbBr_3$ PNCs with different size and high PL QY (93%) were achieved by Huang *et al*. through controlling the temperature of anti-solvent toluene (Figure 2a).[63] With the lower temperature of anti-solvent, smaller PNCs were obtained due to the slower growth processes, resulting in blue-shifted PL. Similar results was achieved by varying the concentration of organic capping ligands. Since the chain structure of ligands creates steric hindrance for the delivery of monomers, the growth rate for each crystal facet will be affected with varying the amount of capping ligands.[64]

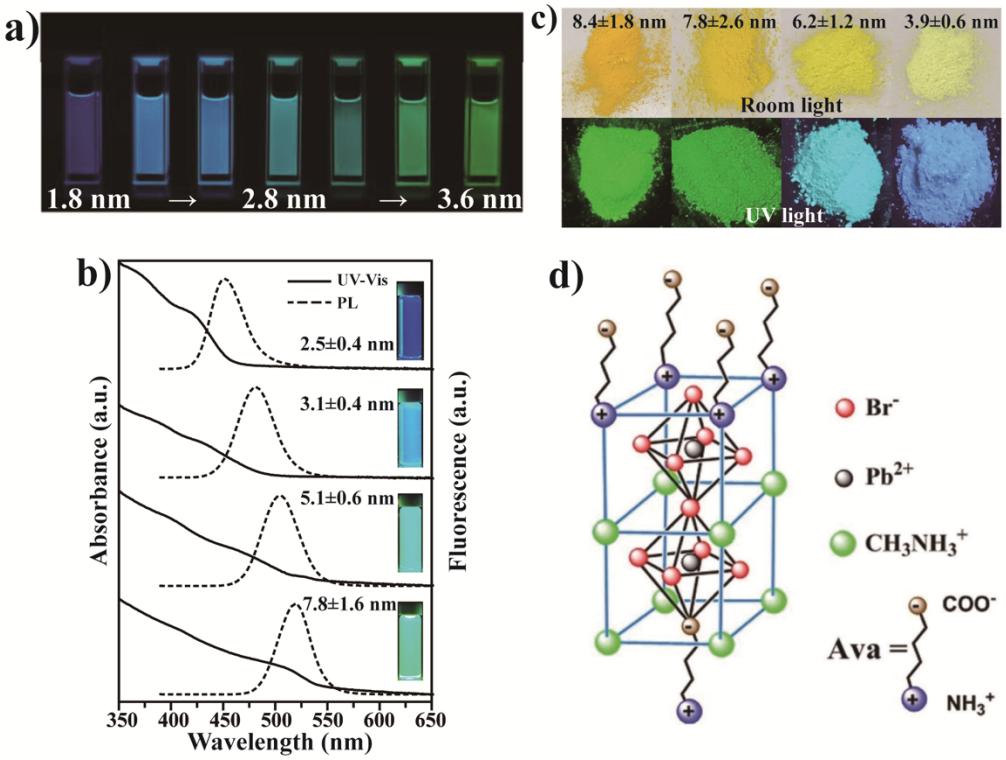

Figure 1-2 - Figure 2 Organic-inorganic $MAPbX_3$ PNCs with tunable size prepared though varying the reactive temperature and concentration of capping ligands. a) Image of $MAPbX_3$ PNCs with tunable size under UV light. b) UV-vis and PL spectra of $MAPbX_3$ PNCs prepared with different concentration of APTES. c) Pictures of $MAPbX_3$ PNCs synthesized with different

concentration of amino acid. d) Schematic illustration of crosslinked $NH_2C_4H_9COOH(MAPbBr_3)_n$ *(n=2)*

In a different approach, branched capping ligand (3-aminopropyl) triethoxysilane (APTES) and polyhedral oligomeric silsesquioxane (POSS) PSS[3(2aminoethyl)amino]propylheptaisobutyl substituted (NH_2-POSS) have been demonstrated as excellent passivating ligand and stabilizers by our group.[21] The size of $MAPbBr_3$ PNCs with high uniformity can be precisely tuned from hundreds of nanometers to several nanometers, owing to their strong steric hindrance (Figure 2b). In contrast, dot, sheet and belt-like PNCs always coexist when straight capping ligands are used.[21, 65-66] Additionally, bidentate amino acid have also been utilized as capping ligands to tune the particle size and layer thickness of $MAPbBr_3$ (Figure 2c).[67] Because of the protonation reaction between $–NH_2$ and –COOH, $–NH_3^+$ end groups can act as $CH_3NH_3^+$ while $COO^–$ functions as $Br^–$ in terms of passivation of surface defect sites (Figure 2d). Therefore, amino acids can function as a capping ligand and linker to tune the particle size and layers of $MAPbBr_3$.[67-68] Similarly, 1D perovskite nanowires, perovskite nanorods and 2D perovskite PNPs can also been prepared by tuning the concentration of amino and carboxylate ligands.[69-70]

1.3.3 Surface Passivation Mechanism

The surface of NCs or QDs, including PNCs or PQDs, plays a critical role in their stability and other properties and functionalities. Surface passivation is a common strategy used to stabilization and functionalization. PNCs are particularly challenging

for surface passivation due to the presence of three components, *e.g.* MA^+, Pb^{2+}, and X^-, each of which likely requires a different ligand for proper passivation, as shown in Figure 3. Therefore, multiple ligands are needed for PNC passivation. Also, given the equilibrium of $CH_3NH_3^+ \rightleftarrows CH_3NH_2 + H^+$ any factor that can cause deprotonation of the $CH_3NH_3^+$ will shift the equilibrium to the right, likely causing degradation since the product CH_3NH_2 is no longer attracted by the halide anions in the crystal.

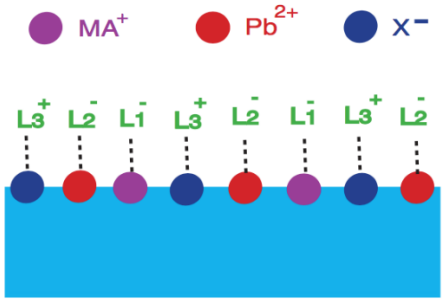

Figure 1-3- Schematic illustration of multiple ligands required for proper passivation of the ternary perovskite.

In order to understand the interaction between the PNCs and surface ligands, Roo *et al*. pioneered the study of $CsPbBr_3$ PNCs surface chemistry using nuclear Magnetic Resonance (NMR) spectroscopy.[33] The loss of surface ligands during the purification procedures was attributed to the highly dynamic ligands binding to the PNCs (Figure 4a), which has also been confirmed by others.[71] By adding excess amine, the interplay between PNCs surface and oleic acid can be enhanced due to the formation of alklammonium oleate. Therefore, adding small amounts of excess amine and carboxylic acid ligands before purification could help to maintain the colloidal integrity

and PL of the PNCs because of the acid-base equilibrium achieved. Through experimental and computational approach, Ravi *et al.* unveiled that oleylammonium binds to the PNCs by substituting surface Cs^+ sites via the formation of H···Br hydrogen bond, which is thermodynamically favored due to the reduced surface rumpling (Figure 4b).[72] Moreover, oleic acid or oleate was not bound to the PNCs surface based on nuclear Overhauser effect spectroscopy (NOESY), but necessary for the stability of PNCs in the washed sample. Similarly, Almeida *et al.* found that the phase and morphology control of $CsPbBr_3$ PNCs can be achieved via altering the concentration and ratio of amino/carboxylic ligands due to the large effect of acid-base equilibrium on the solubility of $PbBr_2$.[73] These studies suggest that the combination of amino and carboxylic acid is critical to the surface passivation, good dispersibility, morphology and phase of PNCs. However, the interaction between ligands and surface of PNCs seems to be generally weak, and ligands with stronger interaction are likely better for stability and need to be explored.

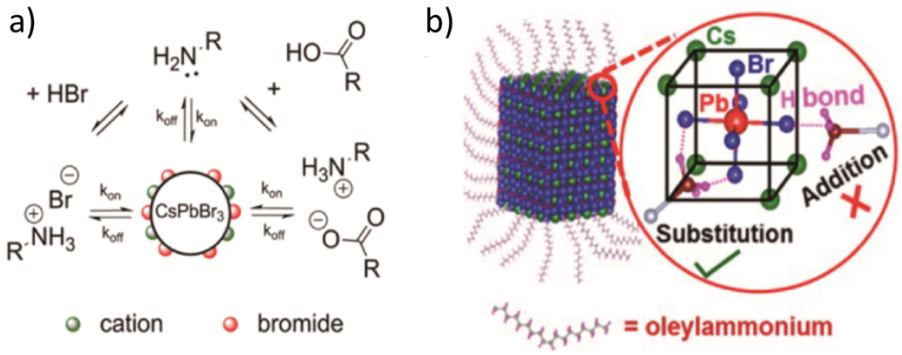

Figure 1-4- a) Schematic representation of the dynamic surface stabilization by amino and carboxylic acid. b) Schematic illustration of the possible binding of oleyammonium to $CsPbBr_3$ by forming hydrogen bonds with Br^-.

1.3.4 Perovskite Film Fabrication Techniques and Effect of Surface Passivation

Fabricating high quality perovskite bulk films is crucial for different applications. Film thickness, morphology and grain size of the resultant perovskite film can significantly affect the charge dissociation rate, diffusion length, charge carrier dynamic and other properties.[74-76] There are several factors contributing to perovskite film quality such as deposition method, film thickness, maximized coverage on substrate, environmental conditions (light, moisture, oxygen), annealing temperature, phase purity, and solvent.[77] However, considering the fact that film morphology and grain sizes are mainly controlled by the crystallization method, understanding and optimization of the crystallization process have been a great interest.[77] One important character of bulk films is the density and distribution of defects that can critically affect their properties and functionality. Similar to PNCs, surface passivation has been used to remove or reduce surface defects, based on ligands such as thiophene and pyridine as Lewis bases[78], carbon material (fullerenes, graphene oxide, and carbon nanotubes)[79-

[80], and additional iodide ions.[8] Here, we briefly discuss a few examples of deposition techniques and related approaches for surface passivation.

1.3.4.1 Film Fabrication Techniques

Several techniques developed for perovskite film fabrication are summarized in Figure 5. Among them, solution processing is the most common as it is simple and low-cost. There are two main approaches with this technique. The first approach involves a "one step" route, also called solvent engineering method, in which the pre-mixed precursor solution is deposited on the substrate by spin coating.[81] Initially, Lee *et al*. successfully fabricated a perovskite film by mixing methyl ammonium halide powder with lead halide in 3:1 stoichiometry ratio in DMF.[82] Later on, other groups investigated the effect of different processing parameters such as precursor stoichiometry[83], other solvents and addition of an anti-solvent to promote fast crystallization, and annealing temperature on perovskite film quality.[84-85]

The second approach is a "two-step" crystallization method that involves sequential deposition. In this approach, the precursor layers are deposited separately and react on the substrate to make the film. This was first reported for $MAPbI_3$ film.[86] PbI_2 is first spun-coated on a mesoporous TiO_2 film and then soaked in CH_3NH_3I solution of isopropanol. This method was subsequently improved by solvent annealing[87] or changing the solvent from DMF to dimethyl sulfoxide (DMSO).[88] Although the two step method is more versatile than the one-step approach,

reproducibility is a major challenge since so many factors, such as immersion time, temperature, and solution concentration, can affect the outcome.

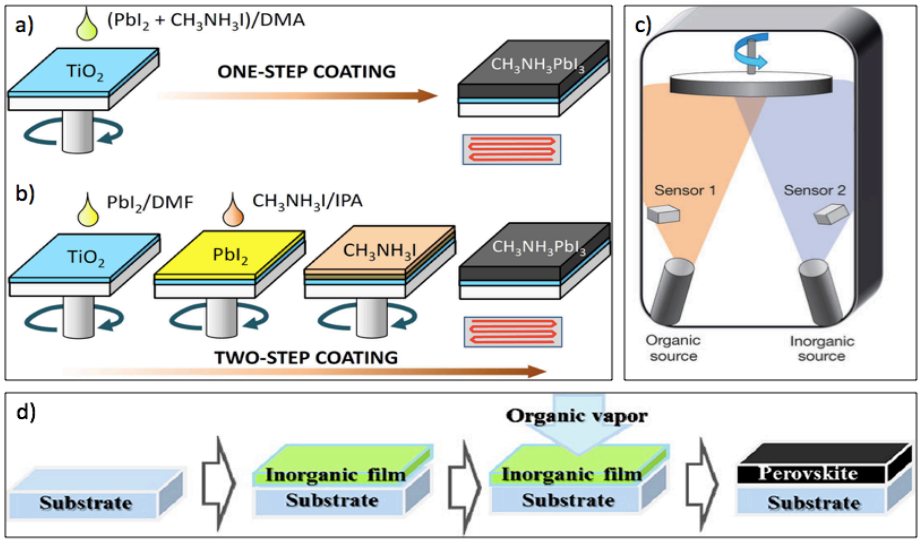

Figure 1-5- Perovskite film fabrication techniques. a) One-step solution process based on the mixture of PbI2 and MAI. b) sequential coating of PbI2 and MAI. c) Dual source co-evaporation using PbCl2 and MAI source. d) Vapor-assisted solution process using the MAI organic vapor to react with the PbI_2 film.

Even though solution processing techniques dominated the perovskite film fabrication field, vapor deposition showed considerable success in producing high quality uniform films. The technique consists of co-evaporation or sequential evaporation of precursors followed by their deposition on a substrate. This was first developed to make $CH_3PbI_{3-x}Cl_x$ perovskite film by co-evaporation of MAI and $PbCl_2$ at 120°C and 350°C respectively in an N_2 rich environment under high vacuum.[16] They deposited the vaporized precursor on a c-TiO_2 laminated FTO glass followed by annealing of the perovskite film for better crystallization. Although the resulting film

has lower concentration of pinholes and smoother surface, choice of substrate was found to affect the crystallization of the perovskite film. MAI, particularly showed lower affinity toward deposition on some substrates causing film decomposition.[89] Tao *et al*. addressed this issue by applying a fullerene intermediate layer that improved the physisorption of MAI on the substrate.[90] Another concern about this technique is the cost associated with high vacuum required for thermal evaporation. Yang *et al*. demonstrated lower temperature hybrid deposition technique called vapor-assisted solution process (VASP).[91] With this method, they deposited PbI_2 precursor by solution processing and then vaporized MAI by heating it in a petri dish at lower temperature (Figure 5d).[91] This method resulted in fabrication of smooth, uniform $MAPbI_3$ film with micrometer sized grains. Figure 6 shows scanning electron microscopy (SEM) images of perovskite films fabricated by this hybrid technique.[16] Later on, yang *et al*. identified formation of $MA_2Pb_3I_8(DMSO)_2$ intermediate phase during the annealing process as the key step in improving film quality and achieving higher efficiency.[92] In general, compared to solution process, the films prepared by vapor deposition show better surface coverage on substrate, higher uniformity, slightly larger grain size, less pinholes and better control on film thickness.

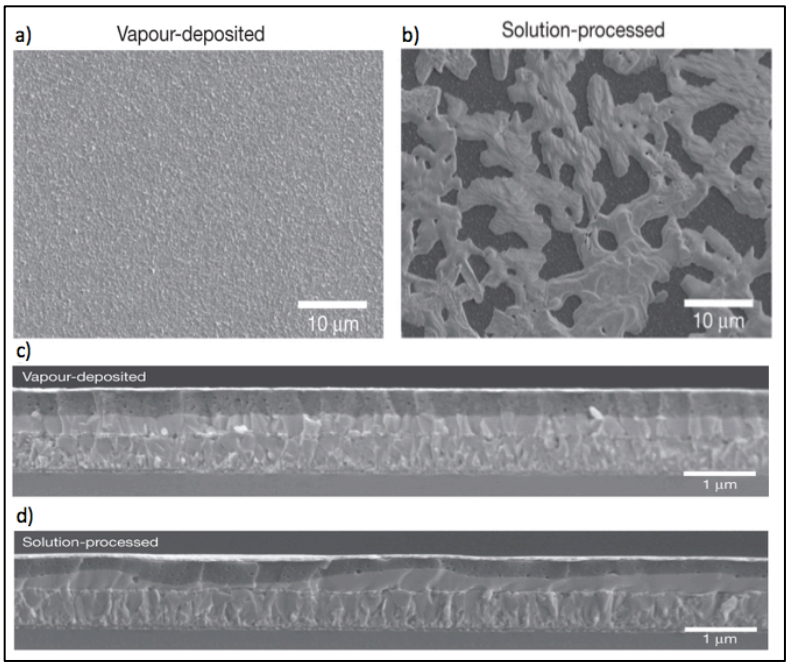

Figure 1-6- Perovskite film morphology: SEM of a) vapor deposited perovskite b) Solution processed perovskite c) transactional view of device fabricated with vapor deposited perovskite d) transactional view of device fabricated with solution processed perovskite.

1.3.4.2 Effect of Surface Passivation

Since surface defects have been suggested and identified as a major contributor to instability of perovskites, different strategies have developed to address this issue, often using surface passivation with organic or inorganic molecules. For example, Yang *et al*. showed that by introducing excess amount of iodide ions into the cation solution, the density of deep defects significantly decreased with concurrent increase in PCE to 22.1%.[8] In another study, the $CH_3NH_3PbI_{3-x}Cl_x$ surface was treated with Lewis bases, thiophene and pyridine, that are suggested to bind to the under-coordinated Pb ions in the perovskite crystal and passivate the defects (Figure 7a and b).[78] However, most of these molecules used for surface passivation limit the charge

transfer properties of the material. Tan *et al.* used chlorine-capped TiO_2 colloidal NC film to improve surface binding at low temperature while mitigating interfacial recombination.[93]

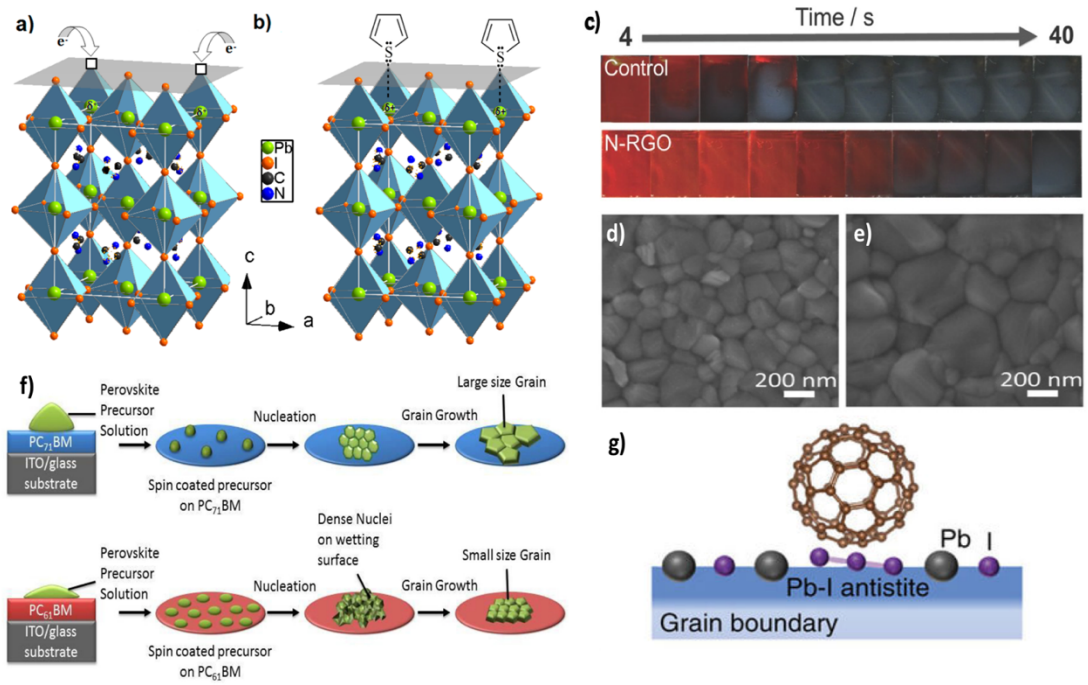

Figure 1-7- Possible nature of trap sites and proposed passivation mechanism. (a) Loss of iodine at the surface of the perovskite leads to vacancy sites (hollow boxes) and a resulting net positive charge residing on the Pb atom (shown in green). (b) Thiophene or p pyridine molecules can donate electron density to the Pb and form a coordinate or dative covalent bond, effectively neutralizing the excess positive charge in the crystal. c) Photographs of perovskite films during crystallization at 100 °C. d) SEM top-view images pristine perovskite and e) perovskite/N-RGO hybrid films. f) Mechanism of perovskite grain growth on $PC_{71}BM$ and $PC_{61}BM$ layers with different wettability. g) a schematic of in situ *passivation of halide-induced deep trap: PCBM adsorbs on Pb-I antisite defective grain boundary during perovskite self-assembly.*

Another passivation approach is to use graphene derivatives. For example, amphiphilic graphene oxide (GO) was used as an insulating buffer layer between the hole transport layer (HTL) and perovskite to decelerate charge recombination.[94] Hadadian *et al*. incorporated N-doped reduced graphene oxide (N-RGO) nanosheets on perovskite and observed simultaneous surface passivation and improved morphology at the interface which, significantly enhanced optical properties.[95]Addition of N-RGO to perovskite film, slowed down the crystallization process and increased the perovskite grain size leading to higher current and fill factor (FF) (Figure 7c-e).[95]

Due to the unique electronic, thermo-stability and versatility of the carbon materials, the other members of this family, *e.g.*, fullerene, carbon, and carbon nanotubes (CNTs), can also serve as passivating ligands for increased efficiency, reduced hysteresis, and improved stability. For instance, Shao *et al*. applied a double fullerene layer ($PC_{61}BM/C_{60}$) onto an $MAPbI_3$ film.[96] Thermal admittance spectroscopy (TAS) analysis confirmed two orders of magnitude less in density of trap states after interfacial layer passivation on the perovskite film, when compared to the device without the interfacial layers. The increased surface passivation effect of [6,6]-phenyl-C61-butyric acid methyl ester ($PC_{61}BM$) on $MAPbI_3$ was observed as a blue-shift in PL spectra of the films and eventually led to reduced recombination at the interface, increased carrier lifetime and mobility, thus resulting a high PCE of around 15%.[96-97] Zhong and co-workers also demonstrated a novel electron-transporting material (ETM) based on mesostructured fullerene which is crystalline, hydro-phobic, and cross-linked, rendering it solvent and heat resistant for successive PSC

fabrication.[98] The resulting mesostructured n−i−p solar cells exhibited reduced recombination and hysteresis, and a PCE above 15%, surpassing the performance of similar devices prepared using mesoporous TiO_2 and well above the performance of planar heterojunction devices on amorphous or crystalline PCBM (Figure 7g).[98] A hierarchical dual scaffolds of a quasi-mesoscopic inorganic (TiO_2) layer and a percolating $PC_{61}BM$ also reported to improve the charge separation and electron transport in bulk perovskite.[99] Another cross-linkable fullerene derivatives as charge collection layers in n−i−p planar junction PSCs was introduced by Wojciechowski *et al*.[100] The cross-linked fullerene layers are insolubilized and deliver improved performance in solar cells enabled by a controllable film thickness. There may be long-term stability benefits due to cross-linking of these materials which is inhibiting morphological changes and crystallization of the fullerene layer.[100] The solar cell device performance was even further improved by using $PC_{71}BM$ ETL (Figure 7f).[79] Upama *et al.* reported a simple method for achieving a low-temperature, hysteresis-free, solution processed PSCs, using fullerene electron transport layer (ETL).[79] The underlying mechanisms of superior performance of devices with $PC_{71}BM$ ETL were correlated with fullerene surface wettability and perovskite grain size. $PC_{71}BM$ fullerene ETL had lower wettability with perovskite precursor solution, assisting the growth of large size perovskite grain. As a result, the $PC_{71}BM$/perovskite film had lower bulk and interface defects leading to better solar cell device performance.[79] The diffusion of ions/molecules within PSCs is an important degradation process in the device. Bi *et al.* designed a nanostructured carbon layer to suppress the diffusion and

improve the stability.[101] This nanocarbon layer benefited the diffusion of electron charge carriers to enable a high-energy conversion efficiency.[101]

Carbon nanotubes with excellent properties have also been extensively used in perovskite based solar cells. For instance, Shapter *et al.* reported major enhancement in the stability and efficiency of PSCs by using single-walled carbon nanotubes (SWCNTs) in the mesoporous photoelectrode.[80] Presence of SWCNTs in the TiO_2 nanoparticles-based photoelectrode, suppressed the hysteresis and therefore enhanced both the light and long-term storage stability of PSCs.[79] In another study, Snaith and co-workers demonstrated a well-designed approach to mitigating thermal degradation by embedding functionalized single-walled CNTs in an insulating polymer matrix, resulting in long-term stability in high-efficiency PSCs.[102]

1.4 Origin of Instability and Strategies for Stabilization of Perovskites

As mentioned earlier, instability of organic-inorganic perovskites is a major obstacle to their practical applications. Environmental factors, such as light, oxygen and humidity, play a critical role in material and device stability. Recent studies have started to shed light on the origin and mechanism of perovskite degradation, and strategies have been developed to stabilize them, involving encapsulation and surface passivation using capping ligand.

1.4.1 Perovskite Degradation Mechanism

Among the factors that affect perovskite stability, light is particularly important for PV applications. The interaction between light and perovskite is found to be

dependent on other environmental factors. For example, the presence of oxygen or a rise in temperature can cause degradation of perovskite in conjunction with light, while light in inert atmosphere does not seem to degrade the perovskite.[20, 103-105] In particular, light with oxygen can lead to the formation of superoxide free radicals that in turn cause deprotonation of the ammonium molecule, forming water and highly volatile methylamine (CH_3NH_2) molecules that evaporate, leaving behind solid PbI_2 film.[20-103] Equations 1 and 2 illustrate the proposed degradation mechanism.

$$CH_3NH_3PbI_3 \rightleftarrows PbI_2 + CH_3NH_3I \qquad (1)$$

$$2CH_3NH_3I + \frac{1}{2}O_2 \xrightarrow{h\nu} 2CH_3NH_2 + H_2O + I_2 \qquad (2)$$

In addition, the degradation can also originate from the photo-oxidative nature of the halide anion (I^-).[20] With light in ambient atmosphere, the iodide anion oxidizes by donating an electron to the surrounding O_2 molecules, transforming it to superoxide free radical (O_2^-) and producing iodine atom (I) that eventually leads to iodine molecule (I_2) formation.[20] The superoxide free radical can degrade perovskite.

Another factor that could degrade perovskite together with light is heat or elevated temperature.[105] Abdelmageed *et al.,* found that perovskite subjected to intense light (~ 3.5 suns) in inert atmosphere at 75ºC degraded into a mixture of lead iodide and metallic lead.[105] It was proposed that the combination of the light and heat led to the dissociation of the Pb-I bonds as in equation 3.[105] To confirm that hypothesis, films of pure PbI_2 were subjected to the same conditions and results indicated the conversion to metallic lead.[105]

$$PbI_2(s) \underset{\lambda,\Delta}{\rightarrow} [Pb^{2+} + 2I^- \rightarrow Pb + 2e^- + 2I^-] \underset{\lambda,\Delta}{\rightarrow} Pb(s) + 2I(g) \quad (3)$$

Furthermore, the role of humidity on the stability of perovskites has been investigated by several studies.[106-107] Yang *et al.* proposed that humidity could break down the structure of the hybrid perovskite by creating hydrate intermediate compound that contained an isolated octahedral lead iodide (PbI_6^{4-}) and a solid PbI_2 as in equation 4.[106] This phase separation in the metal halide segment of the perovskite prevents the reversibility of the damage.[106] Other studies confirmed that phase separation and the hydrate intermediate compound formation.[108-109]

$$4CH_3NH_3PbI_3 + 2H_2O \rightarrow (CH_3NH_3)_4PbI_6 \cdot 2H_2O + 3PbI_2 \quad (4)$$

However, other studies reported that the damages of humidity could be reversible in some cases but irreversible in other cases.[107, 109] According to Zhao *et al.*, an intermediate monohydrated $CH_3NH_3PbI_3 \cdot H_2O$ was discovered after subjecting the perovskite to humidity, with no phase separation in the lead iodide part, as demonstrated in equations 5 and 6.[107] After taken the films out from moisture, the perovskite samples recovered to their initial state to a good extent.[106]

$$CH_3NH_3PbI_3 + H_2O \leftrightarrow CH_3NH_3PbI_3 \cdot H_2O \quad (5)$$

$$CH_3NH_3PbI_3 \cdot H_2O \leftrightarrow CH_3NH_3I + PbI_2 + H_2O \quad (6)$$

Moreover, Leguy *et al*. proposed that the exposure time to moisture determines the reversibility of the degradation process.[109] The suggested explanation was that the degradation process starts with the reversible formation of $CH_3NH_3PbI_3 \cdot H_2O$ followed by the irreversible formation of $(CH_3NH_3)_4PbI_6 \cdot 2H_2O$ with extended exposure time.[109]

To study thermal decomposition, films of $MAPbI_3$ were heated at temperatures up to 600°C and the degradation products were observed by using thermal analytical techniques such as thermal gravimetric analysis (TGA) and differential thermal analysis (DTA) coupled with a mass spectrometer.[110] Results indicated that, as the perovskite degraded, gasses of NH_3 and CH_3I were observed, indicating that the organic cations break down and escape the perovskite structure, leaving only the solid inorganic metal halide PbI_2.[110] The proposed degradation mechanism is given in equation 7.[110]

$$CH_3NH_3PbI_3(s) \xrightarrow{\Delta} NH_3(g) + CH_3I(g) + PbI_2(s) \quad (7)$$

Nevertheless, a more recent study showed that not only the temperature range dictate the degradation pathway and the nature of the gas released, but also the effusion rate conditions.[111] Results showed that within the temperature range (140-240 °C) under high effusion rate conditions, gaseous HI and CH_3NH_2 were released as the perovskite degrade as in equation 8.[111] On the other hand, at higher temperatures (around 400°C) and lower effusion rate conditions, equation 8 applies.[111]

$$CH_3NH_3PbI_3(s) \xrightarrow{\Delta} CH_3NH_2(g) + HI(g) + PbI_2(s) \quad (8)$$

In addition to the environmental factors, surface defects play a significant role in the stability of perovskites. For example, Mosconi *et al*. investigated the role of surface defects in the moisture-induced degradation of $MAPbI_3$ surfaces by carrying out *ab initio* molecular dynamics simulations on atomistic level at the perovskite/water interface.[112] The MAI terminated perovskite surfaces were found to be more inclined to degradation with humidity due to the nucleophile substitution of iodine with water

molecules, while PbI_2 terminated perovskite surfaces showed resistance towards humidity (Figure 8). However, in the case of defective PbI_2 facets, surface lead iodide defects such as $(PbI_2)_n$ vacancies were found to initiate the facial solvation of the perovskite, by producing solvated $[PbI(H_2O)_5]^+$ and $[PbI_2(H_2O)_4]$ species, that spread afterwards causing degradation to the whole bulk of the perovskite material.[112]

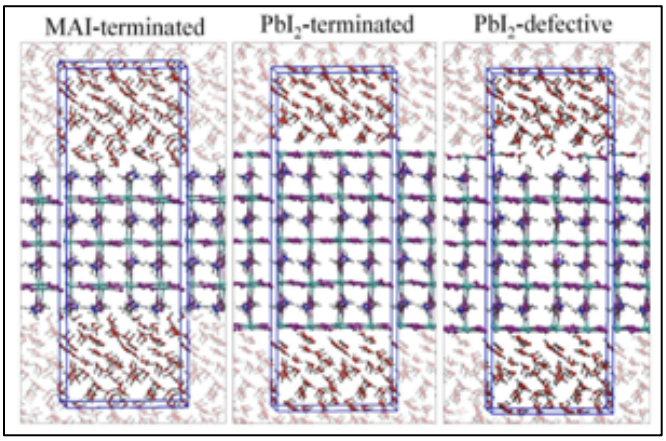

Figure 1-8- Schematic representation of the hydration process of MAI-, PbI2- and defective PbI2- perovskite surfaces.

A similar study was carried out on the interaction of surfaces of $CH_3NH_3PbI_3$ and $CH_3NH_3PbBr_3$ with hydroxyl radicals and hydroxide ions.[113] The desorption of surface CH_3NH_2 is the main step in the degradation process due to the lower activation energy of surface atoms.[113] Hence, PNCs are more prone to experience degradation than bulk or films owing to their higher surface/volume ratio.[114]

1.4.2 Improving Stability of PNCs by Surface Modification

Surface passivation of PNCs using capping ligands can substantially improve their stability again factors that often cause degradation. For instance, didodecyl dimethylammonium sulfide was used as a capping ligand to enhance the stability of cesium lead bromide NCs.[115] The passivated nanocrystals exhibited stability for up to 4 months under ambient conditions (60±5% RH), compared with only 2 hours of stability for the control samples. Other studies investigated the role of other hydrophobic surface passivation treatments to improve air and humidity tolerances of PNCs. For example, poly(methyl methacrylate) PMMA was used to protect methylammonium lead bromide nanocrystals from water in a recent study performed by Li and coworkers.[116] The carbonyl groups of PMMA anchored to the Pb^{+} cations from the perovskite *via* polymer ligand-assisted re-precipitation (PLAR), as shown in Figure 9a, inhibiting the diffusion of water into the perovskite molecules by full coating surface Pb ions.[116] Films were prepared using the polymer treated perovskite nanocrystals through cotton swap painting on glass substrates as shown in Figure 9b, and their stability was tested in two different methods: by immersing the films in deionized water at room temperature for 90 days (Figure 9c), and by dipping the films in deionized water at 90°C for few minutes (Figure 9d). The polymer treatment led to improved surface defects and better water and heat stability.[116] Polyvinylidene fluoride (PVDF) was another polymer matrix used for embedding PNCs in its hydrophobic and thermally stable matrix. Embedded PNCs exhibited 94.6% PL QY and improved

stability against water and UV radiation owing to the interaction between MA^+ and -CF_2-.[117]

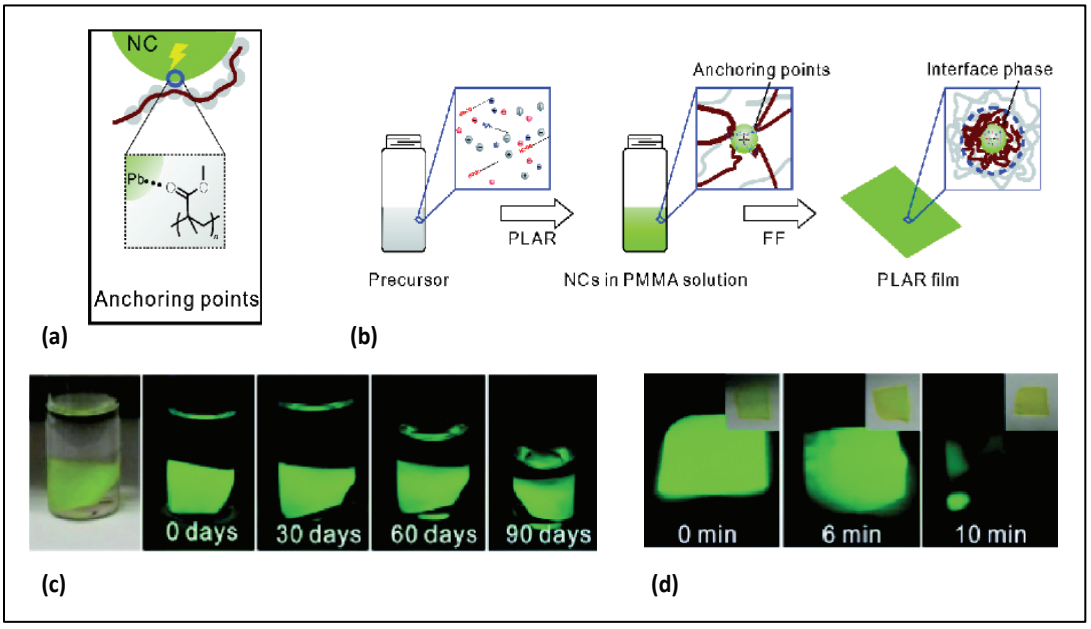

Figure 1-9- (a) Schematic illustration of the anchoring interaction between PMMA and the Pb+ from the PNCs. (b) Schematic illustration of the PMMA/ films preparation steps. (c) Images of PLAR films immersed in deionized water at room temperature for 90 days. (d) I Images of PLAR films subjected to nearly boiling water for 10 minutes.

Another water resisting molecule like polyhedral oligomeric silsesquioxane (POSS) has been used to passivate $CsPbBr_3$ PNCs, which prevented anion exchange and showed great water resistance, resulting in strong green light emitting after ten weeks.[29] Organic acids such as phosphonic acid were also proposed as capping ligand since it can strongly bind to surface Pb^{2+} ions in addition to its strong hydrogen bonding with surface halide ions.[28] In a similar approach, octylphosphonic acid (OPA) dramatically enhances the $CsPbX_3$ stability.[118] Owing to a strong interaction between

OPA and lead atoms, the OPA-capped $CsPbX_3$ NCs not only preserve their high PL QY (>90%) but also achieved a high-quality dispersion in solvents after multiple purification processes.[118]

PNCs passivated by these methods were relatively stabilized to air, however, the instability in polar solvents was still remaining and limiting the perovskite application in biological sensing and solution processing. This instability is usually caused by deprotonation of amino capping ligand by nucleophilic solvent molecules leading to decomposition of PNCs. One of the common methods to overcome this challenge was coating PNCs with silica.[119-121] The first report on embedding PNCs in silica shell used tetramethylorthosilicate (TMOS) as a silica source and the resulting PNC/SiO_2 core–shell particles exhibit improved photostability in both solution and powder forms under illumination for 100 h (Figure 10a).[26] It was suggested that SiO_2 prevent moisture and oxygen penetration. The stability of PNCs embedded in silica shell even further improved by changing silica source to (3-aminopropyl) triethoxysilane (APTES) since the amine groups can also passivate the surface defects on PNCs.[122] Compared to oleyamine as capping ligand, the PL quantum yield of the $CsPbBr_3$ PNCs capped with APTES dropped only 5% after three months (Figure 10b).[122]

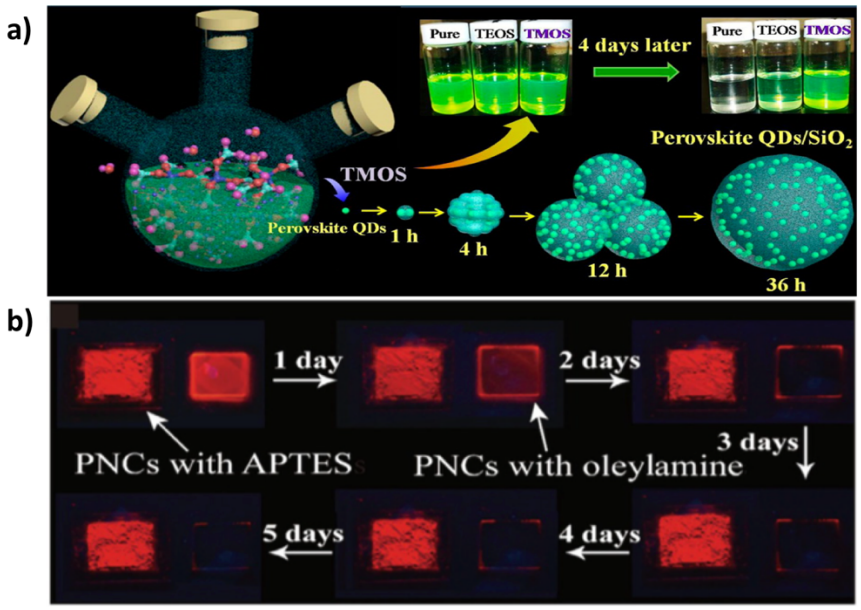

Figure 1-10- a) Schematic of the SiO_2 formation process with increasing stirring time by using TMOS. b) Photographs of red $CsPb(Br/I)_3$ PNCs/SiO_2 powder (passivated by APTES) and red $CsPb(Br/I)_3$ PNC film (passivated by oleylamine) under UV light.

1.4.3 Improved Stability Improvement of Perovskite Thin Film by Surface Modification

Similar to PNCs, surface passivation has been used to stabilize bulk films of perovskites. For example, Marinova *et al*. introduced hindered amine light stabilizers (HALS) such as 2,2,6,6-tetramethylpiperidinyl-4-amonium iodide to suppress degradation of $MAPbI_3$ films.[104] The addition of HALS, mainly on the surface, inhibited the oxidation of I^- to I_2 by interacting with the atmospheric oxygen to form nitroxide radicals, which minimized the interaction of the perovskite with oxygen and acted as a free radical scavenger for superoxide radicals if formed.[104] In addition, surface passivation with a hydrophobic molecule shields perovskite from humidity.[123-126] For instance, oleic acid (OA) was used as a surface passivating agent to significantly

improve the stability of $MAPbI_3$ films and solar cells with humidity (Figures 11a, b).[123] The carboxyl group ($-COO^-$) of OA passivate the surface defects of the perovskite by linking to surface Pb^{2+} and/or $CH_3NH_3^+$.[123] Furthermore, the surface passivation with OA slightly improved the overall performance of the PSCs as the large alkyl molecules of the OA reduced the recombination rate across the hole transport layer (HTL) interface.[123] In another study, engineering of a graded 3D-2D ($MAPbI_3$-$PEA_2Pb_2I_4$) perovskite interface demonstrated advantages with synergistically improved ambient stability and reduced charge recombination.[127] Likewise for the thermal stability, surface treatment with 4-dimethylaminobenzoic acid (4-DMABA) for $MAPbI_3$ films improved their thermal and hygroscopic stability (Figures 11c, d). The carboxyl group of 4-DMABA passivated surface traps (Pb^{2+} sites) of the film, and the longer amino chains protected the perovskite surface.[128] Similarly, carbon nanoparticles (CNPs) was used to significantly enhance the thermal stability of the perovskite that might be due to the changed film morphology.[129]

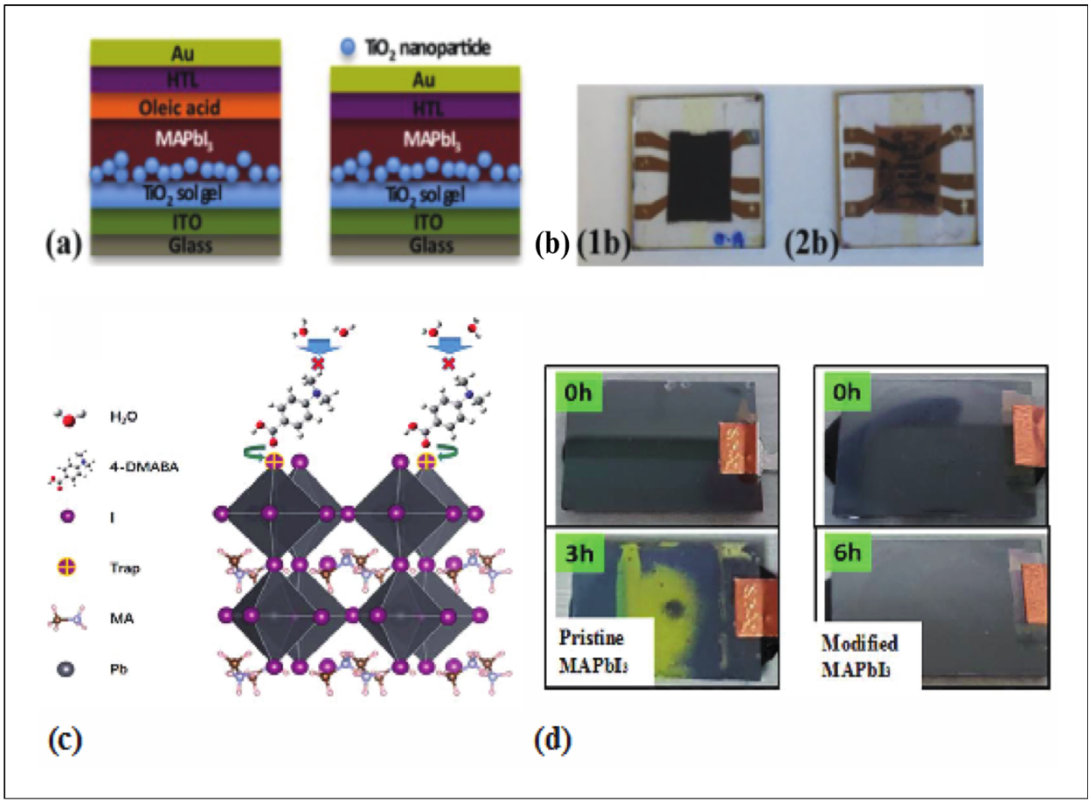

Figure 1-11- Surface passivation of perovskite films and solar cell to enhance stability. (a) Schematic illustrations of PSCs structure with and without surface treatment with oleic acid (OA). (b) Photographs of PSCs with OA (1b) and without OA (2b) after continuous exposure to humidity of 75%RH for 4 months. (c) Schematic graph of surface treatment of perovskite with 4-DMABA molecules. (d) Photographs of perovskite with and without 4-DMABA before and after few hours of aging.

When we compared the passivation strategies between PNCs and bulk films, we realized that the detailed structure of the passivating ligands plays an important role. For example, combination of bulky APTES and linear oleic acid molecule resulted in a very well passivated PNCs with improved stability. However, the same combination does work for bulk film due to steric hindrance between molecules on the surface. On the other hand the stability of bulk film improved significantly using just essentially

linear oleic acid for passivation, which is not effective for PNCs.[123] These findings clearly show the importance of ligand structure in the effectiveness of surface. Figure 12 illustrates the different passivation strategies for PNCs vs bulk films, where bulky headed ligands are effective for PNCs and not bulk while linear ligands are effective for bulk films and not PNCs.

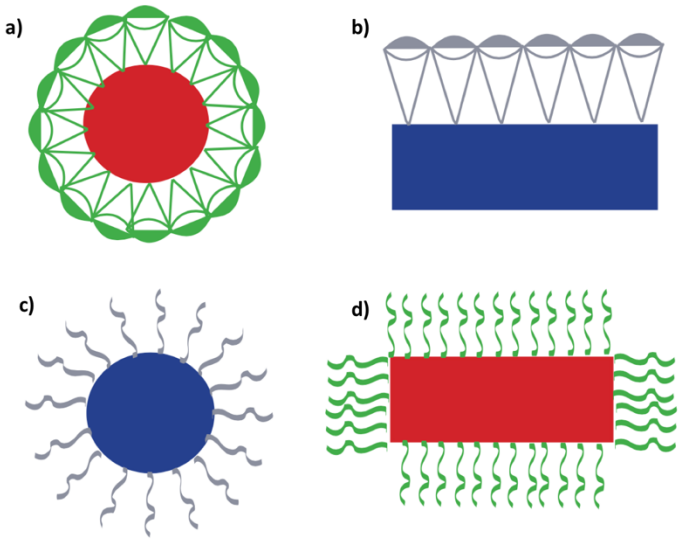

Figure 1-12- Schematic illustration of different passivation schemes for PNCs and bulk films.

1.5 Charge Carrier Dynamic in Organic-Inorganic Metal Halide Perovskites

Study of exciton dynamics of perovskites helps to provide deeper insight into some of the fundamental photophysical and photochemical processes important for applications.[130-132] Two commonly used time resolved techniques are transient absorption (TA) and time resolved photoluminescence (TRPL) spectroscopy. TA is a pump-probe technique used to monitor the ultrafast dynamic of photoinduced short-lived species in molecules or solids, such as free charge carriers, excitons, and polarons.

In this case, the probe pulse monitors the change in absorption following excitation of the pump pulse. In TRPL spectroscopy, the sample is excited with a pulsed laser and the PL intensity is measured as a function of time. The PL is proportional to the population of the emitting states and reports directly on the dynamics of photogenerated species in the material. The dynamics measured are often strongly dependent of the material characteristics, including particle size, shape, crystallinity, morphology, and surface passivation, in the case of NCs or bulk films.

1.5.1 Effect of Surface Modification on Charge Carrier Dynamic in PNCs

The capping ligands of PNCs are important for both their stability and their properties including exciton and charge carrier dynamics.[67, 133] In particular, the capping ligands control surface states that critically affect exciton or charge carrier dynamics including trapping and recombination. For example, the exciton dynamics of green emitted PNCs could be affected by the capping ligands with different chain length.[134] The shorter octylammonium bromide (OABr) capped PNCs exhibit overall lower density of trap states, longer average lifetime of excitons and higher PL QY than PNCs capped with octadecylammonium bromide (ODABr) due to the better solubility of OABr in the medium during synthesis and thus better surface passivation, as shown in Figure 13.

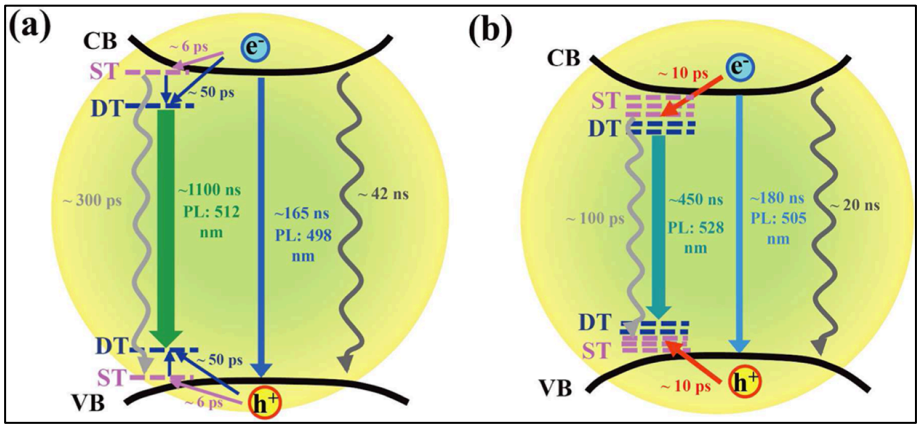

Figure 1-13- Schematic illustration of the energy band structure and proposed assignment of lifetimes of various excitonic processes for (a) OABr capped PNCs and (b) ODABr capped PNCs based on the TA and TRPL investigations.

Other studies also demonstrate that the exciton dynamics of PNCs is strongly related to their surface properties. For instance, Maity *et al*. studied the charge carrier dynamics of $CsPbBr_3$ QD/4,5-dibromofluorescein (DBF) composite.[135] The interfacial hole and electron transfer processes were observed within the time scale at 1-1.25 ps and ~100 fs, which reveals the potential of $CsPbBr_3$ QD/DBF composite for PV applications. In addition, the interactions between tetracyanoethylene (TCNE) and PNCs were studied by monitoring the exciton dynamics.[136] Through the control of the morphology of PNC, the spherical shape of PNCs showed the highest interfacial charge transfer rate compared to that of platelets and cube shapes when mixed with TCNE, attributed to favorable band offsets between spherical PNCs and TCNE. Furthermore, the photoinduced electron transfer at the interface between $FAPbBr_3$ PNCs and C_{60} has been demonstrated.[52] Similarly, the significant interfacial charge transfer can occur in $MAPbBr_3$/p-g-C_3N_4 nanocomposites.[137] Upon the analysis of TRPL results, the

photoexcited electrons can be transferred into the conduction band (CB) of p-g-C_3N_4 from the CB and shallow-trap states of $MAPbBr_3$, and the photoexcited holes could accumulate on the valence band of $MAPbBr_3$, as shown in Figure 14. The significant charge separation of $MAPbBr_3$/p-g-C_3N_4 nanocomposites shows potential in the photodegradation of organic pollutant, p-nitrophenol.

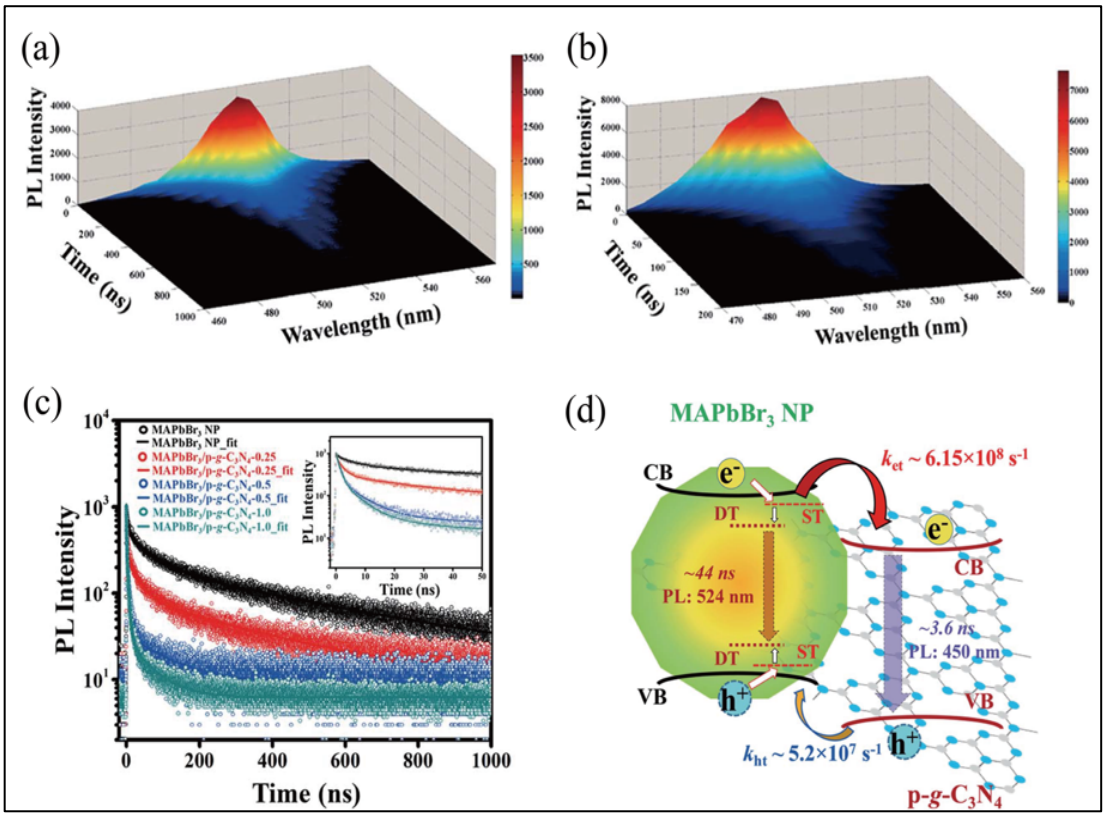

Figure 1-14- Three-dimensional TRPL spectra of (a) $MAPbBr_3$ NP and (b) $MAPbBr_3$/p-g-C_3N_4 nanocomposite. (c) TRPL spectra of $MAPbBr_3$ NPs and $MAPbBr_3$/p-g-C_3N_4 nanocomposite with different composition at their maximum of PL peaks. (d) Schematic illustration of the band structure and proposed assignment of lifetimes and rate constants of various charge carrier recombination and interfacial transfer processes for $MAPbBr_3$/p-g-C_3N_4 nanocomposite based on the charge carrier dynamics studies.

In addition, capping ligand can also affect the phase stability in PNCs. We recently found a correlation among surface property, phase transition, and exciton dynamics for $MAPbBr_3$ NCs capped with APTES and octylammoniumbromide (OABr).[138] Using static and time-resolved PL spectroscopy, a higher energy band is observed in the PL spectra (Figure 15a-d), indicating structural phase transition from tetragonal to orthorhombic at 140 K for PNCs capped with OABr. However, PNCs capped with APTES did not show any structural change even at 20 K. This is attributed to difference in surface energy contribution to their Gibbs free energy, which modifies the crystal phase diagram to an energetically stable cubic phase. This capping ligand-dependent phase transition also decreased the PL lifetime associated with phase transition in the PNCs capped with OABr (Figure 15e-f).[138]

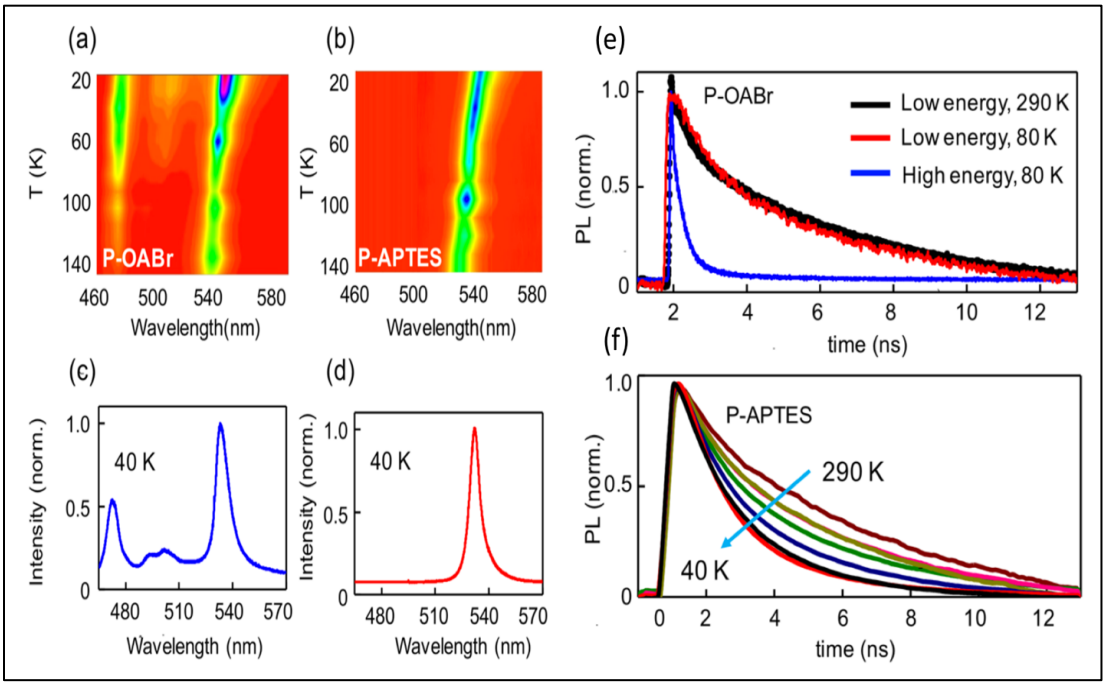

Figure 1-15- PL intensity mapped with the emission wavelength and temperature for (a) P-OABr and (b) P-APTES. Line cuts of the same maps at 40 K for (c) P-OABr and (d) P-APTES. Time-resolved PL curves for (e) P-OABr and (f) P-APTES as functions of temperature.

The same trend was observed previously for perovskite thin films in which long recombination lifetime in tetragonal phase decreased an order of magnitude following transition to orthorhombic phase at lower temperature. Sarang *et al*. attributed this behavior to crossover from free carriers to exciton-dominated radiative recombination.[139] On the other hand, Li *et al.* reported a significant PL lifetime increase of inorganic $CsPbBr_3$ NCs by increasing the temperature up to 300 K, and then a sudden decrease in the lifetime by furtherer increasing the temperature over 300 K, suggesting thermal instability in inorganic PNCs.[140] These findings suggest that the phase stabilization and transition in PNCs depend on surface properties.

1.5.2 Effect of Surface Modification on Charge Carrier Dynamics in Perovskite Bulk Films

There are a number of studies of exciton/charge carrier dynamics in thin films of organic-inorganic metal halide perovskites, especially $MAPbI_3$. However, there are still some challenges in experiment conduction and data interpretation. For instance, charge transfer in perovskite films is strongly dependent on film morphology and surface properties. Preparing a uniform film with smooth surface, good coverage, and few pin holes is not trivial. In addition, environmental factors, such as humidity, light and oxygen, can also affect the photophysical properties of the films, including charge carrier dynamics. Generally, organic-inorganic perovskites are known for having long diffusion length for both electron and hole, from hundred nanometers to micrometers, depending on the thin film quality.[132, 141] Ponesca *et al*. suggested due to low exciton binding energy (E_B<25 meV) in these perovskites, free charge carriers will be generated upon photoexcitation at room temperature rather than bound excitons.[142] The photogenerated charge carriers usually relax to band edge quickly because of electron-phonon coupling.[143] The electron-phonon coupling is weak in perovskites as reported previously.[144] Wu *et al*. demonstrated that charge carriers can be trapped due to electron-phonon coupling, mostly located on the surface or at interfaces.[145] For single crystal $MAPbI_3$ and $MAPbBr_3$, the density of trap states is extremely low (~10^{10} cm^{-3}) and comparable to high quality crystalline silicon.[146-147] But for polycrystalline films, this number was measured to be 10^{15} and 10^{16} cm^{-3} for deep and shallow traps, respectively.[146-147] The dependence of PL lifetime on trap state densities has been also

systematically investigated.[148] The difference in trap densities of single crystal and polycrystalline perovskites suggests high potential for further improving the surface properties of the polycrystalline perovskite films and passivating defects in order to further improve the optical properties.

In this regard, various chemical modifications and surface passivation strategies have been suggested to improve the charge transfer properties. For instance, a new precursor system of $Pb(CH_3CO_2)_2 \cdot 3H_2O$, $PbCl_2$, and CH_3NH_3I was developed to obtain pinhole-free, highly crystallized perovskite films using a one-step spin-coating method.[149] Uncoordinated iodine ions within the perovskite are suggested to be responsible for charge accumulation and consequent recombination losses in PSCs.[150] Supramolecular halogen bond complexation was used to successfully passivate these sites and as a result, the hole recombination time increased from 300 ns in untreated sample to approximately 900 ns after treatment.[150] In a similar approach, trap states on the surface and grain boundaries of the perovskite were demonstrated to be the origin of photocurrent hysteresis.[96] Fullerenes were deposited on top of the perovskite and reduced the trap density by two orders of magnitude. As a result, surface charge recombination lifetime ($\tau_{surface}$) increased about three times in whole-bias range after surface passivation with PCBM as shown in Figures 16a, b. However, the surface passivation did not affect the bulk charge recombination lifetime significantly.[96]

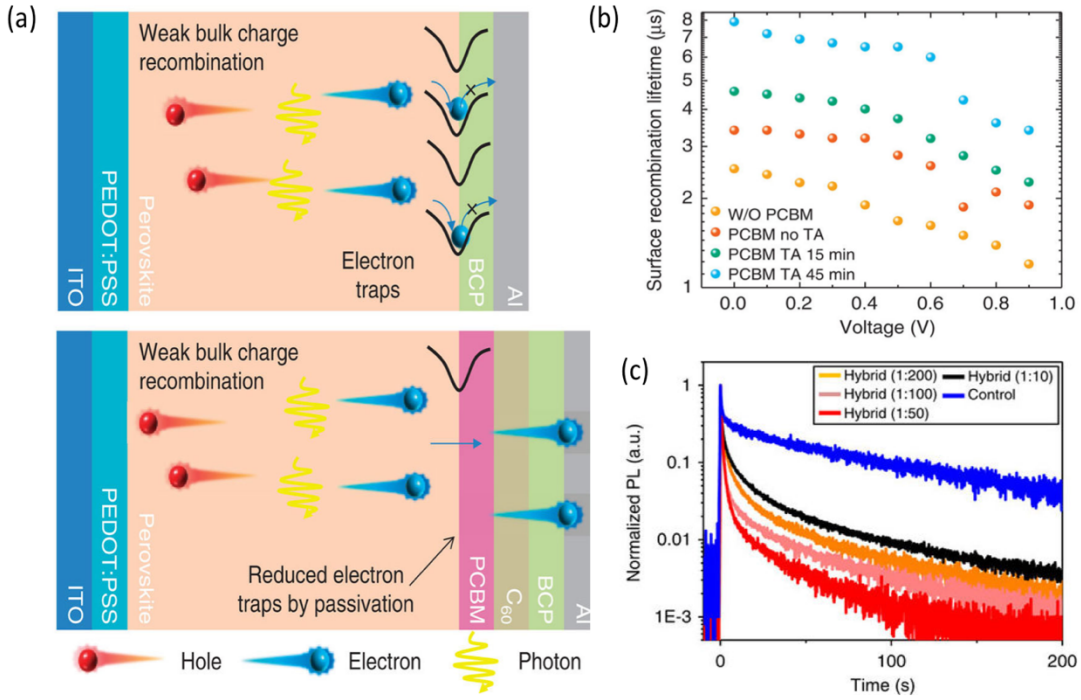

Figure 1-16- a) Schematic of the surface recombination reduction by passivating the trap states. b) surface recombination time with different PCBM passivation conditions under different applied bias. c) Transient photoluminescence of hybrid films with increasing PCBM ratio progressively (orange, pink, red and black) compared with control film on glass (blue), showing the enhanced electron extraction.

The first perovskite PCBM hybrid film was also synthesized by Xu *et al.*[151] in this hybrid structure, PCBM passivates the key PbI_3^- antisite defects during the perovskite self-assembly and time-resolved PL spectroscopy proved that the PCBM phase promotes electron extraction (Figure 16c).[151] There are also studies on controllable self-induced passivation techniques in which excess amount of PbI_2 was used in perovskite grain boundaries and interfaces to passivate the defects and caused substantial enhancement in device performance.[152-153] Time-resolved PL spectroscopy was used to measure the carrier lifetime and elucidate the mechanism of improved

performance. Appearance of PbI_2 phase in perovskite structure after annealing, prolonged the PL lifetime from ~3 ns to ~100 ns, indicating reduced recombination in the film. However, increasing the annealing time and amount of PbI_2 did not affect the lifetime significantly. A proposed mechanism for PbI_2 passivation in $CH_3NH_3PbI_3$ film is shown in Figure 17.[154]

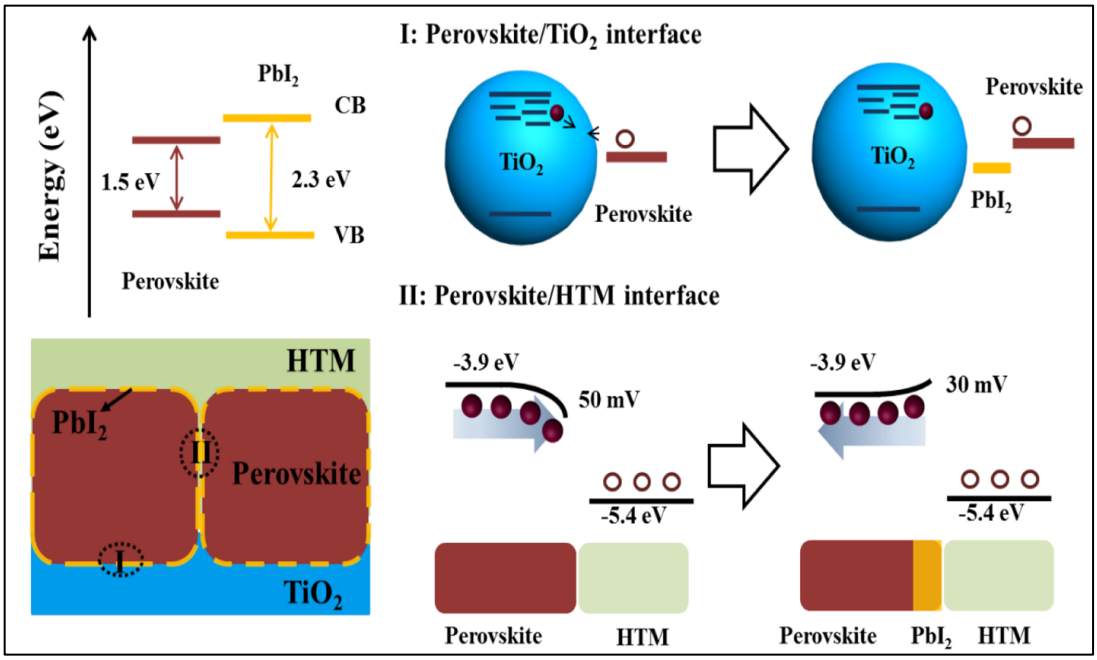

Figure 1-17- The coexistence of PbI_2 and perovskite in the film shows a type I alignment of the band edge, with the band gap of 2.3 and 1.5 eV, respectively. The schematic p−i−n structure is shown in the bottom left. The interface (I) of perovskite/TiO_2 is shown on the top right; and the recombination of electron from TiO_2 and holes from perovskite is reduced by the introduction of PbI_2. The interface (II) of perovskite/HTM is described on the bottom right; the presence of PbI_2 changes the grain to grain boundary bending from downward to upward, which helps to reduce the recombination between the electrons from perovskite and holes from HTM.

Overall, the trap states related to defects in perovskite films can significantly affect their optical properties, carrier dynamics, and device performance. Proper

strategies to control and passivate the surface defects are promising for improving the material properties and their performance in PV and other applications.

1.6 Summary and Outlook

OMH perovskites in the form of NCs or thin films have shown great potential for a broad range of applications including PV solar cells, LEDs, photodetectors, sensors and lasers, owing to their attractive electronic and optical properties. Despite the outstanding progress achieved to date, there are still challenges to overcome. In particular, materials instability, with respect to factors such as oxygen, water moisture and UV light, and high temperature, and in relation to defects, specifically those on the surface, presents a major obstacle to their practical use. Proper surface passivation of surface defects is critical to obtaining high quality NCs and films with good stability and improved properties. Table 1 provides brief summary of some of the similarities and differences between perovskite bulk films and NCs. Most of the differences are due to the extremely large surface-to-volume ratio of the PNCs and associated surface defects that can affect electronic and optical properties.

Table 1-1- Summary of some similarities and differences between perovskite bulk films and nanocrystals.

PROPERTIES	NANOCRYSTALS	BULK MATERIAL
Optical Property	Tunable	Not tunable
Charge Transport	Limited	Fast
Surface/Volume Ratio	Extremely large	Small
Surface Functionalization	Versatile	More restricted
Processability	Convenient	Involved
Synthesis	Multiple approaches	Less options
Density of defects	High	Low
Exciton/chargecarrier dynamics	Complex	Simple
Doping	Yes	Yes

In this review, we focused on size and structural control with variation of capping ligands and how they affect properties of the perovskites. We have also reviewed the degradation mechanism and some of the proposed surface passivation approaches to address instability toward environmental factors. In order to get deeper insight on some of the important photophysical processes in OMH perovskites, their exciton/charge carrier dynamics is also discussed, especially in relation to surface properties.

As for future directions, it is very important to further investigate the origin of instability in these perovskites at the molecular and atomic scale. For instance, X-ray and time resolved spectroscopy could be used to help gain better understanding of the degradation mechanism and identify short-lived reaction intermediates. While some passivation strategies may work for both nanostructures and bulk films, their difference in structure requires different strategies in other situations Further theoretical and

computational work is also needed to help corroborate and guide experimental studies, in terms of computing both static as well as dynamic properties.

Lastly, environmental concerns regarding the presence of lead in perovskites needs to be addressed. Even though synthesis of Sn, Sb and Bi based perovskites has been reported, their properties and performance are so far mostly inferior to that of lead-based perovskites. Therefore, search continues in finding a proper substitute for lead.

1.7 References

1. Green, M. A. In *Recent Advances in Silicon Solar Cell Performance*, Tenth EC Photovoltaic Solar Energy Conference, Springer: 1991.

2. Branker, K.; Pathak, M.; Pearce, J. M., A Review of Solar Photovoltaic Levelized Cost of Electricity. *Renew. Sust. Energ Rev.* **2011**, *15*, 4470-4482.

3. Z. Cheng, J. L., Layered Organic–Inorganic Hybrid Perovskites: Structure, Optical Properties, Film Preparation, Patterning and Templating Engineering. *Cryst. Eng. Comm.* **2010**, *12*, 2646-2662.

4. Grätzel, M., The Light and Shade of Perovskite Solar Cells. *Nat. Mater.* **2014**, *13*, 838.

5. Zhang, W.; Cai, Y.; Xiong, R. G.; Yoshikawa, H.; Awaga, K., Exceptional Dielectric Phase Transitions in a Perovskite-Type Cage Compound. *Angew. Chem. Int. Ed.* **2010**, *122*, 6758-6760.

6. Schouwink, P.; Ley, M. B.; Tissot, A.; Hagemann, H.; Jensen, T. R.; Smrčok, Ľ.; Černý, R., Structure and Properties of Complex Hydride Perovskite Materials. *Nat. Commun.* **2014**, *5*, 5706.

7. Kim, H.-S.; Lee, C.-R.; Im, J.-H.; Lee, K.-B.; Moehl, T.; Marchioro, A.; Moon, S.-J.; Humphry-Baker, R.; Yum, J.-H.; Moser, J. E., Lead Iodide Perovskite Sensitized All-Solid-State Submicron Thin Film Mesoscopic Solar Cell with Efficiency Exceeding 9%. *Sci. Rep.* **2012**, *2*, 591.

8. Yang, W. S.; Noh, J. H.; Jeon, N. J.; Kim, Y. C.; Ryu, S.; Seo, J.; Seok, S. I., High-Performance Photovoltaic Perovskite Layers Fabricated through Intramolecular Exchange. *Science* **2015**, *348*, 1234-1237.

9. Dong, Q.; Fang, Y.; Shao, Y.; Mulligan, P.; Qiu, J.; Cao, L.; Huang, J., Electron-Hole Diffusion Lengths> 175 Mm in Solution-Grown Ch3nh3pbi3 Single Crystals. *Science* **2015**, *347*, 967-970.

10. Cho, H.; Jeong, S.-H.; Park, M.-H.; Kim, Y.-H.; Wolf, C.; Lee, C.-L.; Heo, J. H.; Sadhanala, A.; Myoung, N.; Yoo, S., Overcoming the Electroluminescence Efficiency Limitations of Perovskite Light-Emitting Diodes. *Science* **2015**, *350*, 1222-1225.

11. Tan, Z.-K.; Moghaddam, R. S.; Lai, M. L.; Docampo, P.; Higler, R.; Deschler, F.; Price, M.; Sadhanala, A.; Pazos, L. M.; Credgington, D., Bright Light-Emitting Diodes Based on Organometal Halide Perovskite. *Nat. Nanotechnol.* **2014**, *9*, 687-692.

12. Veldhuis, S. A.; Boix, P. P.; Yantara, N.; Li, M.; Sum, T. C.; Mathews, N.; Mhaisalkar, S. G., Perovskite Materials for Light-Emitting Diodes and Lasers. *Adv. Mater.* **2016**, *28*, 6804-6834.

13. Xing, G.; Mathews, N.; Lim, S. S.; Yantara, N.; Liu, X.; Sabba, D.; Grätzel, M.; Mhaisalkar, S.; Sum, T. C., Low-Temperature Solution-Processed Wavelength-Tunable Perovskites for Lasing. *Nat. Mater.* **2014**, *13*, 476.

14. Zhu, H.; Fu, Y.; Meng, F.; Wu, X.; Gong, Z.; Ding, Q.; Gustafsson, M. V.; Trinh, M. T.; Jin, S.; Zhu, X., Lead Halide Perovskite Nanowire Lasers with Low Lasing Thresholds and High Quality Factors. *Nat. Mater.* **2015**, *14*, 636.

15. Kojima, A.; Teshima, K.; Shirai, Y.; Miyasaka, T., Organometal Halide Perovskites as Visible-Light Sensitizers for Photovoltaic Cells. *J. Am. Chem. Soc.* **2009**, *131*, 6050-6051.

16. Liu, M.; Johnston, M. B.; Snaith, H. J., Efficient Planar Heterojunction Perovskite Solar Cells by Vapour Deposition. *Nature* **2013**, *501*, 395.

17. McMeekin, D. P.; Sadoughi, G.; Rehman, W.; Eperon, G. E.; Saliba, M.; Hörantner, M. T.; Haghighirad, A.; Sakai, N.; Korte, L.; Rech, B., A Mixed-Cation Lead Mixed-Halide Perovskite Absorber for Tandem Solar Cells. *Science* **2016**, *351*, 151-155.

18. Feng Zhang, H. Z., Cheng Chen, Xian-gang Wu, Xiangmin Hu, Hailong Huang, Junbo Han, Bingsuo Zou, Yuping Dong, Brightly Luminescent and Color-Tunable

Colloidal $CH_3NH_3PbX_3$ (X = Br, I, Cl)Quantumdots: Potential Alternatives for Display Technology. *ACS Nano* **2015**, *9*, 4533-4542.

19. Wang, J.; Wang, N.; Jin, Y.; Si, J.; Tan, Z. K.; Du, H.; Cheng, L.; Dai, X.; Bai, S.; He, H., Interfacial Control toward Efficient and Low-Voltage Perovskite Light-Emitting Diodes. *Adv. Mater.* **2015**, *27*, 2311-2316.

20. Abdelmageed, G.; Jewell, L.; Hellier, K.; Seymour, L.; Luo, B.; Bridges, F.; Zhang, J. Z.; Carter, S., Mechanisms for Light Induced Degradation in $MAPbI_3$ Perovskite Thin Films and Solar Cells. *Appl. Phys. Lett.* **2016**, *109*, 233905.

21. Luo, B.; Pu, Y. C.; Lindley, S. A.; Yang, Y.; Lu, L.; Li, Y.; Li, X.; Zhang, J. Z., Organolead Halide Perovskite Nanocrystals: Branched Capping Ligands Control Crystal Size and Stability. *Angew. Chem. Int. Ed.* **2016**, *55*, 8864-8868.

22. Niu, G.; Guo, X.; Wang, L., Review of Recent Progress in Chemical Stability of Perovskite Solar Cells. *J. Mater. Chem. A* **2015**, *3*, 8970-8980.

23. Stranks, S. D.; Snaith, H. J., Metal-Halide Perovskites for Photovoltaic and Light-Emitting Devices. *Nat. Nanotechnol.* **2015**, *10*, 391.

24. Noel, N. K.; Stranks, S. D.; Abate, A.; Wehrenfennig, C.; Guarnera, S.; Haghighirad, A.-A.; Sadhanala, A.; Eperon, G. E.; Pathak, S. K.; Johnston, M. B., Lead-Free Organic–Inorganic Tin Halide Perovskites for Photovoltaic Applications. *Energy Environ. Sci.* **2014**, *7*, 3061-3068.

25. Yang, J.; Siempelkamp, B. D.; Mosconi, E.; De Angelis, F.; Kelly, T. L., Origin of the Thermal Instability in $CH_3NH_3PbI_3$ Thin Films Deposited on Zno. *Chem. Mater.* **2015**, *27*, 4229-4236.

26. Zhang, D.; Han, J.; Li, C.; Wang, J.; Li, X., Detection of Co-Salient Objects by Looking Deep and Wide. *Int. J. Comput. Vision* **2016**, *120*, 215-232.

27. Huang, S.; Li, Z.; Kong, L.; Zhu, N.; Shan, A.; Li, L., Enhancing the Stability of Ch3nh3pbbr3 Quantum Dots by Embedding in Silica Spheres Derived from Tetramethyl Orthosilicate in “Waterless” Toluene. *J. Am. Chem. Soc.* **2016**, *138*, 5749-5752.

28. Koh, W. k.; Park, S.; Ham, Y., Phosphonic Acid Stabilized Colloidal $CsPbX_3$ (X= Br, I) Perovskite Nanocrystals and Their Surface Chemistry. *ChemistrySelect* **2016**, *1*, 3479-3482.

29. Huang, H.; Chen, B.; Wang, Z.; Hung, T. F.; Susha, A. S.; Zhong, H.; Rogach, A. L., Water Resistant $CsPbX_3$ Nanocrystals Coated with Polyhedral Oligomeric

Silsesquioxane and Their Use as Solid State Luminophores in All-Perovskite White Light-Emitting Devices. *Chem. Sci.* **2016**, *7*, 5699-5703.

30. Hao, F.; Stoumpos, C. C.; Cao, D. H.; Chang, R. P.; Kanatzidis, M. G., Lead-Free Solid-State Organic–Inorganic Halide Perovskite Solar Cells. *Nat. Photonics* **2014**, *8*, 489.

31. Schmidt, L. C.; Pertegas, A.; Gonzalez-Carrero, S.; Malinkiewicz, O.; Agouram, S.; Minguez Espallargas, G.; Bolink, H. J.; Galian, R. E.; Perez-Prieto, J., Nontemplate Synthesis of $CH_3NH_3PbBr_3$ Perovskite Nanoparticles. *J. Am. Chem. Soc.* **2014**, *136*, 850-853.

32. Gonzalez-Carrero, S.; Galian, R. E.; Pe´rez-Prieto, J., Maximizing the Emissive Properties of Ch3nh3pbbr3 Perovskite Nanoparticles. *J. Mater. Chem. A* **2015**, *3*, 9187-9193.

33. De Roo, J.; Ibanez, M.; Geiregat, P.; Nedelcu, G.; Walravens, W.; Maes, J.; Martins, J. C.; Van Driessche, I.; Kovalenko, M. V.; Hens, Z., Highly Dynamic Ligand Binding and Light Absorption Coefficient of Cesium Lead Bromide Perovskite Nanocrystals. *ACS Nano* **2016**, *10*, 2071-2081.

34. Tyagi, P.; Arveson, S. M.; Tisdale, W. A., Colloidal Organohalide Perovskite Nanoplatelets Exhibiting Quantum Confinement. *J. Phys. Chem. Lett.* **2015**, *6*, 1911-1916.

35. Sichert, J.A., Tong, Y., Mutz, N., Vollmer, M., Fischer, S., Milowska, K.Z., García Cortadella, R., Nickel, B., Cardenas-Daw, C., Stolarczyk, J.K., et al., A.S., Quantum Size Effect in Organometal Halide Perovskite Nanoplatelets. *Nano Lett.* **2015**, *15*, 6521-6527.

36. Li, X.; Wu, Y.; Zhang, S.; Cai, B.; Gu, Y.; Song, J.; Zeng, H., Cspbx3quantum Dots for Lighting and Displays: Room-Temperature Synthesis, Photoluminescence Superiorities, Underlying Origins and White Light-Emitting Diodes. *Adv. Funct. Mater.* **2016**, *26*, 2435-2445.

37. Tong, Y.; Ehrat, F.; Vanderlinden, W.; Cardenas-Daw, C.; Stolarczyk, J. K.; Polavarapu, L.; Urban, A. S., Dilution-Induced Formation of Hybrid Perovskite Nanoplatelets. *ACS Nano* **2016**, *10*, 10936-10944.

38. Vybornyi, O.; Yakunin, S.; Kovalenko, M. V., Polar-Solvent-Free Colloidal Synthesis of Highly Luminescent Alkylammonium Lead Halide Perovskite Nanocrystals. *Nanoscale* **2016**, *8*, 6278-6283.

39. Imran, M.; Caligiuri, V.; Wang, M.; Goldoni, L.; Prato, M.; Krahne, R.; De

Trizio, L.; Manna, L., Benzoyl Halides as Alternative Precursors for the Colloidal Synthesis of Lead-Based Halide Perovskite Nanocrystals. *J. Am. Chem. Soc.* **2018**, *140*, 2656-2664.

40. Teunis, M. B.; Johnson, M. A.; Muhoberac, B. B.; Seifert, S.; Sardar, R., Programmable Colloidal Approach to Hierarchical Structures of Methylammonium Lead Bromide Perovskite Nanocrystals with Bright Photoluminescent Properties. *Chem. Mater.* **2017**, *29*, 3526-3537.

41. Liu, L., Huang, S., Pan, L., Shi, L.J., Zou, B., Deng, L., Zhong, H., Colloidal Synthesis of $CH_3NH_3PbBr_3$ Nanoplatelets with Polarized Emission through Self-Organization. *Angew. Chem. Int. Ed.* **2017**, *56*, 1780-1783.

42. Wei, S.; Yang, Y.; Kang, X.; Wang, L.; Huang, L.; Pan, D., Room-Temperature and Gram-Scale Synthesis of $CsPbX_3$ (X = Cl, Br, I) Perovskite Nanocrystals with 50-85% Photoluminescence Quantum Yields. *Chem. Commun. (Camb)* **2016**, *52*, 7265-7268.

43. Malgras, V.; Henzie, J.; Takei, T.; Yamauchi, Y., Hybrid Methylammonium Lead Halide Perovskite Nanocrystals Confined in Gyroidal Silica Templates. *Chem. Commun. (Camb)* **2017**, *53*, 2359-2362.

44. Malgras, V.; Tominaka, S.; Ryan, J. W.; Henzie, J.; Takei, T.; Ohara, K.; Yamauchi, Y., Observation of Quantum Confinement in Monodisperse Methylammonium Lead Halide Perovskite Nanocrystals Embedded in Mesoporous Silica. *J. Am. Chem. Soc.* **2016**, *138,* 13874-13881

45. Huang, H.; Xue, Q.; Chen, B.; Xiong, Y.; Schneider, J.; Zhi, C.; Zhong, H.; Rogach, A. L., Top-Down Fabrication of Stable Methylammonium Lead Halide Perovskite Nanocrystals by Employing a Mixture of Ligands as Coordinating Solvents. *Angew. Chem. Int. Ed. Engl.* **2017**, *56*, 9571-9576.

46. Jang, D. M.; Kim, D. H.; Park, K.; Park, J.; Lee, J. W.; Song, J. K., Ultrasound Synthesis of Lead Halide Perovskite Nanocrystals. *J. Mater. Chem. C* **2016**, *4*, 10625-10629.

47. Amendola, V.; Fortunati, I.; Marega, C.; Abdelhady, A. L.; Saidaminov, M. I.; Bakr, O. M., High-Purity Hybrid Organolead Halide Perovskite Nanoparticles Obtained by Pulsed-Laser Irradiation in Liquid. *Chemphyschem* **2017**, *18*, 1047-1054.

48. Wang, L.; Williams, N. E.; Malachosky, E. W.; Otto, J. P.; Hayes, D.; Wood, R. E.; Guyot-Sionnest, P.; Engel, G. S., Scalable Ligand-Mediated Transport Synthesis of Organic-Inorganic Hybrid Perovskite Nanocrystals with Resolved Electronic Structure and Ultrafast Dynamics. *ACS Nano* **2017**, *11*, 2689-2696.

49. Naphade, R.; Nagane, S.; Shanker, G. S.; Fernandes, R.; Kothari, D.; Zhou, Y.; Padture, N. P.; Ogale, S., Hybrid Perovskite Quantum Nanostructures Synthesized by Electrospray Antisolvent-Solvent Extraction and Intercalation. *ACS Appl. Mater. Interfaces* **2016**, *8*, 854-861.

50. Ding, R., Liu, H., Zhang, X., Xiao, J., Kishor, R., Sun, H., Zhu, B., Chen, G., Gao, F., Feng, X. and Chen, J., Flexible Piezoelectric Nanocomposite Generators Based on Formamidinium Lead Halide Perovskite Nanoparticles. *Adv. Funct. Mater.* **2016**, *26*, 7708-7716.

51. Perumal, A., Shendre, S., Li, M., Tay, Y.K.E., Sharma, V.K., Chen, S., Wei, Z., Liu, Q., Gao, Y., Buenconsejo, P.J.S. and Tan, S.T., High Brightness Formamidinium Lead Bromide Perovskite Nanocrystal Light Emitting Devices. *Sci. Rep.* **2016**, *6*, 36733.

52. Nair, V. C.; Muthu, C.; Rogach, A. L.; Kohara, R.; Biju, V., Channeling Exciton Migration into Electron Transfer in Formamidinium Lead Bromide Perovskite Nanocrystal/Fullerene Composites. *Angew. Chem. Int. Ed. Engl.* **2017**, *56*, 1214-1218.

53. Protesescu, L.; Yakunin, S.; Bodnarchuk, M. I.; Bertolotti, F.; Masciocchi, N.; Guagliardi, A.; Kovalenko, M. V., Monodisperse Formamidinium Lead Bromide Nanocrystals with Bright and Stable Green Photoluminescence. *J. Am. Chem. Soc.* **2016**, *138*, 14202-14205.

54. Yuan, F.; Wu, Z.; Dong, H.; Xi, J.; Xi, K.; Divitini, G.; Jiao, B.; Hou, X.; Wang, S.; Gong, Q., High Stability and Ultralow Threshold Amplified Spontaneous Emission from Formamidinium Lead Halide Perovskite Films. *J. Phys. Chem. C* **2017**, *121*, 15318-15325.

55. Li, Q.; Li, H.; Shen, H.; Wang, F.; Zhao, F.; Li, F.; Zhang, X.; Li, D.; Jin, X.; Sun, W., Solid Ligand-Assisted Storage of Air-Stable Formamidinium Lead Halide Quantum Dots Via Restraining the Highly Dynamic Surface toward Brightly Luminescent Light-Emitting Diodes. *ACS Photonics* **2017**, *4*, 2504-2512.

56. Minh, D.N., Kim, J., Hyon, J., Sim, J.H., Sowlih, H.H., Seo, C., Nam, J., Eom, S., Suk, S., Lee, S. and Kim, E., Room-Temperature Synthesis of Widely Tunable Formamidinium Lead Halide Perovskite Nanocrystals. *Chem. Mater.* **2017**, *29*, 5713-5719.

57. Papagiorgis, P.; Protesescu, L.; Kovalenko, M. V.; Othonos, A.; Itskos, G., Long-Lived Hot Carriers in Formamidinium Lead Iodide Nanocrystals. *J. Phys. Chem. C* **2017**, *121*, 12434-12440.

58. Protesescu, L., Yakunin, S., Kumar, S., Bär, J., Bertolotti, F., Masciocchi, N., Guagliardi, A., Grotevent, M., Shorubalko, I., Bodnarchuk, M.I. and Shih, C.J., Dismantling the "Red Wall" of Colloidal Perovskites: Highly Luminescent Formamidinium and Formamidinium-Cesium Lead Iodide Nanocrystals. *ACS Nano* **2017**, *11*, 3119–3134.

59. Lignos, I.; Protesescu, L.; Emiroglu, D. B.; Maceiczyk, R.; Schneider, S.; Kovalenko, M. V.; deMello, A. J., Unveiling the Shape Evolution and Halide-Ion-Segregation in Blue-Emitting Formamidinium Lead Halide Perovskite Nanocrystals Using an Automated Microfluidic Platform. *Nano Lett.* **2018**, *18*, 1246-1252.

60. Richard M. Maceiczyk, K. D. m., Ioannis Lignos, Loredana Protesescu,; Maksym V. Kovalenko, a. A. J. d., Microfluidic Reactors Provide Preparative and Mechanistic Insights into the Synthesis of Formamidinium Lead Halide Perovskite Nanocrystals. *Chem. Mater.* **2017**, *29*, 8433-8439.

61. Wang, C.; Zhang, Y.; Wang, A.; Wang, Q.; Tang, H.; Shen, W.; Li, Z.; Deng, Z., Controlled Synthesis of Composition Tunable Formamidinium Cesium Double Cation Lead Halide Perovskite Nanowires and Nanosheets with Improved Stability. *Chem. Mater.* **2017**, *29*, 2157-2166.

62. Levchuk, I.; Osvet, A.; Tang, X.; Brandl, M.; Perea, J. D.; Hoegl, F.; Matt, G. J.; Hock, R.; Batentschuk, M.; Brabec, C. J., Brightly Luminescent and Color-Tunable Formamidinium Lead Halide Perovskite $FAPbX_3$ (X = Cl, Br, I) Colloidal Nanocrystals. *Nano Lett.* **2017**, *17*, 2765-2770.

63. Huang, H.; Susha, A. S.; Kershaw, S. V.; Hung, T. F.; Rogach, A. L., Control of Emission Color of High Quantum Yield $CH_3NH_3PbBr_3$ perovskite Quantum Dots by Precipitation Temperature. *Adv. Sci.* **2015**, *2*, 1500194.

64. Morris, T.; Zubkov, T., Steric Effects of Carboxylic Capping Ligands on the Growth of the Cdse Quantum Dots. *Colloids Surf., A* **2014**, *443*, 439-449.

65. Ling, Y.; Yuan, Z.; Tian, Y.; Wang, X.; Wang, J. C.; Xin, Y.; Hanson, K.; Ma, B.; Gao, H., Bright Light-Emitting Diodes Based on Organometal Halide Perovskite Nanoplatelets. *Adv. Mater.* **2016**, *28*, 305-311.

66. Pathak, S., Sakai, N., Wisnivesky Rocca Rivarola, F., Stranks, S.D., Liu, J., Eperon, G.E., Ducati, C., Wojciechowski, K., Griffiths, J.T., Haghighirad, A.A., et al., Perovskite Crystals for Tunable White Light Emission. *Chem. Mater.* **2015**, *27*, 8066-8075.

67. Luo, B.; Naghadeh, S. B.; Allen, A. L.; Li, X.; Zhang, J. Z., Peptide-Passivated Lead Halide Perovskite Nanocrystals Based on Synergistic Effect between Amino and

Carboxylic Functional Groups. *Adv. Funct. Mater.* **2017**, *27*, 1604018.

68. Zhang, T.; Xie, L.; Chen, L.; Guo, N.; Li, G.; Tian, Z.; Mao, B.; Zhao, Y., In Situ Fabrication of Highly Luminescent Bifunctional Amino Acid Crosslinked 2d/3d $NH_3C_4H_9COO(CH_3NH_3PbBr_3)$ Perovskite Films. *Adv. Funct. Mater.* **2017**, *27*, 1603568.

69. Lu, C. H.; Hu, J.; Shih, W. Y.; Shih, W. H., Control of Morphology, Photoluminescence, and Stability of Colloidal Methylammonium Lead Bromide Nanocrystals by Oleylamine Capping Molecules. *J. Colloid. Interface. Sci.* **2016**, *484*, 17-23.

70. Aharon, S.; Etgar, L., Two Dimensional Organometal Halide Perovskite Nanorods with Tunable Optical Properties. *Nano Lett.* **2016**, *16*, 3230-3235.

71. Pan, A.; He, B.; Fan, X.; Liu, Z.; Urban, J. J.; Alivisatos, A. P.; He, L.; Liu, Y., Insight into the Ligand-Mediated Synthesis of Colloidal $CsPbBr_3$ Perovskite Nanocrystals: The Role of Organic Acid, Base, and Cesium Precursors. *ACS Nano* **2016**, *10*, 7943-7954.

72. Ravi, V. K.; Santra, P. K.; Joshi, N.; Chugh, J.; Singh, S. K.; Rensmo, H.; Ghosh, P.; Nag, A., Origin of the Substitution Mechanism for the Binding of Organic Ligands on the Surface of Cspbbr3 Perovskite Nanocubes. *J. Phys. Chem. Lett.* **2017**, *8*, 4988-4994.

73. Almeida, G.; Goldoni, L.; Akkerman, Q.; Dang, Z.; Khan, A. H.; Marras, S.; Moreels, I.; Manna, L., Role of Acid-Base Equilibria in the Size, Shape, and Phase Control of Cesium Lead Bromide Nanocrystals. *ACS Nano* **2018**, *12*, 1704-1711.

74. Xiao, Z.; Dong, Q.; Bi, C.; Shao, Y.; Yuan, Y.; Huang, J., Solvent Annealing of Perovskite-Induced Crystal Growth for Photovoltaic-Device Efficiency Enhancement. *Adv. Mater.* **2014**, *26*, 6503-6509.

75. Nie, W.; Tsai, H.; Asadpour, R.; Blancon, J.-C.; Neukirch, A. J.; Gupta, G.; Crochet, J. J.; Chhowalla, M.; Tretiak, S.; Alam, M. A., High-Efficiency Solution-Processed Perovskite Solar Cells with Millimeter-Scale Grains. *Science* **2015**, *347*, 522-525.

76. Lv, B.; Weng, H.; Fu, B.; Wang, X.; Miao, H.; Ma, J.; Richard, P.; Huang, X.; Zhao, L.; Chen, G., Experimental Discovery of Weyl Semimetal Taas. *Phys. Rev. X* **2015**, *5*, 031013.

77. Correa-Baena, J. P.; Anaya, M.; Lozano, G.; Tress, W.; Domanski, K.; Saliba, M.; Matsui, T.; Jacobsson, T. J.; Calvo, M. E.; Abate, A., Unbroken Perovskite:

Interplay of Morphology, Electro-Optical Properties, and Ionic Movement. *Adv. Mater.* **2016**, *28*, 5031-5037.

78. Noel, N. K.; Abate, A.; Stranks, S. D.; Parrott, E. S.; Burlakov, V. M.; Goriely, A.; Snaith, H. J., Enhanced Photoluminescence and Solar Cell Performance Via Lewis Base Passivation of Organic–Inorganic Lead Halide Perovskites. *ACS Nano* **2014**, *8*, 9815-9821.

79. Upama, M. B.; Elumalai, N. K.; Mahmud, M. A.; Wang, D.; Haque, F.; Gonçales, V. R.; Gooding, J. J.; Wright, M.; Xu, C.; Uddin, A., Role of Fullerene Electron Transport Layer on the Morphology and Optoelectronic Properties of Perovskite Solar Cells. *Org. Electron.* **2017**, *50*, 279-289.

80. Batmunkh, M.; Shearer, C. J.; Bat-Erdene, M.; Biggs, M. J.; Shapter, J. G., Single-Walled Carbon Nanotubes Enhance the Efficiency and Stability of Mesoscopic Perovskite Solar Cells. *ACS Appl. Mater. Interfaces* **2017**, *9*, 19945-19954.

81. Im, J.-H.; Kim, H.-S.; Park, N.-G., Morphology-Photovoltaic Property Correlation in Perovskite Solar Cells: One-Step Versus Two-Step Deposition of $CH_3NH_3PbI_3$. *Appl. Mater.* **2014**, *2*, 081510.

82. Lee, M. M.; Teuscher, J.; Miyasaka, T.; Murakami, T. N.; Snaith, H. J., Efficient Hybrid Solar Cells Based on Meso-Superstructured Organometal Halide Perovskites. *Science* **2012**, 1228604.

83. Swarnkar, A.; Marshall, A. R.; Sanehira, E. M.; Chernomordik, B. D.; Moore, D. T.; Christians, J. A.; Chakrabarti, T.; Luther, J. M., Quantum Dot–Induced Phase Stabilization of A-$CsPbI_3$ Perovskite for High-Efficiency Photovoltaics. *Science* **2016**, *354*, 92-95.

84. Jeon, N. J.; Noh, J. H.; Kim, Y. C.; Yang, W. S.; Ryu, S.; Seok, S. I., Solvent Engineering for High-Performance Inorganic–Organic Hybrid Perovskite Solar Cells. *Nat. Mater.* **2014**, *13*, 897.

85. Xiao, M.; Huang, F.; Huang, W.; Dkhissi, Y.; Zhu, Y.; Etheridge, J.; Gray-Weale, A.; Bach, U.; Cheng, Y. B.; Spiccia, L., A Fast Deposition-Crystallization Procedure for Highly Efficient Lead Iodide Perovskite Thin-Film Solar Cells. *Angew. Chem.* **2014**, *126*, 10056-10061.

86. Burschka, J.; Pellet, N.; Moon, S.-J.; Humphry-Baker, R.; Gao, P.; Nazeeruddin, M. K.; Grätzel, M., Sequential Deposition as a Route to High-Performance Perovskite-Sensitized Solar Cells. *Nature* **2013**, *499*, 316.

87. Wang, Y.; Li, S.; Zhang, P.; Liu, D.; Gu, X.; Sarvari, H.; Ye, Z.; Wu, J.; Wang,

Z.; Chen, Z. D., Solvent Annealing of Pbi 2 for the High-Quality Crystallization of Perovskite Films for Solar Cells with Efficiencies Exceeding 18%. *Nanoscale* **2016**, *8*, 19654-19661.

88. Wu, Y.; Islam, A.; Yang, X.; Qin, C.; Liu, J.; Zhang, K.; Peng, W.; Han, L., Retarding the Crystallization of PbI_2 for Highly Reproducible Planar-Structured Perovskite Solar Cells Via Sequential Deposition. *Energy Environ. Sci.* **2014**, *7*, 2934-2938.

89. Olthof, S.; Meerholz, K., Substrate-Dependent Electronic Structure and Film Formation of $MAPbI_3$ Perovskites. *Sci. Rep.* **2017**, *7*, 40267.

90. Tao, C.; Neutzner, S.; Colella, L.; Marras, S.; Kandada, A. R. S.; Gandini, M.; De Bastiani, M.; Pace, G.; Manna, L.; Caironi, M., 17.6% Stabilized Efficiency in Low-Temperature Processed Planar Perovskite Solar Cells. *Energy Environ. Sci.* **2015**, *8*, 2365-2370.

91. Chen, Q.; Zhou, H.; Hong, Z.; Luo, S.; Duan, H.-S.; Wang, H.-H.; Liu, Y.; Li, G.; Yang, Y., Planar Heterojunction Perovskite Solar Cells Via Vapor-Assisted Solution Process. *J. Am. Chem. Soc.* **2013**, *136*, 622-625.

92. Xiao, S.; Bai, Y.; Meng, X.; Zhang, T.; Chen, H.; Zheng, X.; Hu, C.; Qu, Y.; Yang, S., Unveiling a Key Intermediate in Solvent Vapor Postannealing to Enlarge Crystalline Domains of Organometal Halide Perovskite Films. *Adv. Funct. Mater.* **2017**, *27*, 1604944.

93. Tan, H.; Jain, A.; Voznyy, O.; Lan, X.; de Arquer, F. P. G.; Fan, J. Z.; Quintero-Bermudez, R.; Yuan, M.; Zhang, B.; Zhao, Y., Efficient and Stable Solution-Processed Planar Perovskite Solar Cells Via Contact Passivation. *Science* **2017**, *355*, 722-726.

94. Li, W.; Dong, H.; Guo, X.; Li, N.; Li, J.; Niu, G.; Wang, L., Graphene Oxide as Dual Functional Interface Modifier for Improving Wettability and Retarding Recombination in Hybrid Perovskite Solar Cells. *J. Mater. Chem. A* **2014**, *2*, 20105-20111.

95. Hadadian, M.; Correa-Baena, J. P.; Goharshadi, E. K.; Ummadisingu, A.; Seo, J. Y.; Luo, J.; Gholipour, S.; Zakeeruddin, S. M.; Saliba, M.; Abate, A., Enhancing Efficiency of Perovskite Solar Cells Via N-Doped Graphene: Crystal Modification and Surface Passivation. *Adv. Mater.* **2016**, *28*, 8681-8686.

96. Shao, Y.; Xiao, Z.; Bi, C.; Yuan, Y.; Huang, J., Origin and Elimination of Photocurrent Hysteresis by Fullerene Passivation in $CH_3NH_3PbI_3$ Planar Heterojunction Solar Cells. *Nat. Commun.* **2014**, *5*, 5784.

97. Kim, H.; Lim, K.-G.; Lee, T.-W., Planar Heterojunction Organometal Halide Perovskite Solar Cells: Roles of Interfacial Layers. *Energy Environ. Sci.* **2016**, *9*, 12-30.

98. Zhong, Y.; Munir, R.; Balawi, A. H.; Sheikh, A. D.; Yu, L.; Tang, M.-C.; Hu, H.; Laquai, F. d. r.; Amassian, A., Mesostructured Fullerene Electrodes for Highly Efficient N–I–P Perovskite Solar Cells. *ACS Energy Lett.* **2016**, *1*, 1049-1056.

99. Xiao, S.; Chen, H.; Jiang, F.; Bai, Y.; Zhu, Z.; Zhang, T.; Zheng, X.; Qian, G.; Hu, C.; Zhou, Y., Hierarchical Dual-Scaffolds Enhance Charge Separation and Collection for High Efficiency Semitransparent Perovskite Solar Cells. *Adv. Mater. Interfaces* **2016**, *3*, 1600484.

100. Wojciechowski, K.; Ramirez, I.; Gorisse, T.; Dautel, O.; Dasari, R.; Sakai, N.; Hardigree, J. M.; Song, S.; Marder, S.; Riede, M., Cross-Linkable Fullerene Derivatives for Solution-Processed N–I–P Perovskite Solar Cells. *ACS Energy Lett.* **2016**, *1*, 648-653.

101. Bi, E.; Chen, H.; Xie, F.; Wu, Y.; Chen, W.; Su, Y.; Islam, A.; Grätzel, M.; Yang, X.; Han, L., Diffusion Engineering of Ions and Charge Carriers for Stable Efficient Perovskite Solar Cells. *Nat. Commun.* **2017**, *8*, 15330.

102. Habisreutinger, S. N.; Leijtens, T.; Eperon, G. E.; Stranks, S. D.; Nicholas, R. J.; Snaith, H. J., Carbon Nanotube/Polymer Composites as a Highly Stable Hole Collection Layer in Perovskite Solar Cells. *Nano lett.* **2014**, *14*, 5561-5568.

103. Aristidou, N.; Sanchez-Molina, I.; Chotchuangchutchaval, T.; Brown, M.; Martinez, L.; Rath, T.; Haque, S. A., The Role of Oxygen in the Degradation of Methylammonium Lead Trihalide Perovskite Photoactive Layers. *Angew. Chem. Int. Ed.* **2015**, *54*, 8208-8212.

104. Marinova, N.; Franckevičius, M.; Matulaitienė, I.; Devižis, A.; Niaura, G.; Gulbinas, V.; Delgado, J. L., Hindered Amine Light Stabilizers Increase the Stability of Methylammonium Lead Iodide Perovskite against Light and Oxygen. *ChemSusChem* **2017**, *10*, 3760-3764.

105. Abdelmageed, G.; Mackeen, C.; Hellier, K.; Jewell, L.; Seymour, L.; Tingwald, M.; Bridges, F.; Zhang, J. Z.; Carter, S., Effect of Temperature on Light Induced Degradation in Methylammonium Lead Iodide Perovskite Thin Films and Solar Cells. *Sol. Energy Mater. Sol. Cells* **2018**, *174*, 566-571.

106. Yang, J.; Siempelkamp, B. D.; Liu, D.; Kelly, T. L., Investigation of $CH_3NH_3PbI_3$ Degradation Rates and Mechanisms in Controlled Humidity Environments Using in Situ Techniques. *ACS Nano* **2015**, *9*, 1955-1963.

107. Zhao, J., Cai, B., Luo, Z., Dong, Y., Zhang, Y., Xu, H., Hong, B., Yang, Y., Li, L., Zhang, W. and Gao, C., Investigation of the Hydrolysis of Perovskite Organometallic Halide $CH_3NH_3PbI_3$ in Humidity Environment. *Sci. Rep.* **2016**, *6*, 21976.

108. Christians, J. A.; Miranda Herrera, P. A.; Kamat, P. V., Transformation of the Excited State and Photovoltaic Efficiency of $CH_3NH_3PbI_3$ Perovskite Upon Controlled Exposure to Humidified Air. *J. Am. Chem. Soc.* **2015**, *137*, 1530-1538.

109. Leguy, A.M., Hu, Y., Campoy-Quiles, M., Alonso, M.I., Weber, O.J., Azarhoosh, P., Van Schilfgaarde, M., Weller, M.T., Bein, T., Nelson, J. and Docampo, P., Reversible Hydration of $CH_3NH_3PbI_3$ in Films, Single Crystals, and Solar Cells. *Chem. Mater.* **2015**, *27*, 3397-3407.

110. Juarez-Perez, E. J.; Hawash, Z.; Raga, S. R.; Ono, L. K.; Qi, Y., Thermal Degradation of $CH_3NH_3PbI_3$ Perovskite into NH_3 and CH_3I Gases Observed by Coupled Thermogravimetry-Mass Spectrometry Analysis. *Energy Environ. Sci.* **2016**, *9*, 3406-3410.

111. Latini, A.; Gigli, G.; Ciccioli, A., A Study on the Nature of the Thermal Decomposition of Methylammonium Lead Iodide Perovskite, $CH_3NH_3PbI_3$: An Attempt to Rationalise Contradictory Experimental Results. *Sustainable Energy Fuels* **2017**, *1*, 1351-1357.

112. Mosconi, E.; Azpiroz, J. M.; De Angelis, F., Ab Initio Molecular Dynamics Simulations of Methylammonium Lead Iodide Perovskite Degradation by Water. *Chem. Mater.* **2015**, *27*, 4885-4892.

113. Zhang, L.; Sit, P. H. L., Ab Initio Study of Interaction of Water, Hydroxyl Radicals, and Hydroxide Ions with $CH_3NH_3PbI_3$ and $CH_3NH_3PbBr_3$ Surfaces. *J. Phys. Chem. C* **2015**, *119*, 22370-22378.

114. Luo, B.; Naghadeh, S. B.; Zhang, J. Z., Lead Halide Perovskite Nanocrystals: Stability, Surface Passivation, and Structural Control. *ChemNanoMat* **2017**, *3*, 456-465.

115. Pan, J., Sarmah, S.P., Murali, B., Dursun, I., Peng, W., Parida, M.R., Liu, J., Sinatra, L., Alyami, N., Zhao, C., Alarousu, E., Air-Stable Surface-Passivated Perovskite Quantum Dots for Ultra-Robust, Single- and Two-Photon-Induced Amplified Spontaneous Emission. *J. Phys. Chem. Lett.* **2015**, *6*, 5027-5033.

116. Li, X., Xue, Z., Luo, D., Huang, C., Liu, L., Qiao, X., Liu, C., Song, Q., Yan, C., Li, Y. and Wang, T., A Stable Lead Halide Perovskite Nanocrystals Protected by Pmma. *Sci. China Mater.* **2018**, *61*, 363-370.

117. Zhou, Q.; Bai, Z.; Lu, W. g.; Wang, Y.; Zou, B.; Zhong, H., In Situ Fabrication of Halide Perovskite Nanocrystal-Embedded Polymer Composite Films with Enhanced Photoluminescence for Display Backlights. *Adv. Mater.* **2016**, *28*, 9163-9168.

118. Tan, Y.; Zou, Y.; Wu, L.; Huang, Q.; Yang, D.; Chen, M.; Ban, M.; Wu, C.; Wu, T.; Bai, S., Highly Luminescent and Stable Perovskite Nanocrystals with Octylphosphonic Acid as Ligand for Efficient Light Emitting Diodes. *ACS Appl. Mater. Interfaces* **2018**, *10*, 3784-3792.

119. Jun, S.; Lee, J.; Jang, E., Highly Luminescent and Photostable Quantum Dot–Silica Monolith and Its Application to Light-Emitting Diodes. *ACS Nano* **2013**, *7*, 1472-1477.

120. Zhao, B.; Yao, Y.; Gao, M.; Sun, K.; Zhang, J.; Li, W., Doped Quantum Dot@ Silica Nanocomposites for White Light-Emitting Diodes. *Nanoscale* **2015**, *7*, 17231-17236.

121. Han, B.; Shi, L.; Gao, X.; Guo, J.; Hou, K.; Zheng, Y.; Tang, Z., Ultra-Stable Silica-Coated Chiral Au-Nanorod Assemblies: Core–Shell Nanostructures with Enhanced Chiroptical Properties. *Nano Res.* **2016**, *9*, 451-457.

122. Sun, C.; Zhang, Y.; Ruan, C.; Yin, C.; Wang, X.; Wang, Y.; Yu, W. W., Efficient and Stable White Leds with Silica-Coated Inorganic Perovskite Quantum Dots. *Adv. Mater.* **2016**, *28*, 10088-10094.

123. Abdelmageed, G.; Sully, H. R.; Bonabi Naghadeh, S.; El-Hag Ali, A.; Carter, S. A.; Zhang, J. Z., Improved Stability of Organometal Halide Perovskite Films and Solar Cells toward Humidity Via Surface Passivation with Oleic Acid. *ACS Appl. Energy Mater.* **2018**, *1*, 387-392.

124. Hwang, I.; Jeong, I.; Lee, J.; Ko, M. J.; Yong, K., Enhancing Stability of Perovskite Solar Cells to Moisture by the Facile Hydrophobic Passivation. *ACS Appl. Mater. Interfaces* **2015**, *7*, 17330-17336.

125. Guo, X.; McCleese, C.; Gao, W.; Wang, M.; Sang, L.; Burda, C., Investigation of Moisture Stability and Pl Characteristics of Terpineol-Passivated Organic–Inorganic Hybrid Perovskite. *Mater. Renew. Sustain. Energy* **2016**, *5*, 17.

126. Xiong, H.; Rui, Y.; Li, Y.; Zhang, Q.; Wang, H., Hydrophobic Coating over a $CH_3NH_3PbI_3$ Absorbing Layer Towards Air Stable Perovskite Solar Cells. *J. Mater. Chem. C* **2016**, *4*, 6848-6854.

127. Bai, Y.; Xiao, S.; Hu, C.; Zhang, T.; Meng, X.; Lin, H.; Yang, Y.; Yang, S., Dimensional Engineering of a Graded 3d–2d Halide Perovskite Interface Enables

Ultrahigh Voc Enhanced Stability in the P-I-N Photovoltaics. *Adv. Energy Mater.* **2017**, *7*, 1701038.

128. Zhu, H.; Huang, B.; Wu, S.; Xiong, Z.; Li, J.; Chen, W., Facile Surface Modification of $CH_3NH_3PbI_3$ Films Leading to Simultaneously Improved Efficiency and Stability of Inverted Perovskite Solar Cells. *J. Mater. Chem. A* **2018**, *6*, 6255-6264.

129. Yavari, M., Mazloum-Ardakani, M., Gholipour, S., Marinova, N., Delgado, J.L., Turren-Cruz, S.H., Domanski, K., Taghavinia, N., Saliba, M., Grätzel, M., et al., Carbon Nanoparticles in High-Performance Perovskite Solar Cells. *Adv. Energy Mater.* **2018**, *8*, 1702719.

130. Zhao, D.; Yu, Y.; Wang, C.; Liao, W.; Shrestha, N.; Grice, C. R.; Cimaroli, A. J.; Guan, L.; Ellingson, R. J.; Zhu, K., Low-Bandgap Mixed Tin–Lead Iodide Perovskite Absorbers with Long Carrier Lifetimes for All-Perovskite Tandem Solar Cells. *Nat. Energy* **2017**, *2*, 17018.

131. Scheidt, R. A.; Samu, G. F.; Janáky, C.; Kamat, P. V., Modulation of Charge Recombination in $CsPbBr_3$ Perovskite Films with Electrochemical Bias. *J. Am. Chem. Soc.* **2017**, *140*, 86-89.

132. Stranks, S. D.; Eperon, G. E.; Grancini, G.; Menelaou, C.; Alcocer, M. J.; Leijtens, T.; Herz, L. M.; Petrozza, A.; Snaith, H. J., Electron-Hole Diffusion Lengths Exceeding 1 Micrometer in an Organometal Trihalide Perovskite Absorber. *Science* **2013**, *342*, 341-344.

133. Green, M. A.; Ho-Baillie, A.; Snaith, H. J., The Emergence of Perovskite Solar Cells. *Nat. Photonics* **2014**, *8*, 506-514.

134. Luo, B.; Pu, Y.-C.; Yang, Y.; Lindley, S. A.; Abdelmageed, G.; Ashry, H.; Li, Y.; Li, X.; Zhang, J. Z., Synthesis, Optical Properties, and Exciton Dynamics of Organolead Bromide Perovskite Nanocrystals. *J. Phys. Chem. C* **2015**, *119*, 26672-26682.

135. Maity, P.; Dana, J.; Ghosh, H. N., Multiple Charge Transfer Dynamics in Colloidal Cspbbr3 Perovskite Quantum Dots Sensitized Molecular Adsorbate. *J. Phys. Chem. C* **2016**, *120*, 18348-18354.

136. Ahmed, G. H.; Liu, J.; Parida, M. R.; Murali, B.; Bose, R.; AlYami, N. M.; Hedhili, M. N.; Peng, W.; Pan, J.; Besong, T. M., Shape-Tunable Charge Carrier Dynamics at the Interfaces between Perovskite Nanocrystals and Molecular Acceptors. *J. Phys. Chem. Lett.* **2016**, *7*, 3913-3919.

137. Pu, Y.-C.; Fan, H.-C.; Liu, T.-W.; Chen, J.-W., Methylamine Lead Bromide

Perovskite/Protonated Graphitic Carbon Nitride Nanocomposites: Interfacial Charge Carrier Dynamics and Photocatalysis. *J. Mater. Chem. A* **2017**, *5*, 25438-25449.

138. Sarang, S.; Bonabi Naghadeh, S.; Luo, B.; Kumar, P.; Betady, E.; Tung, V.; Scheibner, M.; Zhang, J. Z.; Ghosh, S., Stabilization of the Cubic Crystalline Phase in Organometal Halide Perovskite Quantum Dots Via Surface Energy Manipulation. *J. Phys. Chem. Lett.* **2017**, *8*, 5378-5384.

139. Sarang, S.; Ishihara, H.; Chen, Y.-C.; Lin, O.; Gopinathan, A.; Tung, V. C.; Ghosh, S., Low Temperature Excitonic Spectroscopy and Dynamics as a Probe of Quality in Hybrid Perovskite Thin Films. *Phys. Chem. Chem. Phys.* **2016**, *18*, 28428-28433.

140. Li, J.; Yuan, X.; Jing, P.; Li, J.; Wei, M.; Hua, J.; Zhao, J.; Tian, L., Temperature-Dependent Photoluminescence of Inorganic Perovskite Nanocrystal Films. *RSC Adv.* **2016**, *6*, 78311-78316.

141. Xing, G.; Mathews, N.; Sun, S.; Lim, S. S.; Lam, Y. M.; Grätzel, M.; Mhaisalkar, S.; Sum, T. C., Long-Range Balanced Electron-and Hole-Transport Lengths in Organic-Inorganic $CH_3NH_3PbI_3$. *Science* **2013**, *342*, 344-347.

142. Ponseca Jr, C. S.; Savenije, T. J.; Abdellah, M.; Zheng, K.; Yartsev, A.; Pascher, T. r.; Harlang, T.; Chabera, P.; Pullerits, T.; Stepanov, A., Organometal Halide Perovskite Solar Cell Materials Rationalized: Ultrafast Charge Generation, High and Microsecond-Long Balanced Mobilities, and Slow Recombination. *J. Am. Chem. Soc.* **2014**, *136*, 5189-5192.

143. Zheng, F.; Tan, L. Z.; Liu, S.; Rappe, A. M., Rashba Spin–Orbit Coupling Enhanced Carrier Lifetime in $CH_3NH_3PbI_3$. *Nano lett.* **2015**, *15*, 7794-7800.

144. Zhao, T.; Shi, W.; Xi, J.; Wang, D.; Shuai, Z., Intrinsic and Extrinsic Charge Transport in Ch 3 Nh 3 Pbi 3 Perovskites Predicted from First-Principles. *Sci. Rep.* **2016**, *6*, 19968.

145. Wu, X.; Trinh, M. T.; Niesner, D.; Zhu, H.; Norman, Z.; Owen, J. S.; Yaffe, O.; Kudisch, B. J.; Zhu, X.-Y., Trap States in Lead Iodide Perovskites. *J. Am. Chem. Soc.* **2015**, *137*, 2089-2096.

146. Duan, H.-S.; Zhou, H.; Chen, Q.; Sun, P.; Luo, S.; Song, T.-B.; Bob, B.; Yang, Y., The Identification and Characterization of Defect States in Hybrid Organic–Inorganic Perovskite Photovoltaics. *Phys. chem. chem. phys.* **2015**, *17*, 112-116.

147. Baumann, A.; Väth, S.; Rieder, P.; Heiber, M. C.; Tvingstedt, K.; Dyakonov, V., Identification of Trap States in Perovskite Solar Cells. *J. phys. chem. lett.* **2015**, *6*, 2350-

2354.

148. D'Innocenzo, V.; Srimath Kandada, A. R.; De Bastiani, M.; Gandini, M.; Petrozza, A., Tuning the Light Emission Properties by Band Gap Engineering in Hybrid Lead Halide Perovskite. *J. Am. Chem. Soc.* **2014**, *136*, 17730-17733.

149. Qiu, W.; Merckx, T.; Jaysankar, M.; de la Huerta, C. M.; Rakocevic, L.; Zhang, W.; Paetzold, U.; Gehlhaar, R.; Froyen, L.; Poortmans, J., Pinhole-Free Perovskite Films for Efficient Solar Modules. *Energy Environ. Sci.* **2016**, *9*, 484-489.

150. Abate, A.; Saliba, M.; Hollman, D. J.; Stranks, S. D.; Wojciechowski, K.; Avolio, R.; Grancini, G.; Petrozza, A.; Snaith, H. J., Supramolecular Halogen Bond Passivation of Organic–Inorganic Halide Perovskite Solar Cells. *Nano lett.* **2014**, *14*, 3247-3254.

151. Xu, J.; Buin, A.; Ip, A. H.; Li, W.; Voznyy, O.; Comin, R.; Yuan, M.; Jeon, S.; Ning, Z.; McDowell, J. J., Perovskite–Fullerene Hybrid Materials Suppress Hysteresis in Planar Diodes. *Nat. Commun.* **2015**, *6*, 7081.

152. Cao, D. H.; Stoumpos, C. C.; Malliakas, C. D.; Katz, M. J.; Farha, O. K.; Hupp, J. T.; Kanatzidis, M. G., Remnant PbI_2, an Unforeseen Necessity in High-Efficiency Hybrid Perovskite-Based Solar Cells? *Appl. Mater.* **2014**, *2*, 091101.

153. Chen, Q.; Zhou, H.; Song, T.-B.; Luo, S.; Hong, Z.; Duan, H.-S.; Dou, L.; Liu, Y.; Yang, Y., Controllable Self-Induced Passivation of Hybrid Lead Iodide Perovskites toward High Performance Solar Cells. *Nano lett.* **2014**, *14*, 4158-4163.

Chapter Two

2 Peptide-passivated Lead Halide Perovskite Nanocrystals Based on Synergistic Effect between Amino and Carboxylic Functional Groups

2.1 Abstract

We have developed a new strategy using peptides with amino and carboxylic functional groups as passivating ligands to produce methyl ammonium lead bromide ($CH_3NH_3PbBr_3$) perovskite nanocrystals (PNCs) with excellent optical properties. The well-passivated PNCs can only be obtained when both amino and carboxylic groups were involved, and this is attributed to the protonation reaction between $–NH_2$ and –COOH that is essential for successful passivation of the PNCs. To better understand this synergistic effect, peptides with different lengths have been studied and compared. Due to the polar nature of peptides, peptide-passivated PNCs (denoted as $PNCs_{peptide}$) aggregate and precipitate from nonpolar toluene solvent, resulting in a high product yield (~44%). Furthermore, the size of $PNCs_{peptide}$ can be varied from ~3.9 to 8.6 nm by adjusting the concentration of the peptide, resulting in tunable optical properties due to the quantum confinement effect. In addition, $CsPbBr_3$ PNCs were also synthesized with peptides as capping ligands, further demonstrating the generality and versatility of this strategy, which is important for generating high quality PNCs for photonics applications including LEDs, optical sensing, and imaging.

2.2 Introduction

Luminescent semiconductor nanocrystals (NCs) conjugated with functional biological materials, including enzymes, proteins, peptides and oligonucleotides have been widely used for biosensing and bioimaging applications through their interactions with the target analyte.[1-3] Many of these applications demand NCs with a high photoluminescence (PL) quantum yield (QY), size-tunable emission, and excited state lifetime.

Lead halide perovskite nanocrystals (PNCs) have been the main focus of light-emitting diodes (LEDs) due to their broad tunable emission window (~400-780 nm), high PLQY (~90%), and long PL lifetime (~10-100 ns).[4-17] These properties are also attractive for biological applications such as optical sensing and imaging. However, the instability or high sensitivity of PNCs towards polar solvents hinders their biological applications that often involve polar media such as water.

Several capping ligands, including strain chair ammonium bromide ($C_nH_{2n+1}NH_3Br$),[18, 19], octylamine plus HBr,[20] oleic acid with octylamine,[6, 21, 22] oleic acid with oleylamine,[4, 9, 23-25] and oleic acid with $C_nH_{2n+1}NH_3Br$,[26-28] have been successfully applied to the synthesis of PNCs. The commonality of these capping ligands is the $–NH_2/NH_3^+$ terminal groups. In principle, the surface defect sites of the PNCs passivated by $–NH_2$ or NH_3^+ terminals should have different electric charges. For $CH_3NH_3PbBr_3$ PNCs, it has been reported that the molar ratio of surface atoms ($Br^–/Pb^{2+}$) is around 3.5, which is higher than the stoichiometric ratio of 3.0 for $CH_3NH_3PbBr_3$ bulk materials, indicating a Br-rich and Pb-poor surface of PNCs.[6, 14]

Therefore, we hypothesize that the final form of the effective capping ligand should be R'-NH_3^+ (R' = alkyl chain) after passivation, and the role of oleic acid or HBr, when used, is to protonate the main amino capping ligand, R'-NH_2, and convert it into ammonium R'-NH_3^+, in the process of surface passivation of PNCs.

To date, most of the capping ligands used in the synthesis of PNCs are hydrophobic, due to the instability of PNCs in polar environments.[29] Therefore, it is very challenging to modify PNCs with polar capping ligands. Peptides consisting of two or more amino acids have been recently utilized to improve the hydrophilicity of CdSe quantum dots (QD) for biosensing and bioimaging applications.[30] We hypothesized that peptides containing both amino and carboxylic groups may be effective capping ligands for passivating PNCs. In contrast to the use of separate individual amino and carboxylic capping ligands, a single molecular ligand with both functional groups can substantially simplify the synthesis and improve the applicability of the PNCs produced. Moreover, peptide-functionalized PNCs can be potentially used for biological applications due to their salient optical properties and good compatibility with biological samples.

In this work, we have demonstrated, for the first time to our best knowledge, that well-passivated PNCs can be obtained only when both amino and carboxylic functional groups were present at the same time, and this can be accomplished using single peptide molecules. The ammonium moieties, R'-NH_3^+, generated due to the synergistic effect between amino and carboxylic groups, are most effective for passivating surface defects due to halide ions on the PNCs surface. This strategy was shown to work for

several peptides with different lengths for $CH_3NH_3PbBr_3$ as well as $CsPbBr_3$ PNCs. $PNCs_{peptide}$ with tunable size (~3.9 to 8.6 nm) prepared by adjusting the concentration of the peptide show size-dependent optical properties due to quantum confinement effect. This strategy is general and versatile and can be easily applied to the synthesis of other NCs for different applications.

2.3 Results and discussion

2.3.1 Synergistic effect between amino and carboxylic functional groups

For the synthesis of both $CH_3NH_3PbX_3$ and $CsPbX_3$ (X=Cl, Br, I) PNCs in previous work, several amino capping ligands including straight chain octylamine, oleyamine and branched (3-aminopropyl)triethoxysilane (APTES) have been successfully used, demonstrating the generality of amino capping ligands for the passivation of PNCs.[6,23,31] It was found that presence of oleic acid improves the outcome of the synthesis with amino ligands.[6,14] This improvement in capping efficiency is possibly due to synergistic effect between amino and carboxylic functional groups.

In order to demonstrate this synergistic effect, combinations of APTES and benzoic acid/oleic acid/acetic acid were used in this work. Figure 1 shows the UV-Vis absorption and PL spectra of $CH_3NH_3PbBr_3$ PNCs synthesized using various combinations of APTES and different carboxylic capping ligands such as oleic acid, benzoic acid and acetic acid. A weak PL emission band peaked at 530 nm was observed without any capping ligands, which can be attributed to bulk $CH_3NH_3PbBr_3$.[8] The PL

intensity was enhanced by ~10 or 60 times after adding a certain concentration of oleic acid or APTES capping ligands, respectively. However, the overall PL QY was still low (＜1%), suggesting the poor passivation of PNCs by a single ligand. In contrast, PNCs with significantly higher QY (~32-55%) were obtained when both amino (APTES) and carboxylic ligands (oleic acid, benzoic acid or acetic acid) were used together in the synthesis, clearly showing some synergistic effect between the two ligands used.

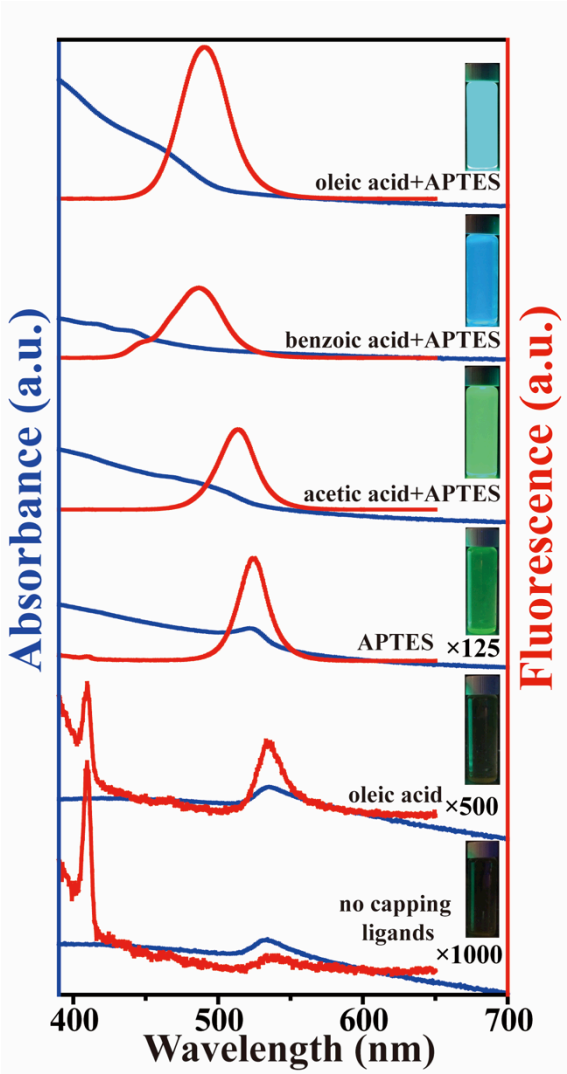

Figure 2-1- UV-Vis absorption (blue) and PL spectra (red, λex = 365 nm) of CH3NH3PbBr3 PNCs synthesized using different amino (APTES, 0.06 mmol/mL) and carboxylic capping ligands (oleic acid/benzoic acid/acetic acid, 0.16 mmol/mL). Inset: photographs of the PNCs under UV lamp irradiation. All the solutions were prepared by injecting 4 μL of the precursor solution into 4 mL toluene. The PL spectra of PNCs synthesized without capping ligands, with oleic acid or with APTES are magnified by 1000, 500 and 125, respectively. The sharp peak centered at 410 nm is from toluene.

When only oleic acid was used in the synthesis, the PL enhancement of $CH_3NH_3PbBr_3$ PNCs is attributed to the passivation of surface Pb^{2+} defects by R-COO^- (R = alkyl chain), which has been previously used to passivate the Pb^{2+} defects of PbS

QDs.[32] However, due to the low density of Pb^{2+} surface defects and small equilibrium constant of oleic acid, the PL enhancement of $CH_3NH_3PbBr_3$ PNCs was very limited. Alternatively, when APTES was used as the capping ligand, the PL enhancement was larger than that of oleic acid, which may be a result of the protonation of APTES by CH_3NH_3Br. In addition, because of the dominant Br^- surface defects in PNCs, the PL enhancement is more sensitive to the amount of R'-NH_3^+ than that of R-COO^- as the former should passivate the Br^- defect sites. Therefore, the enhancement by APTES is larger even with lower concentration. It can be seen from the PL spectra in Figure 1 that the peak position of the main emission band shifts a lot when different carboxylic acids are used, which may be due to different degrees of steric hindrance from the carboxylic capping ligands.[33] Well-passivated PNCs with much higher PL QY (~32%-55%) were obtained when both amino (APTES) and carboxylic capping ligands were used in tandem. This may be attributed to the protonation reaction between amino and carboxylic capping ligands, as shown in Equation 1:

$$\mathrm{R-COOH + R'\text{-}NH_2 \leftrightarrow R-COO^- + R'\text{-}NH_3^+} \quad (1)$$

As illustrated in Figure 2a, the protonation process can generate a large amount of R-COO^- and R'-NH_3^+, which can passivate both Pb^{2+} and Br^- defects, respectively, leading to the formation of well-passivated and colloidally dispersible PNCs in non-polar solvents.[29] Note that R'-$NH_3^+Br^-$ can also be applied as a passivating ligand to passivate PNCs due to the dominant Br^- surface defects of PNCs. However, the dispersibility and PL QY of PNCs are weaker than that of PNCs capped simultaneously with both amino and carboxylic ligands.[18]

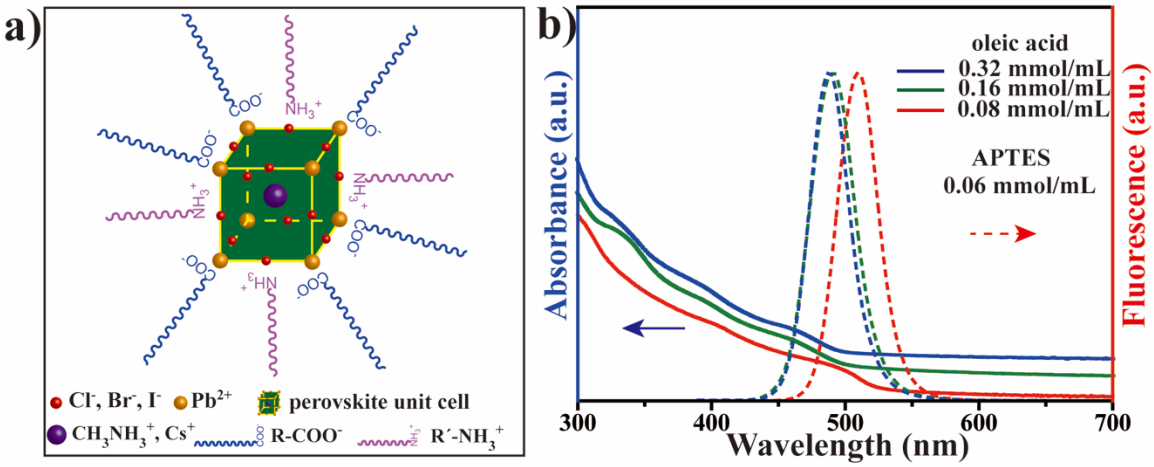

Figure 2-2- (a) A schematic diagram illustrating the surface passivation mechanism of Br and Pb surface defects. (b) UV-Vis electronic absorption (solid lines) and PL spectra (dashed lines, λex = 365 nm) of PNCs prepared with different concentrations of oleic acid and 0.06 mmol/mL APTES.

Based on Equation 1, a high concentration of R-COOH will push the reaction to the right hand side and produce more R'-NH_3^+ and R-COO^-, resulting in the formation of smaller nanoparticles because of the relatively slower delivery rate of perovskite monomers relative to the higher concentration of R'-NH_3^+.[31] The UV-Vis absorption and PL spectra of the PNCs synthesized using different concentrations of oleic acid and 0.06 mmol/mL APTES shown in Figure 2b supports this notation. With increasing the concentration of oleic acid, both the absorption onset and emission band blue-shifted, indicating the formation of smaller PNCs.

2.3.2 Synthesis of PNCs capped with peptides

Based on the above results, well-passivated PNCs can be obtained as long as both amino and carboxylic groups are present at the same time in the synthesis. This led us to hypothesize that a single peptide containing both amino and carboxylic acid functional groups may be effective in passivating PNCs, which is simpler than using two separate ligand molecules.

To demonstrate this, the peptide (12-aminododecanoic acid, 12-AA) was used as a capping ligand in the synthesis of PNCs. A dissolution-precipitation strategy was adopted to synthesize $PNCs_{peptide}$, which is widely used to prepare $CH_3NH_3PbBr_3$ PNCs.[6,8,18,31] Figure 3a shows the photograph of the synthesized $PNCs_{peptide}$ under room light. As it can be seen, the color of $PNCs_{peptide}$ powders shifted from orange to pale yellow depending on the concentration of 12-AA used. More importantly, the product yield of $PNCs_{peptide}$ can reach up to ~44%, which is much higher than that of PNCs capped with octylamine and oleic acid because a large number of large particles was formed and then discarded during the precipitation procedure.[5,6]

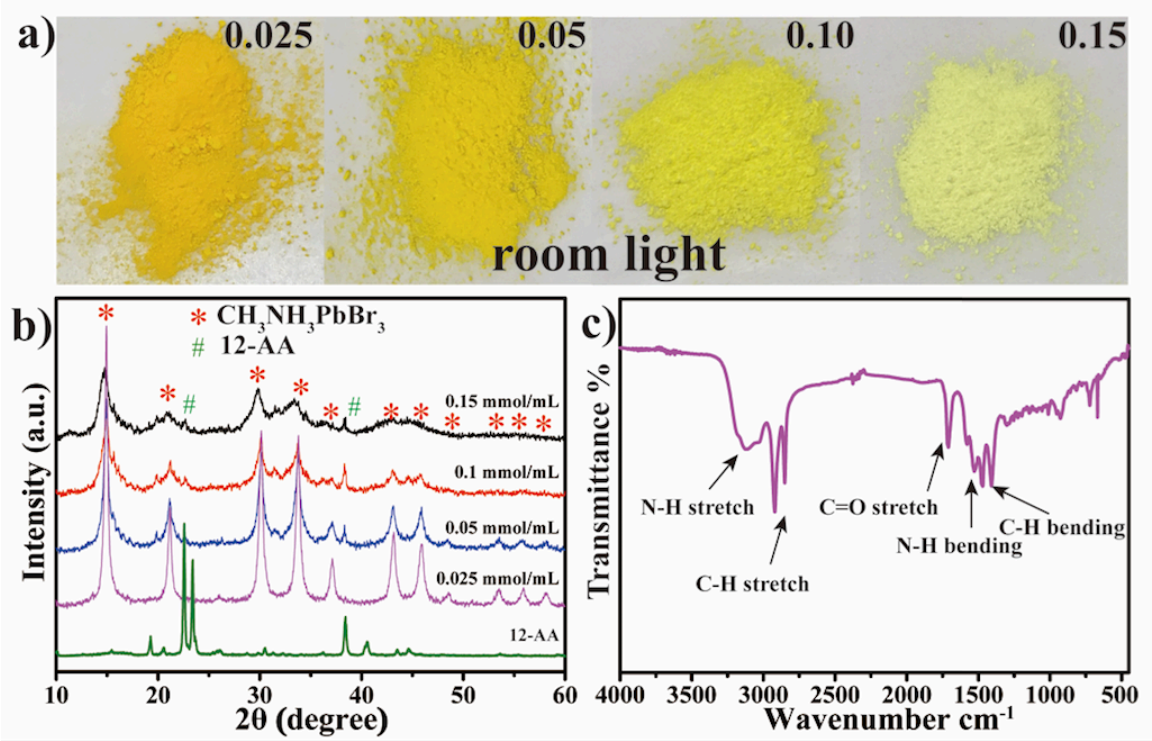

Figure 2-3- (a) Room light photograph and (b) XRD patterns of $PNC_{peptide}$ synthesized with 0.025, 0.05, 0.1, 0.15 mmol/L 12-AA. (c) FT-IR spectrum of $PNC_{peptide}$ prepared with 0.15 mmol/mL 12-AA.

To determine the crystal structure of as prepared products, XRD was carried out, with results shown in Figure 3b. The XRD peaks centered at 14.94°, 21.15°, 30.13°, 33.72°, 37.04°, 43.16°, 45.94°, 48.54°, 53.48°, 55.90° and 58.15° can be assigned to cubic phase of $CH_3NH_3PbBr_3$ perovskite (a = 5.9334 Å, space group = *Pm-3m*), demonstrating that the prepared samples are indeed $CH_3NH_3PbBr_3$ perovskite. Furthermore, with increasing amount of 12-AA, the XRD peaks of $PNC_{peptide}$ became broader, which indicates the formation of smaller PNCs. However, some peaks at 22.58° and 38.39° appear when the concentration of peptide is larger than 0.1

mmol/mL, which can be attributed to 12-AA, suggesting the inhomogeneous reaction between peptide and PNCs at higher concentration of peptide.

In addition, FT-IR spectroscopy was also used to reveal the existence of 12-AA as capping ligands, with representative spectra shown in Figure 3c. The evident absorption peaks at 2845 and 2922 cm^{-1} were assigned to the symmetric and asymmetric C-H stretching mode, respectively.[14,34] The existence of 12-AA on the PNCs surface was confirmed by the stretching mode of C=O (1704 cm^{-1}),[34] indicating that 12-AA is involved in the passivation reaction.

Figure 4 shows the typical TEM images of $PNC_{peptide}$ prepared with different concentrations of 12-AA. As seen in Figure 4a, many nanoparticles with an average diameter ~8.4 nm were embedded in the micron-scaled particles for 0.025 mmol/L 12-AA. With increasing the concentration to 0.05 mmol/L, the average size of $PNC_{peptide}$ decreased to 7.8±2.6 nm (Figure 4b). The size of nanoparticles can be further decreased to 3.9±0.6 nm (Figure 4d) when 0.15 mmol/L 12-AA was used in the synthesis. The trend of decreasing size is consistent with the XRD results. In order to analyze the phase structure of these PNCs, HRTEM was used and a representative image is shown in Figure 4e. The lattice space of 0.3 nm corresponding to the (002) crystal face of cubic $CH_3NH_3PbBr_3$ can be easily identified.[27] The amorphous materials (red dashed line in the TEM images) surrounding the PNCs are considered to be the network of peptides. When the peptide was dissolved in DMF precursor solution, both protonation reaction and peptide bond formation reaction between $–NH_2$ and –COOH will happen within and between peptide molecules. When DMF precursor solution was injected into

toluene, peptide molecules will be attached on the surface defects and restrict the growth of crystal nuclei. However, due to the polar nature of peptides, PNCs capped with peptides will aggregate and precipitate from toluene, as shown in Figure 4f, micron-scaled particles with smooth surface can be found, attributed to the aggregation of peptides.

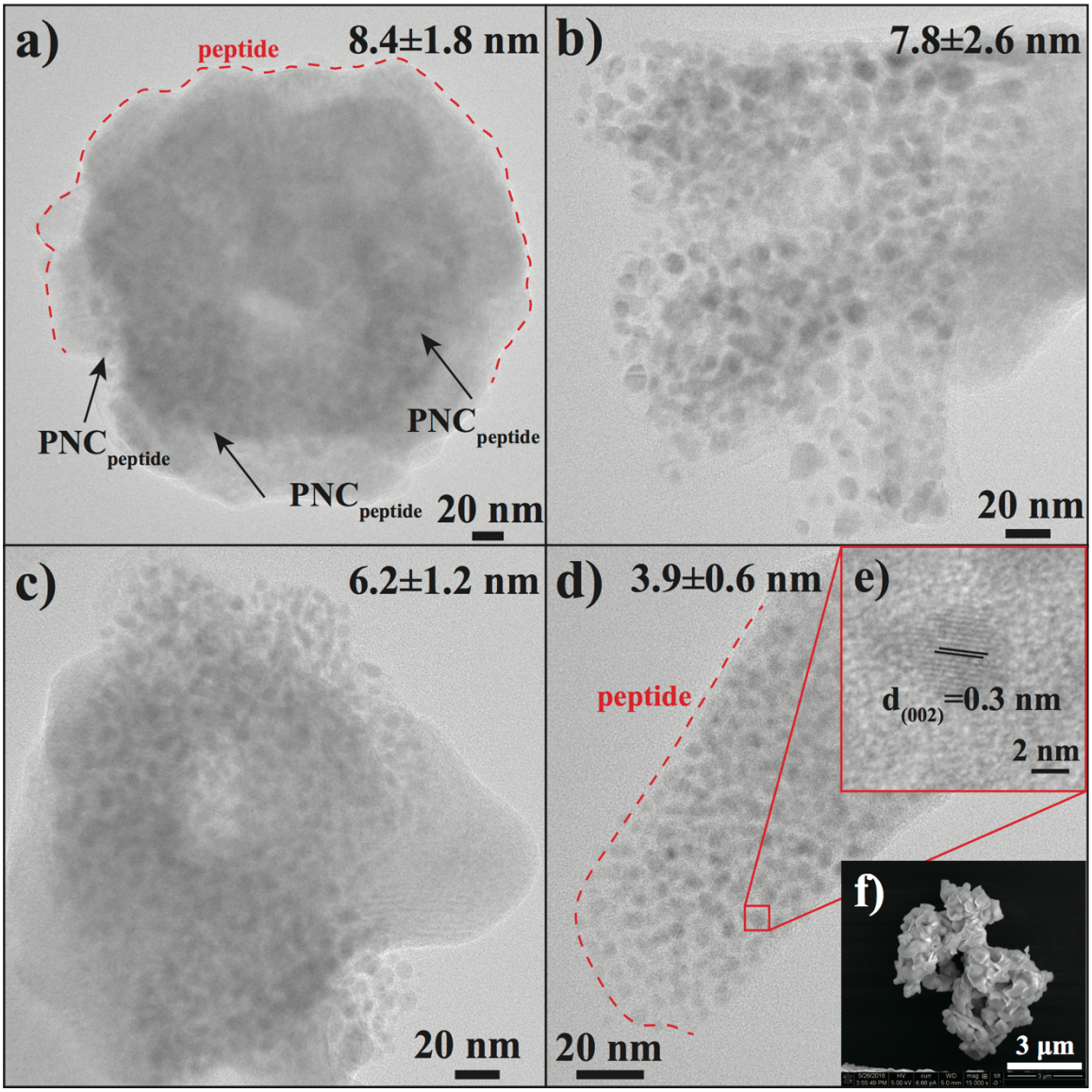

Figure 2-4- TEM images of $PNC_{peptide}$ capped with different amount of 12-AA. (a) 0.025 mmol/L, (b) 0.05 mmol/L, (c) 0.1 mmol/L, and (d) 0.15 mmol/L. HRTEM (e) and SEM images (f) of $PNC_{peptide}$ prepared with 0.15 mmol/L of 12-AA.

We further characterized the surface properties of $PNC_{peptide}$ and bulk materials using XPS spectroscopy as shown in Figure 5, the XPS peaks of $CH_3NH_3PbBr_3$ bulk materials located at 137.7 and 142.6 eV can be assigned to Pb $4f_{7/2}$ and Pb $4f_{5/2}$,

respectively.[35] The peak positions shifted by ~0.9 eV, towards high binding energy (BE), when peptide was used to prepare $PNC_{peptide}$, attributed to the passivation by $-COO^-$. The Br $3d_{5/2}$ and Br $3d_{3/2}$ peaks were observed at 67.6 and 68.5 eV for bulk materials.[36,37] Similar peak shifts (~0.8 eV), towards higher BE, was also be observed for $PNC_{peptide}$, indicative of successful passivation of the surface Br^- defect sites by $-NH_3^+$ in the peptide. Furthermore, the surface atom ratio (Br^-/Pb^{2+}) increased from 3.1 to 3.4 when peptides were used as capping ligands (Table 1), as an indication of Br^- rich surface for PNC, which is in agreement with other studies.[6,14]

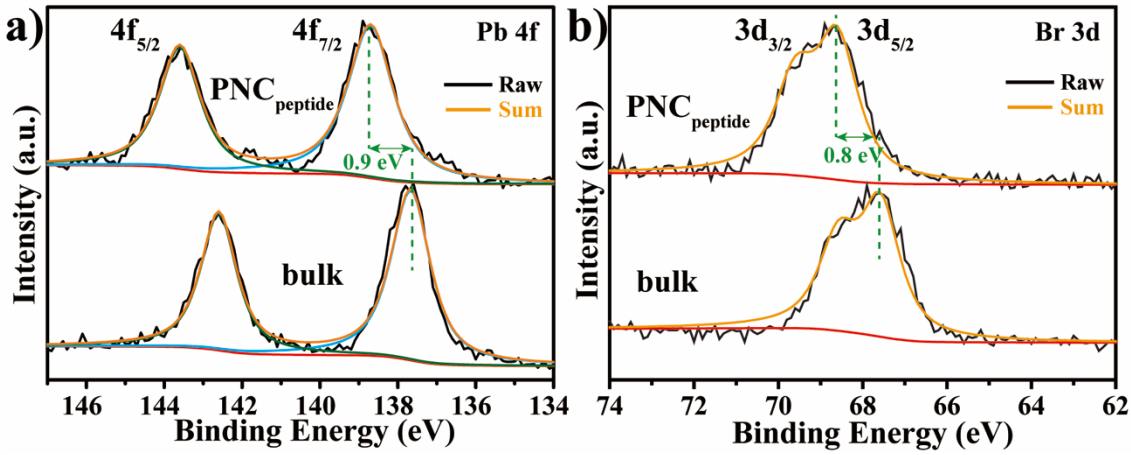

Figure 2-5- Pb 4f and (b) Br 3d XPS spectra of $CH_3NH_3PbBr_3$ bulk materials and $PNC_{peptide}$ prepared with 0.05 mmol/L 12-AA.

Table 2-1- XPS Pb 4f and Br 3d peak ratio for $CH_3NH_3PbBr_3$ bulk materials and $PNC_{peptide}$

	Core level	Area	Br:Pb ratio
$CH_3NH_3PbBr_3$ bulk materials	Pb 4f	469.8	3.1
	Br 3d	1469.3	
$CH_3NH_3PbBr_3$ $PNC_{peptide}$	Pb 4f	484.8	3.4
	Br 3d	1652.9	

2.3.3 Optical properties of $PNC_{peptide}$

Proper surface passivation of NCs or QDs usually results in an enhanced PL emission desired for many applications.[7,33,38] The optical properties of $PNC_{peptide}$ were determined using UV-Vis and PL spectroscopy. The UV-Vis spectrum of $PNC_{peptide}$ shown in Figure 6a exhibits a sharp rise around 560 nm with a saturation at 518 nm when 0.025 mmol/L peptide was used. The absorption onset blue-shifted to ~550, 516 and 481 nm for 0.05, 0.1 and 0.15 mmol/L of peptide, respectively, because of the decrease in size of $PNC_{peptide}$. Correspondingly, the emission bands of $PNC_{peptide}$ peaked at 531, 517, 469 and 449 nm when applying 0.025, 0.05, 0.1 and 0.15 mmol/L of peptide, respectively. However, the fluorescence intensity decreased dramatically when increasing the concentration of peptide to 0.15 mmol/L, which may result from the higher density of surface defects for smaller nanoparticles. Figure 6c presents the photograph of $PNC_{peptide}$ under UV light. It can be clearly seen that the fluorescence changes from green to blue, consistent with the PL spectrum results.

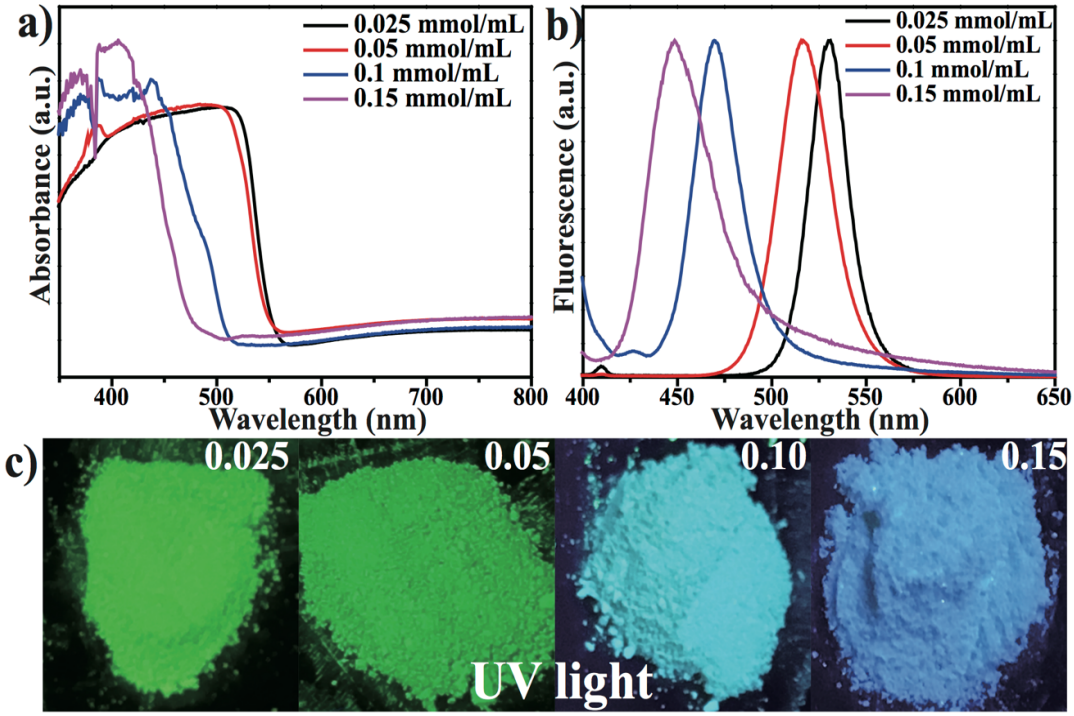

Figure 2-6- (a) UV-Vis absorption, (b) PL spectra (ex = 365 nm) and (c) UV light (ex = 365 nm) photographs of $PNC_{peptide}$ prepared with 0.025, 0.05, 0.1, 0.15 mmol/L 12-AA.

In order to demonstrate the versatility of this method, different lengths of peptides were used for the synthesis of PNCs. The UV-Vis absorption and PL spectra of PNCs prepared with peptides are shown in Figure 7a and b, respectively. A sharp rise of absorption spectra around 550 nm with a saturation at ~505 nm can be observed for each sample. Correspondingly, a narrow and symmetric PL emission band with a maximum at ~516 nm can be easily identified when 6-aminohexanoic acid (6-AA), 8-aminooctanoic acid (8-AA) or 12-AA was used as capping ligand, respectively. We have also attempted to use natural peptides, such as glycine. However, it was not successful since the peptide does not dissolve in DMF even with some heating.

To show generality of the approach, $CsPbBr_3$ PNCs was also synthesized with peptides as capping ligands. As shown in Figure 7c, the sharp rise in UV-Vis absorption and narrow PL emission band indicate the successful formation of $CsPbBr_3$ PNCs. We expect that this strategy can be applied to other PNCs with different metal ions, halides, or organic constituent.

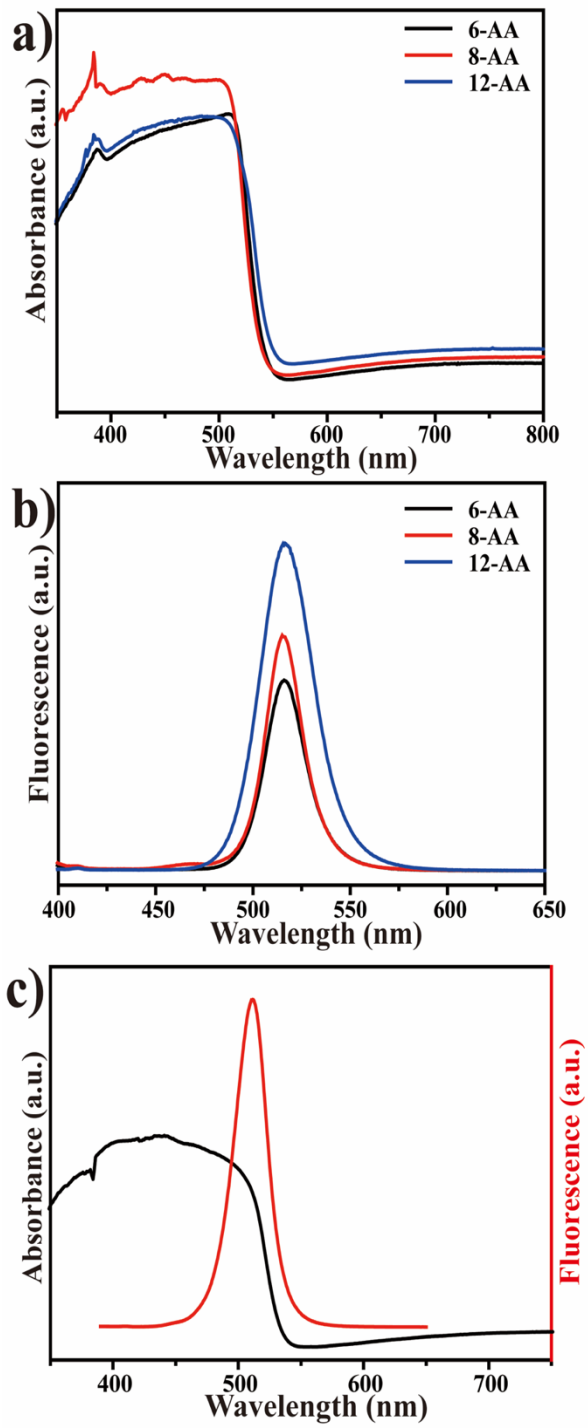

Figure 2-7- (a) UV-Vis absorption and (b) PL spectra (ex=365 nm) of $CH_3NH_3PbBr_3$ $PNC_{peptide}$ prepared with 0.05 mmol/L 6-AA, 8-AA or 12-AA, respectively. (c) UV-Vis absorption and PL spectra (ex = 365 nm) of $CsPbBr_3$ $PNC_{peptide}$ prepared with 0.05 mmol/L 12-AA.

2.4 Experimental Section

Materials: All the chemicals were used as received without further purification, including toluene (Spectroscopic grade, Fisher Scientific), N,N-dimethylformamide (DMF, spectroscopic grade, Fisher Scientific), oleic acid (90%, Alfa Aesar), (3-aminopropyl)triethoxysilane (99%, Sigma Aldrich), $PbBr_2$ (99.99%, Alfa Aesar), CsBr (99.9%, Strem Chemicals), 6-aminohexanoic acid (98.5%, Sigma Aldrich), 8-aminooctanoic acid (99%, Sigma Aldrich), 12-aminododecanoic acid (95%, Sigma Aldrich), benzoic acid (99.5%, Sigma-Aldrich) and acetic acid (99.85%, Sigma-Aldrich).

$CH_3NH_3PbBr_3$ PNCs prepared with APTES and different carboxylic acids: The $CH_3NH_3PbBr_3$ PNCs were synthesized following a method reported previously.[26, 31] 5 mL precursor solution of PNCs was prepared by dissolving 0.16 mmol CH_3NH_3Br, 0.2 mmol $PbBr_2$, 0.3 mmol APTES and 0.8 mmol oleic acid/benzoic acid/acetic acid in DMF solvent and sonicated until the solution became transparent. 4 μL of the precursor solution then was injected slowly into 4 ml toluene for spectrum analysis.

$CH_3NH_3PbBr_3$/$CsPbBr_3$ PNCs prepared with peptides: The precursor solutions for $CH_3NH_3PbBr_3$ PNCs passivated by peptides were prepared by mixing 0.16 mmol CH_3NH_3Br, 0.2 mmol $PbBr_2$ with different amounts (0.025, 0.05, 0.1, 0.15 mmol/L) of 3 different lengths of peptide (6-AA/8-AA/12-AA) and dissolving them in 2 ml DMF solvent followed by heating the solution on hot plates until a transparent solution was formed. All the precursor solution was injected into 50 ml toluene and the solid

precipitate was collected by centrifugation (5000 rpm, 5 min) followed by washing with toluene three times. The collected solid product was dried under vacuum overnight for further analysis. $CsPbBr_3$ PNCs were synthesized similarly by dissolving 0.08 mmol CsBr, 0.1 mmol of $PbBr_2$ and 0.10 mmol of 12-AA in 2 ml DMF and then heating the precursor solution until it was clear. The purifying procedures for $CsPbBr_3$ PNCs were same to that of $CH_3NH_3PbBr_3$ PNCs.

$CH_3NH_3PbBr_3$ bulk materials: The $CH_3NH_3PbBr_3$ bulk materials was obtained by injecting 2 mL DMF precursor solution without any capping ligands into 50 mL toluene. The purifying procedure was the same as that of $CH_3NH_3PbBr_3$ PNCs.

Characterization: UV-Vis diffuse reflectance spectra were collected with a Perkin Elmer Lambda 35 spectrometer. X-ray photoelectron spectra (XPS) were recorded with a PHI 5400/XPS instrument equipped with an Al Kα source operated at 350 W and 10^{-9} Torr. The Fourier transform infrared (FT-IR) measurements were carried out with a Perkin Elmer FT-IR spectrometer (Spectrum One, spectral resolution 4 cm^{-1}), where the samples were prepared by dropping the PNCs solutions onto a KBr substrate. X-Ray diffraction (XRD, Rigaku Americas Miniflex Plus powder diffractometer) analysis was used to obtain the crystalline phase at a voltage of 40 kV and current of 30 mA. The scanning angle range was 10-60^o (2θ) with a rate of 3^o/min. Scanning electron microscopy (SEM, FEI Quanta 3D Dual beam microscopy) and transmission electron microscopy (TEM, Hitachi H-9500) were carried out to obtain the morphology and interlayer spacing of samples at an accelerating voltage of 300 kV.

2.5 Conclusion

In summary, we have demonstrated that synergy between amino and carboxylic groups in the same peptide molecules as capping ligands allows generation of well-passivated PNCs, as exemplified by both $CH_3NH_3PbBr_3$ and $CsPbBr_3$. Furthermore, the size (~3.9-8.6 nm) and optical properties of the $CH_3NH_3PbBr_3$ PNCs can be easily tuned by adjusting the concentration of the peptide. Such PNCs with peptides conjugated on their surface have potential applications in biomedicine including optical sensing and imaging.

2.6 References

1. Algar R.; Anthony T.; and Ulrich K. Beyond labels: a review of the application of quantum dots as integrated components of assays, bioprobes, and biosensors utilizing optical transduction. *Anal. Chim. Acta*. **2010**, 673, 1-25.

2. Yong K.; Indrajit R.; Wing-Cheung L.; and Rui H. Synthesis of cRGD-peptide conjugated near-infrared CdTe/ZnSe core–shell quantum dots for in vivo cancer targeting and imaging. *Chem. Commun.* **2010**, 46, 7136-7138.

3. Li J.; and Jun-Jie Z. Quantum dots for fluorescent biosensing and bio-imaging applications. *Analyst.* **2013**, 138, 2506-2515.

4. Bekenstein, Y.; Koscher, B.A.; Eaton, S.W.; Yang, P; and Alivisatos, A.P. Highly luminescent colloidal nanoplates of perovskite cesium lead halide and their oriented assemblies. *J. Am. Chem. Soc.* **2015**, 137, 16008-16011.

5. Huang, H.; Susha, A.S.; Kershaw, S.V.; Hung, T.F. and Rogach, A.L. Control of emission color of high quantum yield $CH_3NH_3PbBr_3$ perovskite quantum dots by precipitation temperature. *Adv. Sci.* **2015**, 2, 1500194.

6. Zhang, F.; Zhong, H.; Chen, C.; Wu, X.G.; Hu, X.; Huang, H.; Han, J.; Zou, B. and Dong, Y. Brightly luminescent and color-tunable colloidal $CH_3NH_3PbX_3$ (X= Br, I, Cl) quantum dots: potential alternatives for display technology. *ACS nano*, **2015**, 9, 4533-4542.

7. Swarnkar, A.; Chulliyil, R.; Ravi, V.K.; Irfanullah, M.; Chowdhury, A. and Nag, A. Colloidal $CsPbBr_3$ perovskite nanocrystals: luminescence beyond traditional quantum dots. *Ang. Chem. Int. Ed.*, **2015**, 54, 15424-15428.

8. Pathak, S.; Sakai, N.; Wisnivesky Rocca Rivarola, F.; Stranks, S.D.; Liu, J.; Eperon, G.E.; Ducati, C.; Wojciechowski, K.; Griffiths, J.T.; Haghighirad, A.A. and Pellaroque, A. Perovskite crystals for tunable white light emission. *Chem. Mater.* **2015**, 27, 8066-8075.

9. Hoffman, J.B.; Schleper, A.L. and Kamat, P.V. Transformation of Sintered $CsPbBr_3$ Nanocrystals to Cubic $CsPbI_3$ and Gradient $CsPbBr_xI_{3-x}$ through Halide Exchange. *J. Am. Chem*. Soc. **2016**, 138, 8603-8611.

10. Xing, J.; Yan, F.; Zhao, Y.; Chen, S.; Yu, H.; Zhang, Q.; Zeng, R.; Demir, H.V.; Sun, X.; Huan, A. and Xiong, Q. High-efficiency light-emitting diodes of organometal halide perovskite amorphous nanoparticles. *ACS Nano*. **2016**, 10, 6623-6630.

11. Liang, D.; Peng, Y.; Fu, Y.; Shearer, M.J.; Zhang, J.; Zhai, J.; Zhang, Y.; Hamers, R.J.; Andrew, T.L. and Jin, S. Color-pure violet-light-emitting diodes based on layered lead halide perovskite nanoplates. *ACS nano*, **2016**, 10, 6897-6904.

12. Zhang, D.; Yang, Y.; Bekenstein, Y.; Yu, Y.; Gibson, N.A.; Wong, A.B.; Eaton, S.W.; Kornienko, N.; Kong, Q.; Lai, M. and Alivisatos, A.P. Synthesis of composition tunable and highly luminescent cesium lead halide nanowires through anion-exchange reactions. *J. Am. Chem. Soc.* **2016** 138, 7236-7239.

13. Shamsi, J.; Dang, Z.; Bianchini, P.; Canale, C.; Di Stasio, F.; Brescia, R.; Prato, M. and Manna, L. Colloidal synthesis of quantum confined single crystal $CsPbBr_3$ nanosheets with lateral size control up to the micrometer range. *J. Am. Chem*. Soc. **2016**, 138, 7240-7243.

14. Teunis, M.B.; Jana, A.; Dutta, P.; Johnson, M.A.; Mandal, M.; Muhoberac, B.B. and Sardar, R. Mesoscale growth and assembly of bright luminescent organolead halide perovskite quantum wires. *Chem. Mater.* **2016**, 28, 5043-5054.

15. Bhaumik, S.; Veldhuis, S.A.; Ng, Y.F.; Li, M.; Muduli, S.K.; Sum, T.C.; Damodaran, B.; Mhaisalkar, S. and Mathews, N. Highly stable, luminescent core–shell type methylammonium–octylammonium lead bromide layered perovskite nanoparticles. *Chem. Commun.*, **2016***,* 52, 7118-7121.

16. Yuan, Z., Shu, Y., Tian, Y., Xin, Y. and Ma, B. A facile one-pot synthesis of deep blue luminescent lead bromide perovskite microdisks. *Chem. Commun.*, **2016**, 51, 16385-16388.

17. Zhang, X.; Xu, B.; Zhang, J.; Gao, Y.; Zheng, Y.; Wang, K. and Sun, X.W. All-Inorganic Perovskite Nanocrystals for High-Efficiency Light Emitting Diodes: Dual-Phase $CsPbBr_3$-$CsPb_2Br_5$ Composites. *Adv. Func. Mater.* **2016**, 26, 4595-4600

18. Sichert, J.A.; Tong, Y.; Mutz, N.; Vollmer, M.; Fischer, S.; Milowska, K.Z.; García Cortadella, R.; Nickel, B.; Cardenas-Daw, C.; Stolarczyk, J.K. and Urban, A.S. Quantum size effect in organometal halide perovskite nanoplatelets. *Nano letters*, **2015**, 15, 6521-6527.

19. Calabrese, J.; Jones, N.L.; Harlow, R.L.; Herron, N.; Thorn, D.L. and Wang, Y. Preparation and characterization of layered lead halide compounds. *J. Am. Chem. Soc.* **1991**, 113, 2328-2330.

20. Ling, Y.; Yuan, Z.; Tian, Y.; Wang, X.; Wang, J.C.; Xin, Y.; Hanson, K.; Ma, B. and Gao, H. Bright light-emitting diodes based on organometal halide perovskite nanoplatelets. *Adv. Mater.* **2016**, 28, 305-311.

21. Huang, H.; Zhao, F.; Liu, L.; Zhang, F.; Wu, X.G.; Shi, L.; Zou, B.; Pei, Q. and Zhong, H. Emulsion synthesis of size-tunable $CH_3NH_3PbBr_3$ quantum dots: an alternative route toward efficient light-emitting diodes. *ACS Appl. Mater. Interfaces* **2015**, 7, 28128-28133.

22. Deng, W.; Xu, X.; Zhang, X.; Zhang, Y.; Jin, X.; Wang, L.; Lee, S.T. and Jie, J. Organometal Halide Perovskite Quantum Dot Light-Emitting Diodes. *Adv. Funct. Mater.* **2016**, 26, 4797-4802.

23. Wang, Y.; Li, X.; Song, J.; Xiao, L.; Zeng, H. and Sun, H. All-inorganic colloidal perovskite quantum dots: a new class of lasing materials with favorable characteristics. *Adv. Mater*. **2015**, 27, 7101-7108.

24. Akkerman, Q.A.; Motti, S.G.; Srimath Kandada; A.R., Mosconi E.; D'Innocenzo V.; Bertoni, G.; Marras, S.; Kamino, B.A.; Miranda, L.; De Angelis, F. and Petrozza, A. Solution synthesis approach to colloidal cesium lead halide perovskite nanoplatelets with monolayer-level thickness control. *J. Am. Chem*. Soc. **2016**, 138, 1010-1016.

25. Li, X.; Wu, Y.; Zhang, S.; Cai, B.; Gu, Y.; Song, J. and Zeng, H. $CsPbX_3$ quantum dots for lighting and displays: room-temperature synthesis, photoluminescence superiorities, underlying origins and white light-emitting diodes. *Adv. Funct. Mater*. **2016**, 26, 2435-2445.

26. Luo, B.; Pu, Y.C.; Yang, Y.; Lindley, S.A.; Abdelmageed, G.; Ashry, H.; Li, Y.; Li, X. and Zhang, J.Z. Synthesis, optical properties, and exciton dynamics of organolead bromide perovskite nanocrystals. *J. Phys. Chem. C.* **2015**, 119, 26672-26682.

27. Schmidt, L.C.; Pertegás, A.; González-Carrero, S.; Malinkiewicz, O.; Agouram, S.; Mínguez Espallargas, G.; Bolink, H.J.; Galian, R.E. and Pérez-Prieto, J. Nontemplate synthesis of $CH_3NH_3PbBr_3$ perovskite nanoparticles. *J. Am. Chem. Soc.* **2014**, 136, 850-853.

28. Tyagi, P.; Arveson, S.M. and Tisdale, W.A. Colloidal organohalide perovskite nanoplatelets exhibiting quantum confinement. J. Phys. Chem. Lett. **2015**, 6, 1911-1916.

29. Kim, Y.; Yassitepe, E.; Voznyy, O.; Comin, R.; Walters, G.; Gong, X.; Kanjanaboos, P.; Nogueira, A.F. and Sargent, E.H. Efficient luminescence from perovskite quantum dot solids. *ACS Appl. Mater. Interfaces.* **2015**, 7, 25007-25013.

30. Zhou, M. and Ghosh, I. Quantum dots and peptides: a bright future together. *Biopolymers,* **2007**, 88, 325-339.

31. Luo, B.; Pu, Y.C.; Lindley, S.A.; Yang, Y.; Lu, L.; Li, Y.; Li, X. and Zhang, J.Z. Organolead halide perovskite nanocrystals: branched capping ligands control crystal size and stability. *Angew. Chem. Int. Ed.* **2016**, 55, 8864-8868.

32. Yang, Z.; Janmohamed, A.; Lan, X.; García de Arquer, F.P.; Voznyy, O.; Yassitepe, E.; Kim, G.H.; Ning, Z.; Gong, X.; Comin, R. and Sargent, E.H. Colloidal quantum dot photovoltaics enhanced by perovskite shelling. *Nano letters*, **2015**, 15, 7539-7543.

33. Morris, T. and Zubkov, T., 2014. Steric effects of carboxylic capping ligands on the growth of the CdSe quantum dots. *Colloids and Surfaces A: Physicochem. and Eng. Aspects*, **2014**, 443, 439-449.

34. Hofmann, A.; Thierbach, S.; Semisch, A.; Hartwig, A.; Taupitz, M.; Rühl, E. and Graf, C. Highly monodisperse water-dispersable iron oxide nanoparticles for biomedical applications. *J. Mater. Chem.* **2010**, 20, 7842-7853.

35. Ng, T.W.; Chan, C.Y.; Lo, M.F.; Guan, Z.Q. and Lee, C.S. Formation chemistry of perovskites with mixed iodide/chloride content and the implications on charge transport properties. *J. Mater. Chem. A*. **2015**, 3, 9081-9085.

36. Naphade, R., Nagane, S., Shanker, G.S., Fernandes, R., Kothari, D., Zhou, Y., Padture, N.P. and Ogale, S. Hybrid Perovskite Quantum Nanostructures Synthesized by Electrospray Antisolvent–Solvent Extraction and Intercalation. *ACS Appl. Mater. Interfaces.* **2016**, 8, 854-861.

37. Tang, J.; Kemp, K.W.; Hoogland, S.; Jeong, K.S.; Liu, H.; Levina, L.; Furukawa, M.; Wang, X.; Debnath, R.; Cha, D. and Chou, K.W. Colloidal-quantum-dot photovoltaics using atomic-ligand passivation. *Nat. Mater.* **2011**, 10, 765.

38. Pu, Y.C. and Hsu, Y.J. Multicolored $Cd_{1-x}Zn_xSe$ quantum dots with type-I core/shell structure: single-step synthesis and their use as light emitting diodes. *Nanoscale.* **2014**, 6, 3881-3888.

Chapter Three

3 Size Dependence of Charge Carrier Dynamic in Organometal Halide Perovskite Nanocrystals: Deciphering the Radiative vs Non-radiative Components

3.1 Abstract

In this work, we have successfully synthesized and characterized three differently sized (3.1, 5.7, and 9.3 nm) methyl ammonium lead bromide ($CH_3NH_3PbBr_3$) perovskite nanocrystals (PNCs) passivated using (3-Aminopropyl) triethoxysilane (APTES) and oleic acid (OA) as capping ligands. These PNCs show size-dependent absorption (440 nm-520 nm) and photoluminescence (PL) (470 to 530 nm), with the middle-sized PNCs exhibiting the highest PL quantum yield (~91%). The effect of size on the exciton/charge carrier dynamic of PNCs is studied using transient absorption spectroscopy (TA) and time resolved photoluminescence (TRPL). The middle-sized PNCs (PNC_{35_APTES}) show slower early time recombination compared to that of the larger and smaller PNCs, suggesting optimized passivation of surface trap states. The observed PL lifetime and QY are analyzed to determine the size dependence of the radiative and non-radiative decay components. The radiative lifetime is found to decrease with decreasing PNC size, which seems to be primarily determined by the PNC core, while the non-radiative lifetime is longest for the middle-sized PNCs, which

is strongly influenced by the presence of bandgap states that depend on surface passivation. A kinetic model is proposed to explain the observed dynamics results, including the size dependence. This study demonstrates the competing effect between size and surface properties in determining the dynamics and optical properties of PNCs.

3.2 Introduction

Organometal halide perovskites (OMHP) have been widely studied in recent years due to their promising applications in the field of photonics, especially photovoltaics (PV). Their novel optical and electrical properties include high absorption coefficients, tunable and narrow emission, long exciton lifetimes, and fast charge carrier diffusion (8-33 $cm^2 V^{-1} s^{-1}$).[1,2,3] When combined with easy and low cost processing, they demonstrate strong potential for applications beyond PV, such as light emitting diodes (LEDs), photodetectors, sensors, lasers, and photoelectrochemical cells.[4,5,6,7,8] Since the first reported power conversion efficiency (PCE) of ~3.8% for a perovskite-based PV cells in 2009,[9] significant progress has been made in understanding the fundamental properties of the materials and improving solar cell structures for higher efficiency. Recently, a PCE exceeding 25% has been reported for a tandem silicon-OMHP solar cell.[10]

Despite significant potential, there are challenges limiting large-scale application of OMHPs. Instability toward environmental factors such as UV light, humidity, oxygen, solvent and temperature are some of the most challenging issues. Several studies have correlated these instabilities to OMHP surface properties such as

the presence of defects.[11,12] These defects, which can be formed as a result of chemical and structural changes in the material,[13] are also a detrimental factor impacting device performance as they provide recombination channels for photogenerated charge carriers.[11,14,15] Therefore, various strategies for surface modification and defect passivation, including addition of molecular capping ligands, organic polymers, and metal oxide shells, have been used in order to improve the chemical and physical stability that is critical for maintaining device performance over time.[16,17,18,19]

Because perovskite nanocrystals (PNCs) or perovskite quantum dots (PQDs) have a large surface-to-volume (S/V) ratio, they are considered to be great models for developing stabilization and passivation strategies.[20] In addition, PNCs possess tunable energy levels and optical properties due to the quantum confinement effects, especially when their size is smaller than the Bohr exciton radius.[21] This can be used to control the functionalities of the materials for different applications. For instance, PNCs with diameters of <10 nm show strongly blue shifted PL, high exciton binding energy (E_b), low exciton diffusion length (L_D), and higher PL quantum yield (PLQY), compared to larger particles and bulk material.[22,23,24] This potentially enables complex device designs based on cascade energy transfer using these PNCs.[25] Additionally, one-photon linear absorption cross section of $CsPbBr_3$ PNCs was found to strongly depend on size.[26] For $CsPbBr_3$ PNCs with edge length above ~7 nm, spectral signatures are mostly similar to that of bulk material, though some new kinetic processes emerge at high fluence in nanometer sized crystals.[27] However, for smaller PNCs (~4 nm) strong quantum confinement effects manifest in their spectral dynamics, resulting in discrete

energy states, enhanced bandgap renormalization energy, and departure from a Boltzmann statistical carrier cooling.[27]

Ultrafast spectroscopy techniques such as transient absorption (TA) and time resolved PL (TRPL) have been employed as powerful tools for probing exciton and charge carrier dynamics, including charge transfer and recombination, which are highly relevant to application in solar cell and LEDs. To date, most time-resolved dynamics studies of perovskites have focused on the photophysical properties of 2D structures[28,29,30,31,32] or mechanisms of carrier generation and transfer between PNCs and electron/hole acceptors[28,33,34,35]. There are also a few studies on the effects of capping ligands on the charge carrier dynamics of PNCs.[16,36] However, there is still a lack of understanding of the effect of NC size and associated surface passivation on charge carrier dynamics. Determining the size dependence of dynamics as well as optical properties of PNCs can lead to their optimized design and development for PV and other applications.

In this work, we synthesized methylammonium lead bromide ($CH_3NH_3PbBr_3$) NCs using a combination of APTES and OA as capping ligand for proper passivation. The concentration of APTES was varied to control the size of PNCs. Characterization techniques such as UV-Vis absorption, photoluminescence (PL), powder X-ray diffraction (XRD), high resolution transmission electron microscopy (HR-TEM), ultrafast transient absorption (TA), and time-resolved PL (TRPL) were used to determine the photophysical properties of the materials and their dependence on particle size and extent of surface passivation.

3.3 Materials and Methods

3.3.1 Materials

All chemicals were used as received without further purification: Toluene (spectroscopic grade, Fisher Scientific), *N*,*N*-dimethylformamide (DMF, spectroscopic grade, Fisher Scientific), Methylammonium bromide (Greatcell Solar Australia Pty Ltd), Lead bromide (98+%, Alfa Aesar), oleic acid (90%, Alfa Aesar), (3-Aminopropyl) triethoxysilane (99%, Sigma-Aldrich).

3.3.2 Synthesis

A ligand-assisted reprecipitation method was used to synthesize the $CH_3NH_3PbBr_3$ NCs. Briefly, 0.157 mmol of methylammonium bromide (MABr) and 0.200 mmol of lead bromide ($PbBr_2$) were dissolved in 400 μL *N*,*N*-dimethylformamide (DMF) and sonicated until clear. 100 μL of oleic acid and varying amounts of (3-Aminopropyl) triethoxysilane (APTES) (20 μL, 35 μL, and 50 μL) were added to separate solutions to control the particle size. The precursor solution was further sonicated to reach a homogeneous solution and then injected into 5 mL toluene to precipitate and collect the nanocrystals. The resultant nanocrystals were centrifuged at 6000 rpm for 5 minutes and washed with toluene 2 times to remove unreacted precursors. A portion of the collected precipitate was dried for powder XRD characterization and the rest was re-dispersed in toluene for film fabrication.

3.3.3 Characterization and Instruments

UV–Vis and fluorescence spectra of the prepared nanocrystal films were collected on an Agilent Technologies Cary 60 and FluoroMax-3, respectively. XRD was used to obtain the crystalline phase at a voltage of 40 kV and current of 30 mA using a Rigaku America Miniflex Plus powder diffractometer at the home institution. The scanning angle range was 10–60° (2θ) with a rate of 3° min^{-1}. Transmission electron microscopy (TEM) and high-resolution TEM (HRTEM) were carried out to investigate the size, morphology, and lattice spacing of the PNCs. The TEM study was carried out using a FEI UT Tecnai HRTEM microscope operated at a 200 kV accelerating voltage.

3.3.3.1 Femtosecond Transient Absorption (TA) Spectroscopy

The femtosecond transient absorption measurements were carried out using a Quantronix laser system consisting of an Er-doped fiber oscillator, regenerative amplifier, and diode-pumped Nd:YLF pump laser (527 nm) described previously.[37] In this system, the amplified beam splits in a 1:9 ratio to generate a white light continuum (WLC) probe pulse (450–750 nm) and feed an optical parametric amplifier respectively. To study power dependence, all samples were photoexcited using a 390 nm beam with various pulse energies (750, 323 and 190 nJ/pulse). The pump and probe were overlapped on the sample spatially and temporally. The transient absorption data was collected using a charge-coupled device (CCD) detector over a temporal delay interval of 0–1000 ps between the pump and probe pulses. The transient absorption data was plotted in 3D using MATLAB and the single wavelength decay of the absorption overtime was fitted using either triple or double exponential decay functions.

3.3.3.2 Time-resolved Photoluminescence

Time-correlated single photon counting (TCSPC) was carried out on a home-built apparatus. The excitation source was a pulsed Super K EXTREME (NKT Photonics) supercontinuum laser coupled to a Super K SELECT (NKT Photonics) acousto-optic filter and external RF driver (NKT Photonics) to select the wavelength of the excitation pulse. Measurements were carried out at a 19.4 MHz pulse repetition rate. The sample was excited by vertically polarized light, with emission collected under magic angle conditions. Emitted light was collimated and refocused by a set of achromatic doublets (Thorlabs). Long pass filters were used to minimize the influence of the reflected excitation beam. Emission wavelengths were selected by an Acton Spectra Pro SP-2300 monochromator (Princeton Instruments), on which two detectors were mounted for steady-state and time-resolved measurements. An air-cooled PIXIS 100 CCD (Princeton Instruments) was used to record the steady-state spectra on the fly. A hybrid PMT with minimal after-pulsing (Becker and Hickl) was used to record the time-resolved fluorescence decay. An SPC-130 photon counting module (Becker and Hickl) coupled to a Simple-Tau 130 table top TCSPC system was used for photon counting. Collection was carried out until approximately 10,000 counts (ranging from 12s - 100s, depending on sample fluorescence yield of the sample) were reached in the main channel. Measurements were repeated multiple times and averaged.

3.4 Results and Discussion

3.4.1 Structural Characterization of PNCs by XRD and TEM

$CH_3NH_3PbBr_3$ NCs were synthesized using a dissolution-precipitation method as reported previously[38], and size control was achieved by varying the amount of APTES capping ligand used in synthesis. Structural properties of PNCs were characterized using XRD and TEM as shown in Figure 1(a-d). For 20, 35 and 50 μL of APTES, spherical PNCs with average sizes of 9.3± 0.7, 5.7± 0.2 nm, and 3.1± 0.2 nm were obtained, respectively. Corresponding to the amount of APTES used (20, 35, and 50 μL), these samples are labeled PNC_{20_APTES}, PNC_{35_APTES}, and PNC_{50_APTES}, respectively. As expected, increasing the concentration of APTES decreased the size of the resultant PNCs. This trend may be attributed to the coordinating effect of capping ligands which slows down the rate of monomer transfer to the PNCs surface and thereby limits growth.[39] The relative uniformity of all sizes is due to the strong steric hindrance of branched APTES ligands, as reported previously.[38] Interlayer spacing of 2.6 Å and 2.9 Å ,shown in the inset HRTEM images, could be assigned to the (0 2 1) and (0 0 2) planes of cubic $CH_3NH_3PbBr_3$, as reported in previous studies.[40] The XRD patterns shown in Figure 1d were used to determine the crystal structure of the PNCs. The peaks centered at 14.80°, 21.03°, 29.98°, 33.55°, 36.93°, 42.83°, and 45.69° can be indexed to cubic phase $CH_3NH_3Br_3$ perovskite, indicating sample crystallinity and purity.[40] When the amount of APTES was increased, significant broadening in XRD peaks was observed, due to the presence of smaller PNCs and amorphous silica as a result of higher concertation of APTES on the samples.[41] Further increase of APTES concentration resulted in the formation of bulk material instead of PNCs.

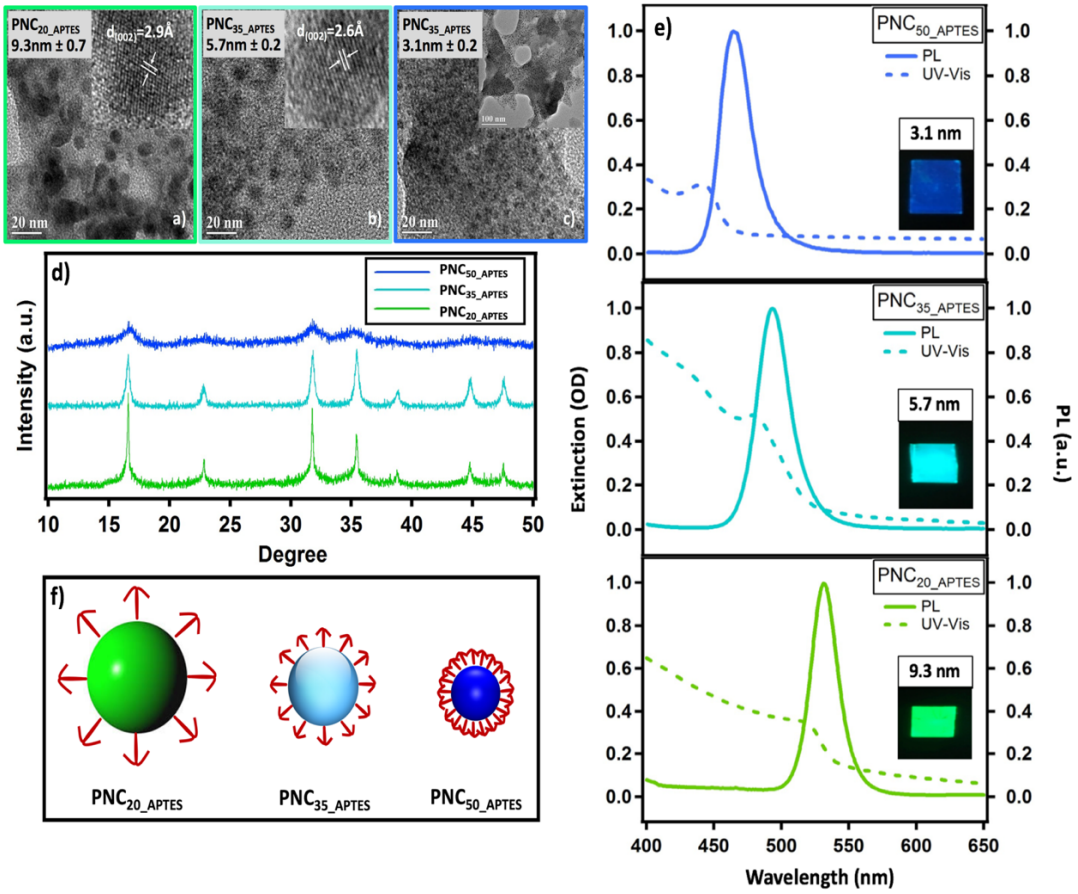

Figure 3-1- TEM images of a) PNC_{20_APTES} b) PNC_{35_APTES}, and c) PNC_{50_APTES}. (Insets: HRTEM images of PNC_{20_APTES}, PNC_{35_APTES}, and amorphous matrix of APTES. d) XRD pattern of PNC_{20_APTES}, PNC_{35_APTES}, and PNC_{50_APTES}. e) UV-Vis and PL spectra (λex=360 nm) of PNC_{20_APTES}, PNC_{35_APTES}, and PNC_{50_APTES} spin coated on glass substrate at 4500 rpm. (Insets are digital pictures of the PNC_{APTES} films under UV light). f) Schematic representation of competing effect between proper defect passivation of the PNCs and steric hindrance as a function of capping ligand concentration.

3.4.2 Band Edge Absorption and Steady State PL

For each sample, uniform films were prepared by spin coating to further study the optical properties of the material and assess the dependence on PNC size. Figure 1e shows the band edge absorption and steady state photoluminescence spectra of the

prepared films. Because the Bohr radius of $CH_3NH_3Br_3$ perovskites is 2.0 nm, the synthesized PNCs, specially (PNC_{50_APTES}), may exhibit quantum confinement effects due to their small size and proximity to Bohr radius.[42] As shown in Figure 1e, the UV-Vis spectra of PNC_{20_APTES} exhibits an excitonic absorption peak at 520 nm with an extended tail at lower energies due to the scattering of the relatively larger particles. However, in films of PNCs made with 35 μL and 50 μL of APTES the absorption onset is blue-shifted to 490 nm and 440 nm, respectively, due to the decrease in PNC size. A similar blue shift was observed for the narrow and symmetric PL emission bands, moving from 530 nm for PNC_{20_APTES} to 470 nm for PNC_{50_APTES} after excitation at 360 nm (λ_{ex}). The narrow emission peaks and the small full width at half maximum (FWHM) corroborates the uniformity in particle size and morphology shown in the TEM images in Figure 1. In addition, larger a Stokes shift (~41 meV) was observed as the PNC size decreased from 9.3 nm to 3.1 nm. This size-dependent Stokes shift has been reported previously for CdSe QDs as well as all-inorganic PNCs such as $CsPbBr_3$.[43] Theoretical calculations have revealed the presence of an inherent, size-dependent confined hole state above the valence band for $CsPbBr_3$ NCs between the sizes of 2-5 nm. This hole state is proposed to be dark in absorption but bright in emission due to its low population density, which explains the size-dependent Stokes shift.[43] Since, cesium orbitals didn't contribute to this identified confined hole state, this size-dependent stokes shift can be assumed to be a general feature in other PNCs similar to what we observed here for $CH_3NH_3PbBr_3$ PNCs.

Absolute PLQY of each sample was measured and all three-sized PNCs exhibited high PLQY similar to what was reported in a previous study using a combination of APTES and OA capping ligands.[44] This is attributed to a proton transfer reaction between the carboxylic group of OA and the amine group of APTES, resulting in carboxylate anion and ammonium cation moieties that can simultaneously passivate the Pb^{2+} or MA^{+} and Br^{-} charge defects on the PNCs surface.[44] In addition, APTES is also unique in that its cone-shaped structure can promote steric hindrance and prevent solvent or other molecules such as oxygen or water from reaching the PNCs surface. Furthermore, through hydrolysis, it may produce a silica layer that further stabilizes the PNCs surface.[38] However, our result demonstrate that the defect passivation efficiency of APTES is size-dependent. The absolute PLQY of PNC_{20_APTES}, PNC_{35_APTES}, and PNC_{50_APTES} are measured to be 54%, 91%, and 76%, respectively.

A comparison of the PLQY for the different sizes demonstrates the competing effect between proper passivation of surface defects and steric hindrance of capping ligands. For instance, steric hindrance between large, cone-shaped capping ligands may prevent them from efficient passivation. On the other hand, due to the small amount of capping ligand used in the synthesis of larger particles the passivation may be relatively incomplete. Therefore, the middle-sized PNCs made with 35μL APTES exhibit optimal combination of passivation considerations, resulting in 91% PLQY. Figure 1f schematically represents the effect of capping ligand concentration and PNCs size on surface passivation efficiency. The disparity between the particles in passivation

efficiency as a function of size and capping ligand concentration is expected to significantly affect the charge carrier dynamics in these PNCs.

3.4.3 Charge Carrier Dynamic Study via Ultrafast Transient Absorption Spectroscopy

Femtosecond transient absorption (TA) spectra of PNC films were recorded by exciting at 390 nm (above band edge) and the band edge absorption of each PNC (data available in SI) probing with a white light (450-700 nm) as a function of time delay between the pump and probe pulses. While analyzing the decay of transient absorption/bleach signal can provide very useful information about the charge carrier dynamics in PNCs, the possibility of non-linear processes such as Auger recombination or exciton-exciton annihilation can make the interpretation of the data more complicated.[45] To avoid such processes interfering with data analysis, each sample was pumped with multiple pulse energies (190, 85, 50, and 20 nJ/pulse) to investigate power-dependence in the recombination dynamics. Similar to what has been reported previously for different types of PNCs, a power dependence was observed when higher pulse energies were used for excitation (Figure 2a-c).[45,36,46] This is suggested to be the result of doubly excited PNCs which are referred to as biexcitons. The relative amplitude of the fast component increases as the probability of more than one excitation occupying each particle escalates. Makarov *et al*. proposed multiexciton states in $CsPbX_3$ PNCs and reported a deviation in the size-dependent biexciton Auger lifetimes from what had been previously observed in other NCs systems.[47] This excitation energy dependence of the TA dynamics also indicates the shallow nature of

trap states which are mainly located near band edge.[46] Most importantly, when the power increased from 50 to 190 nJ/pulse, the larger particles exhibited a greater power-dependence. This arises from the difference in the number of atoms per particle, resulting in larger particles absorbing more photons per pulse.[45] In addition, further increasing the amount of capping ligand to make smaller particles, isolates the individual PNCs, confining the charge carriers within a single particle, limiting the bimolecular recombination and eventually resulting in excitation energy-independent decay dynamics.[48] Below 190 nJ/pulse, samples were in a linear regime with excitation energy and data from 85 nJ/pulse excitation was used for the dynamics studies.

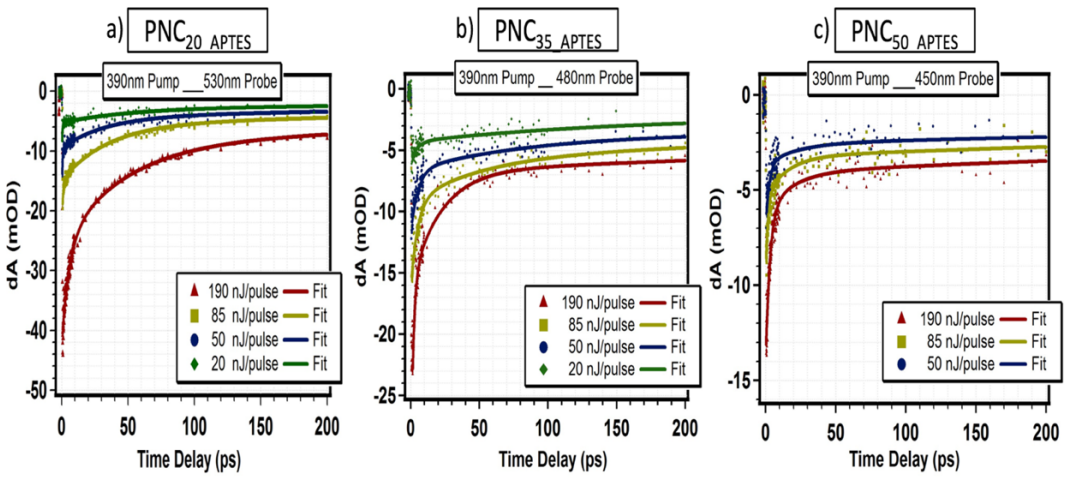

Figure 3-2- Transient bleach spectra of different sizes of PNC_{APTES} a) PNC_{20_APTES}, b) PNC_{35_APTES}, and c) PNC_{50_APTES} excited with 390 nm beam with 190, 85, 50, and 20 nJ/pulse energies.

Figure 3 shows 3D (a-c) and 2D (d-f) representation of transient absorption data as a function of wavelength and delay time between pump and probe pulses.

Assignment of the transitions to different probed species and identifying the nature of these species is not trivial without proper knowledge of the electronic band structure. However, a combination of confinement in space and the delocalized nature of conduction and valence band in addition to the short time scale investigated, suggest that the probed species are mostly excitons at early times but these excitons can dissociate to electron and holes over time.[49] As is shown in Figure 3a, for PNC_{20_APTES} a transient absorption (TA, excited-state absorption) signal at 500 nm and a relatively broad transient bleach (TB, ground-state depletion) signal at 530 nm was observed. Similar features were also observed for PNC_{35_APTES} with a shift in signal positions to 450 nm (TA) and 480 nm (TB) (Figure 3b). However, for the PNC_{50_APTES} sample, the TA signal fell out of the detection limit of our instrument and was not detectable while the TB signal observed at 455 nm (Figure 3c). For this reason, the TB signal in all samples was used for the comparison of carrier dynamics. The TB signals were attributed to the depopulation of the ground state since the peak position matches with the first excitonic absorption of each sample shown in UV-Vis spectra (Figure 1e).[36,46] There is also a possibility of small stimulated emission contributing to this bleach signal.[50] Considering the fact that 390 nm excitation generates excitons above the band edge, some intra-band cooling (cooling of hot excitons to the band edge excitonic state) might also happen.[51] Because our pump wavelength is above the bandgap and larger than the kinetic energy of electron itself, the signals most probably originate from higher energy levels within the valence and conduction band.[49] The short lived signal (<~1ps) at 500nm (dark green spectra), observed in Figure 3d for PNC_{20_APTES}, can be

attributed to this intra-band cooling of hot electrons, while the same signal was not observed for the smaller sizes, which might be due to their larger bandgap resulting in lower energy of the transitions.

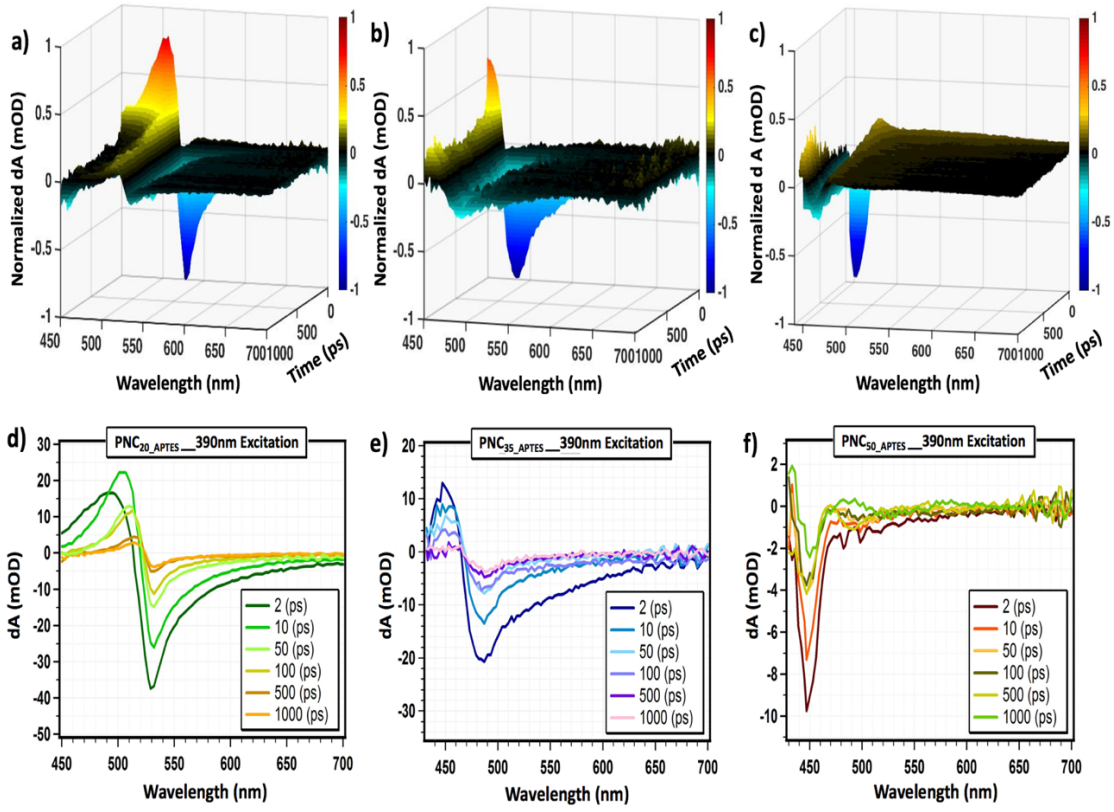

Figure 3-3- Three-dimensional (top) and two-dimensional (bottom) plots of transient absorption profiles after excitation with a 390 nm pump (85 nJ/pulse) as a function of probe wavelength (450-700nm) and delay time (0-1000ps) for different sizes of PNC_{APTES} films prepared with different amount of APTES.

Figure 4 shows the normalized single wavelength TB signal of each sample from 0-1000 ps and 0-200 ps (inset). The probe wavelength for each sample corresponds to the wavelength of maximum TB amplitude. The recovery of these TB

signals was fit with a triple exponential function and the corresponding fitting parameters are reported in Table 1.

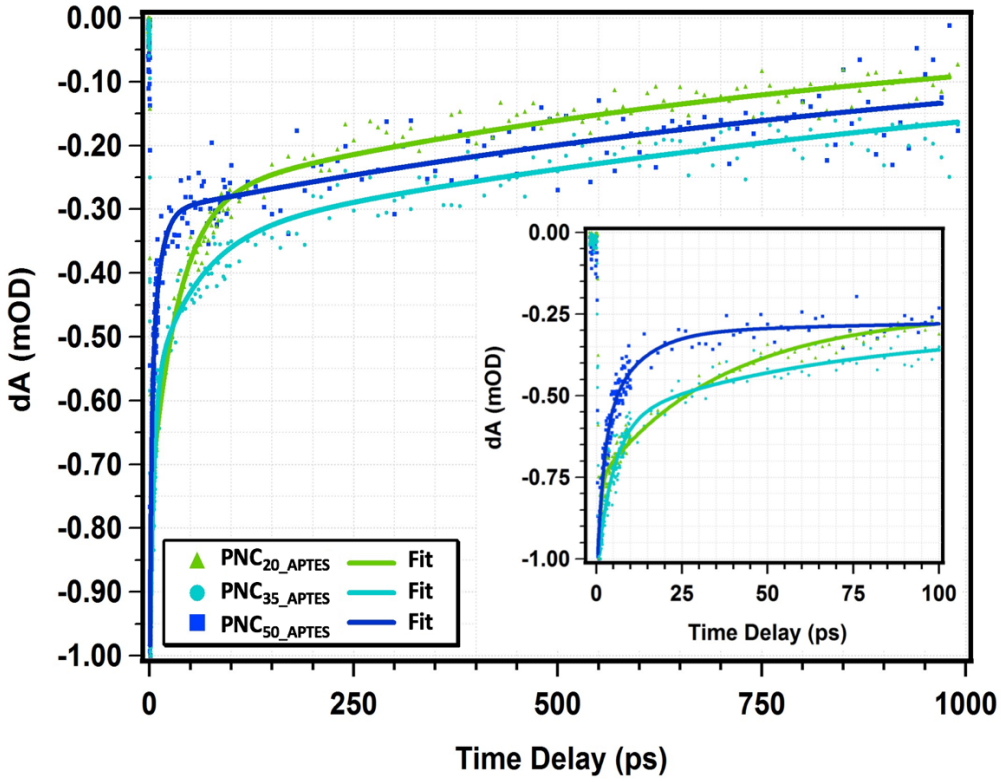

Figure 3-4- Normalized ultrafast transient bleach decay profile of different sizes of PNC_{APTES} (markers) from 0-1000 ps and inset is from 0-100 ps. The decay profiles are fitted using a triple exponential function (solid line).

As demonstrated in Figure 4, there is a significant difference in the charge carrier lifetime of the three PNC_{APTES} samples. The average recovery lifetime of these three sizes of PNCs was calculated to be 874 ps, 1316 ps, and 1177 ps for PNC_{20_APTES}, PNC_{35_APTES}, and PNC_{50_APTES} respectively, using the following equation:

$$Average\ \tau = \frac{A_1\tau_1^2+A_2\tau_2^2+A_3\tau_3^2}{A_1\tau_1+A_2\tau_2+A_3\tau_3} \qquad (1)$$

It should be noted that the transient signal does not fully recover during the time window studied (1000 ps). Also, because the last time constant (τ_3) is greater than the time window allowed by our delay stage, it cannot be verified. Although this induces uncertainty in our determination of average lifetime, the resultant values serve as helpful estimations of the lifetime of our PNCs.

Table 3-1- Fitting parameters of single wavelength (λmax) transient bleach recovery of PNC_{APTES} films fitted with triple exponential function.

Sample	A_1	τ_1 (ps)	A_2	τ_2 (ps)	A_3	τ_3 (ps)	$\langle\tau\rangle$ (ps)
PNC_{20_APTES}	-0.51 ± 0.04	3.57 ± 0.38	-0.33 ± 0.02	43.07 ± 3.42	-0.14 ± 0.01	1108 ± 116	874
PNC_{35_APTES}	-0.60 ± 0.1	6.30 ± 2.27	-0.19 ± 0.17	122.15 ± 25.1	-0.21 ± 0.13	1238 ± 232	1316
PNC_{50_APTES}	-0.69 ± 0.03	4.06 ± 0.44	-0.14 ± 0.04	27.21 ± 7.06	-0.22 ± 0.02	801 ± 43	1177

The recovery of the TB signal represents the photogenerated electrons and holes disappearing through charge recombination and trapping processes. The observed multi exponential nature of this recovery is due to the combination of radiative and non-radiative (trapping) processes. As reported previously, TB recovery is very sensitive to degree of surface passivation.[52] As shown in Table 1, we observed fast, medium and slow decay processes for each sample. The fast and medium decays are attributed to charge trapping in shallow and deep trap states, respectively and the slow decay is consistent with bimolecular electron-hole recombination. [53] However, by increasing the

concentration of capping ligand in small PNCs, individuals PNCs are isolated by their capping ligands and there is no electronic communication between them. Thus, photogenerated charges ultimately recombine via geminate processes.[48]

Incorporation of capping ligands for defect passivation has been shown to suppress the rapid (<1 ps) trapping of charge carriers in bulk materials.[53] The passivation of surface defects also resulted in a significant increase of PL intensity, pointing to the role of these defects in nonradiative recombination. It has been recently reported that well-passivated $CH_3NH_3PbBr_3$ NCs exhibit a PLQY close to unity, similar to what we observed for PNC_{35_APTES}.[54] As discussed previously, there is a competing effect between proper defect passivation and steric hindrance as a function of capping ligand concentration. The middle-sized particles with diameter of 5.7 nm and 35 μL of APTES as capping ligand are expected to have enough capping ligand to effectively passivate the trap states, but the particle size is not so small that steric hindrance begin to dominate, and the ligands cannot fully passivate the surface. The TB fitting parameters in Table 1 show that the initial time constant (τ_1) for PNC_{35_APTES} (6.30 ps) is significantly larger than that for PNC_{20_APTES} and PNC_{50_APTES} (3.57 ps and 4.06 ps, respectively). Considering that fast early decay lifetimes correspond to charge carrier trapping in shallow trap states[53,36], this result suggests a lower density of shallow traps (near the surface) in PNC_{35_APTES} as a result of proper passivation.

The proper passivation in the middle size PNCs (PNC_{35_APTES}) is further confirmed by analysis of the second time constant (τ_2) in the decay process. The second time constant is related to carrier recombination in deeper trap states.[53] By comparing

the τ_2 values for these three samples, it can be concluded that there are higher density of shallow traps in PNC_{20_APTES} while the small particles (PNC_{50_APTES}) bandgap is more dominated by deeper trap states. The last time component also corresponds to non-trap-assisted recombination of the charge carriers including either bimolecular or geminate electron-hole recombination.

In order to better understand the physical processes associated with the exciton and charge carrier dynamics of these three-sized PNCs, we used a kinetic model (Figure S1) to fit the TA/TB signals, similar to what has been done previously.[55] Briefly, the proposed model involves five different states including CB, CB_{edge}, ST, DT, and VB. The rate constant for each transition is adjusted iteratively and chosen based on which one best fit the experimental results. Detailed explanation of the model is given in SI. By using this model, we were able to assign time constants to the corresponding physical processes such as band edge cooling of hot electrons in larger particles, trapping into and decaying from shallow and deep trap states (Table S1). This kinetic modeling provides us a possible scenario for the relaxation processes involved, which will be discussed later.

3.4.4 Time-resolved Photoluminescence

In NCs, PL can be a combination of emission from both band edge and trap states.[15] Controlling the surface properties by passivating trap states, can significantly increase the ratio of band edge over trap state emission and the PLQY, respectively. Usually, when exciting NCs at energies above bandgap, after hot carriers cool to the

band edge, they go through trapping in shallow and deep trap states. Following the charge carrier trapping in shallow and deep trap states, they can undergo radiative or non-radiative recombination. Depending on the nature and density of trap states, timescales for trap-assisted recombination can vary from a few ps to ns.[15] Here, time-resolved PL was used to investigate the excited-state radiative relaxation dynamics.

Figure 5 shows the PL decay traces of prepared films of the three samples excited at the band edge of each samples, and the emission was collected at 530 nm, 500 nm, and 470 nm for PNC_{20_APTES}, PNC_{35_APTES}, and PNC_{50_APTES}, respectively. The PL decay were fitted using a double exponential function and the fitting parameters are reported in Table 2. Similar to TA measurements, PL dynamics are also a combination of trap-assisted (faster early time recombination) and non-trap-assisted (longer time constants) charge-carrier recombinations.[53] The early lifetime of the samples is similar to what was observed in the TA study with middle-sized particles (PNC_{35_APTES}), which had a time constant ~2 times longer than larger and smaller particles. Considering that the PL lifetime can also be correlated with the density of trap states in the material, it is reasonable to conclude that the slower early-time recombination in PNC_{35_APTES} (3.9 ns) relative to PNC_{20_APTES} (2.1 ns) and PNC_{50_APTES} (1.5 ns) is due to better passivation of trap states. This further confirms the higher density of shallow and deep traps in large and small particles as shown with the TA study. On the other hand, the slower component of the PL decay (τ_2) is attributed to non-trap assisted electron-hole recombination pathways. The longer time component (τ_2) and respectively, average lifetime drastically decreased as the PNC size got smaller. The average lifetime of each

sample, from large to small particle size, was calculated to be 19 ns, 7.5 ns, and 4.7 ns using Equation 1 described previously. A similar trend of decrease in PL lifetime was observed previously when going from bulk material to particle sizes in the strong quantum confinement regime.[48] Even though the PL dynamics of middle-sized PNCs (PNC_{35_APTES}) indicates lower density of trap states, which agrees with TA data, the average PL lifetime of larger particles still surpasses it due to higher amplitude of slow decay component. This result indicates the synergistic effect of size and surface properties on PL decay dynamics. For example, by changing the size and respectively the bandgap in PNCs, the relative position of trap states to band edge and their coupling is changing which may result in availability of different decay pathways. On the other hand, due to the presence of relatively more traps in the large PNCs, there is a higher possibility for charge carriers to go through multi-step non-radiative decay. This information in addition to measured PLQY was used to further complete the proposed model on the effect of size and capping ligand concentration on charge carrier dynamics and deciphering the competing effect between size and surface properties on radiative and non-radiative decay processes.

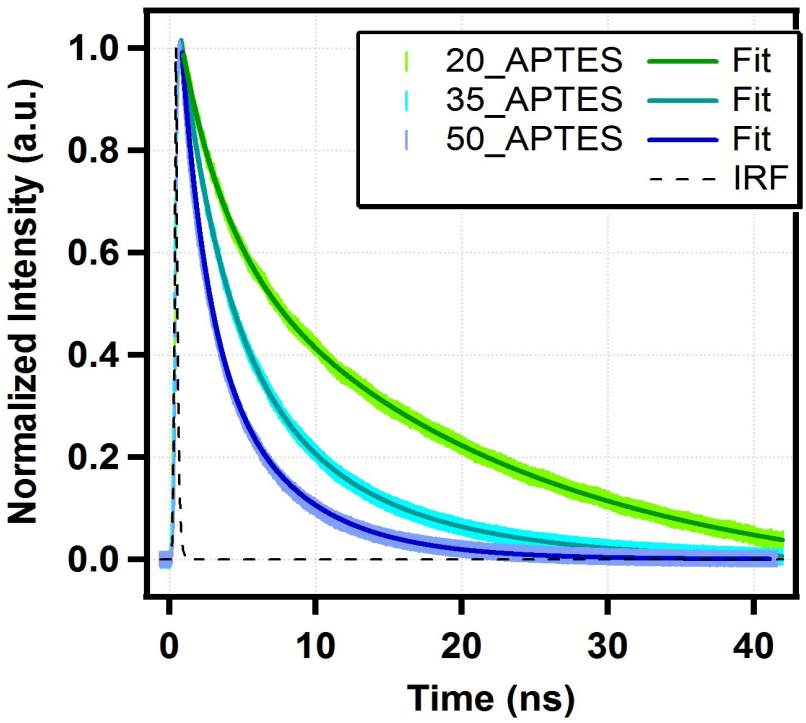

Figure 3-5- PL decay traces of PNC_{APTES} films prepared with different concentrations of APTES; 20μL(red) {λex=520nm, λem=530nm, 35μL(green) {λex=490nm, λem=500nm} and 50μL(blue) {λex=440nm λem=470nm}.

Table 3-2- Fitting parameters of time-resolved PL decay of PNC_{APTES} films

Sample	Excitation	Emission	A_1	τ_1 (ns)	A_2	τ_2 (ns)	$\langle\tau\rangle$ (ns)
PNC_{20_APTES}	520nm	530nm	0.33 ± 0.031	2.1 ± 0.013	0.67 ± 0.060	20 ± 0.001	19
PNC_{35_APTES}	490nm	500nm	0.50 ± 0.019	3.9 ± 0.031	0.50 ± 0.017	9.1 ± 0.001	7.5
PNC_{50_APTES}	440nm	470nm	0.48 ± 0.012	1.5 ± 0.073	0.52 ± 0.023	5.5 ± 0.14	4.7

3.4.5 Mechanism of Exciton/Charge Carrier Recombination

Charge carrier dynamics in PNCs are usually more complex compared to the bulk material due to the presence of multiple states, such as shallow and deep traps, within the bandgap. Due to the shorter timescale of TA study in ps time regime, the measurement provides information about the faster transitions such as hot electrons cooling to band edge and charge carriers trapping in shallow and deep trap states near the band edge. However, further decaying from these trap states usually happens in ns timescale and can be studied using TRPL. Using the experimental TA and TRPL data and kinetic modeling (available in SI), we propose a simple mechanism to help explain the possible relaxation processes involved in the different sized PNC_{APTES}, as shown in Figure 6 (a-c). The proposed exciton/charge carrier relaxation processes of PNC_{APTES} samples involve the conduction band (CB), conduction band edge (CB_{edge}), shallow trap (ST) states, deep trap (DT) states, and valance band (VB) as shown in the Figure S1. In these PNCs, an exciton is generated after excitation with energy above the bandgap. In tens of femtoseconds the exciton dissociates into electron and hole. Depending on the bandgap and its energy difference with excitation wavelength and the excess kinetic energy of the charge carriers, the charge carriers will go through intra-band cooling and relax back to the band edge (CB_{edge}) through electron-phonon interaction.[56] Due to the larger difference in bandgap and excitation energy, this process is only observed for the larger particles (PNC_{20_APTES}) which had the smallest bandgap. Even though this process can occur for the other particle sizes as well, it was not detected with our instrument resolution. After charge carriers relax to the band edge, they can go through multiple pathways, however due to energy gap between the states,

some of them are kinetically more favorable than others. Our proposed model based on the extracted information from the dynamics studies demonstrates that due to low concentration of capping ligand in large particles, there is a high density of non-passivated shallow trap states near the band edge that can cause faster recombination in early times. Furthermore, while higher concentration of capping ligand in PNC_{50_APTES} passivated more surface defects, steric hindrance caused by bulky capping ligand (APTES) acted as a detrimental factor. Meanwhile the middle-sized particles presented an optimum combination of ligand concentration and surface passivation without facing steric hindrance which significantly lowered the density of shallow traps.

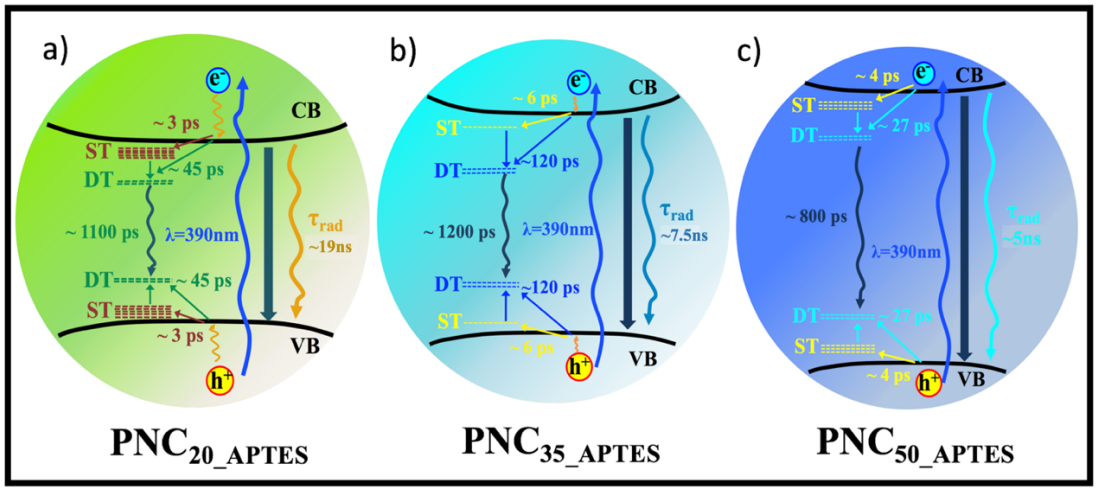

Figure 3-6- Schematic illustration of proposed band structure and various dynamic processes and lifetimes for a) PNC_{20_APTES}, b) PNC_{35_APTES}, and c) PNC_{50_APTES}.

The rate of charge carrier transfer between different states is calculated using the kinetic model and summarized in Table S1. After charge carriers relax to the band

edge or shallow trap states, they can further go through radiative and non-radiative recombination. These following transitions happen in ns timescale and depending on the density of trap states in the PNCs, the ratio of these radiative and non-radiative transitions might be different as shown in equation 2.

$$\frac{1}{\tau_{obs}} = \frac{1}{\tau_r} + \frac{1}{\tau_{nr}} \quad (2)$$

Where (τ_{obs}), (τ_r), and (τ_{nr}) are the average PL lifetime, radiative lifetime, and non-radiative lifetime, respectively. The PLQY provides a measure of the radiative vs non-radiative processes. The change in density of trap states as a result of changing size and passivation efficiency can alter the recombination pathway and lifetime for a photogenerated charge carrier, thereby affecting the PLQY. The relationship between observed PL lifetime (τ_{obs}), radiative lifetime (τ_r), and PLQY is shown in equation 3.

$$\tau_r = \frac{\tau_{obs}}{PLQY} \quad (3)$$

Using the average observed lifetime and the measured PLQY for these different sized PNCs, the τ_r and τ_{nr} calculated for each particle and reported in Table 3.

Table 3-3- Calculated radiative and non-radiative lifetime for PNC_{APTES} at different sizes.

Sample	τ_{obs} (ns)	τ_r (ns)	τ_{nr}(ns)	PLQY
PNC_{20_APTES}	19	35	45	54%
PNC_{35_APTES}	7.5	8.2	83	91%
PNC_{50_APTES}	4.7	6.2	19	76%

Calculated values for τ_r and τ_{nr} are summarized in Table 3. The τ_r significantly decreased by reducing the PNCs size, going from 35 ns for PNC_{20_APTES} to 6.2 ns for PNC_{50_APTES}. This descending trend is similar to what observed for the average PL lifetime (τ_{obs}). Though this is not in agreement with the trend we observed for PLQY and early time recombination lifetime measured by TA spectroscopy, it is not quite unexpected. Theoretical and experimental studies previously reported on various QD systems indicate the strong size dependence of τ_r,[57,58,59] which decreases dramatically by decreasing the diameter of NCs, mostly attributed to quantum confinement effect.[59] On the other hand, the τ_{nr} is calculated to be the longest (83 ns) for the middle-sized PNCs and to decrease significantly for the smaller and larger sizes. It has been shown previously that higher density of trap states result in higher possibility of non-radiative recombination, resulting in shorter τ_{nr}.[60] Therefore, the longest τ_{nr} observed for PNC_{35_APTES} confirms lower density of trap states leading the recombination processes towards spontaneous emission.. These results also confirmed by high PLQY (91%) measured for PNC_{35_APTES}, which can also be attributed to defect passivation efficiency. Considering each one of these radiative and non-radiative lifetimes are factor of both

NCs size and surface properties, the calculated lifetimes are suggesting competing effect between these factors. This result suggests that effect of surface properties is more dominant on τ_{nr}, while the core size effect is more pronounced in τ_r. This information derived from experimental and calculated values resulted in achieving a more detailed model on effect of size on charge carrier dynamic and elucidating the mechanism behind the high PL efficiency in the middle-sized particles.

3.5 Conclusion

In summary, we have synthesized three different sized $CH_3NH_3PbBr_3$ PNCs, ranging from 9.3 nm to 3.1 nm, by changing the amount of APTES used as capping ligands. By decreasing the size, absorption and emission spectra of the PNCs blue shifted, which is due to the strong quantum confinement effect, especially for the smaller PNCs with diameter less than the Bohr radius. The PLQY measured to be significantly higher (91%) for the middle-sized PNCs (PNC_{35_APTES}) compared to the smaller and larger ones. Similar non-linear trend with respect to size observed in early time recombination lifetime measured by TA study. Using the experimental data and kinetic modeling, we assigned observed time constants to corresponding physical processes involved in the PNC_{APTES} samples and correlated some of them to size effect. The fast and medium time constant in TA signal decay, attributed to shallow and deep trap states recombination, were measured to be ~2 times longer in PNC_{35_APTES} than those for the other sizes. Similarly, the extracted rate of charge carrier transfer from CB_{edge} to ST in the kinetic model was smaller for middle-sized PNCs than the other

sizes. These results suggested more efficient passivation of surface traps in the middle-sized PNCs. We suggest that the middle-sized PNCs have an optimal amount of capping ligand which mitigate steric hindrance of the large cone-shaped APTES, while properly passivating the defects. On the other hand, the observed PL lifetime (τ_{obs}) descended by decreasing the size. Using τ_{obs} and measured PLQY, radiative (τ_r) and non-radiative (τ_{nr}) components of the PL lifetime are determined to understand the size effect. Interestingly, τ_r exhibited strong dependence to PNCs core size, as it decreased drastically by decreasing PNC size. However, τ_{nr} was mainly dominated by effect of surface properties, since it was longest for the well-passivated middle-sized PNCs (PNC_{35_APTES}). Considering both of these lifetimes are dependent on size and surface properties, the results demonstrate the competing effect between these two factors. Based on all the results, we proposed a model of the band structure to explain the various dynamic processes and lifetimes.

Supporting Information

Kinetic Modeling of Charge Carrier Dynamics

In order to better understand the physical processes associated with the exciton dynamics of the PNC_{APTES}, we use a kinetic model to fit the observed TA/TB signals obtained at the lowest pump power. The proposed exciton relaxation processes of PNC_{APTES} samples involve the conduction band (CB), conduction band edge (CB_{edge}), shallow trap (ST) state, deep trap (DT) state, and valance band (VB) as shown in the

Figure S1. The rate constants were adjusted iteratively and finally chosen based on best fit to the experimental results. Table S1 shows a summary of the rate constants from each state to the TA/TB signals that provide the best fit to the experimental results for the PNC_{APTES}.

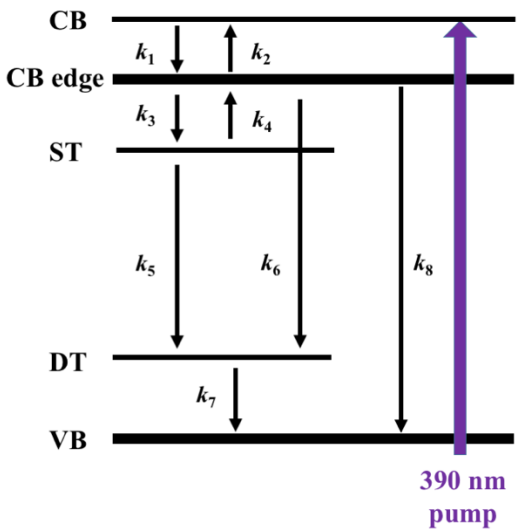

Figure S1. Proposed kinetic model and energy levels to explain the dynamics of PNC_{APTES}.

Table S1. Summary of rate constants used in the kinetic model that provides the best fit the exciton or charge carrier dynamics of the PNC_{APTES}.

	k_1 (ps^{-1})	k_2 (ps^{-1})	k_3 (ps^{-1})	k_4 (ps^{-1})	k_5 (ps^{-1})	k_6 (ps^{-1})	k_7 (ps^{-1})	k_8 (ps^{-1})
PNC_{20_APTES}	0.84	0.07	0.25	0.02	0.04	0.022	0.02	0.0009
PNC_{35_APTES}	-	-	0.12	0.01	0.03	0.0083	0.005	0.0008
PNC_{50_APTES}	-	-	0.18	0.02	0.03	0.037	0.01	0.001

Several assumptions are made with regard to the modeling in order to properly compare with the experimental results. First, the absorption cross section of each state

is assumed to be the same. This is for simplicity since it is not currently easy to determine the absorption cross section for each state, especially the excited states. Consequently, the modeled signal is only proportional to the carrier concentration (or population). Second, the backward rate constants are approximately an order of magnitude smaller than forward rate constants. This is because the carriers are expected to relax more quickly from a higher energy state to a lower energy state than other way around. Finally, the initial state was assumed to have a positive signal value ($[\mathrm{CB}]_0$=1), the CB edge, two bandgap states and VB have zero signal ($[\mathrm{CB\ edge}]_0$=0, $[\mathrm{ST}]_0$=0 and $[\mathrm{DA}]_0$=0, $[\mathrm{VB}]_0$= 0). The chosen rate constants are used to generate the modeled data by the following equations:

$$\frac{d[\mathrm{CB}]}{dt} = -k_1[\mathrm{CB}] + k_2[\mathrm{CB\ edge}]$$

$$\frac{d[\mathrm{CB\ edge}]}{dt} = k_1[\mathrm{CB}] - k_2[\mathrm{CB\ edge}] - k_3[\mathrm{CB\ edge}] + k_4[\mathrm{ST}] - k_6[\mathrm{CB\ edge}] - k_8[\mathrm{CB\ edge}]$$

$$\frac{d[\mathrm{ST}]}{dt} = k_3[\mathrm{CB\ edge}] - k_4[\mathrm{ST}] - k_5[\mathrm{ST}]$$

$$\frac{d[\mathrm{DT}]}{dt} = k_5[\mathrm{ST}] + k_6[\mathrm{CB\ edge}] - k_7[\mathrm{DT}]$$

$$\frac{d[\mathrm{VB}]}{dt} = k_7[\mathrm{DT}] + k_8[\mathrm{CB}]$$

For each individual state, we generated a plot that represents the population over time, including the [VB], [CB], [CB edge], [ST] and [DT], for PNC_{APTES}, as shown in Figure S2. The CB population curve shows an exponential decay. As the CB population decays, the CB_{edge} and ST population increases. Subsequent to the ST population increase, the electron relaxes into the DT, which represents as a simultaneous decrease in ST population and increase in DT population. At last, as the DT population decrease, the VB population increases.

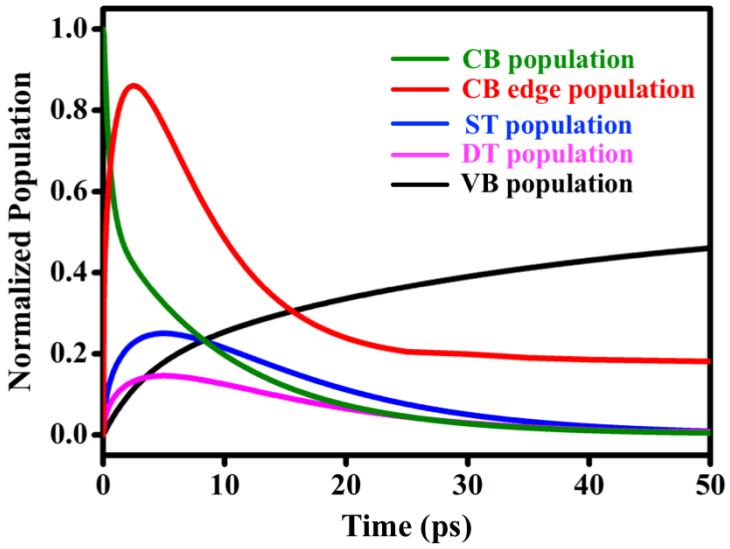

Figure S2. Populations of individual states as a function of time of PNC_{APTES} samples.

Since the TA/TB signal contains contributions from different states, we need to account for that by summing up the modeled signals from relevant states to fit the exciton relaxation from CB and VB. By combining the contribution of 65% from the [CB], 25% from the [CB edge] and 10% contribution of the [ST], a curve could be generated that fit the observed TA signal at 500 nm of PNC_{20_APTES} in Figure S3. As

shown in Figure S4, by combining the contribution of 20% from both of the [CB edge] , 20% contribution of the [ST], 20% contribution of the [DT] states and subtracting the [VB] with 40% contribution, a curve could be generated that fit the observed TB signal of PNC_{20_APTES} samples. When the negative contribution of 30% from the [VB] and the positive contribution of 20% from the [CB edge], 25% from the both of [ST] and [DT] states, a curve could be generated that fit the TB recovery of PNC_{35_APTES} samples. As summarized the 20% contribution of [CB edge], 15% contribution of [ST] and 15% contribution of [DT] states, and then subtract 50% contribution of [VB], a curve could be generated that fit the observed TB recovery of PNC_{50_APTES} samples. we believe that the time constants give the right order of magnitude for the lifetimes of the key physical process and the modeling does provide some further insight into the dynamics than simple mathematical fittings that are usually done.

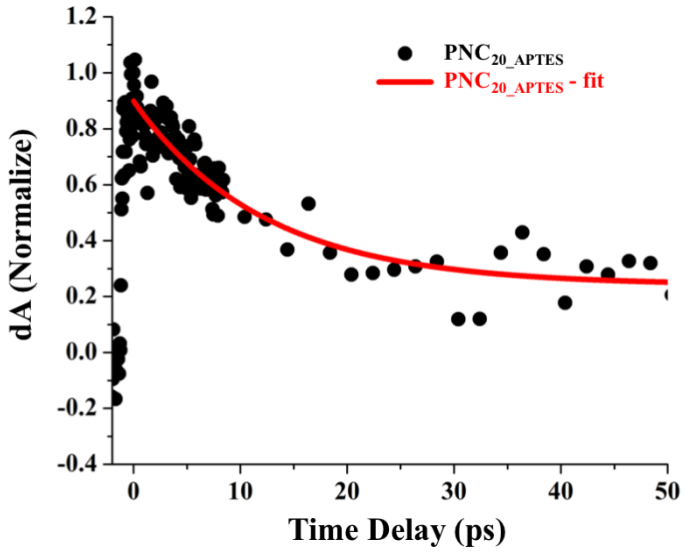

Figure S3. Experiment data vs. modeled data of PNC_{20_APTES} samples for TA decay.

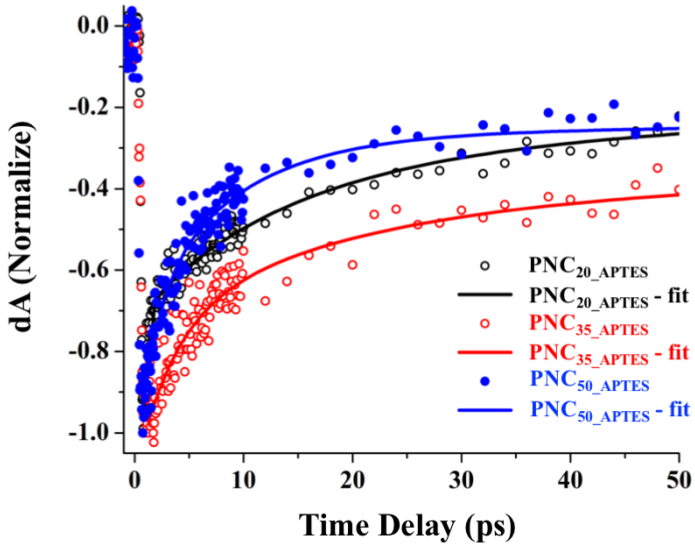

Figure S4. Experiment data vs. modeled data of PNC_{APTES} samples for TB recovery.

Using this kinetic model, we were able to assign time constants to corresponding physical processes happening in PNC_{APTES}. For PNC_{20_APTES}, due to the larger energy of excitation compared to band gap, we were able to observe the transition from CB to CB edge which is happening in 1.2 ps. Following transition of charge carriers to the CB edge they decay to ST states and time constant for this transition was calculated to be 3 ps, from ST to DT was 23 ps, from CB to DT was 45 ps, from DT to VB was 50 ps, and from CB to VB was 1111 ps, respectively. These time constants for the same transitions calculated to be 6 ps, 33 ps, 120 ps, 200 ps, and 1250 ps for PNC_{35_APTES}. While, for PNC_{50_APTES} the time constants were 4 ps, 33 ps, 27 ps, 100 ps,

and 1000 ps, respectively. Even though these time constants might be somewhat off, because of several assumptions made in this modeling, we still believe they can provide further insight on kinetic of key physical processes happening in PNC_{APTES} samples. This information helped proposing a clearer model of the bandgap, demonstrated in the manuscript.

Transient Absorption of PNC_{APTES} Samples Excited at the Band edge Absorption

In addition, to have better comparison between these different-sized PNCs, the transient absorption measurements were also carried by exciting the PNCs at their optical band gap. For this purpose, PNC_{20_APTES}, PNC_{35_APTES}, and PNC_{50_APTES} were excited at 510 nm, 480 nm and 430 nm, respectively. Figure S5 shows 3D representation of transient absorption data as a function of wavelength and delay time between pump and probe pulses. Similar to what observed after excitation with 390 nm beam, for PNC_{20_APTES} a transient absorption (TA, excited-state absorption) signal at 500 nm and a relatively broad transient bleach (TB, ground-state depletion) signal at 530 nm was observed. Similar features were also observed for PNC_{35_APTES} with a shift in signal positions to 450 nm (TA) and 480 nm (TB). However, for the PNC_{50_APTES} sample, the TA signal fell out of the detection limit of our instrument and was not detectable while the TB signal observed at 455 nm.

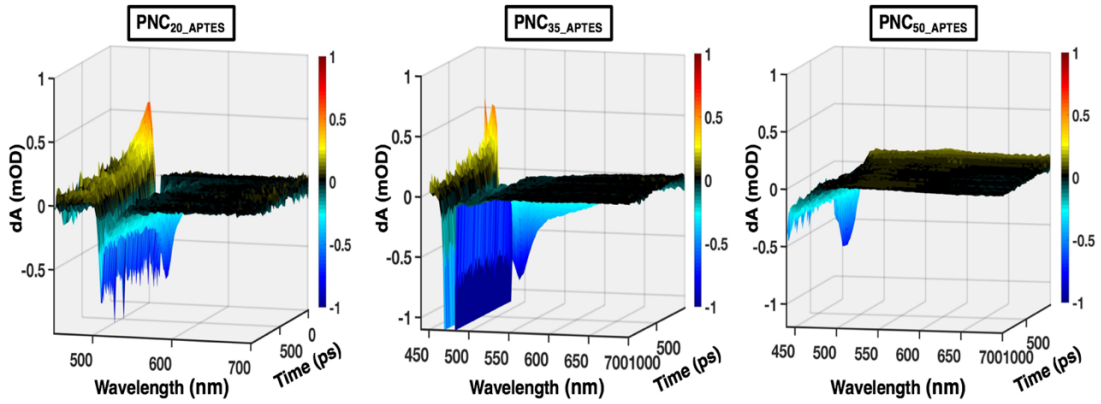

Figure S5. Three-dimensional plots of transient absorption profiles after excitation with of PNC_{20_APTES}, PNC_{35_APTES}, and PNC_{50_APTES} with 510 nm, 480 nm, and 430 nm pump, respectively as a function of probe wavelength (450-700nm) and delay time (0-1000ps).

In order to compare the dependence of the charge carrier dynamics on excitation wavelength in these PNC_{APTES} samples, we analyzed the normalized single wavelength TB signal of PNC_{20_APTES} sample excited at 390 nm (above band edge absorption) and 510 nm (band edge absorption). Figure S6 shows the normalized single wavelength TB signal from 0-1000 ps. The probe wavelength for each sample corresponds to the wavelength of maximum TB amplitude. The recovery of these TB signals was fit with a triple exponential function and the corresponding fitting parameters are reported in Table 1.

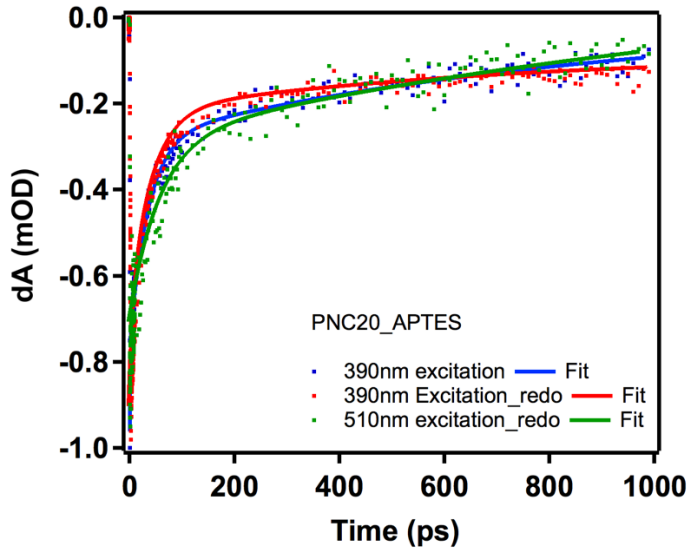

Figure S6. Normalized ultrafast transient bleach decay profile of PNC_{20_APTES} excited at 390 nm and 510 nm, from 0-1000 ps. The decay profiles are fitted using a triple exponential function (solid line).

In order to test reproducibility of the data, the 390 nm excitation was also repeated with a new sample. As it is shown in figure S6, the decay dynamic in these three experiments have significant overlap and the small difference observed is within the noise range. Specially the data collected at 510 nm excitation is noisier due the interference of the excitation beam and the signal which is shown in figure S5. The detailed fitting parameters for these experiments is reported in table S2. This data shows no significant dependence of charge carrier dynamic to excitation wavelength in these different sized PNC_{APTES} samples.

Table S2. Fitting parameters and average lifetime of single wavelength (λ_{max}) transient bleach recovery of PNC_{APTES} films fitted with triple exponential function.

PNC_{20_APTES}	A_1	τ_1 (ps)	A_2	τ_2 (ps)	A_3	τ_3 (ps)
390nm Ex	0.51 ± 0.04	3.57 ± 0.38	0.33 ± 0.02	43.07 ± 3.42	0.14 ± 0.01	1108 ± 116
390nm Ex-Redo	0.55 ± 0.02	3.28 ± 0.02	0.28 ± 0.02	35.3 ± 18	0.17 ± 0.01	1287 ± 83
510nm Ex	0.48 ± 0.02	4.02 ± 0.02	0.31 ± 0.01	52 ± 4.4	0.11 ± 0.01	988 ± 76

As discussed in the manuscript and reported previously[1], recovery of TB signal is very sensitive to degree of surface passivation. For these PNCs, which are excited at their band edge absorption, we observed fast, medium and slow decay processes. The fast and medium decays are attributed to charge trapping in shallow and deep trap states, respectively and the slow decay is consistent with bimolecular electron-hole recombination.[2] The decay dynamic of PNCs excited at 510 nm is similar to what observed after 390 nm excitation. The time constants of (τ_1=3.57 ps, τ_2=43.07 ps, and τ_3=1108 ps) after 390 nm excitation are very close to resulted time constants (τ_1=4.02 ps, τ_2=52 ps, and τ_3=988 ps) after 510 nm excitation for larger particles (PNC_{20_APTES}). This result confirms no excitation wavelength dependence of the dynamic in these PNC_{APTES} samples.

References

(1) Kim, H.-S.; Lee, C.-R.; Im, J.-H.; Lee, K.-B.; Moehl, T.; Marchioro, A.; Moon, S.-J.; Humphry-Baker, R.; Yum, J.-H.; Moser, J. E.; et al. Lead Iodide Perovskite Sensitized All-Solid-State Submicron Thin Film Mesoscopic Solar Cell with Efficiency Exceeding 9%. *Sci. Rep.* **2012**, *2*, 591.

(2) Yang, W. S.; Noh, J. H.; Jeon, N. J.; Kim, Y. C.; Ryu, S.; Seo, J.; Seok, S. I. High-Performance Photovoltaic Perovskite Layers Fabricated through Intramolecular Exchange. *Science* **2015**, *348*, 1234–1237.

(3) Dong, Q.; Fang, Y.; Shao, Y.; Mulligan, P.; Qiu, J.; Cao, L.; Huang, J. Electron-Hole Diffusion Lengths;175 Mm in Solution-Grown $CH_3NH_3PbI_3$ Single Crystals. *Science* **2015**, *347*, 967–970.

(4) Cho, H.; Jeong, S.-H.; Park, M.-H.; Kim, Y.-H.; Wolf, C.; Lee, C.-L.; Heo, J. H.; Sadhanala, A.; Myoung, N.; Yoo, S.; et al. Overcoming the Electroluminescence Efficiency Limitations of Perovskite Light-Emitting Diodes. *Science* **2015**, *350*, 1222–1225.

(5) Tan, Z.-K.; Moghaddam, R. S.; Lai, M. L.; Docampo, P.; Higler, R.; Deschler, F.; Price, M.; Sadhanala, A.; Pazos, L. M.; Credgington, D.; et al. Bright Light-Emitting Diodes Based on Organometal Halide Perovskite. *Nat. Nanotechnol.* **2014**, *9* , 687–692.

(6) Veldhuis, S. A.; Boix, P. P.; Yantara, N.; Li, M.; Sum, T. C.; Mathews, N.; Mhaisalkar, S. G. Perovskite Materials for Light-Emitting Diodes and Lasers. *Adv. Mater.* **2016**, *28*, 6804–6834.

(7) Xing, G.; Mathews, N.; Lim, S. S.; Yantara, N.; Liu, X.; Sabba, D.; Grätzel, M.; Mhaisalkar, S.; Sum, T. C. Low-Temperature Solution-Processed Wavelength-Tunable Perovskites for Lasing. *Nat. Mater.* **2014**, *13*, 476–480.

(8) Zhu, H.; Fu, Y.; Meng, F.; Wu, X.; Gong, Z.; Ding, Q.; Gustafsson, M. V.; Trinh, M. T.; Jin, S.; Zhu, X.-Y. Lead Halide Perovskite Nanowire Lasers with Low Lasing Thresholds and High Quality Factors. *Nat. Mater.* **2015**, *14*, 636–642.

(9) Kojima, A.; Teshima, K.; Shirai, Y.; Miyasaka, T. Organometal Halide Perovskites as Visible-Light Sensitizers for Photovoltaic Cells. *J. Am. Chem. Soc.* **2009**, *131*, 6050–6051.

(10) McMeekin, D. P.; Sadoughi, G.; Rehman, W.; Eperon, G. E.; Saliba, M.; Hörantner, M. T.; Haghighirad, A.; Sakai, N.; Korte, L.; Rech, B. A Mixed-Cation Lead Mixed-Halide Perovskite Absorber for Tandem Solar Cells. *Science* **2016**, *351*, 151–155.

(11) Yang, J.; Siempelkamp, B. D.; Mosconi, E.; De Angelis, F.; Kelly, T. L. Origin of the Thermal Instability in $CH_3NH_3PbI_3$ Thin Films Deposited on ZnO. *Chem. Mater.* **2015**, *27*, 4229–4236.

(12) Lee, Y. M.; Park, J.; Yu, B. D.; Hong, S.; Jung, M.-C.; Nakamura, M. Surface Instability of Sn-Based Hybrid Perovskite Thin Film, $CH_3NH_3SnI_3$: The Origin of Its Material Instability. *J. Phys. Chem. Lett.* **2018**, *9*, 2293–2297.

(13) Wang, L.; McCleese, C.; Kovalsky, A.; Zhao, Y.; Burda, C. Femtosecond Time-Resolved Transient Absorption Spectroscopy of $CH_3NH_3PbI_3$ Perovskite Films: Evidence for Passivation Effect of PbI2. *J. Am. Chem. Soc.* **2014**, *136*, 12205–12208.

(14) Snaith, H. J.; Abate, A.; Ball, J. M.; Eperon, G. E.; Leijtens, T.; Noel, N. K.; Stranks, S. D.; Wang, J. T.-W.; Wojciechowski, K.; Zhang, W. Anomalous Hysteresis in Perovskite Solar Cells. *J. Phys. Chem. Lett.* **2014**, *5*, 1511–1515.

(15) Wheeler, D. A.; Zhang, J. Z. Exciton Dynamics in Semiconductor Nanocrystals. *Adv. Mater.* **2013**, *25*, 2878–2896.

(16) Sarang, S.; Bonabi Naghadeh, S.; Luo, B.; Kumar, P.; Betady, E.; Tung, V.; Scheibner, M.; Zhang, J. Z.; Ghosh, S. Stabilization of the Cubic Crystalline Phase in Organometal Halide Perovskite Quantum Dots via Surface Energy Manipulation. *J. Phys. Chem. Lett.* **2017**, *8*, 5378–5384.

(17) Huang, S.; Li, Z.; Kong, L.; Zhu, N.; Shan, A.; Li, L. Enhancing the Stability of $CH_3NH_3PbBr_3$ Quantum Dots by Embedding in Silica Spheres Derived from Tetramethyl Orthosilicate in "Waterless" Toluene. *J. Am. Chem. Soc.* **2016**, *138*, 5749–5752.

(18) Koh, W.; Park, S.; Ham, Y. Phosphonic Acid Stabilized Colloidal $CsPbX_3$ (X=Br, I) Perovskite Nanocrystals and Their Surface Chemistry. *ChemistrySelect* **2016**, *1*, 3479–3482.

(19) Huang, H.; Chen, B.; Wang, Z.; Hung, T. F.; Susha, A. S.; Zhong, H.; Rogach, A. L. Water Resistant $CsPbX_3$ Nanocrystals Coated with Polyhedral Oligomeric Silsesquioxane and Their Use as Solid State Luminophores in All-Perovskite White Light-Emitting Devices. *Chem. Sci.* **2016**, *7*, 5699–5703.

(20) Naghadeh, S. B.; Luo, B.; Abdelmageed, G.; Pu, Y.-C.; Zhang, C.; Zhang, J. Z. Photophysical Properties and Improved Stability of Organic–Inorganic Perovskite by Surface Passivation. *J. Phys. Chem. C* **2018**, *122*, 15799–15818.

(21) Sichert, J. A.; Tong, Y.; Mutz, N.; Vollmer, M.; Fischer, S.; Milowska, K. Z.; García Cortadella, R.; Nickel, B.; Cardenas-Daw, C.; Stolarczyk, J. K.; et al. Quantum Size Effect in Organometal Halide Perovskite Nanoplatelets. *Nano Lett.* **2015**, *15*, 6521–6527.

(22) Kim, Y.-H.; Cho, H.; Lee, T.-W. Metal Halide Perovskite Light Emitters. *PNAS* **2016**, *113*, 11694–11702.

(23) Kim, Y.; Yassitepe, E.; Voznyy, O.; Comin, R.; Walters, G.; Gong, X.; Kanjanaboos, P.; Nogueira, A. F.; Sargent, E. H. Efficient Luminescence from Perovskite Quantum Dot Solids. *ACS Appl. Mater. Interfaces* **2015**, *7*, 25007–25013.

(24) Zhang, F.; Zhong, H.; Chen, C.; Wu, X.; Hu, X.; Huang, H.; Han, J.; Zou, B.; Dong, Y. Brightly Luminescent and Color-Tunable Colloidal $CH_3NH_3PbX_3$ (X = Br, I, Cl) Quantum Dots: Potential Alternatives for Display Technology. *ACS Nano* **2015**, *9*, 4533–4542.

(25) Yu Chin, X.; Perumal, A.; Bruno, A.; Yantara, N.; A. Veldhuis, S.; Martínez-Sarti, L.; Chandran, B.; Chirvony, V.; Shu-Zee Lo, A.; So, J.; et al. Self-Assembled Hierarchical Nanostructured Perovskites Enable Highly Efficient LEDs via an Energy Cascade. *Energy Environ. Sci.* **2018**, *11*, 1770–1778.

(26) Chen, J.; Žídek, K.; Chábera, P.; Liu, D.; Cheng, P.; Nuuttila, L.; Al-Marri, M. J.; Lehtivuori, H.; Messing, M. E.; Han, K.; et al. Size- and Wavelength-Dependent

Two-Photon Absorption Cross-Section of $CsPbBr_3$ Perovskite Quantum Dots. *J. Phys. Chem. Lett.* **2017**, *8*, 2316–2321.

(27) Butkus, J.; Vashishtha, P.; Chen, K.; Gallaher, J. K.; Prasad, S. K. K.; Metin, D. Z.; Laufersky, G.; Gaston, N.; Halpert, J. E.; Hodgkiss, J. M. The Evolution of Quantum Confinement in $CsPbBr_3$ Perovskite Nanocrystals. *Chem. Mater.* **2017**, *29*, 3644–3652.

(28) Sheng, C.; Zhang, C.; Zhai, Y.; Mielczarek, K.; Wang, W.; Ma, W.; Zakhidov, A.; Vardeny, Z. V. Exciton versus Free Carrier Photogeneration in Organometal Trihalide Perovskites Probed by Broadband Ultrafast Polarization Memory Dynamics. *Phys. Rev. Lett.* **2015**, *114*, 116601.

(29) Tanaka, K.; Kondo, T. Bandgap and Exciton Binding Energies in Lead-Iodide-Based Natural Quantum-Well Crystals. *Sci. Technol. Adv. Mater.* **2003**, *4*, 599–604.

(30) Grancini, G.; Srimath Kandada, A. R.; Frost, J. M.; Barker, A. J.; De Bastiani, M.; Gandini, M.; Marras, S.; Lanzani, G.; Walsh, A.; Petrozza, A. Role of Microstructure in the Electron–Hole Interaction of Hybrid Lead Halide Perovskites. *Nat. Photonics* **2015**, *9*, 695–701.

(31) Ponseca, C. S.; Savenije, T. J.; Abdellah, M.; Zheng, K.; Yartsev, A.; Pascher, T.; Harlang, T.; Chabera, P.; Pullerits, T.; Stepanov, A.; et al. Organometal Halide Perovskite Solar Cell Materials Rationalized: Ultrafast Charge Generation, High and Microsecond-Long Balanced Mobilities, and Slow Recombination. *J. Am. Chem. Soc.* **2014**, *136*, 5189–5192.

(32) Milot, R. L.; Sutton, R. J.; Eperon, G. E.; Haghighirad, A. A.; Martinez Hardigree, J.; Miranda, L.; Snaith, H. J.; Johnston, M. B.; Herz, L. M. Charge-Carrier Dynamics in 2D Hybrid Metal–Halide Perovskites. *Nano Lett.* **2016**, *16*, 7001–7007.

(33) Edri, E.; Kirmayer, S.; Mukhopadhyay, S.; Gartsman, K.; Hodes, G.; Cahen, D. Elucidating the Charge Carrier Separation and Working Mechanism of $CH_3NH_3PbI_{3-x}Cl_x$ Perovskite Solar Cells. *Nat. Commun.* **2014**, *5*, 3461.

(34) Johnston, M. B.; Herz, L. M. Hybrid Perovskites for Photovoltaics: Charge-Carrier Recombination, Diffusion, and Radiative Efficiencies. *Acc. Chem. Res.* **2016**, *49*, 146–154.

(35) Saba, M.; Cadelano, M.; Marongiu, D.; Chen, F.; Sarritzu, V.; Sestu, N.; Figus, C.; Aresti, M.; Piras, R.; Lehmann, A. G.; et al. Correlated Electron–Hole Plasma in Organometal Perovskites. *Nat. Commun.* **2014**, *5*, 5049.

(36) Luo, B.; Pu, Y.-C.; Yang, Y.; Lindley, S. A.; Abdelmageed, G.; Ashry, H.; Li, Y.; Li, X.; Zhang, J. Z. Synthesis, Optical Properties, and Exciton Dynamics of Organolead Bromide Perovskite Nanocrystals. *J. Phys. Chem. C* **2015**, *119*, 26672–26682.

(37) Shen, S.; Guo, P.; Wheeler, D. A.; Jiang, J.; Lindley, S. A.; Kronawitter, C. X.; Zhang, J. Z.; Guo, L.; Mao, S. S. Physical and Photoelectrochemical Properties of Zr-Doped Hematite Nanorod Arrays. *Nanoscale* **2013**, *5*, 9867–9874.

(38) Luo, B.; Pu, Y.-C.; Lindley, S. A.; Yang, Y.; Lu, L.; Li, Y.; Li, X.; Zhang, J. Z. Organolead Halide Perovskite Nanocrystals: Branched Capping Ligands Control Crystal Size and Stability. *Angew. Chem. Int. Ed. 55*, 8864–8868.

(39) Morris, T.; Zubkov, T. Steric Effects of Carboxylic Capping Ligands on the Growth of the CdSe Quantum Dots. *Colloids Surf. A:* **2014**, *443*, 439–449.

(40) Schmidt, L. C.; Pertegás, A.; González-Carrero, S.; Malinkiewicz, O.; Agouram, S.; Mínguez Espallargas, G.; Bolink, H. J.; Galian, R. E.; Pérez-Prieto, J. Nontemplate Synthesis of $CH_3NH_3PbBr_3$ Perovskite Nanoparticles. *J. Am. Chem. Soc.* **2014**, *136*, 850–853.

(41) Chen, X.; Jiang, J.; Yan, F.; Tian, S.; Li, K. A Novel Low Temperature Vapor Phase Hydrolysis Method for the Production of Nano-Structured Silica Materials Using Silicon Tetrachloride. *RSC Adv.* **2014**, *4*, 8703–8710.

(42) Tanaka, K.; Takahashi, T.; Ban, T.; Kondo, T.; Uchida, K.; Miura, N. Comparative Study on the Excitons in Lead-Halide-Based Perovskite-Type Crystals $CH_3NH_3PbBr_3$ $CH_3NH_3PbI_3$. *Solid State Commun.* **2003**, *127*, 619–623.

(43) Brennan, M. C.; Herr, J. E.; Nguyen-Beck, T. S.; Zinna, J.; Draguta, S.; Rouvimov, S.; Parkhill, J.; Kuno, M. Origin of the Size-Dependent Stokes Shift in $CsPbBr_3$ Perovskite Nanocrystals. *J. Am. Chem. Soc.* **2017**, *139*, 12201–12208.

(44) Luo, B.; Naghadeh, S. B.; Allen, A.; Li, X.; Zhang, J. Z. Peptide-Passivated Lead Halide Perovskite Nanocrystals Based on Synergistic Effect between Amino and Carboxylic Functional Groups. *Adv. Funct. Mater. 27*, 1604018.

(45) Roberti, T. W.; Cherepy, N. J.; Zhang, J. Z. Nature of the Power-Dependent Ultrafast Relaxation Process of Photoexcited Charge Carriers in II-VI Semiconductor Quantum Dots: Effects of Particle Size, Surface, and Electronic Structure. *J. Chem. Phys.* **1998**, *108*, 2143–2151.

(46) Mondal, N.; Samanta, A. Complete Ultrafast Charge Carrier Dynamics in Photo-Excited All-Inorganic Perovskite Nanocrystals ($CsPbX_3$). *Nanoscale* **2017**, *9*, 1878–1885.

(47) Makarov, N. S.; Guo, S.; Isaienko, O.; Liu, W.; Robel, I.; Klimov, V. I. Spectral and Dynamical Properties of Single Excitons, Biexcitons, and Trions in Cesium–Lead-Halide Perovskite Quantum Dots. *Nano Lett.* **2016**, *16*, 2349–2362.

(48) Godin, R.; Ma, X.; González-Carrero, S.; Du, T.; Li, X.; Lin, C.-T.; McLachlan, M. A.; Galian, R. E.; Pérez-Prieto, J.; Durrant, J. R. Tuning Charge Carrier Dynamics and Surface Passivation in Organolead Halide Perovskites with Capping Ligands and Metal Oxide Interfaces. *Adv. Opt. Mater.* **2018***, 6*, 1701203.

(49) Wheeler, D. A.; Fitzmorris, B. C.; Zhao, H.; Ma, D.; Zhang, J. Ultrafast Exciton Relaxation Dynamics of PbS and Core/Shell PbS/CdS Quantum Dots. *Sci. China Chem.* **2011**, *54*, 2009–2015.

(50) Manser, J. S.; Christians, J. A.; Kamat, P. V. Intriguing Optoelectronic Properties of Metal Halide Perovskites. *Chem. Rev.* **2016**, *116*, 12956–13008.

(51) Christians, J. A.; Manser, J. S.; Kamat, P. V. Multifaceted Excited State of $CH_3NH_3PbI_3$. Charge Separation, Recombination, and Trapping. *J. Phys. Chem. Lett.* **2015**, *6*, 2086–2095.

(52) Klimov, V. I.; McBranch, D. W. Femtosecond 1P to 1S Electron Relaxation in Strongly Confined Semiconductor Nanocrystals. *Phys. Rev. Lett.* **1998**, *80*, 4028–4031.

(53) Zhang, Z.-Y.; Wang, H.-Y.; Zhang, Y.-X.; Hao, Y.-W.; Sun, C.; Zhang, Y.; Gao, B.-R.; Chen, Q.-D.; Sun, H.-B. The Role of Trap-Assisted Recombination in

Luminescent Properties of Organometal Halide $CH_3NH_3PbBr_3$ Perovskite Films and Quantum Dots. *Sci. Rep.* **2016**, *6*, 27286.

(54) Chirvony, V. S.; González-Carrero, S.; Suárez, I.; Galian, R. E.; Sessolo, M.; Bolink, H. J.; Martínez-Pastor, J. P.; Pérez-Prieto, J. Delayed Luminescence in Lead Halide Perovskite Nanocrystals. *J. Phys. Chem. C* **2017**, *121*, 13381–13390.

(55) Pu, Y.-C.; Kibria, M. G.; Mi, Z.; Zhang, J. Z. Ultrafast Exciton Dynamics in InGaN/GaN and Rh/Cr2O3 Nanoparticle-Decorated InGaN/GaN Nanowires. *J. Phys. Chem. Lett.* **2015**, *6*, 2649–2656.

(56) Kambhampati, P. Unraveling the Structure and Dynamics of Excitons in Semiconductor Quantum Dots. *Acc. Chem. Res.* **2011**, *44*, 1–13.

(57) de Mello Donegá, C.; Koole, R. Size Dependence of the Spontaneous Emission Rate and Absorption Cross Section of CdSe and CdTe Quantum Dots. *J. Phys. Chem. C* **2009**, *113*, 6511–6520.

(58) Neogi, A.; Everitt, H.; Morkoc, H.; Kuroda, T.; Tackeuchi, A. Size Dependence of Carrier Recombination Efficiency in GaN Quantum Dots. *IEEE Trans. Nanotechnol.* **2005**, *4*, 297–299.

(59) Assefa, G. Mechanisms of Electroluminescence in Silicon Nanostructures. *Am. J. Con. Mat. Phys.* **2018**, *8*, 1–4.

(60) Wetzelaer, G.-J. A. H.; Scheepers, M.; Sempere, A. M.; Momblona, C.; Ávila, J.; Bolink, H. J. Trap-Assisted Non-Radiative Recombination in Organic–Inorganic Perovskite Solar Cells. *Adv. Mater.* **2015**, *27*, 1837–1841.

Chapter Four

4 Size-dependent Crystalline Phase Stability of Hybrid Perovskite Nanocrystals at Different Temperatures

4.1 Abstract

In recent years organic-inorganic perovskite nanocrystals (PNCs) have been studied extensively because of their great optical and photophysical properties. Perovskite showed significant potential to substitute expensive silicon in the photovoltaic and LEDs applications. However, perovskites commercialization is hindered by their instability toward environmental factors such as oxygen, light, humidity, and temperature. Thermal instability is specifically important since it thermal induced variation in crystal phase structure can affect materials optimal performance in devices. In this work, we studied effect of particles size controlled by varying the APTES capping ligand concentration on thermal stability of the $MAPbBr_3$ NCs. The structural and optical properties of the PNCs were investigated at different temperatures using UV-Vis, photoluminescence (PL), temperature dependent PL, temperature dependent time resolved PL (TRPL), cryo-XRD, and cryo-EM. The preliminary results showed spectral blue shift of the PL peak by decreasing the temperature from 300 K to 20 K, which is opposite of what was observed for large and middle-sized particles. The lifetime of the smaller PNCs also decreased by increasing the temperature. These

results can be possibly due to crystal phase transition in the small particles. Understanding the correlation of particle size and capping ligand concentration with thermal phase stability can help with optimizing PNCs for better device performance.

4.2 Introduction

Organic-inorganic metal halide perovskite nanocrystals have attracted significant attention in recent years as a potential alternative for high cost silicon in photovoltaic applications. Perovskite nanomaterials with ABX_3 formula (where A is organic/inorganic cation, B is metal cation such as Pb or Sn, and X is a halide anion such as Cl, Br, and I) offers flexibility in composition variation which can tune their optical and structural properties. In addition, easy and low-cost processing, tunable bandgap, large absorption coefficient, long exciton lifetime, and large charge carrier mobility[1–3] makes them outstanding candidates for various applications, such as PV solar cells, light-emitting diodes (LEDs), photodetectors, sensors, lasers, and photoelectrochemical cells.[4–8] However, the rapid degradation of material[9,10], Hysteresis[11,12] and their instability toward environmental factors such as light, oxygen, humidity and temperature[9,13,14] hinder their commercialization. Several studies have correlated these instabilities to surface properties such as the presence of defects.[15,16] These defects, which can be formed as a result of chemical and structural changes in the material, are also a detrimental factor impacting device performance as they provide recombination channels for photogenerated charge carriers.[17,18] Therefore, various strategies for surface modification and defect passivation, including addition

of molecular capping ligands, organic polymers, and metal-oxide shells, have been used in order to improve the chemical and physical stability that is critical for maintaining device performance over time.[19–24] Perovskite nanocrystals (PNCs) because of their large surface to volume ratio are considered as good models to design these passivation strategies. Furthermore, crystal phase plays an important role in perovskite stability and device performance. For example, substitution of methylammonium (MA) with formamidinium (FA) significantly enhances chemical stability, but FA based perovskite crystals have a phase transition to the yellow non perovskite polymorph (δ -phase), very close to photovoltaic operational temperatures, making the device performance unpredictable.[25] Perovskite in general have unit cells composed of five atoms in a cubic structure (α phase), where cation B has six nearest neighbor anions X and cation A has twelve.[26] However, maintaining this high symmetry cubic structure is very difficult. Therefore, perovskite can only stay in α-cubic at temperatures higher than 330° C.[27] It is also reported that bromide-based perovskite crystals do exist in a pseudo cubic phase at room temperature due to the difference in the ionic radii of Br^- and I^-, with the smaller Br^- helping in stabilizing the cubic lattice.[28] Interestingly, the phase diagram is also tunable by crystal size, as evident from the fact that iodide based PQDs exist in the cubic phase at room temperature.[29] In addition to optimizing the composition, capping ligand can also affect the phase stability in PNCs. It was previously observed for perovskite thin films that the long recombination lifetime in the tetragonal phase decreased an order of magnitude following the transition to the orthorhombic phase at lower temperature. The same

trend was Sarang et al. attributed this behavior to crossover from free carriers to exciton-dominated radiative recombination.[30] On the contrary, Li et al. reported a significant PL lifetime increase of inorganic $CsPbBr_3$ NCs by increasing the temperature to 300 K and then a sudden decrease in the lifetime by further increasing the temperature over 300 K, suggesting thermal instability in inorganic PNCs.[31] We recently found a correlation among surface property, phase transition, and exciton dynamics for $MAPbBr_3$ NCs capped with APTES and OABr.[32] In this study, a higher energy band observed in the PL spectra, indicating a structural phase transition from tetragonal to orthorhombic at 140 K for PNCs capped with OABr. However, PNCs capped with APTES did not show any structural change even at 20 K. This is attributed to the difference in surface energy contribution to their Gibbs free energy, which modifies the crystal phase diagram to an energetically stable cubic phase. This capping ligand-dependent phase transition also decreased the PL lifetime associated with phase transition in the PNCs capped with OABr.[32] Our group previously studied the effect of size and APTES concentration as capping ligand on charge carrier dynamics in $MAPbBr_3$ PNCs. Here in this chapter, we studied the affect of PNC size and APTES concentration on crystal phase stability and its dependence to temperature. We used UV-Vis, photoluminescence (PL), temperature dependent PL, temperature dependent time resolved PL (TRPL), cryo-XRD, and cryo-EM to study the phase structure at different temperatures. Our preliminary results show the reverse trend in PL peak position shift at lower temperatures compared to middle and larger size. On the other hand, the lifetime of the smaller PNCs decreased by increasing the temperature, which

is the opposite of the larger sizes. These results can be due to crystal lattice expansion or phase transition in the small particles. Understanding the effect of particle size and capping ligand concentration on thermal phase stability will eventually help in designing materials with better device performance.

4.3 Experimental

4.3.1 Materials

All chemicals were used as received without further purification: toluene (spectroscopic grade, Fisher Scientific), *N*,*N*-dimethylformamide (DMF, spectroscopic grade, Fisher Scientific), methylammonium bromide (MABr) (Greatcell Solar Australia Pty Ltd), lead bromide (98+%, Alfa Aesar), OA (90%, Alfa Aesar), and APTES (99%, Sigma-Aldrich).

4.3.2 Synthesis

A ligand-assisted reprecipitation method was used to synthesize the $CH_3NH_3PbBr_3$ NCs. Briefly, 0.157 mmol of MABr and 0.200 mmol of lead bromide ($PbBr_2$) were dissolved in 400 μL DMF and sonicated until clear. 100 μL of OA and varying amounts of APTES (20, 35, and 50 μL) were added to separate solutions to control the particle size. The precursor solution was further sonicated to reach a homogeneous solution and then injected into 5 mL toluene to precipitate and collect the nanocrystals. The resultant nanocrystals were centrifuged at 6000 rpm for 5 min and washed with toluene twice to remove unreacted precursors. A portion of the

collected precipitate was dried for powder XRD characterization and the rest was redispersed in toluene for film fabrication.

4.3.3 Characterization and Instruments

UV–vis and fluorescence spectra of the prepared nanocrystal films were collected on Agilent Technologies Cary 60 and FluoroMax-3, respectively. XRD was used to obtain the crystalline phase at a voltage of 40 kV and a current of 30 mA using a Rigaku America Miniflex Plus powder diffractometer. The scanning angle range was 10–60° (2θ) with a rate of 3° min^{-1}. TEM and HRTEM were carried out to investigate the size, morphology, and lattice spacing of the PNCs. The TEM study was carried out using a FEI UT Tecnai HRTEM microscope operated at a 200 kV accelerating voltage. The PL data were taken using an Acton 300i spectrometer and then dispersed onto a thermoelectrically cooled charge-coupled device (CCD) with a spectral resolution of 0.18 nm. For time-resolved PL measurements, we used a time-correlated single-photon counting (TCSPC) system (Picoquant) in conjunction with the pulsed source. The temperature-dependent measurements were done in a cryo free system from Advanced Research Systems with a base temperature of 10 K.

4.4 Results and Discussion

4.4.1 TEM, UV-Vis and PL Spectroscopy

Controlling the particle sizes was achieved using different concentration of APTES as capping ligand in the dissolution–precipitation synthesis method similar to what reported previously.[33] TEM images in Fig. 1 (a-c) shows formation of spherical and uniform particles, with average sizes of 9.2 ± 0.5, 5.1 ± 0.3, and 3.1 ± 0.2 nm when

20, 35, and 50 μL of APTES was used in the synthesis. These samples are labeled PNC_{20_APTES}, PNC_{35_APTES}, and PNC_{50_APTES}, respectively. As shown in TEM images, the size of resultant PNCs was decreased by increasing the APTES concentration. This trend is due to the coordinating effect of capping ligands which slows down the rate of monomer transfer to the PNC surface and thereby limits growth. The relative uniformity of all sizes is due to the strong steric hindrance of branched APTES ligands, as reported previously.[33] UV-Vis and steady state PL spectroscopy was also used to study their optical properties as shown in Fig. 1(d-f). These optical characterizations were performed on thin films of each sample deposited on glass substrate by spin coating. As shown in Fig 1 (d-f) the UV–vis spectra of PNC_{20_APTES} exhibit an excitonic absorption peak at 520 nm with an extended tail at lower energies due to the scattering of the relatively larger particles. However, the absorption onset of PNC_{35_APTES} and PNC_{50_APTES} is blue-shifted to 490 and 440 nm, respectively. This spectral shift is due to the decrease in PNC size as reported previously.[34–36] after excitation at 360 nm (λ_{ex}), similar blue shift was observed for the narrow and symmetric PL emission bands, moving from 530 nm for PNC_{20_APTES} to 470 nm for PNC_{50_APTES} . These narrow emission peaks and the small full width at half-maximum indicates the uniform distribution in particle size as shown in the TEM images in Fig. 1 (d-f). In addition, a larger Stokes shift (~41 meV) was observed as the PNC size decreased from 9.2 to 3.1 nm. This size-dependent Stokes shift has been reported previously for CdSe QDs as well as all-inorganic PNCs such as $CsPbBr_3$.[37] Theoretical calculations have revealed the presence of an inherent, size-dependent confined hole state above the valence band

(VB) for $CsPbBr_3$ NCs between the sizes of 2–5 nm. This hole state is proposed to be dark in absorption but bright in emission due to its low population density, which explains the size-dependent Stokes shift.[37] Because cesium orbitals did not contribute to this identified confined hole state, this size-dependent stokes shift can be assumed to be a general feature in other PNCs similar to what we observed here for $CH_3NH_3PbBr_3$ PNCs.

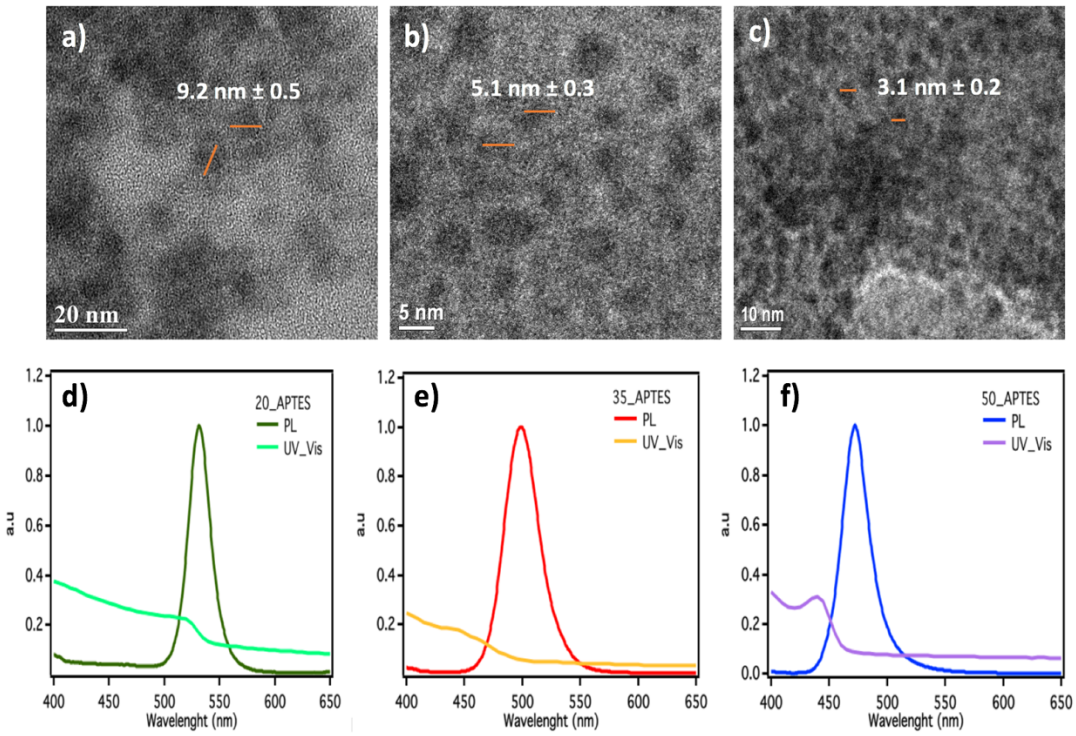

Figure 4-1- TEM images of (a) PNC_{20_APTES}, (b) PNC_{35_APTES}, and (c) PNC_{50_APTES}. (d) UV–vis and PL spectra (λex = 360 nm) of PNC_{20_APTES}, (e) PNC_{35_APTES}, and (f) PNC_{50_APTES} spin-coated on the glass substrate at 4500 rpm.

4.4.2 Temperature Dependent PL

Generally, in semiconductor nanomaterials the band gap energy increases as temperature decrease. This change in band structure with temperature is

due to the temperature induced lattice dilatation and electron–lattice interaction.[38] The renormalization of the band energies due to electron-lattice interaction consists of two terms: The Debye-Waller (DW) and the self-energy (SE) corrections. Usually, for the semiconductor nanomaterials with direct band gaps both terms decrease by increasing the temperature.[38,39] The thermal lattice expansion is mostly due to a positive hydrostatic pressure coefficient of the gaps, while the gap reduction arising from electron-phonon interaction is proportional to the Bose-Einstein phonon occupation number.[38] However, Perovskite showed atypical dependence of band gap energy to temperature, which is attributed to its reverse band structure.[27,10,40,41] Fig. 2 (a-c) shows PL intensity of differently sized PNCs mapped with the emission wavelength and temperature. As shown in Fig 2a and 2c, large and middle-sized particles with the diameter of 9.2 and 5.1 nm showed obvious red shift in PL spectra as the temperature decreased from 300 K to 20 K. This is similar to what was reported previously for various different perovskite nanocrystals. [32,40,41] As discussed before, this spectral red shift happens as a result of thermal lattice expansion and electron-lattice interaction in the materials with reverse band gap such as perovskite. In Fig. 2 d and e, the line cuts of the same maps are represented at 20, 100, 200, and 290 K. It is clearly showed that the PL spectra maximum of PNC_{20_APTES} shifted from 530 nm at room temperature (RT) to 552 nm at 20K. similarly for PNC_{35_APTES} the spectra shifted from 490 nm at RT to 505 nm at 20 K. in addition to the spectral shift, the full width half maximum (FWHM) decreased significantly by lowering the temperature. This can be simply related to the Varshni effect.[42] The PL spectra in general is formed by emission from

different localized states at the same time which results in larger FWHM at RT. At higher temperatures (up to 300 K) the thermal activation energy enables the carriers in the lower energy levels to hop and occupy the higher energy levels of the strongly localized states, which leads to the blueshift of the peak energy and the increase of the FWHM.[43] The change in line shape observed for $PNCs_{20\_APTES}$ and $PNCs_{35\_APTES}$ at lower temperatures is also consistent with the lower thermal energy, which reduces homogeneous broadening.[42]

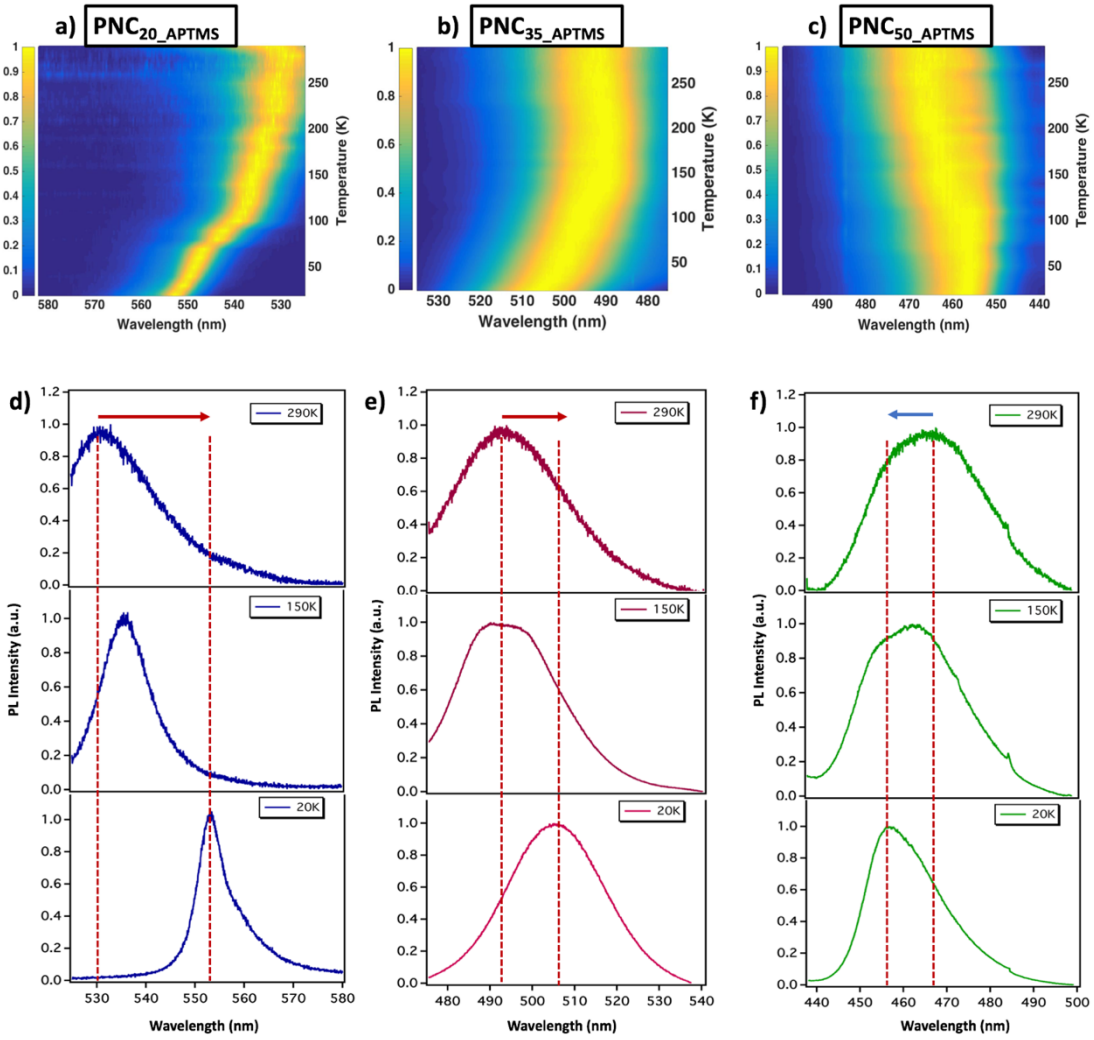

Figure 4-2- PL intensity mapped with the emission wavelength and temperature for (a) P-OABr and (b) P-APTMS (a) PNC_{20_APTMS}, (b) PNC_{35_APTMS}, and (c) PNC_{50_APTMS}. Line cuts of the same maps at 20, 150, and 290 K for (d) PNC_{20_APTMS}, (e) PNC_{35_APTMS}, and (f) PNC_{50_APTMS}.

However, the PL spectra of the smallest PNCs (PNC_{50_APTES}) with diameter of 3.1 nm showed an opposite trend and slightly blue shifted with decreasing the temperature. Similar spectral blue shift was reported previously for $MAPbI_3$ and $MAPbBr_3$ perovskite nanomaterial and was attributed to crystal phase change.[40,41,44,45] The spectral shift onset started at ~160 K which is the temperature that was reported as

phase transition region from tetragonal to orthorhombic.[44] In some other studies, it has been shown that this phase change and spectral shift is significantly dependent on halide size. Saran *et al.* investigated the PL of ($CsPbX_3$, where X is Cl, Br, or I) NC perovskites.[46] They reported a wide broadening of the excitonic linewidth in these NCs, which arises from strong exciton–phonon coupling. $CsPbBr_3$ and $CsPbI_3$ NCs displayed a general redshift of their emission energy peak with reducing temperature. However, the $CsPbCl_3$ NCs with smaller halide in the structure displayed a blueshift and underwent a structural phase transition at ≈ 175–200 K. This temperature-dependent change from an initial blueshift to a redshift is attributed to a phase change in the crystal structure.[46]

4.4.3 Temperature Dependent TRPL

Structural phase transition in PNCs is accompanied by changes in charge carrier behavior, including both the type of carriers that dominate recombination (bimolecular or excitonic) as well the associated time scales. To study the effect of size and capping ligand concentration on the charge carrier lifetime as a function of temperature, we measured low-temperature time-resolved PL of all three samples (PNC_{20_APTES}, PNC_{35_APTES}, and PNC_{50_APTES}) between 290 and 20 K. The average lifetimes of exciton decay for all PNC_{APTES} samples were calculated by fitting the data in Fig. 3 to a stretched exponential fit to account for continuous higher-order recombinations.[47] The values of these recombination times, extracted from fits, are plotted in bottom plots of figure 3 for PNC_{35_APTES} and PNC_{50_APTES}. All the particles showed average lifetime of

2-3 ns. However, even without the benefit of quantitative analysis, a difference between the trends with temperature is clearly visible. For large and middle sized PNCS (PNC_{20_APTES} and PNC_{35_APTES}), the time-resolved curves show a continuous and gradual decrease of exciton lifetime with temperature. Based on previous reports, this reduction in charge carrier lifetime with lowering temperature arises from the interactions of free and trapped excitons with surface states or localized states as relaxation pathways.[31,48–51] However, the lifetime of smaller PNCs (PNC_{50_APTES}) showed reverse behavior compared to large and medium sized PNCs and decreased by increasing the temperature. Similar behavior in PL lifetime was previously observed when $CsPbI_3$, $CsPbBr_3$, and $CsPbCl_3$ were compared.[52] But it is not clear yet if this is trap-related recombination which cause this reverse lifetime trend.

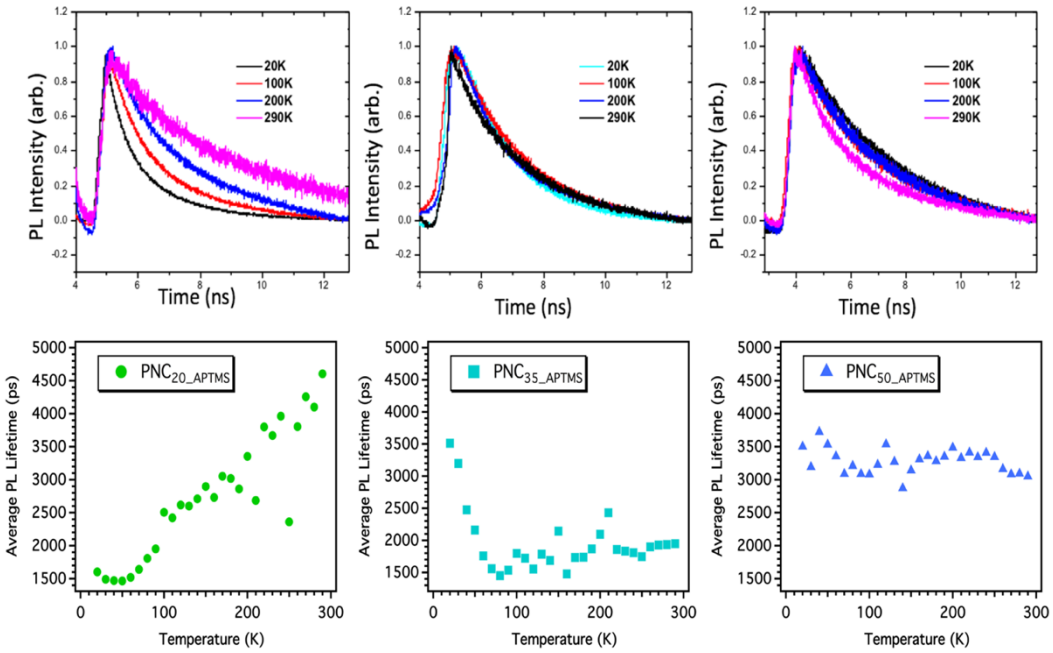

Figure 4-3- Time-resolved PL curves for (a) PNC_{20_APTES}, (b) PNC_{35_APTES}, and (c) PNC_{50_APTES} as functions of temperature. Recombination lifetimes extracted from stretched exponential fits for PNC_{35_APTES} and PNC_{50_APTES} are plotted in (d) and (e).

4.4.4 Cryo XRD

In order to understand the reason behind the atypical behavior of the PNC_{50_APTES} and investigate the possibility of phase change in these NCs, cryo XRD measurements were performed. XRD peaks of all three samples at temperatures ranging from 15 K to 300 K is shown in Fig 4.

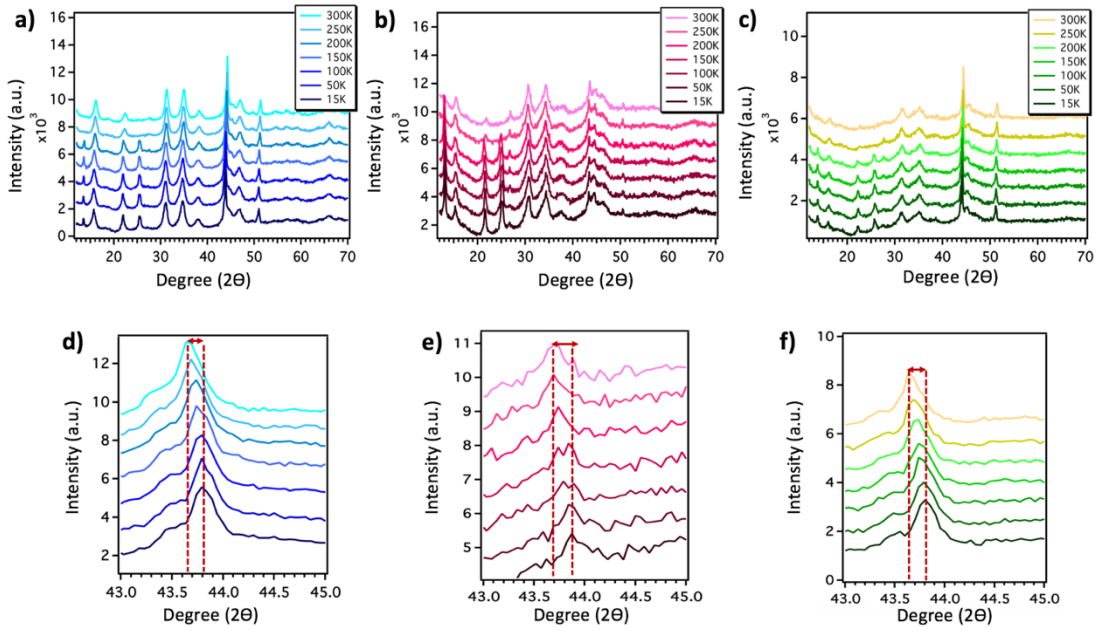

Figure 4-4- XRD peaks of (a) PNC_{20_APTES}, (b) PNC_{35_APTES}, and (c) PNC_{50_APTES} at temperatures ranging from 15 K to 300 K. The bottom panels are zoomed in peaks of (d) PNC_{20_APTES}, (e) PNC_{35_APTES}, and (f) PNC_{50_APTES} from 43 to 45 degree.

The XRD patterns shown in Fig.4 were used to determine the crystal structure of the PNCs. The peaks centered at 14.80°, 21.03°, 29.98°, 33.55°, 36.93°, 42.83°, and 45.69° can be indexed to the cubic phase $CH_3NH_3Br_3$ perovskite, indicating sample crystallinity and purity.[53] When the amount of APTES was increased, significant broadening in XRD peaks was observed because of the presence of smaller PNCs and amorphous silica as a result of higher concentration of APTES on the samples.[54] Further increase of APTES concentration resulted in the formation of the bulk material instead of PNCs. As shown in Fig 4 (d-f) all the peaks shifted toward large diffraction angles as the temperature decreased due change in cell parameters caused by lattice contraction.[40]

In these cryo XRD patterns no appearance of new peak or peak splitting was observed. However, by lowering the temperature from 300 K to 20 K, the peak observed at 14.8 degree got narrower and its intensity increased significantly in PNC_{20_APTES}. While, the same peak was observed initially for PNC_{50_APTES} at room temperature, but completely disappeared as the temperature went down to 15 K. This result can probably indicate the transition from cubic phase at lower temperatures for PNC_{50_APTES}. However, since the peak intensities are low and within the noise range, it is difficult to draw solid conclusion. Therefore, new samples were prepared for cryo-XRD at lower scanning rate to intensify the peaks.

4.4.5 Cryo TEM

It was discussed previously that lowering the temperature can cause change in cell parameters and lattice contraction in the PNCs, consequently. In order to study this lattice parameter change, high resolution TEM images were collected for PNC_{20_APTES}, PNC_{35_APTES}, and, PNC_{50_APTES} at 300 K and 96 K. Fig. 5 represent the HR-TEM images of PNC_{35_APTES} at 96 K and 300 K and the d-spacing in the lattice was measured for six different particles at both temperatures. The resultant d-spacing and the average is reported in Table 1. As it can be seen in Table 1, aside from small differences, the average d-spacing for the PNCs didn't changed at different temperatures. This might mostly be due to rotation of PNCs under the microscope which is a common phenomenon. This rotation eventually results in inaccurate measurement of the lattice parameters. Even though this lattice contraction and expansion was reported in

previous literatures for PNCs and was confirmed by peak shift in temperature dependent PL and shift in XRD peaks, it was not clearly observed in this measurement.

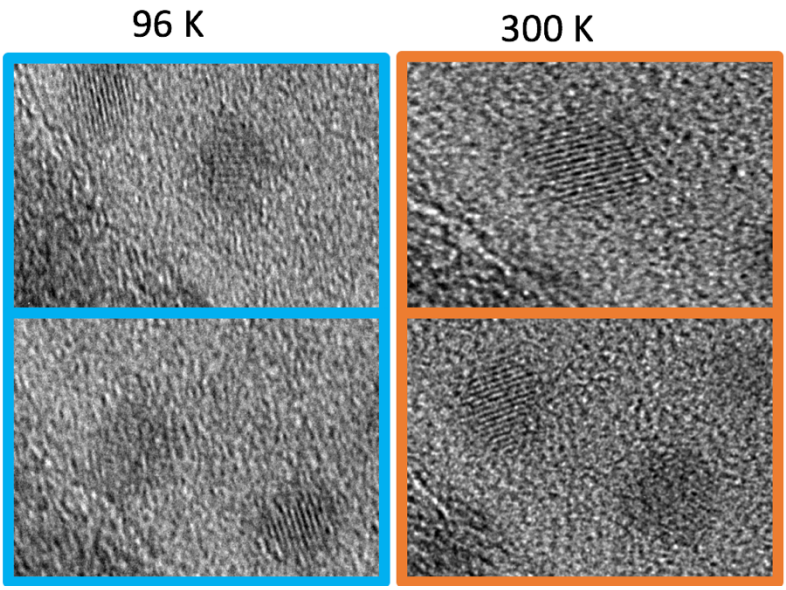

Figure 4-5- HR-TEM images of PNC_{35_APTES} at 96 K and 300 K.

Table 4-1- d-spacing of 6 different PNC_{35_APTES} at 96 K and 300 K.

Particle	d-spacing at 96 K	d-spacing at 300 K
#1	0.29	0.29
#2	0.29	0.29
#3	0.29	0.28
#4	0.29	0.28
#5	0.30	0.29
#6	0.28	0.28
Average	0.29	0.29

4.5 Conclusion and Future Work

Recent researches showed importance of optimizing surface of perovskite nanocrystals for improving their optical and photophysical properties. The surface defects are reported to be responsible for materials instability toward environmental factors including light, oxygen, humidity and temperature. Among these factors, temperature can specifically alter materials properties and therefore hinder their performance in device. Selection of capping ligand was also shown to be important for proper passivation of surface defects. In this work, various concentration of APTES as a branched and efficient capping ligand was used to control the particle size and investigate their optical and structural properties as a function of temperature. HR-TEM was used to determine the particle sizes to be 9.2, 5.1, and 3.1 nm with 20, 35, 50 μL of APTES was used, respectively. Room temperature steady state UV-Vis and PL showed size dependence spectral shift. Additionally, the temperature dependent PL was measured for all three particles and PNC_{35_APTES} showed slight blue shift in the PL spectra which is opposite of what was observed for large and middle-sized PNCs. This blue shift at low temperature was suggested to be an indication of phase transition from tetragonal to orthorhombic. Since the phase transition can affect the charge carrier dynamics and recombination lifetime, the TRPL measurement was done to investigate the decay profile of these different sized PNCs. Interestingly, the small PNCs showed increase in lifetime with lowering the temperature, which is contradictory to the trend observed for large and small particles. The cryo-XRD was also done to investigate the possibility of phase transition, however, due to low peak intensity didn't result in solid conclusion. For the future work, it is planned to do cryo-XRD at lower scanning rate to

achieve higher peak resolution. Temperature dependent Raman is also suggested as a powerful tool to detect phase transition in these NCs.

4.6 References

(1) Kim, H.-S.; Lee, C.-R.; Im, J.-H.; Lee, K.-B.; Moehl, T.; Marchioro, A.; Moon, S.-J.; Humphry-Baker, R.; Yum, J.-H.; Moser, J. E.; et al. Lead Iodide Perovskite Sensitized All-Solid-State Submicron Thin Film Mesoscopic Solar Cell with Efficiency Exceeding 9%. *Sci. Rep.* **2012**, *2*, 591.

(2) Yang, W. S.; Noh, J. H.; Jeon, N. J.; Kim, Y. C.; Ryu, S.; Seo, J.; Seok, S. I. High-Performance Photovoltaic Perovskite Layers Fabricated through Intramolecular Exchange. *Science* **2015**, *348* (6240), 1234–1237.

(3) Dong, Q.; Fang, Y.; Shao, Y.; Mulligan, P.; Qiu, J.; Cao, L.; Huang, J. Electron-Hole Diffusion Lengths > 175 Mm in Solution-Grown CH3NH3PbI3 Single Crystals. *Science* **2015**, *347* (6225), 967–970.

(4) Cho, H.; Jeong, S.-H.; Park, M.-H.; Kim, Y.-H.; Wolf, C.; Lee, C.-L.; Heo, J. H.; Sadhanala, A.; Myoung, N.; Yoo, S.; et al. Overcoming the Electroluminescence Efficiency Limitations of Perovskite Light-Emitting Diodes. *Science* **2015**, *350* (6265), 1222–1225.

(5) Tan, Z.-K.; Moghaddam, R. S.; Lai, M. L.; Docampo, P.; Higler, R.; Deschler, F.; Price, M.; Sadhanala, A.; Pazos, L. M.; Credgington, D.; et al. Bright Light-Emitting

Diodes Based on Organometal Halide Perovskite. *Nat. Nanotechnol.* **2014**, *9* (9), 687–692.

(6) Veldhuis, S. A.; Boix, P. P.; Yantara, N.; Li, M.; Sum, T. C.; Mathews, N.; Mhaisalkar, S. G. Perovskite Materials for Light-Emitting Diodes and Lasers. *Adv. Mater.* **2016**, *28* (32), 6804–6834.

(7) Xing, G.; Mathews, N.; Lim, S. S.; Yantara, N.; Liu, X.; Sabba, D.; Grätzel, M.; Mhaisalkar, S.; Sum, T. C. Low-Temperature Solution-Processed Wavelength-Tunable Perovskites for Lasing. *Nat. Mater.* **2014**, *13* (5), 476–480.

(8) Zhu, H.; Fu, Y.; Meng, F.; Wu, X.; Gong, Z.; Ding, Q.; Gustafsson, M. V.; Trinh, M. T.; Jin, S.; Zhu, X.-Y. Lead Halide Perovskite Nanowire Lasers with Low Lasing Thresholds and High-Quality Factors. *Nat. Mater.* **2015**, *14* (6), 636–642.

(9) Niu, G.; Guo, X.; Wang, L. Review of Recent Progress in Chemical Stability of Perovskite Solar Cells. *J. Mater. Chem. A* **2015**, *3* (17), 8970–8980.

(10) Misra, R. K.; Aharon, S.; Li, B.; Mogilyansky, D.; Visoly-Fisher, I.; Etgar, L.; Katz, E. A. Temperature- and Component-Dependent Degradation of Perovskite Photovoltaic Materials under Concentrated Sunlight. *J. Phys. Chem. Lett.* **2015**, *6* (3), 326–330.

(11) Snaith, H. J.; Abate, A.; Ball, J. M.; Eperon, G. E.; Leijtens, T.; Noel, N. K.; Stranks, S. D.; Wang, J. T.-W.; Wojciechowski, K.; Zhang, W. Anomalous Hysteresis in Perovskite Solar Cells. *J. Phys. Chem. Lett.* **2014**, *5* (9), 1511–1515.

(12) Raga, S. R.; Jung, M.-C.; Lee, M. V.; Leyden, M. R.; Kato, Y.; Qi, Y. Influence of Air Annealing on High Efficiency Planar Structure Perovskite Solar Cells. *Chem. Mater.* **2015**, *27* (5), 1597–1603.

(13) Abdelmageed, G.; Jewell, L.; Hellier, K.; Seymour, L.; Luo, B.; Bridges, F.; Zhang, J. Z.; Carter, S. Mechanisms for Light Induced Degradation in MAPbI3 Perovskite Thin Films and Solar Cells. *Appl. Phys. Lett.* **2016**, *109* (23), 233905.

(14) Han, Y.; Meyer, S.; Dkhissi, Y.; Weber, K.; M. Pringle, J.; Bach, U.; Spiccia, L.; Cheng, Y.-B. Degradation Observations of Encapsulated Planar CH 3 NH 3 PbI 3 Perovskite Solar Cells at High Temperatures and Humidity. *J. Mater. Chem. A* **2015**, *3* (15), 8139–8147.

(15) Lee, Y. M.; Park, J.; Yu, B. D.; Hong, S.; Jung, M.-C.; Nakamura, M. Surface Instability of Sn-Based Hybrid Perovskite Thin Film, CH3NH3SnI3: The Origin of Its Material Instability. *J. Phys. Chem. Lett.* **2018**, *9* (9), 2293–2297.

(16) Yang, J.; Siempelkamp, B. D.; Mosconi, E.; De Angelis, F.; Kelly, T. L. Origin of the Thermal Instability in CH3NH3PbI3 Thin Films Deposited on ZnO. *Chem. Mater.* **2015**, *27* (12), 4229–4236.

(17) Wheeler, D. A.; Zhang, J. Z. Exciton Dynamics in Semiconductor Nanocrystals. *Adv. Mater.* **2013**, *25* (21), 2878–2896.

(18) Naghadeh, S. B.; Luo, B.; Pu, Y.-C.; Schwartz, Z.; Hollingsworth, W. R.; Lindley, S. A.; Brewer, A. S.; Ayzner, A. L.; Zhang, J. Z. Size Dependence of Charge Carrier Dynamics in Organometal Halide Perovskite Nanocrystals: Deciphering

Radiative Versus Nonradiative Components. *J. Phys. Chem. C* **2019**, *123* (7), 4610–4619.

(19) Bu, X.; Westbrook, R. J. E.; Lanzetta, L.; Ding, D.; Chotchuangchutchaval, T.; Aristidou, N.; Haque, S. A. Surface Passivation of Perovskite Films via Iodide Salt Coatings for Enhanced Stability of Organic Lead Halide Perovskite Solar Cells. *Sol. RRL* **2019**, *3* (2), 1800282.

(20) Bai, Y.; Lin, Y.; Ren, L.; Shi, X.; Strounina, E.; Deng, Y.; Wang, Q.; Fang, Y.; Zheng, X.; Lin, Y.; et al. *Oligomeric Silica-Wrapped Perovskites Enable Synchronous Defect Passivation and Grain Stabilization for Efficient and Stable Perovskite Photovoltaics*; SSRN Scholarly Paper ID 3346989; Social Science Research Network: Rochester, NY, 2019.

(21) Jiang, Q.; Zhao, Y.; Zhang, X.; Yang, X.; Chen, Y.; Chu, Z.; Ye, Q.; Li, X.; Yin, Z.; You, J. Surface Passivation of Perovskite Film for Efficient Solar Cells. *Nat. Photonics* **2019**, 1.

(22) Huang, S.; Li, Z.; Kong, L.; Zhu, N.; Shan, A.; Li, L. Enhancing the Stability of CH3NH3PbBr3 Quantum Dots by Embedding in Silica Spheres Derived from Tetramethyl Orthosilicate in “Waterless” Toluene. *J. Am. Chem. Soc.* **2016**, *138* (18), 5749–5752.

(23) Koh, W.; Park, S.; Ham, Y. Phosphonic Acid Stabilized Colloidal $CsPbX_3$ (X=Br, I) Perovskite Nanocrystals and Their Surface Chemistry. *ChemistrySelect 1* (13), 3479–3482.

(24) Huang, H.; Chen, B.; Wang, Z.; Hung, T. F.; Susha, A. S.; Zhong, H.; Rogach, A. L. Water Resistant CsPbX3 Nanocrystals Coated with Polyhedral Oligomeric Silsesquioxane and Their Use as Solid State Luminophores in All-Perovskite White Light-Emitting Devices. *Chem. Sci.* **2016**, *7* (9), 5699–5703.

(25) Zheng, X.; Wu, C.; Jha, S. K.; Li, Z.; Zhu, K.; Priya, S. Improved Phase Stability of Formamidinium Lead Triiodide Perovskite by Strain Relaxation. *ACS Energy Lett.* **2016**, *1* (5), 1014–1020.

(26) Yin, W.-J.; Shi, T.; Yan, Y. Unique Properties of Halide Perovskites as Possible Origins of the Superior Solar Cell Performance. *Adv. Mater.* **2014**, *26* (27), 4653–4658.

(27) Yin, W.-J.; Yang, J.-H.; Kang, J.; Yan, Y.; Wei, S.-H. Halide Perovskite Materials for Solar Cells: A Theoretical Review. *J. Mater. Chem. A* **2015**, *3* (17), 8926–8942.

(28) Sheng, R.; Ho-Baillie, A.; Huang, S.; Chen, S.; Wen, X.; Hao, X.; Green, M. A. Methylammonium Lead Bromide Perovskite-Based Solar Cells by Vapor-Assisted Deposition. *J. Phys. Chem. C* **2015**, *119* (7), 3545–3549.

(29) Yakunin, S.; Protesescu, L.; Krieg, F.; Bodnarchuk, M. I.; Nedelcu, G.; Humer, M.; De Luca, G.; Fiebig, M.; Heiss, W.; Kovalenko, M. V. Low-Threshold Amplified Spontaneous Emission and Lasing from Colloidal Nanocrystals of Caesium Lead Halide Perovskites. *Nat. Commun.* **2015**, *6*, 8056.

(30) Sarang, S.; Ishihara, H.; Chen, Y.-C.; Lin, O.; Gopinathan, A.; Tung, V. C.; Ghosh, S. Low Temperature Excitonic Spectroscopy and Dynamics as a Probe of

Quality in Hybrid Perovskite Thin Films. *Phys. Chem. Chem. Phys.* **2016**, *18* (41), 28428–28433.

(31) Li, J.; Yuan, X.; Jing, P.; Li, J.; Wei, M.; Hua, J.; Zhao, J.; Tian, L. Temperature-Dependent Photoluminescence of Inorganic Perovskite Nanocrystal Films. *RSC Adv.* **2016**, *6* (82), 78311–78316.

(32) Sarang, S.; Bonabi Naghadeh, S.; Luo, B.; Kumar, P.; Betady, E.; Tung, V.; Scheibner, M.; Zhang, J. Z.; Ghosh, S. Stabilization of the Cubic Crystalline Phase in Organometal Halide Perovskite Quantum Dots via Surface Energy Manipulation. *J. Phys. Chem. Lett.* **2017**, *8* (21), 5378–5384.

(33) Luo, B.; Pu, Y.-C.; Lindley, S. A.; Yang, Y.; Lu, L.; Li, Y.; Li, X.; Zhang, J. Z. Organolead Halide Perovskite Nanocrystals: Branched Capping Ligands Control Crystal Size and Stability. *Angew. Chem. Int. Ed. 55* (31), 8864–8868.

(34) Lin, K.-F.; Cheng, H.-M.; Hsu, H.-C.; Lin, L.-J.; Hsieh, W.-F. Band Gap Variation of Size-Controlled ZnO Quantum Dots Synthesized by Sol–Gel Method. *Chem. Phys. Lett.* **2005**, *409* (4), 208–211.

(35) Kondratenko, T. S.; Smirnov, M. S.; Ovchinnikov, O. V.; Shabunya-Klyachkovskaya, E. V.; Matsukovich, A. S.; Zvyagin, A. I.; Vinokur, Y. A. Size-Dependent Optical Properties of Colloidal CdS Quantum Dots Passivated by Thioglycolic Acid. *Semiconductors* **2018**, *52* (9), 1137–1144.

(36) Bain, D.; Maity, S.; Paramanik, B.; Patra, A. Core-Size Dependent Fluorescent Gold Nanoclusters and Ultrasensitive Detection of Pb2+ Ion. *ACS Sustain. Chem. Eng.* **2018**, *6* (2), 2334–2343.

(37) Brennan, M. C.; Herr, J. E.; Nguyen-Beck, T. S.; Zinna, J.; Draguta, S.; Rouvimov, S.; Parkhill, J.; Kuno, M. Origin of the Size-Dependent Stokes Shift in $CsPbBr_3$ Perovskite Nanocrystals. *J. Am. Chem. Soc.* **2017**, *139* (35), 12201–12208.

(38) Francisco-López, A.; Charles, B.; Weber, O. J.; Alonso, M. I.; Garriga, M.; Campoy-Quiles, M.; Weller, M. T.; ~Goñi, A. R. On the Role of the Electron-Phonon Interaction in the Temperature Dependence of the Gap of Lead Halide Perovskites. *ArXiv190310204 Cond-Mat* **2019**.

(39) Cui, M.; Zhang, Z.; Wang, Y.; Finch, A.; Townsend, P. D. Temperature Dependence of Bulk Luminescence from ZnO. *Luminescence* **2018**, *33* (4), 654–659.

(40) Wang, K.-H.; Li, L.-C.; Shellaiah, M.; Sun, K. W. Structural and Photophysical Properties of Methylammonium Lead Tribromide ($MAPbBr_3$) Single Crystals. *Sci. Rep.* **2017**, *7* (1), 13643.

(41) Kong, W.; Ye, Z.; Qi, Z.; Zhang, B.; Wang, M.; Rahimi-Iman, A.; Wu, H. Characterization of an Abnormal Photoluminescence Behavior upon Crystal-Phase Transition of Perovskite $CH_3NH_3PbI_3$. *Phys. Chem. Chem. Phys.* **2015**, *17* (25), 16405–16411.

(42) Varshni, Y. P. Temperature Dependence of the Energy Gap in Semiconductors. *Physica* **1967**, *34* (1), 149–154.

(43) Wan-Ru, Z.; Weng, G.-E.; Ming-Ming, L.; Zeng-Cheng, L.; Jian-Ping, L.; Jiang-Yong, Z.; Bao-Ping, Z. Temperature Dependence of Emission Properties of Self-Assembled InGaN Quantum Dots. *Chin. Phys. Lett.* **2014**, *31*, 114205.

(44) Chen, C.; Hu, X.; Lu, W.; Chang, S.; Shi, L.; Li, L.; Zhong, H.; Han, J.-B. Elucidating the Phase Transitions and Temperature-Dependent Photoluminescence of $MAPbBr_3$ Single Crystal. *J. Phys. Appl. Phys.* **2018**, *51* (4), 045105.

(45) Whitfield, P. S.; Herron, N.; Guise, W. E.; Page, K.; Cheng, Y. Q.; Milas, I.; Crawford, M. K. Structures, Phase Transitions and Tricritical Behavior of the Hybrid Perovskite Methyl Ammonium Lead Iodide. *Sci. Rep.* **2016**, *6* (1).

(46) Saran, R.; Heuer-Jungemann, A.; Kanaras, A. G.; Curry, R. J. Giant Bandgap Renormalization and Exciton–Phonon Scattering in Perovskite Nanocrystals. *Adv. Opt. Mater. 5* (17), 1700231.

(47) Lee, K. C. B.; Siegel, J.; Webb, S. E. D.; Lévêque-Fort, S.; Cole, M. J.; Jones, R.; Dowling, K.; Lever, M. J.; French, P. M. W. Application of the Stretched Exponential Function to Fluorescence Lifetime Imaging. *Biophys. J.* **2001**, *81* (3), 1265–1274.

(48) Milot, R. L.; Eperon, G. E.; Snaith, H. J.; Johnston, M. B.; Herz, L. M. Temperature-Dependent Charge-Carrier Dynamics in $CH_3NH_3PbI_3$ Perovskite Thin Films. *Adv. Funct. Mater.* **2015**, *25* (39), 6218–6227.

(49) Fang, H.-H.; Wang, F.; Adjokatse, S.; Zhao, N.; Even, J.; Antonietta Loi, M. Photoexcitation Dynamics in Solution-Processed Formamidinium Lead Iodide Perovskite Thin Films for Solar Cell Applications. *Light Sci. Appl.* **2016**, *5* (4), e16056.

(50) Wei, K.; Xu, Z.; Chen, R.; Zheng, X.; Cheng, X.; Jiang, T. Temperature-Dependent Excitonic Photoluminescence Excited by Two-Photon Absorption in Perovskite $CsPbBr_3$ Quantum Dots. *Opt. Lett.* **2016**, *41* (16), 3821–3824.

(51) Diroll, B. T.; Nedelcu, G.; Kovalenko, M. V.; Schaller, R. D. High-Temperature Photoluminescence of $CsPbX_3$ (X = Cl, Br, I) Nanocrystals. *Adv. Funct. Mater.* **2017**, *27* (21), 1606750.

(52) Diroll, B. T.; Zhou, H.; Schaller, R. D. Low-Temperature Absorption, Photoluminescence, and Lifetime of $CsPbX_3$ (X = Cl, Br, I) Nanocrystals. *Adv. Funct. Mater.* **2018**, *28* (30), 1800945.

(53) Schmidt, L. C.; Pertegás, A.; González-Carrero, S.; Malinkiewicz, O.; Agouram, S.; Mínguez Espallargas, G.; Bolink, H. J.; Galian, R. E.; Pérez-Prieto, J. Nontemplate Synthesis of $CH_3NH_3PbBr_3$ Perovskite Nanoparticles. *J. Am. Chem. Soc.* **2014**, *136* (3), 850–853.

(54) Chen, X.; Jiang, J.; Yan, F.; Tian, S.; Li, K. A Novel Low Temperature Vapor Phase Hydrolysis Method for the Production of Nano-Structured Silica Materials Using Silicon Tetrachloride. *RSC Adv.* **2014**, *4* (17), 8703–8710.

Chapter Five

5 Improved Photocatalytic Activities and Charge Carrier Dynamics of CdS-based Heterostructures

5.1 Abstract

In recent years, semiconductor photocatalysts has been widely studied as photon absorbers in artificial light driven water splitting for hydrogen evolution reaction (HER). Among them, CdS has attracted extensive attention due to its narrow bandgap for efficient absorption of visible-light and negative potential of its conduction band edge for the reduction of protons. However, Pure CdS has low activity and rapid photo corrosion which makes it unfavorable for hydrogen evolution reaction (HER). In Pure CdS photogenerated electron and hole pairs cannot be efficiently separated and transferred, therefore loading cocatalysts on CdS surface add more functionality or flexibility compared to Pure CdS. These hierarchical structures provide high activation potentials for HER and suppresses the photo corrosion of CdS. Moreover, charge injection from the narrow bandgap to the adjacent material leads to efficient charge separation and prolongs the electron lifetime by the elimination of the charge carrier recombination probability. Here we synthesized 1D CdS nanowires decorated with various nanomaterials including MoS_2 nanosheets, NiS, NiS_2, Ni_3S_2, and $NiCo_2S_4$ nanoparticles on the surface and studied their improved photocatalytic activity. To gain

deeper insight into the mechanism behind the enhanced performance, ultrafast transient absorption (TA) techniques was used to probe the charge carrier dynamics. The results indicated the importance of optimizing molar ratio of the components in the heterostructure to achieve efficient performance.

5.2 Introduction

Among the potential renewable energy resources, hydrogen is highly attractive owing to its highest specific energy of combustion and no production of harmful by-product.[1,2] Hydrogen production by photocatalytic water splitting using solar light is better than traditional electrochemical and thermochemical technologies that require electric or thermal energies.[3–6] To date, good progress has been made in developing visible light-driven semiconductor photocatalysts for H_2 evolution from water splitting, including metal oxides,[7–10] sulfides,[11–17] metal-organic frameworks (MOFs),[18] and carbon nitrides (C_3N_4).[19–21] Among them, CdS is extensively studied due to its absorption of visible light and appropriate band positions for watersplitting.[22,23] However, pristine CdS shows poor photostability and inefficient photogenerated electron-hole pair separation.[24,25] Therefore, it is highly desired to explore strategies to improve the stability and charge carrier separation of CdS. One approach is to construct CdS-based heterojunction or nanocomposite materials.[4,26–28] For example, metal sulfides such as MoS_2 can enhance the photocatalytic activity of CdS in heterojunction systems.[29–34] One dimensional (1D) CdS/MoS_2 core-shell heterostructures exhibited enhanced visible light activity for H_2 production.[30] Similarly, WS_2/CdS nanocomposite

also displayed more effective photocatalytic hydrogen evolution and better photostability than pure CdS nanoparticles.[31] Other transition metal sulfides, such as NiS[33,35]and Ag_2S,[34] have also shown excellent performance as cocatalysts for photocatalytic H_2 evolution. Nonetheless, several problems still exist with these approaches. First, interfacial charge transfer between photocatalyst and cocatalyst is limited by their small contact surface area. Second, charge transport is inefficient due to low conductivity. Third, the Gibbs free energy is not optimal for H_2 evolution. Nickel sulfide (Ni_3S_2), a low-cost and abundance transition metal sulfide, is considered a good substitute for noble metals in hydrogen evolution reactions (HERs) and electrocatalysis. Recently, CNT/Ni_3S_2 hierarchical structures have demonstrated high efficiency photocatalytic H_2 evolution, with ultrathin Ni_3S_2 nanosheets as cocatalyst facilitating the transfer of photogenerated electrons.[36] Ni_3S_2 NWs decorated with CdS NPs have also shown significantly enhanced photocatalytic H_2 evolution with visible light.[12] In section 5.4.1 of this chapter, we discuss fabrication of CdS NWs with Ni_3S_2 NPs to construct Ni_3S_2/CdS nanocomposites through a facile two-step solvothermal technique. The photocatalytic H_2 production activity of the as-prepared catalysts was evaluated utilizing lactic acid as sacrificial reagent in aqueous solution under visible light irradiation ($\lambda \geq 400$nm). All results showed that the binary Ni_3S_2/CdS hybrids displayed much higher photocatalytic H_2 production activity than bare CdS NWs, with optimal H_2 evolution rate of 21.98 mmol $h^{-1}g^{-1}$. Transient absorption (TA) studies revealed that the carrier lifetime in 10%-Ni_3S_2/CdS was about four times shorter than

that of pristine CdS NWs, indicating efficient charge transfer from CdS to Ni_3S_2, consistent with the photocatalytic results.

Molybdenum disulfide (MoS_2), with a layered structure composed of three stacked atom layers (S–Mo–S), has also been extensively investigated as an excellent cocatalyst for facilitating separation of photoinduced carriers and reducing photocorrosion. Li *et al*. first reported that the activity of producing H_2 for 0.2 wt% MoS_2/CdS was enhanced 36 times compared to pristine CdS, which was even higher than 0.2 wt% Pt/CdS under the same reaction conditions.[29,37] Following this work, MoS_2/CdS nanocomposites with different physical dimensions have been constructed and applied to HER.[30,31,38–41] Among them, one-dimension (1D) CdS nanostructures have attracted considerable interests due to their large aspect ratio, high electron mobility and fast electron transport with short radial distances.[30,42] MoS_2 has three phases:1T, 2H and 3R. Among them, metallic 1T-MoS_2 has attracted more attention in improving HER performance, due to the large exposure of edge sites, excellent electronic conductivity and high density of trap states and vacancies. Therefore, coupling 1D CdS with 1T-MoS_2 would seem to be a promising approach to achieve high efficiency for solar H_2 evolution. In part 5.4.2 of this chapter, we discus fabrication of MoS_2/CdS nanocomposite structures with the optimized amount of 1T-MoS_2 for PEC and photocatalytic HER applications. Enhanced PEC activity for HER with optimal amount of 1T-MoS_2 is attributed to improved charge separation and transfer in CdS facilitated by MoS_2.

As another potential material for these heterostructures, nickel sulfide (NiS), a p-type semiconductor, has attracted attention because of its low-cost, good electrical properties, and other unique property such as high electrocatalytic effect toward the polysulfide reaction.[37,38] For example, Zhang *et al.* prepared NiS modified TiO_2 using solvothermal method for the photocatalytic H_2 production with an evolution rate of 0.7 mmol $h^{-1}g^{-1}$.[31] Chen *et al*. also synthesized g-C_3N_4/NiS hybrid photocatalysts through in situ template-free ion-exchange process with H_2 production rate of 0.45 mmol $h^{-1}g^{-1}$.[39] Furthermore, Xu *et al*. found that NiS can be employed as cocatalyst of CdS for photocatalytic water splitting from lactic sacrificial solution via a simple hydrothermal method, and the H_2 evolution rate reached 2.8 mmol h^{-1}.[40] Yu *et al*. developed NiS nanoparticle decorated CdS nanorods photocatalysts using a convenient two-step hydrothermal approach, with an H_2 evolution rate of 1.13 mmol $h^{-1}g^{-1}$.[30] As far as we know, 1D NiS/CdS nanowire composite has yet to be applied to HER. In the meantime, the water-splitting process is inherently unfavorable thermodynamically, and rapid reaction between O_2 and H_2 produced limited hydrogen production. To address this issue, one approach is to put in sacrificial agents to expend the oxygen-derived groups generated, preventing subsequent O_2 production and its reverse reaction with H_2. Besides, the sacrificial agents serve as hole scavengers, increasing the separation efficiency of electrons and holes. One ideal scenario to address these issues is by photo reforming of alcohols in the photocatalytic HER. The photo reforming of alcohols, for example methanol,[42,43] ethanol[44] or glycerol,[45] has been completely investigated over the past decade. These alcohols are classified the first generation of

biofuels, as they are derived from biomass, such as starches, sugars, or vegetable oils. However, the consumption of these substances as a hydrogen precursor prevents their application in food industry. Therefore, the lignocellulosic biomass has been used as second generation of biofuels, since they can be planted in combination with crop or on barren soil. Lignocellulose contains three main biopolymers, that is lignin (15–20%), hemicellulose (25–35%) and cellulose (40–50%).[46] Lignin is the most stubborn of the three components of lignocellulosic biomass. Therefore, if lignin could also serve as sacrificial agents (hole scavengers) to reduce the rate of charge carrier recombination, the photocatalytic method for degradation of lignin can be used in conjunction with the production of hydrogen from water splitting. Nevertheless, this approach has not been extensively investigated previously. In section 5.4.3 of this chapter, we fabricated 1D NiS/CdS nanocomposites using a two-step solvothermal method. The nanocomposite shows obvious enhanced HER activity compared to pure CdS nanowires (NWs). The H_2 evolution rate obtained using the optimized photocatalyst is up to 147.7 μmol $h^{-1}g^{-1}$($\lambda \geq 400$ nm) and the apparent quantum efficiency (AQE) was 44.9% from aqueous solution of lignin and lactic acid. The stronger light absorption and more efficient electron transfer of the nanocomposites are confirmed by UV–vis spectroscopy and the photo-electrochemical properties, which could lead to the enhanced photo-catalytic water splitting ability in comparison with that of pristine CdS. Furthermore, the effect of the NiS loading on charge carrier dynamics has been researched using femtosecond transient absorption (TA) spectroscopy, which offers information about charge separation and transfer from CdS

to NiS. These results also prove that the appropriate amount of NiS can substantially enhance charge carrier separation and transfer, correlating with significant enhancement in the photocurrent density. This work demonstrates the potential of NiS/CdS nanocomposite as an effective photocatalyst for hydrogen evolution utilizing lignocellulosic biomass.

NiS_2 is another type of nanoparticles that has been used as an efficient noble-metal-free cocatalyst to improve the photocatalytic H_2 evolution of $CdLa_2S_4$ [47] and C_3N_4 [48,49] due to its good electrical and optical properties.[50] To our knowledge, there have been no reports of 1D CdS NWs decorated by NiS_2 cocatalyst for improving photocatalytic H_2 evolution. Although photocatalytic water splitting has been demonstrated a few decades ago, it is still a challenge for photocatalysts to efficiently produce hydrogen from pure water without sacrificial agents.[51,52] In most cases, the photocatalytic HER from water is carried out with an excess of sacrificial reagent such as alcohols, sugars and organic acids.[51,53] From a practical and economic point of view, hydrogen production would not involve such valuable chemicals as sacrificial agents. Cellulosic material, as the most abundant component of biomass, is considered as a promising renewable resource for sustainable hydrogen generation. Cellulosic biomass can be converted into hydrogen and other valuable products through several thermochemical processes such as hydrolysis by acids or enzymes. However, because of the rigid intra- and inter-molecular hydrogen bonds in cellulose, the conversion of cellulose to liquid fuels and high value chemicals requires extremely harsh reaction conditions. On the other hand, the separation and purification of the valuable bio-

products from the reaction medium is rather difficult, which is still an issue to be resolved for the practical application. If cellulose could be photocatalytically decomposed into the bio-products, it is possible to obtain hydrogen using generated intermediates as the sacrificial electron donors during the cellulose decomposition process. The hydrogen production assisted by the cellulose decomposition may also be more practical and feasible compared to the photocatalytic water splitting. Only a few researches about the photocatalytic cellulose degradation have been reported, but the degradation of cellulose with the simultaneous generation of hydrogen is limited. In section 5.4.4 of this chapter, using NiS_2 as cocatalyst for boosting the photocatalytic H_2 evolution activity of CdS NWs is reported. The binary NiS_2/CdS nanocomposites with different compositions were successfully prepared by a facile two-step solvothermal method. The photocatalytic H_2 evolution activity of the as-prepared samples was tested using lactic acid as sacrifical agent under visible light. All results indicated that the binary NiS_2/CdS nanocomposites exhibited much better photocatalytic H_2 evolution activity than pure CdS NWs or NiS_2 NPs, with optimal H_2 evolution rate of 14.49 mmol h^{-1} g^{-1}. Photoelectrochemical (PEC) and transient absorption (TA) studies revealed the high efficiency charge transfer from CdS to NiS_2, consistent with the photocatalytic results. Meanwhile, hydrogen generation from cellulose solution was carried out under UV-Vis light irradiation, which demonstrated the potential of NiS_2/CdS nanocomposite as an effective photocatalyst for hydrogen evolution utilizing biomass.

Recently, metallic sulfides, especially Ni-Co sulfide, have been found to exhibit strong electrochemical performance due to their small bandgap energy and high conductivity.[54,55] Moreover, binary Ni-Co sulfide can provide rich redox reactions than single metal sulfides such as NiS and Co_9S_8,[56,57] owing to the combined effect from both the nickel and cobalt ions with different valence states.[35,57–60] For instance, ternary $NiCo_2S_4$ has been applied as an advanced electrode material for high-efficiency supercapacitors and electrocatalysts in water splitting.[61,62] To date, $NiCo_2S_4$ has not been utilized in conjunction with CdS for photocatalysis applications. In section 5.4.5 synthesis of composite structures composed of 1D CdS nanowires (NWs) and $NiCo_2S_4$ nanoparticles (NPs) fabricated in an aqueous phase through a hydrothermal method is discussed. Compared to pristine CdS NWs, the heterostructure composites show improved hydrogen evolution reaction (HER) activity from water splitting with visible-light-driven. The enhancement can be ascribed to the formation of the Schottky junction that enhanced the separation and transfer of photoinduced charge carriers. In addition, the composites show good stability with the use appropriate hole scavengers.

5.3 Experimental

5.3.1 CdS Nanowires Synthesis

In a typical process, cadmium diethyldithiocarbamate ($Cd(S_2CNEt_2)_2$), prepared by sediment from a stoichiometric precursor mixture of cadmium chloride (0.01 mol) and sodium diethyldithiocarbamate trihydrate (0.01 mol) in 50 mL of deionized water, was transferred to a Teflon-lined stainless steel autoclave with. Then,

the autoclave was filled with 40 mL of ethylenediamine. The autoclave was heated at 180 °C for 24 h and then cooled down to room temperature. The pale yellow sediment was collected and washed several times with absolute ethanol and deionized water. The final products were dried in a vacuum oven at 60 °C for 12 h.

5.3.2 Nanocomposites Synthesis

The Ni_3S_2/CdS nanocomposites were synthesized using a typical solvothermal method. Briefly, a certain amount of the as-prepared CdS NWs (1.445 g) were suspended in 30 mL absolute alcohol and stirred vigorously for 30 min. Then a known amount of $NiCl_6 \cdot 6H_2O$ and CH_4N_2S were dissolved in the above prepared suspension under strong magnetic agitation. After stirring for another 30 min, it was transferred into a Teflon-lined autoclave with 50 mL capacity followed by solvothermal treatment at 180°C for 12 h. After cooling down to room temperature naturally, the obtained precipitate was filtered via centrifugation, rinsed using alcohol and deionized water for several times, respectively, and then dried in vacuum at 60°C overnight. The prepared photocatalysts with different contents of Ni_3S_2 on CdS NWs were abbreviated as *x*%-Ni_3S_2/CdS (*x* was the molar ratio of Ni_3S_2 to CdS NWs), and *x* was referred as 5, 10, 20 and 30, respectively.

For the MoS_2/CdS nanocomposites, a certain amount of thioacetamide (C_2H_5NS) and sodium molybdate ($Na_2MoO_4 \cdot 2H_2O$) (the molar ratio of S and Mo is 2.0) were dissolved into 36 mL of deionized water and stirred until the transparent solution was formed. Then, 0.72 g of as-prepared CdS NWs was added into the above

transparent solution. The theoretical molar ratio of MoS2 and CdS (1.0, 2.0, 5.0, 10.0, 15.0 and 20.0) was varied by adjusting the MoS_2 amount.

The 1D NiS/CdS nanocomposites were also assembled by a similar template-free and mild two-step solvothermal method. The molar ratio of NiS and CdS was varied (0.1, 0.2, 0.4, 0.6, 0.8 and 1.0) by adjusting the CdS amount.

For synthesizing NiS_2/CdS Nanocomposites, a certain amount of $Ni(NO_3)_2 \cdot 6H_2O$ and $Na_2S_2O_3$ were dissolved in the CdS suspension under further magnetic agitation. Then, 20 mL ethylene glycol [$(CH_2OH)_2$] and 1.2 mL 0.5 $mol \cdot L^{-1}$ oxalic acid ($H_2C_2O_4$) solution were slowly added into the above mixture. After stirred for another 0.5 h, it was transferred into a Teflon-lined autoclave with 50 mL capacity followed by solvothermal treatment at 180 °C for 12 h. The prepared samples with different contents of NiS_2 on CdS NWs were abbreviated as *x* %NiS_2/CdS (*x* was the molar ratio of NiS_2 to CdS NWs), and *x* was referred as 5, 10, 20, 40, 60, 80 and 100, respectively.

Fabrication of $NiCo_2S_4$/CdS nanowires with different molar addition ratios of $NiCo_2S_4$ NPs. Specifically, a certain amount of the CdS NWs (1.445 g) was sonicated thoroughly in 30 mL DI water for 5 min and then continuously stirred for 15 min. Next, a given amount of $NiCl_6 \cdot 6H_2O$, $CoCl_6 \cdot 6H_2O$, thiourea (TU), and 8ml of $NH_3 \cdot H_2O$ were added into the CdS NWs dispersion under vigorous stirring for 20 min. Then, the mixture was transferred into a 50 mL stainless steel autoclave with a Teflon liner and kept at 180 °C for 12 h. The obtained precipitates were collected, washed thoroughly with deionized water and ethanol, and finally dried in an oven at 60 °C overnight. The

precipitates of CdS NWs–$NiCo_2S_4$ NPs composites with different molar addition ratios of $NiCo_2S_4$ NPs were obtained. The specific molar addition ratios of $NiCo_2S_4$ NPs in the CdS NWs–$NiCo_2S_4$ NPs composites were respectively controlled to be 0.05, 0.1, 0.2 and 0.3, denoted as 5%-$NiCo_2S_4$/CdS, 10%-$NiCo_2S_4$/CdS, 20%-$NiCo_2S_4$/CdS, 30%-$NiCo_2S_4$/CdS.

5.3.3 Ultrafast Transient Absorption Spectroscopy

The femtosecond transient absorption (TA) measurements were carried out using a Quantronix laser system as described previously.[44] The system consists of an Er-doped fiber oscillator, regenerative amplifier and diode-pumped Nd: YLF pump laser (527 nm). The seed beam after amplification splits to a white light continuum probe pulse (450−750 nm) and feed an optical parametric amplifier with 1:9 ratio, respectively. The output of optical parametric amplifier was tuned to 390 nm and used to excite the samples, which were prepared as thin films using spin coating technique, with various pulse energies (750, 323 and 190 nJ per pulse) to study power dependence. After overlapping pump and probe on the sample spatially and temporally, the TA data was collected using a charge-coupled device (CCD) detector over a temporal delay interval of 0–1000 ps between the pump and probe pulses.

5.4 Results and Discussion

5.4.1 Ni_3S_2/CdS Nanocomposites

5.4.1.1 Photocatalytic Activity and Transient Absorption Study of Ni_3S_2/CdS Nanocomposites

The photocatalytic H_2 production of CdS NWs and Ni_3S_2/CdS nanocomposites was evaluated under visible-light irradiation ($\lambda \geq 400$ nm) with 2 vol% lactic acid as sacrificial reagent. H_2 production over the Ni_3S_2/CdS nanocomposites with different Ni_3S_2 content showed an obvious increase in the whole photocatalytic reaction process.[63] All the Ni_3S_2/CdS nanocomposites exhibited much higher rates of H_2 production than that of pure CdS NWs, indicating the Ni_3S_2 NPs loading facilitates H_2 production. However, the H_2 production rates of Ni_3S_2/CdS nanocomposites first increases and then decreases with increasing Ni_3S_2 loading. The optimal molar ratio of Ni_3S_2 and CdS for Ni_3S_2/CdS nanocomposites was determined to be about 10 mol%, which shows the highest H_2 evolution rate of 22.0 mmol h^{-1} g^{-1}, much higher than that of pure CdS NWs (0.03 mmol h^{-1} g^{-1}).[63] These results demonstrated that loading suitable amount of Ni_3S_2 NPs on the surface of CdS NWs could increase the visible light absorption and facilitate charge separation, thus accelerating H_2 evolution.

Ultrafast TA measurements were used to probe the charge carrier dynamics and gain deeper insight into the origin of improved photocatalytic performance. Three samples, including pure CdS NWs, 10%-Ni_3S_2/CdS nanocomposites, and 30%-Ni_3S_2/CdS nanocomposites, were deposited on a glass substrate using spin coating. The prepared films were excited with 400 nm pump pulses at different pulse energies (615, 310, 170 nJ/pulse) to investigate the excitation energy dependence of the dynamics due to possible non-linear processes such as exciton-exciton annihilation and Auger

recombination. Here we present data in the linear regime to avoid complication due to non-linear processes. Hence, data collected with 615 nJ/pulse excitation energy were used to compare the samples due to their large signal to noise ratio (S/N). The 3D TA data are shown in Fig 1(a-c) as a function of probe wavelength and time delay between pump and probe pulses.

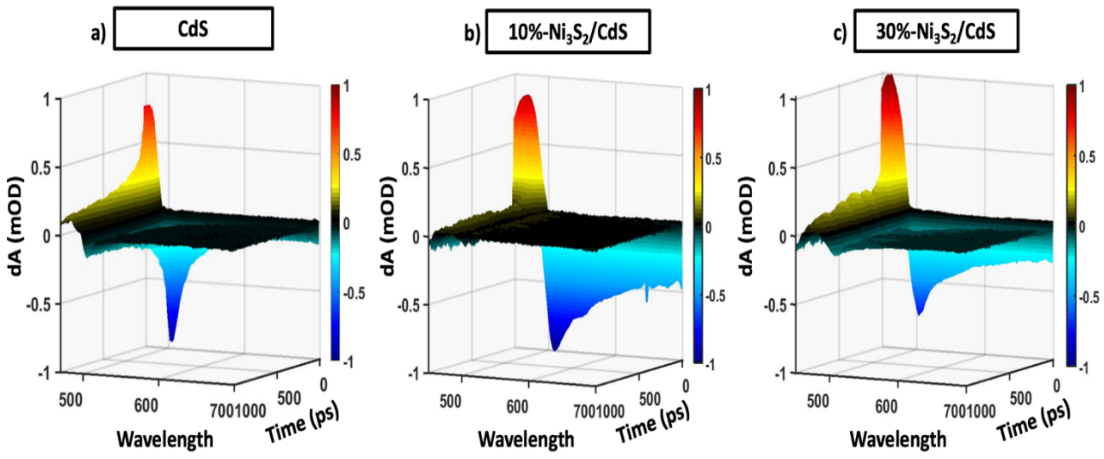

Figure 5-1- 3D representation of transient absorption (TA) and transient bleach (TB) profile of a) CdS NWs, b) 10%-Ni_3S_2/CdS nanocomposites, and c) 30%-Ni_3S_2/CdS nanocomposites, excited at 400 nm with pulse energy of 615 nJ/pulse

As shown in Fig. 1, each of these samples exhibits a TA signal leaked at 475 nm attributed to absorption of excited state electrons in CdS NWs and a broad transient bleach (TB) signal from 500 nm to 700 nm, attributed to depletion of ground state electrons in CdS NWs as reported previously.[33,64] With deposition of Ni_3S_2 NPs to the surface of CdS NWs, the TA/TB peaks positions did not change, as the amount added is small. Analyzing the decay of these signals, attributed primarily to electron and hole

recombination, provides information about the charge carrier dynamic and charge transfer from CdS to Ni_3S_2.

Fig. 2 shows the single wavelength decay traces of TA signal for CdS NWs, 10%-Ni_3S_2/CdS, and 30%-Ni_3S_2/CdS nanocomposites. There is a significant difference among these samples in their decay dynamics and corresponding lifetimes. The decays are fitted using a double exponential function and the fitting parameters are reported in Table 1.

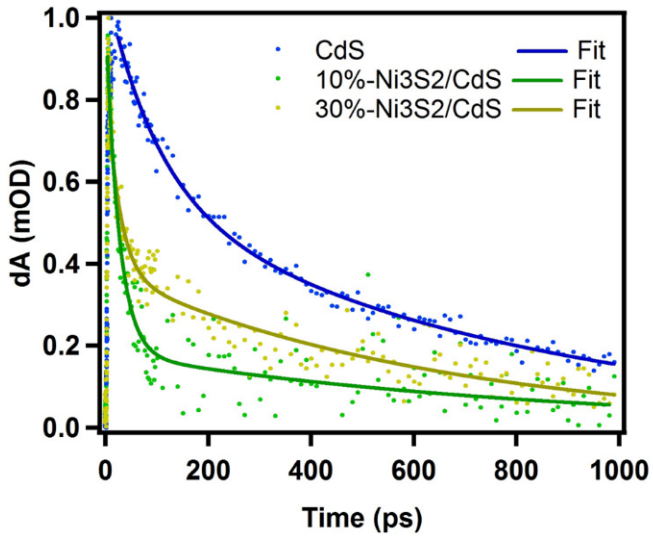

Figure 5-2- Normalized TA decay profile of CdS NWs (blue), 10%-Ni_3S_2/CdS (green), and 30%-Ni_3S_2/CdS (yellow) nanocomposites. The TA decay over time was fitted using double exponential function.

Table 5-1- Fitting parameters of TA signal recovery of CdS NWs, 10%-Ni_3S_2/CdS nanocomposites, and 30%-Ni_3S_2/CdS nanocomposites fitted with double exponential function.

Sample	A_1	τ_1	A_2	τ_2 (ps)	Y	Average τ (ps)
CdS	0.45 ± 0.017	99 ± 8.6	0.54 ± 0.018	751 ± 42	0 ± 0	686
10%-Ni_3S_2/CdS	0.82 ± 0.021	15 ± 1.2	0.17 ± 0.012	237 ± 51	0 ± 0	185
30%-Ni_3S_2/CdS	0.56 ± 0.043	25 ± 3.7	0.43 ± 0.031	490 ± 44	0 ± 0	461

Based on the fitting parameters on Table 1, each sample has two decay time constants. In the case of pure CdS, the excitons generated after photoexcitation can recombine through multiple possible pathways. Some of the excitons recombine through shallow and deep trap states via trap state-mediated recombination. Since this process usually happens on the tens of ps timescale, the faster time component of the decay is attributed to recombination mediated by trap states.[44] The longer time constant observed in the TA signal decay is attributed to recombination between the conduction band (CB) electron and valence band (VB) hole.[65] To help extract the charge transfer rate from CdS to Ni_3S_2, we calculate the average lifetime as follows.

$$\tau_{ave} = \frac{A_1\tau_1^2 + A_2\tau_2^2}{A_1\tau_1 + A_2\tau_2} \quad (1)$$

The average lifetime (τ_{ave}) for the pure CdS NWs is calculated to be 686 ps. However, by addition of 10% Ni_3S_2, τ_{ave} significantly decreased to 185 ps. This decrease in lifetime is attributed to electron transfer from the CB of CdS to Ni_3S_2.[66,67] Assuming

the electron in Ni_3S_2 has no or weaker absorption of the probe light than in CdS, the electron transfer from CdS to Ni_3S_2 would result in shorter lifetime, as observed. On the other hand, in a similar study, using Pt as cocatalyst on the surface of CdS nanorods, it has been shown that photoexcited holes can be delocalized to the surface of CdS. Therefore, the close proximity between the delocalized holes and electrons transferred to Pt NPs results in a faster recombination rate and shorter lifetime.[67] Due to resemblance between the Pt/CdS system and Ni_3S_2/CdS nanocomposites studied here, the shorter lifetime observed may be due to a similar reason, i.e. delocalization of photogenerated hole to the surface of CdS and thereby faster recombination with the electron transferred to Ni_3S_2. While this shorter lifetime might seem to contradict the higher photocatalytic efficiency observed for this 10%-Ni_3S_2/CdS nanocomposites, it should be noted that in the photocatalytic H_2 evolution measurements, lactic acid was present in the solution as a hole scavenger which reduces electron-hole recombination. No hole scavenger was present in the TA measurements, so one may not be able to directly correlate the two experimental results.

Further increasing the amount of Ni_3S_2 in 30%-Ni_3S_2/CdS resulted in a lifetime of 461 ps, which is longer than 185 ps in 10%-Ni_3S_2/CdS. As shown in TEM images, addition of 10% Ni_3S_2 resulted in formation of a thin and uniform layer of Ni_3S_2 on CdS NWs. This uniform layer provides intimate contact and an efficient interaction at the interface that can promote charge transfer from CdS NWs to Ni_3S_2 NPs. However, by further increasing the amount of Ni_3S_2 to 30%, the Ni_3S_2 NPs grow as flocculant structures

that actually lead to reduced surface coverage or interaction with CdS, and thereby slower charge transfer.

Further increasing the amount of Ni_3S_2 in 30%-Ni_3S_2/CdS resulted in a lifetime of 461 ps, which is longer than 185 ps in 10%-Ni_3S_2/CdS. As shown in TEM images[63], addition of 10% Ni_3S_2 resulted in formation of a thin and uniform layer of Ni_3S_2 on CdS NWs. This uniform layer provides intimate contact and an efficient interaction at the interface that can promote charge transfer from CdS NWs to Ni_3S_2 NPs. However, by further increasing the amount of Ni_3S_2 to 30%, the Ni_3S_2 NPs grow as flocculant structures that actually lead to reduced surface coverage or interaction with CdS, and thereby slower charge transfer. The electron transfer rate constant (k_{ET}) from CdS NWs to Ni_3S_2 NPs can be calculated using the following equation:

$$k_{ET} = \frac{1}{\tau_{ave}(Ni_3S_2/CdS)} - \frac{1}{\tau_{ave}(CdS)} \qquad (2)$$

The k_{ET} calculated to be 3.9×10^9 s^{-1} and 7.1×10^8 s^{-1} for 10%-Ni_3S_2/CdS and 30%-Ni_3S_2/CdS nanocomposites, respectively. This smaller electron transfer rate for 30%-Ni_3S_2/CdS is consistent with decreased photocatalytic activity of the 30%-Ni_3S_2/CdS nanocomposites compared to 10%-Ni_3S_2/CdS with larger k_{ET}. This suggests the importance of optimizing the amount of cocatalyst (Ni_3S_2) on the CdS surface for achieving efficient photocatalytic activity in the material.

5.4.1.2 Photocatalytic mechanism of Ni_3S_2/CdS nanocomposites

We propose a possible HER mechanism for photocatalytic H_2 production and interfacial charge transfer in Ni_3S_2/CdS nanocomposites under illumination of visible light, as illustrated in Fig. 10. In this system, CdS is the primary light absorber, and upon photoexcitation, photoinduced electrons are generated in the valence band (VB) and holes in the conduction band (CB). These photogenerated charge carriers can go through multiple pathways, including shallow and deep trap states or direct recombination.[66] Only a small fraction of photogenerated electrons can participate in photocatalytic reaction and reduce H^+ ions to H_2, due to the fast recombination of photoinduced electron and hole pairs in pure CdS NWs, leading to low H_2 production.

The addition of Ni_3S_2 NPs to the surface of CdS NWs can significantly improve the H_2 production. The major photocatalytic HER process on Ni_3S_2/CdS nanocomposites are summarized in Eqs. (3-6). Followed by absorbing the photons, CdS NWs generate electron and hole pairs (Eq. 3). By loading Ni_3S_2 NPs on the CdS NWs, the photogenerated electrons in the CB of CdS NWs can be transferred to Ni_3S_2 NPs. This electron transfer is also thermodynamically favorable due to the appropriate work function of Ni_3S_2 with respect to CB of CdS. The charge carrier dynamics study using TA spectroscopy also confirmed this efficient transfer as manifested in significantly shorter lifetime in Ni_3S_2/CdS nanocomposites compared to pure CdS NWs. The Ni_3S_2 NPs serve as a capture site of electrons generated in CdS and effectively improve the separation of photoexcited electron-hole pairs. At the same time, lactic acid in the solution acts as a sacrificial reagent, being oxidized by holes (hole scavenger), to

further prevent electron-hole recombination and improves the chance for electrons to participate in the photocatalytic H_2 evolution reaction on the surface of Ni_3S_2 NPs. In acid solutions, three principal reactions are assumed to predominate when H_2 is evolved, showed as Eqs. (3-6).[68]

$$CdS + h\nu \rightarrow CdS\,(e^- + h^+) \quad (3)$$

$$Ni_3S_2 + e^- + H_3O^+ \rightarrow Ni_3S_2 - H_{ads} + H_2O \quad (4)$$

$$Ni_3S_2 - H_{ads} + e^- + H_3O^+ \rightarrow Ni_3S_2 + H_2 + H_2O \quad (5)$$

$$Ni_3S_2 - H_{ads} + Ni_3S_2 - H_{ads} \rightarrow 2Ni_3S_2 + H_2 + H_2O \quad (6)$$

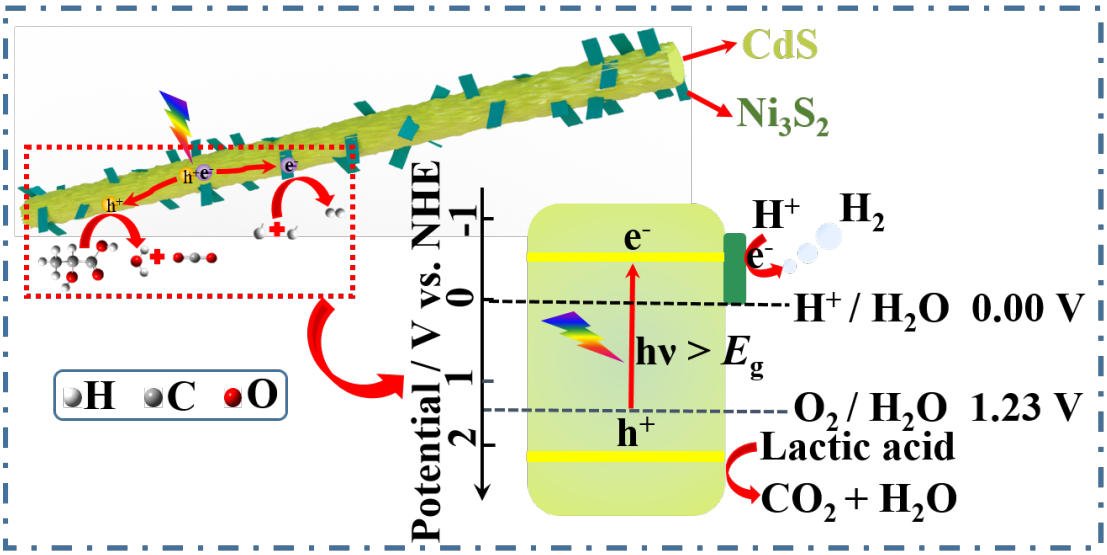

Figure 5-3- Proposed mechanism for photocatalytic H2 production and charge transfer for the photocatalysts of Ni_3S_2/CdS nanocomposites under visible light irradiation.

5.4.2 MoS_2/CdS Nanocomposites

5.4.2.1 Photocatalytic Activity and Transient Absorption Study of MoS_2/CdS Nanocomposites

Photocatalytic hydrogen evolution over CdS, MoS_2 and MoS_2/CdS nanocomposites were evaluated under visible light irradiation ($\lambda \geq 400$ nm) in aqueous solution containing glucose and lactic acid or lactic acid alone as hole scavengers. Pure CdS showed a very low photocatalytic activity during the reaction process, which is attributed to fast recombination of photogenerated charge carriers and less active sites in CdS NWs. Loading MoS_2 on the surface of CdS NWs significantly enhances the average rates of H_2 evolution. When the theoretical molar ratio of MoS_2 and CdS is 5%, the H_2 production rate reaches an optimal value, which is approximately 86.3 or 56.7 times higher than that of pure CdS NWs using glucose and lactic acid or lactic acid as sacrificial agent, respectively. However, further increasing amount of MoS_2 in the nanocomposites leads to a decrease of H_2 evolution activity, which may be attributed to excessive MoS_2 that competes with CdS for light absorption.

Ultrafast TA spectroscopy was used to study the charge carrier separation and transfer through the system. CdS NWs, 5%-MoS_2/CdS and 20%-MoS_2/CdS were excited with 390 nm pump laser pulses. Fig. 4(a–c) show 3D and 2D representation of TA data as a function of probe wavelength and delay time between pump and probe pulses.

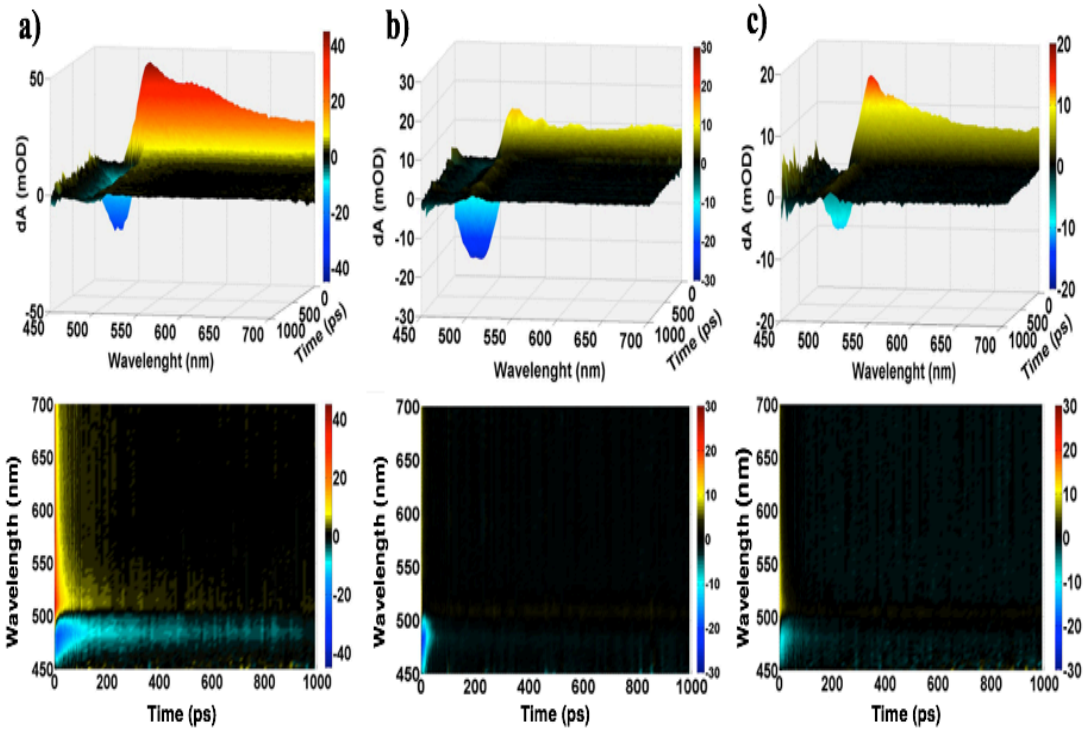

Figure 5-4- 3D(top) and 2D(bottom) representation of the transient absorption of a) CdS nanowires; b) 5%-MoS2/CdS; c) 20%-MoS2/CdS excited with 390 nm pump (750 nJ/pulse)

As it is shown in Fig. 4, a transient bleach (TB) feature at 480 nm and a broad TA feature from 500 to 700 nm was observed for CdS nanowires. As reported previously the transient bleach signal can be attributed to absorption of photogenerated carriers.[69,70] No significant difference was observed in spectral profile of CdS upon addition of MoS_2 even at 20%; however, the charge carrier lifetime changed dramatically. Analyzing the decay of transient bleach/absorption signal can provide useful information about charge carrier dynamic of CdS with MoS_2 addition. However, some non-linear dynamic processes such as exciton-exciton annihilation or Auger recombination can interfere with data interpretation. Three pulse energies (750, 323

and 190 nJ per pulse) were used to study power-dependent dynamics of the nanocomposites. Because no power dependence was observed in the sample's dynamics, we analyzed the data with the highest signal to noise ratio at 750 nJ per pulse. Fig. 5 (a–c) show the normalized single wavelength TB (480 nm) and TA (510 nm) signal of CdS nanowires, 5%-MoS_2/CdS and 20%-MoS_2/CdS nanocomposites, respectively, from 0 to 1,000 ps. For better comparison, transient bleach signal of all 3 samples were plotted together in Fig. 5d. The recovery of signals was fit with double exponential function and the fitting parameters are reported in Table 2.

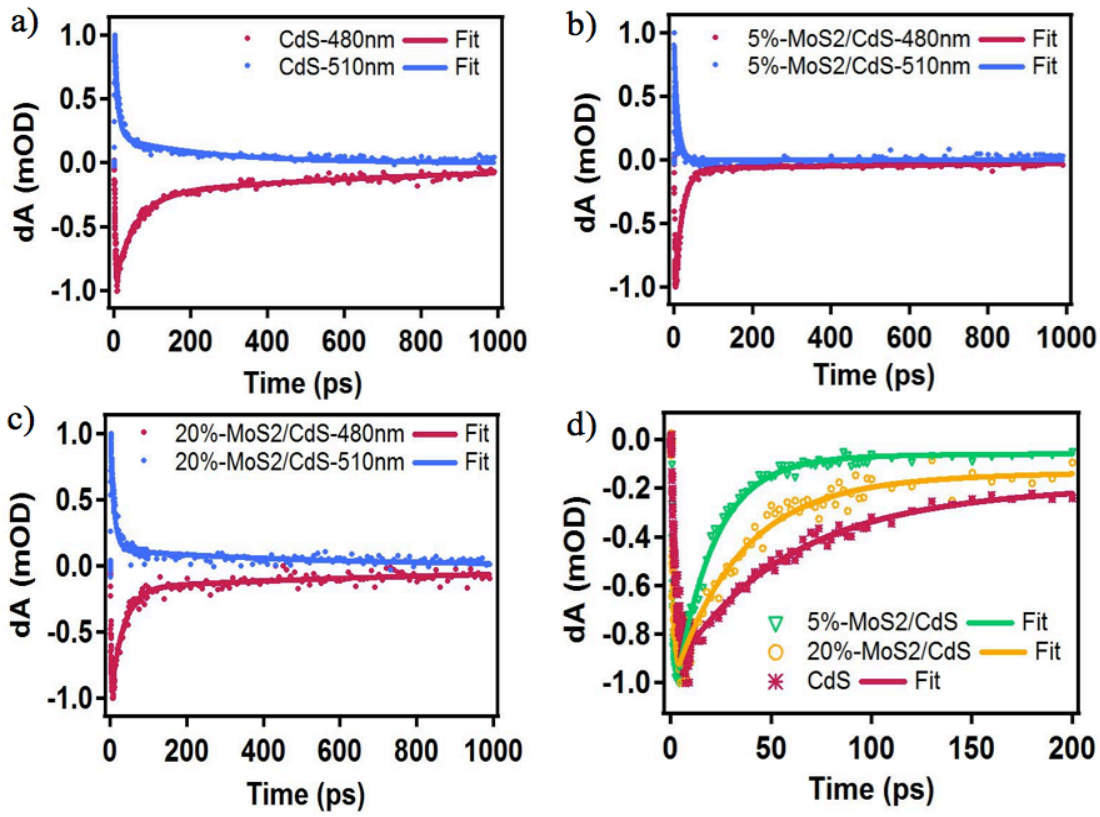

Figure 5-5- Normalized ultrafast transient bleach/absorption decay profile of a) CdS nanowire b) 5%-MoS2/CdS c)20%-MoS2/CdS and d) transient bleach recovery of all 3 samples. The decay profiles are fitted using a double exponential function.

Table 5-2- Fitting parameters of transient bleach recovery of CdS, 5%-MoS2/CdS and 20%-MoS2/CdS fitted with double exponential function and calculated average lifetime <τ>.

Sample	A	τ_1 (ps)	B	τ_2 (ps)	$<\tau>$	Y
CdS	-0.25 ± 0.01	52.86 ± 2.66	-0.71 ± 0.01	853 ± 89	837	0 ± 0
5%-MoS2/CdS	-0.95 ± 0.01	20.04 ± 0.68	0.06 ± 0	125 ± 14	50	0 ± 0
20%-MoS2/CdS	-0.86 ± 0.01	32.62 ± 1.85	-0.17 ± 0.01	360 ± 27	257	0 ± 0

The average recovery lifetime of CdS nanowires, 5%- MoS_2/CdS and 20%-MoS_2/CdS are calculated to be 837 ps, 50 ps and 257 ps respectively, using Equation 1. As demonstrated in Fig. 5d and average lifetimes, there is significant difference in charge carrier dynamic of CdS in the presence of MoS_2 on the surface. Decorating 5% MoS_2 on CdS nanowire shortened the average life time of CdS by factor of approximately 17, attributed to efficient electron transfer from CdS to MoS_2.[71] This fast electron transfer will prevent undesirable recombination of electron-hole, promote better charge separation and improve the catalytic activity of nanocomposite for the HER reaction. One may expect that higher concentration of MoS_2 on CdS surface should shorten the charge carrier lifetime and improve the charge carrier separation even further. However, upon further addition of MoS_2 to 20%, the average lifetime now increased by factor of 5, compared to 5%-MoS_2/CdS, while the photocatalytic activity also decreased at the same time. SEM images of the MoS_2/CdS nanocomposites at

different ratios may help to explain this behavior. As shown in TEM images[64], a thin and uniform layer of MoS_2 was coated on the surface of CdS nanowires at 5% molar ratio, providing intimate contact for charge transfer at the heterointerface. However, by increasing the MoS_2 concentration up to 20%, the growth of flocculent structures may lead to reduced surface contact and charge transfer.

5.4.2.2 Schematic mechanism for enhanced photocatalytic H_2 evolution activity of MoS_2/CdS nanocomposites

A possible mechanism for enhanced photocatalytic H_2 evolution from water using MoS_2/CdS nanocomposites is proposed as shown in Fig. 6. Under visible light irradiation, electron-hole pairs generated in CdS NWs are quickly recombined, leading to low photoactivity. For MoS_2/CdS nanocomposite, the photogenerated electrons in the conduction band (CB) of CdS can be transferred to MoS_2 due to the lower energy level of MoS_2 than the CB edge of CdS. Importantly, the large and intimate interfacial contact between CdS and MoS2 should facilitate the electron transfer from CdS to MoS_2. The electrons transferred to MoS_2 react with H_2O to generate H_2 ($2H_2O + 2e^- \rightarrow H_2 + 2OH^-$). Meanwhile, the photoinduced holes in the VB of CdS can oxidize hole sacrificial agents, as described by the pathway I/II in Fig. 6. When the lactic acid is used as only hole scavenger, the reaction products are CO_2 and H_2O (pathway I). When glucose and lactic acid are used as sacrificial agents together, the photogenerated holes in CdS can react with OH^-, producing $OH^{\bullet}$ radicals. The $OH^{\bullet}$ radicals then react rapidly with glucose, which leads to the formation of carboxylic acid (H−COOH) and finally

CO_2 and H^+.[72] In this process, the $OH^{\bullet}$ radicals are consumed, and protons are produced simultaneously, resulting in a higher H_2 production (pathway II).[73,74] The overall reaction of oxidation could be depicted by $C_6H_{12}O_6 + 6H_2O \rightarrow 6CO_2\uparrow + 12H_2\uparrow$.

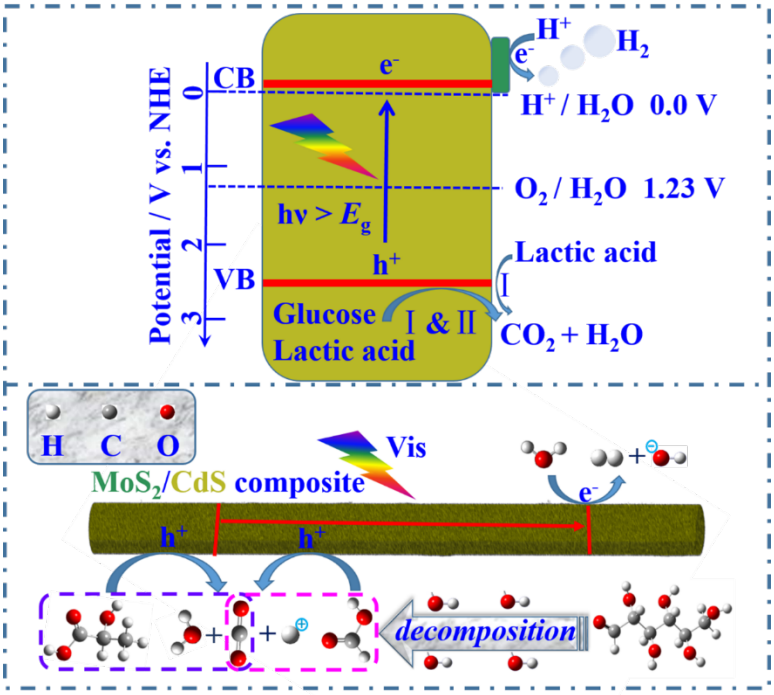

Figure 5-6- Scheme for the photocatalytic hydrogen production over MoS2/CdS nanocomposites under visible light.

5.4.3 NiS/CdS Nanocomposites

5.4.3.1 Photocatalytic Activity and Transient Absorption Study of NiS/CdS Nanocomposites

Photocatalytic hydrogen production over pure CdS NWs and NiS/ CdS nanocomposites were evaluated under visible light irradiation using mixed solution containing lactic acid alone or lignin and lactic acid as hole scavenger. Pure CdS NWs showed a relatively negative photocatalytic activity during the reaction process, which is attributed to rapid recombination of photoinduced charge carriers and small number of active sites in CdS NWs. Loading NiS on the surface of CdS significantly enhanced the average rates of H_2 production. Notably, when the molar ratio of NiS and CdS is 0.2, the H_2 production rate obtains an optimal value, which is approximately 5041 or 31 times than that of CdS NWs in lignin and lactic acid or lactic acid aqueous solution, respectively. However, further increasing the amount of NiS in the nanocomposites led to a yield decrease of H_2 production, which may derive from the masking effect of NiS where the facilitated light absorption of NiS reduced the light absorption of CdS.[53,75].

To obtain further insight on charge carrier separation and transfer processes of the NiS/CdS nanocomposites, ultrafast transient absorption (TA) spectroscopy was used to explore the charge carrier dynamics in CdS NWs and their dependence on the NiS content. Fig. 7(a–c) shows the TA data of pure CdS, 0.2-NiS/CdS and 1.0-NiS/CdS, excited with 390 nm pump laser pulses, as a function of probe wavelength and delay time between the pump and probe pulses. The spectral profile of pure CdS and the CdS/NiS nanocomposites are mostly similar, which is due to small amount of NiS in the nanocomposite compared to CdS. The TA feature observed at 460–500 nm can be ascribed to absorption of photogenerated electrons in conduction band (CB) of CdS. The strong and broad transient bleach (TB) feature spanned from 500 to 750 nm

can also be ascribed to hole absorption in the valence band (VB) of CdS as reported before.[44] The decay observed in the TB signal is ascribed to electron and hole recombination. Analyzing the decay of TB signal can provide useful insight about the behavior of the CdS with or without the NiS decorated on the surface. However, some high-order kinetic processes for instance exciton-exciton annihilation or Auger recombination can happen and interfere with correct interpretation of the data.[69,76] In order to refrain these non-linear dynamic processes, we performed pump power dependence study (750, 323 and 190 nJ/pulse) and observed slight power dependence in earlier recombination time with high pump energy (750 nJ/pulse). Because of the power dependence at high pump power, we chose to analyze data with pump energy of 323 nJ/pulse for comparing these three samples, which do not involve non-linear effect and have good signal to noise (S/N) ratio.

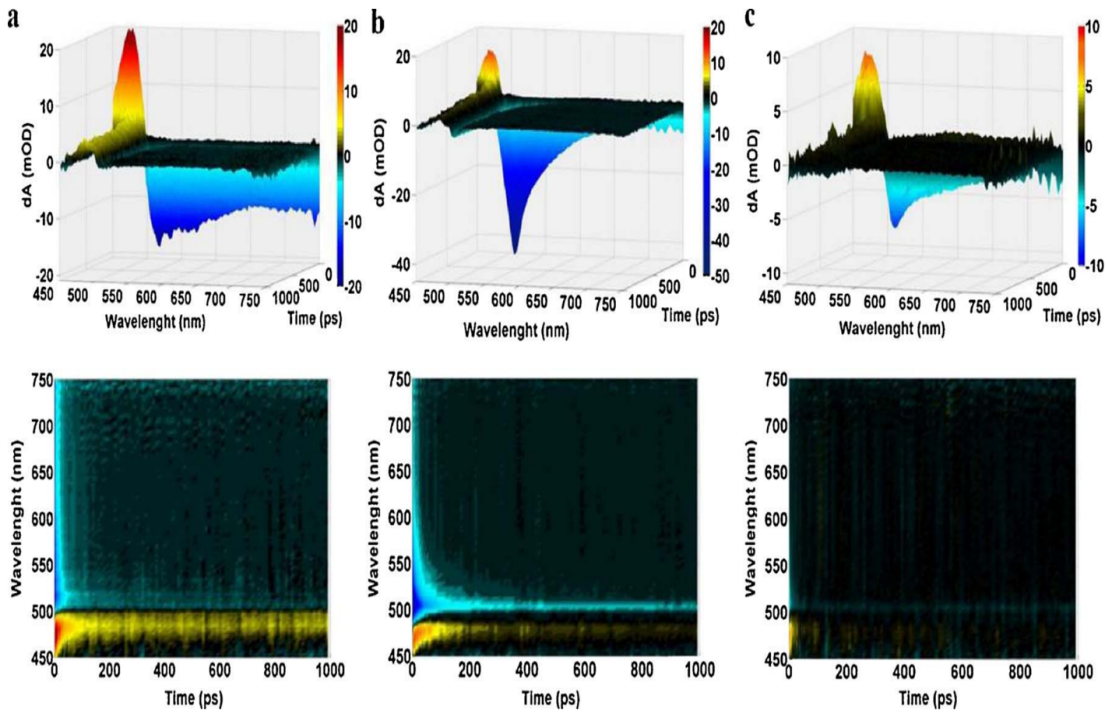

Figure 5-7- 3 and 2-dimensional representation of the TA of a) CdS nanowires; b) 0.2-NiS/CdS; c) 1.0-NiS/CdS after excitation with 390 nm pump (323 nJ/pulse).

Fig. 8 shows the normalized, single wavelength ultrafast TB signals of CdS, 0.2-NiS/CdS and 1.0-NiS/CdS nanocomposites on the 0-1000 and 0-100 ps time scales. The TB signal recovery was fit with double exponential function and the fitting variables are reported in Table 3.

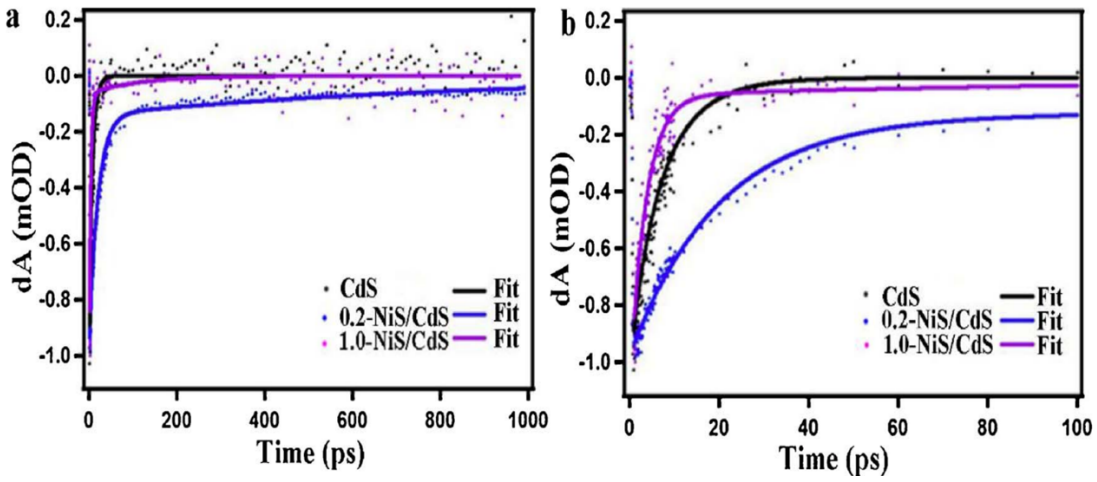

Figure 5-8- Normalized ultrafast transient bleach decay profile of CdS nanowire (black), 0.2-NiS/CdS (blue) and 1.0-NiS/CdS (purple). The decay profiles are fitted using a double exponential function.

Table 5-3- Fitting parameters of transient bleach recovery of CdS, 0.2-NiS/CdS and 1.0-NiS/CdS fitted with double exponential function and calculated average lifetime (τ).

Sample	A_1	τ_1 (ps)	A_2	τ_2 (ps)	Average τ (ps)
CdS	0.72	8.8 ± 0.4	0.28	3.6 ± 0.1	8
0.2-NiS/CdS	0.83	20.0 ± 0.1	0.14	879 ± 17	776
1.0-NiS/CdS	0.94	3.5 ± 0.1	0.05	117 ± 9	76

Based on the resultant time constants, the recovery lifetime for CdS nanowires are 8.8 ± 0.4 ps and 3.6 ± 0.1 ps, for 0.2-NiS/CdS are 20 ± 1 ps and 879 ± 17 ps and for 1.0-NiS/CdS are 3.5 ± 0.1 ps and 117 ± 9 ps. According to previous studies, usually the fast time component of the decay is attributed to exciton relaxation due to presence of shallow trap states in semiconductor materials while the slower component is due to charge carrier recombination mediated by deeper traps.[65] The average charge carrier lifetime of the samples also calculated using equation 1 for better comparison. The average lifetime calculated to be 8 ps, 776 ps and 76 ps for CdS, 0.2-NiS/CdS and 1.0-

NiS/CdS, respectively. Based on these results, the overall charge carrier recombination is faster in CdS nanowires than 1.0-NiS/CdS and 0.2-NiS/CdS nanocomposites, respectively (CdS < 1.0-NiS/CdS < 0.2-NiS/CdS), which is in agreement with the performance of the material for HER. Longer charge carrier lifetime is expected to lead to better performance of the photocatalyst as the charge carriers are more likely to participate in redox reactions rather than recombining. However, increasing the molar ratio of NiS from 0.2 to 1.0 caused faster recombination in earlier time regime. From the structural characterizations such as TEM images,[33] we know that higher ratio of NiS will form aggregations on the surface of CdS NWs. Therefore, this earlier fast recombination in the 1.0-NiS/CdS nanocomposite is possibly due to charge carrier trapping by the NiS aggregates. The dynamics results seem to indicate that NiS presence on CdS NWs can improve the charge separation. However, there is an optimal ratio for efficient separation (0.2-NiS/CdS) and beyond that point, NiS aggregates will cause faster recombination and thereby poorer photocatalytic performance of the NiS/CdS nanocomposites.

5.4.3.2 Mechanism for the photocatalytic hydrogen evolution

Based on all the above discussion, a model is putted forward to explain the mechanism of the overall HER reactions, as shown in Fig. 9. Electrons and holes are first generated in CdS when it is excited with light ($\lambda \geq 400$ nm). Although the CB edge of CdS is more negative than the reduction potential of H^+/H_2, the rate of hydrogen evolution is low over pure CdS because of the fast recombination of photoinduced

charge carriers. When NiS nanoparticles are loaded on the surface of CdS, due to the less negative CB of NiS than that of CdS, the photogenerated electrons in the CB of CdS can be transferred to NiS nanoparticles. More importantly, the intimate interfacial junction between NiS and CdS plays an essential role in facilitating electron transmit from CdS to NiS. The NiS also acts as active sites because unsaturated sulfide ions of NiS possess strong affinity for H^+ in the solution and can thus enhance the photocatalytic performance. The photoinduced holes in the VB of CdS can oxidize hole scavengers, described by the pathway I/II in Fig. 9. When only the lactic acid acts as sacrificial agent, the holes can be just consumed by the one substance (pathway I). While taking the lignin as an additional hole scavenger, it will produce methanol, ethanol, formaldehyde, formic acid and oxalic acid during the HER process, which provides an extra pathway for reaction of the holes (pathway II). The fast consumption of the holes can greatly inhibit recombination of the electron and hole, thereby suppressing the photocorrosion of CdS and enhancing the H_2 evolution rate. The results suggest that reaction of the hole is a rate limiting step in the overall photocatalytic reactions.

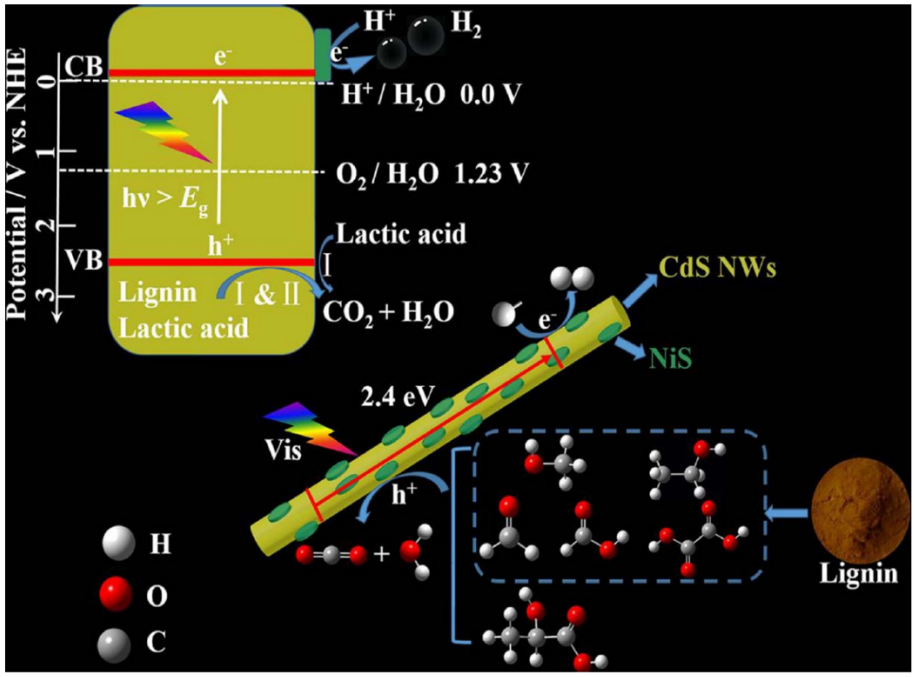

Figure 5-9- Scheme for the photocatalytic hydrogen production over NiS/CdS nanocomposites under visible light.

5.4.4 NiS_2/CdS Nanocomposites

5.4.4.1 Photocatalytic Activity and Transient Absorption Study of NiS_2/CdS Nanocomposites

The photocatalytic H_2 production of as-prepared samples was evaluated. Time-dependent H_2 production over the NiS_2/CdS nanocomposites with different NiS_2 content showed an obvious increase in the whole photocatalytic reaction process under visible light irradiation ($\lambda \geq 400$ nm). All the NiS_2/CdS nanocomposites exhibited much higher rates of H_2 production than that of pure CdS and NiS_2, indicating the loading of NiS_2 on the CdS surface facilitates H_2 production. The H_2 production rates of NiS_2/CdS nanocomposites first increases and then decreases with increasing NiS_2 content. The

decrease may be ascribed to light shielding and scattering effects or NiS_2 competing for absorption of light with CdS.[63] The optimal molar ratio of NiS_2 and CdS for NiS_2/CdS nanocomposites was determined to be around 40 mol%, which shows the highest H_2 evolution rate of 14.49 mmol h^{-1} g^{-1}. These results demonstrated that loading suitable amount of NiS_2 on the surface of CdS could increase the visible light absorption and facilitate charge separation, thus accelerating H_2 evolution. Photocatalytic H_2 production activity over the 40%-NiS_2/CdS nanocomposite was evaluated in the presence of single 10 $g \cdot L^{-1}$ cellulose as sacrificial agent under UV-Vis light irradiation. When the photocatalytic reaction time exceeded 60 min, the H_2 production started. The 40%-NiS_2/CdS nanocomposite obtained a hydrogen evolution rate of 52.88 $\mu mol \cdot h^{-1} \cdot g^{-1}$, which demonstrated the potential application of H_2 evolution utilizing cellulosic biomass for NiS_2/CdS nanocomposites.

In order to study the origin of the enhancement in photocatalytic activity of the NiS_2/CdS nanocomposites, charge carrier dynamics in these samples were studied using transient absorption spectroscopy. For this measurement, four samples including CdS, 10%-NiS_2/CdS, 40%-NiS_2/CdS, and 100%-NiS_2/CdS nanocomposites were deposited on a glass substrate and excited with 400 nm laser pulses. These samples were excited with different pulse energies, and no energy dependence of the dynamics was observed. This result eliminates the possibility of nonlinear processes such as exciton-exciton annihilation and Auger recombination. Data obtained at 600 nJ/pulse had higher signal to noise ratio, therefore it was used to further analyze the charge carrier decay dynamics. The differential absorption of the samples as a function of the

probe wavelength and the time delay between pump and probe pulses is shown in Figure 10 (a-d).

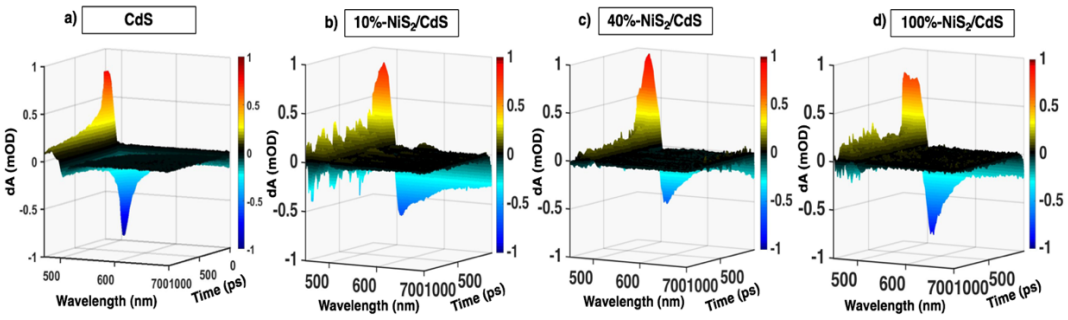

Figure 5-10- 3D representation of TA and transient bleach (TB) profile of a) CdS, b)10%-NiS2/CdS, c) 40%-NiS2/CdS, and d) 100%-NiS2/CdS excited at 400nm with pulse energy of 615 nJ/pulse.

The sharp TA signal at 475 nm which was observed for all samples in figure 10 is attributed to absorption of photoexcited electrons in conduction band (CB) of CdS. The other relatively broad TB signal in 500-700 nm can also be attributed to the absorption of hole in valence band (VB) of CdS as reported previously.[56,77] Studying the decay of these signals, which is due to electron-hole recombination over time provides information about the charge carrier dynamic and charge transfer between CdS and NiS_2. Therefore, normalized single wavelength decay of TA signal at 475 nm for CdS, 10%-NiS_2/CdS, 40%-NiS_2/CdS, and 100%-NiS_2/CdS nanocomposites from 0-1000 ps is demonstrated in Figure 11. The decay profile of these samples was fit using a double exponential function and fitting parameters are reported in table 4.

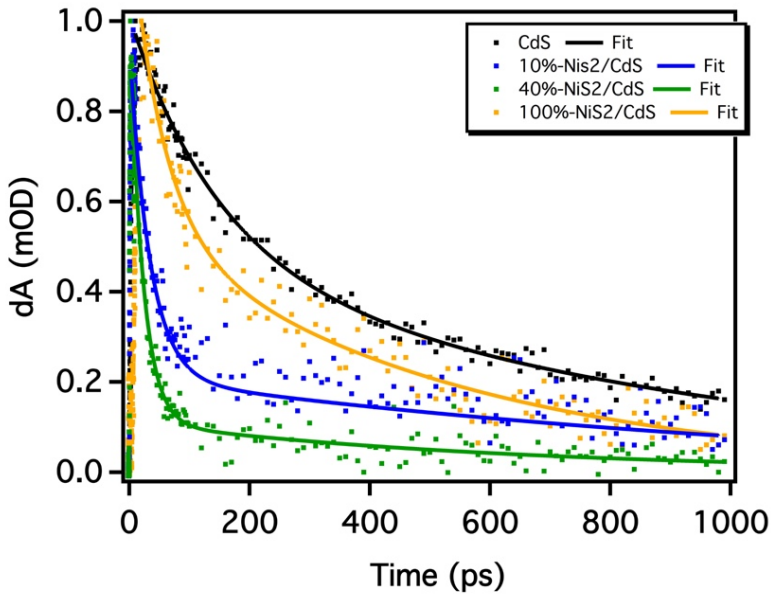

Figure 5-11- Normalized ultrafast transient absorption decay profile of CdS (black), 10%-NiS2/CdS (blue), 40%-NiS2/CdS (green), and 100%-NiS2/CdS (orange). The TA decay over time was fitted using double exponential function.

Table 5-4- Fitting parameters of TA signal recovery of CdS, 10%-NiS2/CdS, 40%-NiS2/CdS, and 100%-NiS2/CdS fitted with double exponential function.

Sample	A_1	τ_1 (ps)	A_2	τ_2 (ps)	Y	Average τ (ps)
CdS	0.51 ± 0.05	142 ± 16	0.49 ± 0.05	884 ± 90	0 ± 0	778
10%-NiS_2/CdS	0.66 ± 0.04	22 ± 1.2	0.34 ± 0.04	525 ± 114	0 ± 0	486
40%-NiS_2/CdS	0.89 ± 0.01	21 ± 2.6	0.11 ± 0.01	325 ±24	0 ± 0	220
100%-NiS_2/CdS	0.55 ± 0.04	54 ± 7.5	0.44 ± 0.04	617 ± 41	0 ± 0	562

Since photoexcited charge carriers can recombine through various pathways, two different time constants were extracted from the signal decay of each sample. The shorter time constant which is reported as τ_1 in Table 1 is attributed to trap state-mediated recombination, which usually occurs within tens of ps. On the other hand, the longer time constant (τ_2), is attributed to recombination of CB electron and VB hole.

However, addition of NiS_2 to the CdS surface introduce a new pathway for charge transfer between these two materials at the interface. By calculating the average lifetime (τ_{ave}) using equation 1 the rate of this charge transfer can be obtained. As shown in Table 4 the τ_{ave} is calculated to be 778, 486, 220, and 562 ps for CdS, 10%-NiS_2/CdS, 40%-NiS_2/CdS, and 100%-NiS_2/CdS, respectively. The average lifetime significantly decreased initially by addition of NiS_2 nanoparticles to the CdS surface, which is due to electron transfer from CB of CdS to NiS_2.[52,78] It was also reported previously that photoexcited holes in CdS can be delocalized to the surface, which increase the proximity of transferred electrons to holes.[79] This result in faster electron-hole recombination and shorter lifetime consequently. Considering photogenerated charge carriers participate in the hydrogen evolution reaction, the shorter τ_{ave} in 40%-NiS_2/CdS seems contradictory with its efficient photocatalytic performance. However, it should be noted that lactic acid was present as a hole scavenger in the reaction, which inhibits electron-hole recombination. Since TA measurements were performed on a film without lactic acid, there is no direct correlation between these two experimental results.

The τ_{ave} increased from 220 ps to 562 ps by further increasing the NiS_2 molar ratio to 100%. This is due to agglomeration of NiS_2 nanoparticles on the surface as shown in TEM images. Formation of these flocculant constructions reduces the surface coverage and decreases effective interaction and charge transfer between two materials consequently. However, addition of 40% NiS_2 resulted in formation of uniform thin layer on the surface, which accelerate the charge transfer at the interface. The rate of

charge transfer (k_{ET}) for different molar ratios of cocatalyst can be calculated using equation 2. The k_{ET} calculated to be 7.7×10^8 s^{-1}, 3.2×10^9 s^{-1}, and 4.9×10^8 s^{-1} for 10%-NiS_2/CdS, 40%- NiS_2/CdS, and 100%-NiS_2/CdS nanocomposites, respectively. The higher k_{ET} for 40%- NiS_2/CdS is consistent with its high photocatalytic activity. This result emphasizes on importance of optimizing the ratio of cocatalyst to achieve efficient photocatalytic activity at the heterojunctions.

5.4.4.2 Photocatalytic mechanism of NiS_2/CdS nanocomposites

Based on the discussion above, the possible photocatalytic mechanism of NiS_2/CdS nanocomposite is shown in Fig. 12. Under illumination, photogenerated electrons in valence band (VB) of CdS will be transited to conduction band (CB) and the holes are left in VB of CdS. These electrons have several ways to be consumed. They can recombine with the holes inside the material and the species on the particle surface or react with protons to produce H_2.[12] Therefore, if the recombination could be efficiently prohibited, the H_2 evolution rate would be improved because more electrons were used to produce H_2. When NiS_2 was loaded on the surface of CdS, the electron transferred from CdS to NiS_2 was efficiently improved due to the appropriate work function of NiS_2 as compared to CB of CdS. PEC and TA studies confirmed the efficient charge transfer in NiS_2/CdS nanocomposites compared to pure CdS. The NiS_2 serves as an acceptor of the electrons generated in CdS and effectively improve the separation of photogenerated electron-hole pairs. Meanwhile, the holes can be consumed by the sacrificial agent, which prevent the electron-hole recombination, thus

improving the chance for electrons to participate in the photocatalytic H_2 evolution. The major chemical reaction pertaining to the photocatalytic process may be followed as Eqs. (7-9). During the photocatalytic reaction process, CdS absorbs the incident photons and generates electron-hole pairs (Eq. 7). Then the photogenerated electrons transfer from CdS to NiS_2, where H^+ is reduced to atomic H and then evolves as H_2 (Eqs. 8-9).

$$CdS + h\nu \rightarrow CdS\ (e^- + h^+) \qquad (7)$$

$$NiS_2 + e^- + H^+ \rightarrow HNiS_2 \qquad (8)$$

$$HNiS_2 + e^- + H^+ \rightarrow NiS_2 + H_2 \qquad (9)$$

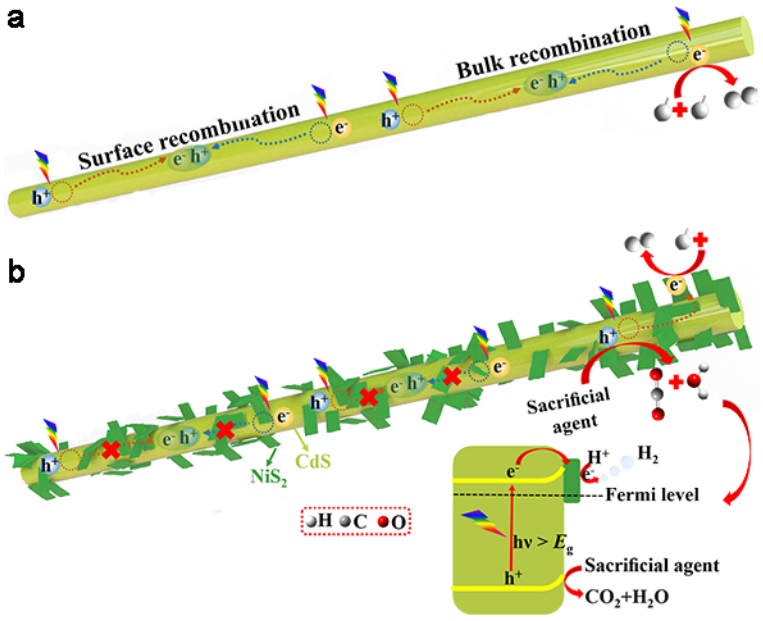

Figure 5-12- Scheme for the photocatalytic hydrogen production over NiCo2S4/CdS nanocomposites under visible light.

5.4.5 $NiCo_2S_4$/CdS Nanocomposites

5.4.5.1 Photocatalytic Activity and Transient Absorption Study of $NiCo_2S_4$/CdS Nanocomposites

hydrogen evolution from photocatalytic water splitting over pure CdS NWs and $NiCo_2S_4$/CdS heterojunctions were evaluated under visible light irradiation ($\lambda \geq 400$ nm) utilizing aqueous solution containing lactic acid as hole scavenger. Pure CdS NWs showed a quite low HER activity, which is mainly caused to fast recombination of photogenerated electron-hole pairs and small quantity of active sites. Loading $NiCo_2S_4$ on the surface of CdS NWs obviously improved the average rates of H_2 formation. When the molar ratio of $NiCo_2S_4$ and CdS is 10%, the H_2 evolution rate has a highest value of 20.0 $mmol \cdot h^{-1} \cdot g^{-1}$. However, further increasing the content of $NiCo_2S_4$ led to a decrease of H_2 evolution activity, which may originate from the aggregation of $NiCo_2S_4$ where the increased light absorption of $NiCo_2S_4$ but decreased the light absorption of CdS.

Using ultrafast transient absorption (TA) measurements helped to further study the charge carrier dynamics and elucidate the origin of the enhanced photocatalytic performance. In this experiment, CdS NWs, 10%-$NiCo_2S_4$/CdS, 20%-$NiCo_2S_4$/CdS and 30%-$NiCo_2S_4$/CdS heterojunctions deposited on a glass slide substrate and were excited with 400 nm laser pulses. Since some non-linear dynamic processes including exciton-exciton annihilation and Auger recombination can interfere with proper data analysis and understanding the materials behavior, pulse energy dependence experiment was also done. For this experiment all the samples were pumped with three

pulse energies (615, 310, 170 nJ/pulse) and no power dependence in charge carrier dynamics was observed for the samples. Therefore, the data obtained with 615 nJ/pulse energies was used to analyze the dynamics due to higher signal to noise ratio. Figs. 13(a-d) show the differential absorption of the samples as a function of the probe wavelength and the time delay between pump and probe pulses.

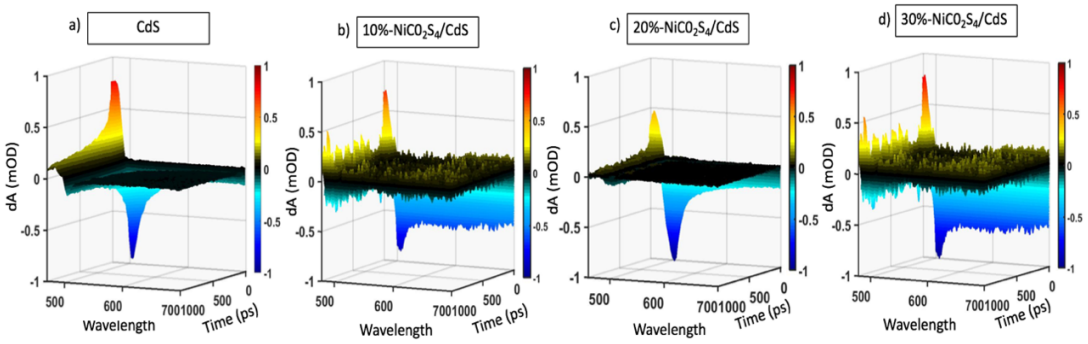

Figure 5-13- 3D representation of TA and transient bleach (TB) profile of a) CdS, b)10%-NiCo2S4/CdS, c)20%-NiCo2S4/CdS, and d) 30%-NiCo2S4/CdS excited at 400nm with pulse energy of 615 nJ/pulse.

As demonstrated in Fig. 13, a sharp TA signal at 480 nm and a relatively broad TB signal spanning from 500-700 nm were observed. The process of absorption of photogenerated electrons in CB of CdS generates the TA signal; whereas, the TB feature can be attributed to the absorption of hole in valence band (VB) of CdS as reported previously by us and other groups.[25,48]Information about the charge carrier dynamic and charge transfer from CdS to $NiCo_2S_4$ can be obtained from studying the observed decay of these features which are due to electron-hole recombination over time.

Fig. 14 displays the normalized single wavelength decay of the TA signal at 480 nm for 10%-$NiCo_2S_4$/CdS, 20%-$NiCo_2S_4$/CdS, 30%-$NiCo_2S_4$/CdS and bare CdS samples from 0-1000 ps. Double exponential function was used to fit these decay profiles and the fitting parameters are reported in Table 5.

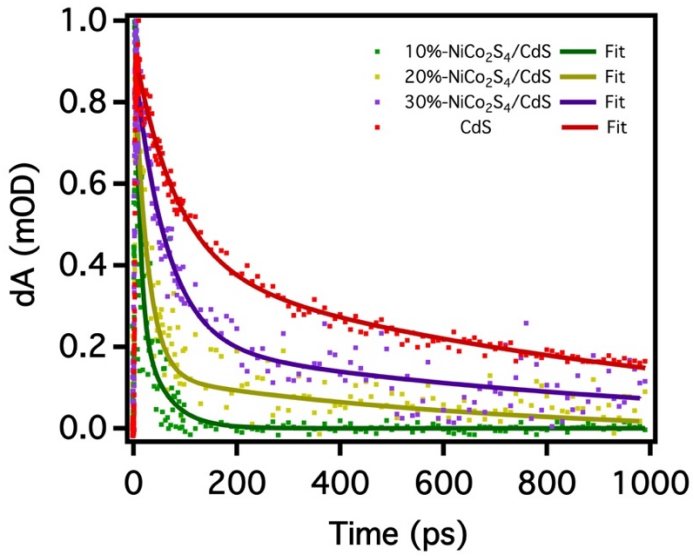

Figure 5-14- Normalized ultrafast transient absorption decay profile of 10%-NiCo2S4/CdS (green), 20%-NiCo2S4/CdS (yellow), 30%-NiCo2S4/CdS (purple) and CdS (red). The TA decay over time was fitted using double exponential function.

Table 5-5- Fitting parameters of TA signal recovery of 10%-NiCo2S4/CdS, 20%-NiCo2S4/CdS, 30%-NiCo2S4/CdS and CdS fitted with double exponential function.

Sample	A_1	τ_1 (ps)	A_2	τ_2 (ps)	Y	Average τ
10%-	0.81±0.15	9.8±1.0	0.19±0.17	48±15	0±0	30
20%-$NiCo_2S_4$/CdS	0.87±0.021	25±2.6	0.13±0.022	667±147	0±0	530
30%-$NiCo_2S_4$/CdS	0.78±0.11	61±5.0	0.22±0.031	831±236	0±0	670
CdS	0.56±0.017	82±5.6	0.43±0.018	993±74	0±0	904

Two different time constants are reported for each sample in Table 5. These two-time constants can be attributed to different recombination pathways for

photoexcited charge carriers in CdS. Trap state-mediated recombination typically occurs within tens of ps, while recombination between the CB electron and VB hole occurs on a longer timescale.[49,50] Therefore, the faster decay component, (τ_1), is ascribed to trap state-mediated recombination and the slower decay component, (τ_2), is attributed to CB electron and VB hole recombination. However, by depositing $NiCo_2S_4$ NPs on the surface of CdS NWs, some charge carriers will be transferred at the interface. In order to find the rate of charge transfer from CdS to $NiCo_2S_4$ and proper comparison between the samples, the average lifetime (τ_{ave}) can be calculated using equation 1. The τ_{ave} for the pure CdS NWs is ca. 904 ps. However, addition of 10% $NiCo_2S_4$, remarkably decreased the τ_{ave} to 30 ps. This dramatic change in lifetime is ascribed to electron transfer from the CB of CdS to $NiCo_2S_4$.[51,52] Considering the TA signal arises only from absorption of CdS NWs, the electron transfer from CdS to $NiCo_2S_4$ would result in shorter lifetime, as observed. Additionally, as observed in another study of loading Pt on the surface of CdS NWs, photoexcited holes in CdS can be delocalized to the surface. Therefore, proximity between the delocalized holes of CdS and electrons transferred to deposited NPs will result faster rate of recombination and consequently shorter lifetime[53,54] This shorter lifetime appears contradictory with the higher photocatalytic efficiency reported earlier for this 10%-$NiCo_2S_4$/CdS nanocomposites. However, the presence of lactic acid in the solution for the photocatalytic H_2 evolution measurement serves as a hole scavenger, which inhibits electron-hole recombination. Since no hole scavenger was used in the TA measurements, there is no direct correlation between these two experimental results.

Further increasing the content of $NiCo_2S_4$ to 20 mol% and 30 mol% prolonged the average lifetime to 530 ps and 670 ps, respectively, which are longer than that of 10%-$NiCo_2S_4$/CdS. The reason for this can be explained in TEM images. Addition of 10% $NiCo_2S_4$ formed a uniform and thin layer of $NiCo_2S_4$ on CdS NWs which resulted in close contact and effective interaction at the interface. This efficient interaction can facilitate charge transfer from CdS NWs to $NiCo_2S_4$ NPs. However, further increasing the amount of $NiCo_2S_4$ to 30% will result in aggregation of the $NiCo_2S_4$ NPs and forming flocculant constructions. This will lead to decreased surface coverage or reduced interaction with CdS, thus slowing down charge transfer.

The rate constant of electron transfer (k_{ET}) from CdS NWs to $NiCo_2S_4$ NPs can be obtained by employing equation 2. The k_{ET} calculated to be 3.3×10^{11} s^{-1}, 7.1×10^{9} s^{-1}, and 1.5×10^{9} s^{-1} for 10%-$NiCo_2S_4$/CdS, 20%- $NiCo_2S_4$/CdS and 30%-$NiCo_2S_4$/CdS heterojunctions, respectively. In comparison to 10%-$NiCo_2S_4$/CdS with larger k_{ET}, this decreased electron transfer rate for 20%-$NiCo_2S_4$/CdS and 30%-$NiCo_2S_4$/CdS are in accordance with their decreased photocatalytic activity. This indicates the need to optimize the amount of cocatalyst ($NiCo_2S_4$) on the surface of CdS to achieve efficient photocatalytic activity at the heterojunctions.

5.4.5.2 Photocatalytic Mechanism of $NiCo_2S_4$/CdS Nanocomposites

On the basis of all the above experimental and theoretical results, the mechanism of the overall photocatalytic HER is proposed, as shown in Fig. 15. Electrons and holes are first generated in CdS with visible light excitation ($\lambda \geq 400$

nm). Although the conduction band (CB) edge of CdS is more negative than the reduction potential of H^+/H_2, the activity of HER is still poor for pure CdS due to the low photogenerated charge separation efficiency. For $NiCo_2S_4$/CdS nanocomposite, the CB photogenerated electrons of CdS are transferred to metallic $NiCo_2S_4$ owing to the more positive work function of $NiCo_2S_4$ than that of CdS. Importantly, the Schottky junction forms between $NiCo_2S_4$ and CdS owing to their large and intimate interfacial contact, which facilitates electron transfer from CdS to $NiCo_2S_4$. The $NiCo_2S_4$ affords reduction active sites since its unsaturated sulfide ions have strong affinity for H^+, thus enhancing the photocatalytic HER activity. The valence band (VB) holes left in CdS can oxidize hole scavengers, as illustrated in Fig. 15. The electron-hole recombination can effectively be prohibited as the fast consumption of the holes by lactic acid, thereby protecting CdS from the photocorrosion and increasing the H_2 generation rate.

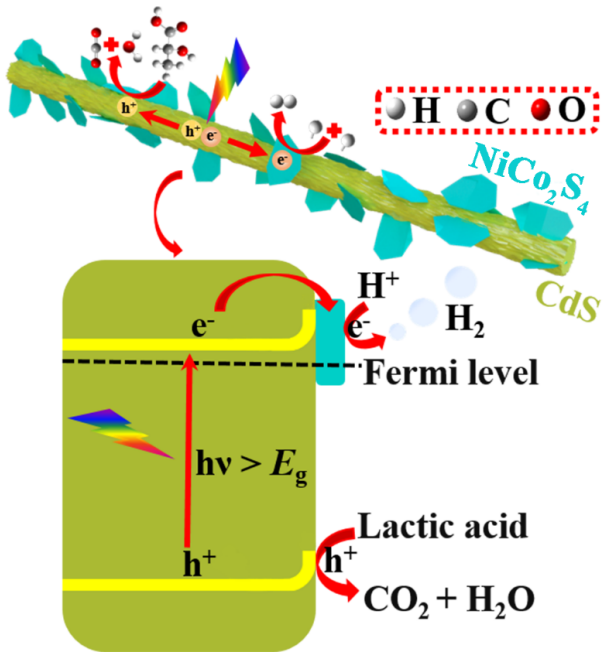

Figure 5-15- Proposed scheme for the photocatalytic HER over NiCo2S4/CdS nanocomposites under visible light.

5.5 Conclusion

In summary, 1D Ni_3S_2/CdS, MoS_2/CdS, NiS/CdS, NiS_2/CdS, and $NiCo_2S_4$/CdS heterostructures have been successfully synthesized using a two-step hydrothermal strategy. In this chapter we showed loading optimal amount of nanostructures on the CdS NWs surface can significantly improve the photocatalytic activity of the heterostructure for hydrogen evolution reaction. This enhancement is mostly due to efficient charge transfer from CdS to the other nanostructure on the surface and inhibiting the electron-hole recombination, consequently.

Different molar ratios of each nanostructure have been studied and optimal amount of cocatalyst is investigated. This optimal amount determined to be 10%, 5%, 20%, 40%, and 10% for Ni_3S_2/CdS, MoS_2/CdS, NiS/CdS, NiS_2/CdS, and

$NiCo_2S_4$/CdS, respectively. These studies show having less than these optimum amounts wouldn't efficiently cover the surface. On the other hand, larger amount would result in aggregation in the surface and provide trap states for further charge recombination. However, TEM images demonstrated formation of thin and uniform layer of the nanostructures at their optimum concentrations, which will result in efficient charge transfer. These results demonstrated that loading suitable amount of NiS_2 on the surface of CdS could increase the visible light absorption and facilitate charge separation, thus accelerating H_2 evolution.

Efficiency of charge transfer in these nanocomposites was studied using ultrafast transient absorption measurement and the rate of charge transfer at the interface was calculated. This charge transfer rate was calculated to be higher for the nanocomposites with the higher photocatalytic activity at each series as expected. The strategy developed in this work can further provide reference for other visible-light-driven photocatalysis systems to construct noble-metal-free nanocomposites.

5.6 References

(1) Yu, X.; Shavel, A.; An, X.; Luo, Z.; Ibáñez, M.; Cabot, A. Cu2ZnSnS4-Pt and Cu2ZnSnS4-Au Heterostructured Nanoparticles for Photocatalytic Water Splitting and Pollutant Degradation. *J. Am. Chem. Soc.* **2014**, *136* (26), 9236–9239.

(2) Xu, F.; Zhang, L.; Cheng, B.; Yu, J. Direct Z-Scheme TiO2/NiS Core–Shell Hybrid Nanofibers with Enhanced Photocatalytic H2-Production Activity. *ACS Sustainable Chem. Eng.* **2018**, *6* (9), 12291–12298.

(3) Banerjee, T.; Haase, F.; Savasci, G.; Gottschling, K.; Ochsenfeld, C.; Lotsch, B. V. Single-Site Photocatalytic H2 Evolution from Covalent Organic Frameworks with Molecular Cobaloxime Co-Catalysts. *J. Am. Chem. Soc.* **2017**, *139* (45), 16228–16234.

(4) Kudo, A.; Miseki, Y. Heterogeneous Photocatalyst Materials for Water Splitting. *Chem. Soc. Rev.* **2008**, *38* (1), 253–278.

(5) Li, J.; Wu, N. Semiconductor-Based Photocatalysts and Photoelectrochemical Cells for Solar Fuel Generation: A Review. *Catal. Sci. Technol.* **2015**, *5* (3), 1360–1384.

(6) Cui, Y.; Pan, Y.-X.; Qin, H.; Cong, H.-P.; Yu, S.-H. A Noble-Metal-Free CdS/Ni3S2@C Nanocomposite for Efficient Visible-Light-Driven Photocatalysis. *Small Methods* **2018**, *2* (12), 1800029.

(7) Yu, W.; Chen, J.; Shang, T.; Chen, L.; Gu, L.; Peng, T. Direct Z-Scheme g-C3N4/WO3 Photocatalyst with Atomically Defined Junction for H2 Production. *Applied Catalysis B: Environmental* **2017**, *219*, 693–704.

(8) Núñez, J.; Fresno, F.; Platero-Prats, A. E.; Jana, P.; Fierro, J. L. G.; Coronado, J. M.; Serrano, D. P.; de la Peña O'Shea, V. A. Ga-Promoted Photocatalytic H2 Production over Pt/ZnO Nanostructures. *ACS Appl. Mater. Interfaces* **2016**, *8* (36), 23729–23738.

(9) Wen, J.; Li, X.; Liu, W.; Fang, Y.; Xie, J.; Xu, Y. Photocatalysis Fundamentals and Surface Modification of TiO2 Nanomaterials. *Chinese Journal of Catalysis* **2015**, *36* (12), 2049–2070.

(10) Hu, Q.; Huang, J.; Li, G.; Jiang, Y.; Lan, H.; Guo, W.; Cao, Y. Origin of the Improved Photocatalytic Activity of Cu Incorporated TiO2 for Hydrogen Generation from Water. *Applied Surface Science* **2016**, *382*, 170–177.

(11) Zhang, M.; Lin, H.; Cao, J.; Guo, X.; Chen, S. Construction of Novel S/CdS Type II Heterojunction for Photocatalytic H2 Production under Visible Light: The Intrinsic Positive Role of Elementary α-S. *Chemical Engineering Journal* **2017**, *321*, 484–494.

(12) Li, Z.; Chen, X.; Shangguan, W.; Su, Y.; Liu, Y.; Dong, X.; Sharma, P.; Zhang, Y. Prickly Ni3S2 Nanowires Modified CdS Nanoparticles for Highly Enhanced Visible-Light Photocatalytic H2 Production. *International Journal of Hydrogen Energy* **2017**, *42* (10), 6618–6626.

(13) Li, Z.; Zhang, Q.; Dan, M.; Guo, Z.; Zhou, Y. A Facile Preparation Route of Bi2S3 Nanorod Films for Photocatalytic H2 Production from H2S. *Materials Letters* **2017**, *201*, 118–121.

(14) Song, S.; Liang, Z.; Fu, W.; Peng, T. Preparation of Single-Crystalline AgIn5S8 Octahedrons with Exposed {111} Facets and Its Visible-Light-Responsive Photocatalytic H2 Production Activity. *ACS Appl. Mater. Interfaces* **2017**, *9* (20), 17013–17023.

(15) Ma, S.; Xu, X.; Xie, J.; Li, X. Improved Visible-Light Photocatalytic H2 Generation over CdS Nanosheets Decorated by NiS2 and Metallic Carbon Black as Dual Earth-Abundant Cocatalysts. *Chinese Journal of Catalysis* **2017**, *38* (12), 1970–1980.

(16) Vinokurov, V. A.; Stavitskaya, A. V.; Ivanov, E. V.; Gushchin, P. A.; Kozlov, D. V.; Kurenkova, A. Yu.; Kolinko, P. A.; Kozlova, E. A.; Lvov, Y. M. Halloysite Nanoclay Based CdS Formulations with High Catalytic Activity in Hydrogen Evolution Reaction under Visible Light Irradiation. *ACS Sustainable Chem. Eng.* **2017**, *5* (12), 11316–11323.

(17) Li, Q.; Guo, B.; Yu, J.; Ran, J.; Zhang, B.; Yan, H.; Gong, J. R. Highly Efficient Visible-Light-Driven Photocatalytic Hydrogen Production of CdS-Cluster-Decorated Graphene Nanosheets. *J. Am. Chem. Soc.* **2011**, *133* (28), 10878–10884.

(18) Shen, L.; Liang, R.; Wu, L. Strategies for Engineering Metal-Organic Frameworks as Efficient Photocatalysts. *Chinese Journal of Catalysis* **2015**, *36* (12), 2071–2088.

(19) Akple, M. S.; Low, J.; Wageh, S.; Al-Ghamdi, Ahmed. A.; Yu, J.; Zhang, J. Enhanced Visible Light Photocatalytic H2-Production of g-C3N4/WS2 Composite Heterostructures. *Applied Surface Science* **2015**, *358*, 196–203.

(20) Cui, Y.; Wang, Y.; Wang, H.; Cao, F.; Chen, F. Polycondensation of Ammonium Thiocyanate into Novel Porous G-C3N4 Nanosheets as Photocatalysts for Enhanced Hydrogen Evolution under Visible Light Irradiation. *Chinese Journal of Catalysis* **2016**, *37* (11), 1899–1906.

(21) Lin, Z.; Lin, L.; Wang, X. Thermal Nitridation of Triazine Motifs to Heptazine-Based Carbon Nitride Frameworks for Use in Visible Light Photocatalysis. *Chinese Journal of Catalysis* **2015**, *36* (12), 2089–2094.

(22) Li, Q.; Li, X.; Wageh, S.; Al-Ghamdi, A. A.; Yu, J. CdS/Graphene Nanocomposite Photocatalysts. *Advanced Energy Materials* **2015**, *5* (14), 1500010.

(23) Zhang, J.; Wageh, S.; Al-Ghamdi, AhmedA.; Yu, J. New Understanding on the Different Photocatalytic Activity of Wurtzite and Zinc-Blende CdS. *Applied Catalysis B: Environmental* **2016**, *192*, 101–107.

(24) Xu, F.; Zhang, J.; Zhu, B.; Yu, J.; Xu, J. CuInS2 Sensitized TiO2 Hybrid Nanofibers for Improved Photocatalytic CO2 Reduction. *Applied Catalysis B: Environmental* **2018**, *230*, 194–202.

(25) Xu, F.; Xiao, W.; Cheng, B.; Yu, J. Direct Z-Scheme Anatase/Rutile Bi-Phase Nanocomposite TiO2 Nanofiber Photocatalyst with Enhanced Photocatalytic H2-Production Activity. *International Journal of Hydrogen Energy* **2014**, *39* (28), 15394–15402.

(26) Qu, Y.; Duan, X. Progress, Challenge and Perspective of Heterogeneous Photocatalysts. *Chem. Soc. Rev.* **2013**, *42* (7), 2568–2580.

(27) Zhang, N.; Yang, M.-Q.; Liu, S.; Sun, Y.; Xu, Y.-J. Waltzing with the Versatile Platform of Graphene to Synthesize Composite Photocatalysts. *Chem. Rev.* **2015**, *115* (18), 10307–10377.

(28) Xu, Y.; Tu, W.; Yin, S.; Kraft, M.; Zhang, Q.; Xu, R. Self-Template Synthesis of CdS/NiSx Heterostructured Nanohybrids for Efficient Photocatalytic Hydrogen Evolution. *Dalton Trans.* **2017**, *46* (32), 10650–10656.

(29) Zong, X.; Yan, H.; Wu, G.; Ma, G.; Wen, F.; Wang, L.; Li, C. Enhancement of Photocatalytic H2 Evolution on CdS by Loading MoS2 as Cocatalyst under Visible Light Irradiation. *J. Am. Chem. Soc.* **2008**, *130* (23), 7176–7177.

(30) Han, B.; Liu, S.; Zhang, N.; Xu, Y.-J.; Tang, Z.-R. One-Dimensional CdS@MoS2 Core-Shell Nanowires for Boosted Photocatalytic Hydrogen Evolution under Visible Light. *Applied Catalysis B: Environmental* **2017**, *202*, 298–304.

(31) Chen, J.; Wu, X.-J.; Yin, L.; Li, B.; Hong, X.; Fan, Z.; Chen, B.; Xue, C.; Zhang, H. One-Pot Synthesis of CdS Nanocrystals Hybridized with Single-Layer Transition-Metal Dichalcogenide Nanosheets for Efficient Photocatalytic Hydrogen Evolution. *Angewandte Chemie International Edition* **2015**, *54* (4), 1210–1214.

(32) Zhang, W.; Wang, Y.; Wang, Z.; Zhong, Z.; Xu, R. Highly Efficient and Noble Metal-Free NiS/CdS Photocatalysts for H2 Evolution from Lactic Acid Sacrificial Solution under Visible Light. *Chem. Commun.* **2010**, *46* (40), 7631–7633.

(33) Li, C.; Wang, H.; Naghadeh, S. B.; Zhang, J. Z.; Fang, P. Visible Light Driven Hydrogen Evolution by Photocatalytic Reforming of Lignin and Lactic Acid Using One-Dimensional NiS/CdS Nanostructures. *Applied Catalysis B: Environmental* **2018**, *227*, 229–239.

(34) Shen, S.; Guo, L.; Chen, X.; Ren, F.; Mao, S. S. Effect of Ag2S on Solar-Driven Photocatalytic Hydrogen Evolution of Nanostructured CdS. *International Journal of Hydrogen Energy* **2010**, *35* (13), 7110–7115.

(35) Zhang, W.; Wang, Y.; Wang, Z.; Xu, R. Highly Efficient and Noble Metal-Free NiS / CdS Photocatalysts for H 2 Evolution from Lactic Acid Sacrificial Solution under Visible Light w. *Chem. Commun.* **2010**, *46*, 7631–7633.

(36) Zhu, T.; Wu, H. B.; Wang, Y.; Xu, R.; Lou, X. W. (David). Formation of 1D Hierarchical Structures Composed of Ni3S2 Nanosheets on CNTs Backbone for Supercapacitors and Photocatalytic H2 Production. *Advanced Energy Materials* **2012**, *2* (12), 1497–1502.

(37) Zong, X.; Wu, G.; Yan, H.; Ma, G.; Shi, J.; Wen, F.; Wang, L.; Li, C. Photocatalytic H2 Evolution on MoS2/CdS Catalysts under Visible Light Irradiation. *J. Phys. Chem. C* **2010**, *114* (4), 1963–1968.

(38) Chen, G.; Li, D.; Li, F.; Fan, Y.; Zhao, H.; Luo, Y.; Yu, R.; Meng, Q. Ball-Milling Combined Calcination Synthesis of MoS2/CdS Photocatalysts for High Photocatalytic H2 Evolution Activity under Visible Light Irradiation. *Applied Catalysis A: General* **2012**, *443–444*, 138–144.

(39) Chang, K.; Li, M.; Wang, T.; Ouyang, S.; Li, P.; Liu, L.; Ye, J. Drastic Layer-Number-Dependent Activity Enhancement in Photocatalytic H2 Evolution over NMoS2/CdS ($n \geq 1$) Under Visible Light. *Advanced Energy Materials* **2015**, *5* (10), 1402279.

(40) He, J.; Chen, L.; Wang, F.; Liu, Y.; Chen, P.; Au, C.-T.; Yin, S.-F. CdS Nanowires Decorated with Ultrathin MoS2 Nanosheets as an Efficient Photocatalyst for Hydrogen Evolution. *ChemSusChem* **2016**, *9* (6), 624–630.

(41) Ma, S.; Xie, J.; Wen, J.; He, K.; Li, X.; Liu, W.; Zhang, X. Constructing 2D Layered Hybrid CdS Nanosheets/MoS2 Heterojunctions for Enhanced Visible-Light Photocatalytic H2 Generation. *Applied Surface Science* **2017**, *391*, 580–591.

(42) Liu, C.; Dasgupta, N. P.; Yang, P. Semiconductor Nanowires for Artificial Photosynthesis. *Chem. Mater.* **2014**, *26* (1), 415–422.

(43) Katz, M. J.; Riha, S. C.; Jeong, N. C.; Martinson, A. B. F.; Farha, O. K.; Hupp, J. T. Toward Solar Fuels: Water Splitting with Sunlight and "Rust"? *Coordination Chemistry Reviews* **2012**, *256* (21), 2521–2529.

(44) Han, S.; Pu, Y.-C.; Zheng, L.; Zhang, J. Z.; Fang, X. Shell-Thickness Dependent Electron Transfer and Relaxation in Type-II Core–Shell CdS/TiO2 Structures with Optimized Photoelectrochemical Performance. *J. Mater. Chem. A* **2015**, *3* (45), 22627–22635.

(45) Zhan, X.; Wang, Q.; Wang, F.; Wang, Y.; Wang, Z.; Cao, J.; Safdar, M.; He, J. Composition-Tuned ZnO/ZnxCd1–XTe Core/Shell Nanowires Array with Broad Spectral Absorption from UV to NIR for Hydrogen Generation. *ACS Appl. Mater. Interfaces* **2014**, *6* (4), 2878–2883.

(46) Zhu, G.; Bao, C.; Liu, Y.; Shen, X.; Xi, C.; Xu, Z.; Ji, Z. Self-Regulated Route to Ternary Hybrid Nanocrystals of Ag–Ag2S–CdS with near-Infrared

Photoluminescence and Enhanced Photothermal Conversion. *Nanoscale* **2014**, *6* (19), 11147–11156.

(47) Weber, Th.; Muijsers, J. C.; van Wolput, J. H. M. C.; Verhagen, C. P. J.; Niemantsverdriet, J. W. Basic Reaction Steps in the Sulfidation of Crystalline MoO3 to MoS2, As Studied by X-Ray Photoelectron and Infrared Emission Spectroscopy. *J. Phys. Chem.* **1996**, *100* (33), 14144–14150.

(48) Zhao, L.; Jia, J.; Yang, Z.; Yu, J.; Wang, A.; Sang, Y.; Zhou, W.; Liu, H. One-Step Synthesis of CdS Nanoparticles/MoS2 Nanosheets Heterostructure on Porous Molybdenum Sheet for Enhanced Photocatalytic H2 Evolution. *Applied Catalysis B: Environmental* **2017**, *210*, 290–296.

(49) Xu, J.; Cao, X. Characterization and Mechanism of MoS2/CdS Composite Photocatalyst Used for Hydrogen Production from Water Splitting under Visible Light. *Chemical Engineering Journal* **2015**, *260*, 642–648.

(50) Yang, Y.; Rodríguez-Córdoba, W.; Xiang, X.; Lian, T. Strong Electronic Coupling and Ultrafast Electron Transfer between PbS Quantum Dots and TiO2 Nanocrystalline Films. *Nano Lett.* **2012**, *12* (1), 303–309.

(51) Zhang, J.; Wang, L.; Liu, X.; Li, X.; Huang, W. High-Performance CdS–ZnS Core–Shell Nanorod Array Photoelectrode for Photoelectrochemical Hydrogen Generation. *J. Mater. Chem. A* **2014**, *3* (2), 535–541.

(52) Li, J.; Cushing, S. K.; Zheng, P.; Senty, T.; Meng, F.; Bristow, A. D.; Manivannan, A.; Wu, N. Solar Hydrogen Generation by a CdS-Au-TiO2 Sandwich

Nanorod Array Enhanced with Au Nanoparticle as Electron Relay and Plasmonic Photosensitizer. *J. Am. Chem. Soc.* **2014**, *136* (23), 8438–8449.

(53) Shen, L.; Luo, M.; Liu, Y.; Liang, R.; Jing, F.; Wu, L. Noble-Metal-Free MoS2 Co-Catalyst Decorated UiO-66/CdS Hybrids for Efficient Photocatalytic H2 Production. *Applied Catalysis B: Environmental* **2015**, *166–167*, 445–453.

(54) Zhao, G.; Sun, Y.; Zhou, W.; Wang, X.; Chang, K.; Liu, G.; Liu, H. Superior Photocatalytic H 2 Production with Cocatalytic Co/Ni Species Anchored on Sulfide Semiconductor. *Adv. Mater.* **2017**, *29*, 1703258.

(55) Ma, X.; Li, J.; An, C.; Feng, J.; Chi, Y.; Liu, J.; Zhang, J. Ultrathin Co (Ni) - Doped MoS_2 Nanosheets as Catalytic. *Nano Res.* **2016**, *9* (8), 2284–2293.

(56) Li, C.; Wang, H.; Bonabi, S.; Zhong, J.; Fang, P. Applied Catalysis B: Environmental Visible Light Driven Hydrogen Evolution by Photocatalytic Reforming of Lignin and Lactic Acid Using One-Dimensional NiS / CdS Nanostructures. *Appl. Catal. B Environ.* **2018**, *227*, 229–239.

(57) Wu, L.; Wang, Q.; Li, J.; Long, Y.; Liu, Y.; Song, S. Co 9 S 8 Nanoparticles-Embedded N / S-Codoped Carbon Nanofibers Derived from Metal – Organic Framework-Wrapped CdS Nanowires for Efficient Oxygen Evolution Reaction. *Small* **2018**, *14*, 174035.

(58) Meng, J.; Yu, Z.; Li, Y.; Li, Y. PdS-Modified CdS / NiS Composite as an Efficient Photocatalyst for H 2 Evolution in Visible Light. *Catal. Today* **2014**, *225*, 136–141.

(59) Faber, M. S.; Lukowski, M. A.; Ding, Q.; Kaiser, N. S.; Jin, S. Earth-Abundant Metal Pyrites (FeS_2, CoS_2, NiS_2, and Their Alloys) for Highly Efficient Hydrogen Evolution and PolysulFide Reduction Electrocatalysis. *J. Phys. Chem. C* **2014**, *118*, 21347–21356.

(60) Tan, P.; Liu, Y.; Zhu, A.; Zeng, W.; Cui, H.; Pan, J. Rational Design of Z-Scheme System Based on 3D Hierarchical CdS Supported 0D Co9S8 Nanoparticles for Superior Photocatalytic H2 Generation. *ACS Sustain. Chem. Eng.* **2018**, *6*, 10385–10394.

(61) Xiao, J.; Wan, L.; Yang, S.; Xiao, F.; Wang, S. Design Hierarchical Electrodes with Highly Conductive $NiCo_2S_4$ Nanotube Arrays Grown on Carbon Fiber Paper for High- Performance Pseudocapacitors. *Nano Lett.* **2014**, *14*, 831–838.

(62) Liu, Q.; Jin, J.; Zhang, J. $NiCo_2S_4$ @ Graphene as a Bifunctional Electrocatalyst for Oxygen Reduction and Evolution Reactions. *ACS Appl. Mater. Inter.* **2013**, *5*, 5002–5008.

(63) Wang, H.; Naghadeh, S. B.; Li, C.; Cherrette, V. L.; Fang, P.; Xu, K.; Zhang, J. Z. Enhanced Photoelectrochemical and Photocatalytic Properties of CdS Nanowires Decorated with Ni3S2 Nanoparticles under Visible Light Irradiation. *J. Electrochem. Soc.* **2019**, *166* (5), H3146–H3153.

(64) Wang, H.; Naghadeh, S. B.; Li, C.; Ying, L.; Allen, A.; Zhang, J. Z. Enhanced Photoelectrochemical and Photocatalytic Activities of CdS Nanowires by Surface Modification with MoS2 Nanosheets. *Sci. China Mater.* **2018**, *61* (6), 839–850.

(65) Cooper, J. K.; Ling, Y.; Longo, C.; Li, Y.; Zhang, J. Z. Effects of Hydrogen Treatment and Air Annealing on Ultrafast Charge Carrier Dynamics in ZnO Nanowires Under in Situ Photoelectrochemical Conditions. *J. Phys. Chem. C* **2012**, *116* (33), 17360–17368.

(66) Han, S.; Pu, Y.-C.; Zheng, L.; Hu, L.; Zhang, J. Z.; Fang, X. Uniform Carbon-Coated CdS Core–Shell Nanostructures: Synthesis, Ultrafast Charge Carrier Dynamics, and Photoelectrochemical Water Splitting. *J. Mater. Chem. A* **2016**, *4* (3), 1078–1086.

(67) Simon, T.; Carlson, M. T.; Stolarczyk, J. K.; Feldmann, J. Electron Transfer Rate vs Recombination Losses in Photocatalytic H2 Generation on Pt-Decorated CdS Nanorods. *ACS Energy Lett.* **2016**, *1* (6), 1137–1142.

(68) Pu, Z.; Liu, Q.; Asiri, A. M.; Luo, Y.; Sun, X.; He, Y. 3D Macroporous MoS_2 Thin Film: In Situ Hydrothermal Preparation and Application as a Highly Active Hydrogen Evolution Electrocatalyst at All PH Values. *Electrochimica Acta* **2015**, *168*, 133–138.

(69) Wheeler, D. A.; Zhang, J. Z. Exciton Dynamics in Semiconductor Nanocrystals. *Advanced Materials* **2013**, *25* (21), 2878–2896.

(70) Shen, S.; Guo, P.; Wheeler, D. A.; Jiang, J.; Lindley, S. A.; Kronawitter, C. X.; Zhang, J. Z.; Guo, L.; Mao, S. S. Physical and Photoelectrochemical Properties of Zr-Doped Hematite Nanorod Arrays. *Nanoscale* **2013**, *5* (20), 9867–9874.

(71) Liu, Q.; Shang, Q.; Khalil, A.; Fang, Q.; Chen, S.; He, Q.; Xiang, T.; Liu, D.; Zhang, Q.; Luo, Y.; et al. In Situ Integration of a Metallic 1T-MoS2/CdS

Heterostructure as a Means to Promote Visible-Light-Driven Photocatalytic Hydrogen Evolution. *ChemCatChem* **2016**, *8* (16), 2614–2619.

(72) Caravaca A.; Jones W.; Hardacre C.; Bowker M. H2 Production by the Photocatalytic Reforming of Cellulose and Raw Biomass Using Ni, Pd, Pt and Au on Titania. *Proceedings of the Royal Society A: Mathematical, Physical and Engineering Sciences* **2016**, *472* (2191), 20160054.

(73) Li, C.; Wang, H.; Ming, J.; Liu, M.; Fang, P. Hydrogen Generation by Photocatalytic Reforming of Glucose with Heterostructured CdS/MoS2 Composites under Visible Light Irradiation. *International Journal of Hydrogen Energy* **2017**, *42* (27), 16968–16978.

(74) Wang, L.; Wang, W.; Shang, M.; Yin, W.; Sun, S.; Zhang, L. Enhanced Photocatalytic Hydrogen Evolution under Visible Light over Cd1−xZnxS Solid Solution with Cubic Zinc Blend Phase. *International Journal of Hydrogen Energy* **2010**, *35* (1), 19–25.

(75) Yuan, Y.-J.; Wang, F.; Hu, B.; Lu, H.-W.; Yu, Z.-T.; Zou, Z.-G. Significant Enhancement in Photocatalytic Hydrogen Evolution from Water Using a MoS2 Nanosheet-Coated ZnO Heterostructure Photocatalyst. *Dalton Trans.* **2015**, *44* (24), 10997–11003.

(76) Burda, C.; Link, S.; Mohamed, M. B.; El-Sayed, M. The Pump Power Dependence of the Femtosecond Relaxation of CdSe Nanoparticles Observed in the Spectral Range from Visible to Infrared. *J. Chem. Phys.* **2002**, *116* (9), 3828–3833.

(77) Han, S.; Pu, Y.; Zheng, L.; Zhang, Z. Shell-Thickness Dependent Electron Transfer and Relaxation in Type-II Core–Shell CdS/TiO2 Structures with Optimized Photoelectrochemical Performance. *J. Mater. Chem. A* **2015**, *3*, 22627–22635.

(78) Wu, K.; Rodríguez-Córdoba, W. E.; Yang, Y.; Lian, T. Plasmon-Induced Hot Electron Transfer from the Au Tip to CdS Rod in CdS-Au Nanoheterostructures. *Nano Lett.* **2013**, *13* (11), 5255–5263.

(79) Wu, K.; Zhu, H.; Liu, Z.; Rodríguez-Córdoba, W.; Lian, T. Ultrafast Charge Separation and Long-Lived Charge Separated State in Photocatalytic CdS–Pt Nanorod Heterostructures. *J. Am. Chem. Soc.* **2012**, *134* (25), 10337–10340.

Chapter 6

6 Effect of Targeting Ligand on Photothermal Therapy Efficiency Using Hollow Gold Nanoparticles

6.1 Abstract

Plasmonic nanoparticles in general have been studied extensively for various applications including photocatalysis, sensing, optoelectronic and nanomedicine due to their unique optical and structural properties. Among these plasmonic nanomaterials hollow gold nanoparticles (HGNs) attracted significant attention for bio applications such as photothermal therapy (PTT). These HGNs have inert and biocompatible properties and most importantly their size and surface plasmon resonance is tunable by controlling size and shell thickness. This provides the opportunity to tune the particle size suitable for penetrating through the cell membrane and absorb light at the NIR region which is known as biological window. These HGNs can be easily modified on the surface and be conjugated to various targeting ligands including antibody, peptide and other small molecules such as folate. Optimizing the targeting ligand is crucial factor for efficient PTT. Here in this study, we synthesized 40 nm HGNs and conjugated them to anti_EGFR antibody and GE-11 peptide, which both target EGF receptors on cancer cells. The conjugated HGNs were characterized using UV-Vis, photoluminescence (PL), Inductively coupled plasma-optical emission spectrometry

(ICP_OES), bicinchoninic acid assay (BCA), fluorescence microscopy, and confocal microscopy. The preliminary results showed significantly higher cell death with peptide conjugated HGNs (91%) compared to antibody-conjugated HGNs (54%). Different hypotheses was discussed as possible explanation for this enhanced PTT efficiency including possible particle internalization, better binding to receptors due to small ligand size, and most importantly closer proximity of HGNs to the cell surface resulting in more efficient heath transfer.

6.2 Introduction

In recent years, plasmonic nanomaterials attracted significant attention in the field of photocatalysis,[1–3] optoelectronics,[4–7] solar energy conversion,[1,8,9] sensing,[10–12] and nanomedicine[1,13–15] because of their tunable optical and electronic properties and specially their surface plasmon resonance (SPR).[4,16] The surface plasmon resonance is the resonant oscillation of conduction band electrons at the interface between negative and positive permittivity material stimulated by incident light that result in strong absorption and scattering at the oscillation frequency.[17,18] Depending on the specific application, nanoparticles with higher absorption or scattering might be preferred. For Instance, for sensing applications nanoparticles with higher scattering to absorption ratio is favorable. However, in most biomedical applications the goal is to design nanoparticles with maximum absorption. In addition, the SPR in plasmonic nanoparticles in significantly dependent on size and structure. Therefore, their optical properties including the absorption/scattering ratio is highly tunable for any given application.[19–

[24] In Biological applications such as photothermal therapy (PTT) in particular it is important to tune the SPR into near IR region (NIR) to be compatible with the transparency window of biological tissue called “biological window”.[25,26] In PTT metal nanoparticles are delivered to cancerous cells using a targeting ligand and illuminated by light, which cause rapid particle heating, increasing the cellular temperature significantly, and inducing cell death, respectively.[27–30] There are significant number of publications on synthesis of NIR plasmonic nanostructures such as nanorods, spherical nanoparticles, nanocages, and nanoshells.[31–35] Among all these structures, spherical nanoparticles demonstrated the best performance in cellular uptake and photothermal conversion efficiency (PCE).[36–39] Spherical solid gold nanoparticles seem to be a good candidate for PTT application, however, their SPR absorption is between 520-540 nm depending on their size.[40,41] This absorption wavelength limits their application in PTT as it is below the biological window. It has been shown previously that the SPR can redshift by formation of aggregates, but the their spectral inhomogeneity and large size is not desirable for PTT application.[42,43]

Hollow gold nanoparticles (HGNs) have been introduced as potential candidate for many biological applications such as cancer cell imaging, detection, and therapy.[27,44–50] These HGNs are uniform, nontoxic, biocompatible structures, which are highly tunable from visible to NIR region by controlling both diameter and shell thickness.[31,51] They can be also easily functionalized for bioconjugation with various targeting ligands due to their native surface chemistry. Their symmetric and spherical shape is also suitable for easy cellular penetration. HGNs also have a single

homogeneously broadened SPR, which can provide strong absorbance for every particle in the system. In addition, the thin shell diameter facilitates rapid electron-phonon coupling, allowing for more efficient conversion of absorbed photons to heat than solid gold particles.[52,53]

For an efficient PTT, in addition to synthesizing the appropriate nanoparticles, it is important to design surface modification strategies for efficient cancer cell targeting and nanoparticle delivery. Ligand targeting allows selective delivery of therapeutic and imaging agents to cancer cells while avoiding collateral damage to healthy tissues. Various targeting ligands including antibodies[54,55], aptamers[56,57], small protein scaffolds[58], peptides[59–62] and low-molecular-weight non-peptidic ligands[63–66] have been reported previously. Antibody-conjugated drugs have already shown great success and two of them are in the market,[67] and many more in clinical trials. However, the recent clinical development of multiple low-molecular-weight targeting ligands such as peptide suggests that these smaller targeted conjugates could be poised for similar success. Recent studies show, smaller ligand-targeted drugs are more advantageous in their pharmacokinetics[62], antigenicity[68] , *in vivo* and *in vitro* stability[69], conjugation chemistry[70,71], ease and cost of manufacturing[72], and ability to penetrate solid tumours[73–79] compared with their larger, more complex counterparts.

In this chapter, we studied the effect of targeting ligand on PTT efficiency for oral cancer treatment using HGNs. A monoclonal anti-EGFR antibody and GE11 peptide were conjugated to the HGNs using a heterobifunctional

polyethylene glycol (PEG) molecule for targeting the epidermal growth factor receptors (EGFR) overexpressed on the cell membrane of oral squamous cell carcinoma (cell line A-431) and *in vitro* PTT experiments were performed. The nanoparticles conjugation, and delivery was investigated using various characterization techniques including UV-Vis, photoluminescence (PL), Inductively coupled plasma-optical emission spectrometry (ICP_OES), bicinchoninic acid assay (BCA), fluorescence microscopy, and confocal microscopy. The preliminary results show significantly higher cell death with peptide conjugated HGNs (91%) compared to antibody-conjugated NPs (54%). Based on these results we proposed three different hypotheses for this improved efficiency. Peptide because of its relatively small size should be able to link the HGN in closer proximity to the cancer cell, as depicted in Figure 1. This could result in an increase in the effective heat transferred from the HGN to the cell target, which may increase cell death efficacy. In addition, the smaller size of peptide may accelerate the particle internalization and result in more permanent damage to cell nuclei. In this Chapter, we investigated each hypothesis and studied the effect of targeting ligand on PTT efficiency.

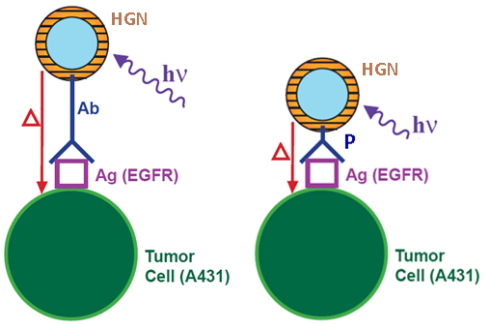

Figure 6-1- Schematic of HGN-mediated PTT with antibody versus peptide linkers.

6.3 Experimental

6.3.1 HGNs Synthesis

Cobalt chloride hexahydrate (99.99%), trisodium citrate dehydrate (>99%), sodium borohydride (99%), citric acid (99%), and chloroauric acid trihydrate (ACS reagent grade), were obtained from Fisher Scientific. All water used in the syntheses was 18 MΩ Milli-Q filtered.

Hollow gold nanoparticles used in this study were prepared by two different methods as reported previously.[51,80] Briefly, the cobalt particle were synthesized using total of 100 µL of aqueous 0.4 M cobalt chloride ($CoCl_2$) and 100 µL of 0.1 M aqueous sodium citrate added to 100 mL of water. The clear solution was pumped down for 5 min then exposed to N_2 to deoxygenate the solution. After ~2 min under N_2 gas, 400 µL of freshly prepared 0.25 M sodium borohydride ($NaBH_4$) was added to the solution. The solution was stirred until the color changed from clear to brown to gray, indicating the reduction of Co^{2+} ions in solution to Co^0 nanoparticles. A total of 175 µL of 0.1 M aqueous citric acid was then injected and the solution as capping ligand to increase the

rate of sodium borohydride hydrolysis and to prevent aggregation. Finally, 30 mL of cobalt template solution was added to 10 mL of water containing 20 μL of 0.1 M aqueous chloroauric acid ($HAuCl_4$) solution and mixed. After an immediate, slight color change from gray to blue-gray, the particles are exposed to air and swirled until the color change is complete to purple, blue, or green, depending on particle parameters. The gold shell forms within seconds onto the cobalt particle. If there is stoichiometrically less gold than cobalt a cobalt seed particle will remain within the gold shell. Upon exposure to oxygen, this cobalt core oxidizes and dissolves, revealing the true color of the HGNs solution. Resultant HGNs were centrifuged twice at 13000 rpm for 3 minutes and resuspended in ultrapure water to a concentration of 4.0 OD.

6.3.2 HGNs PEGylation

Heterobifunctional polyethylene glycol functionalized with orthopyridyl disulfide and succinimidyl valerate (OPSS-PEG-SVA) was purchased from Laysan Bio, Inc.

For PEGylation of HGNs, 100 μl of 1 mg/mL OPSS-PEG-SVA was added to 500 μL of 4.0 OD HGNs and shaken overnight. The resultant HGNs-PEG solution was centrifuged once at 13000 rpm for 3 minutes to remove residual PEG and resuspended in ultrapure water.

6.3.3 HGNs Bioconjugation

FITC-labeled anti-EGFR Rat monoclonal [ICR10] antibody (ab) was purchased

from Abcam Inc. FITC labeled and Lysin modified GE11 peptide was purchased from LifeTein LLC. Henry's Balanced Salt Solution (HBSS) was purchased from Life Technologies Corporation, and human oral squamous cell carcinoma cell line (A-431) was purchased from ATCC.

As-prepared HGNs-PEG solutions were centrifuged once for 3 min at 13000 rpm and resuspended in 500 μL of water. 100 μL of antibody was added to the HGNs-PEG and shaken overnight. The resultant HGNs-PEG-ab solutions were centrifuged three times at 13000 rpm for 3 minutes to remove unbound antibody and resuspended in water to an OD of 4.0.

Similarly, 100 μL of GE11 peptide dissolved in 500 μL of 1:4 ratio DMSO:water solution was added to 500 μL washed HGNs_PEG solution. The resultant HGNs-PEG-peptide solutions were centrifuged three times at 13000 rpm for 3 minutes to remove unbound peptide and resuspended in water to an OD of 4.0. The schematic presentation of the conjugation protocol is shown in Fig. 2.

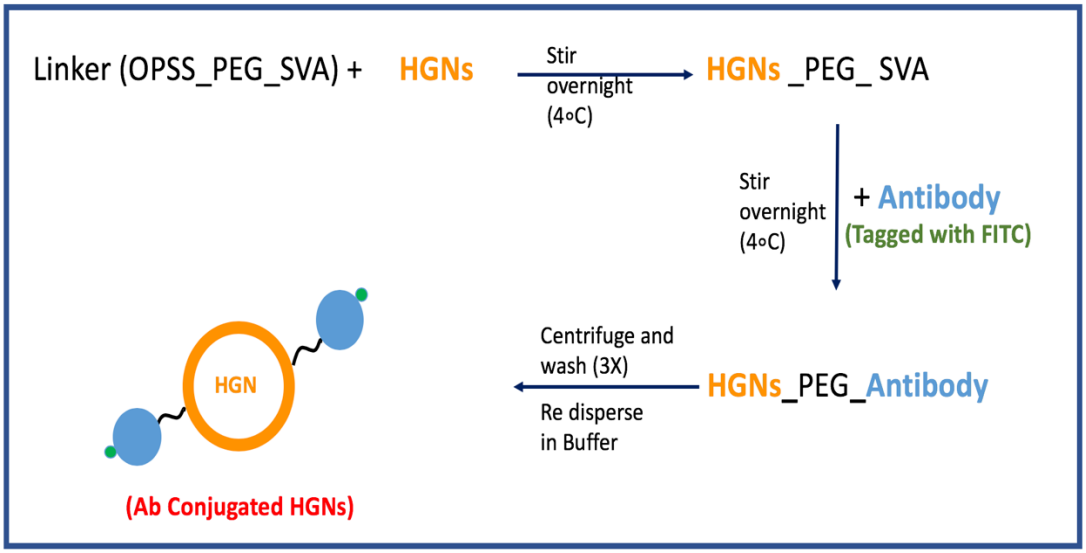

Figure 6-2- Schematic representation of HGNs bioconjugation protocol

6.3.4 HGNs Structure and Conjugation Characterization

The synthesized HGNs characterized by UV-Vis spectroscopy. UV–vis spectra were recorded with an Agilent Technologies Cary 60 UV–vis spectrophotometer using a 700 µL quartz cuvette with 10 mm optical path length.

Scanning electron microscopy (SEM) was performed on a FEI Quanta 3D field emission microscope operated at 10.00 kV acceleration voltage. HGN solutions were dropped onto a hexagonal, 400 mesh copper grid with a carbon support film of standard 5–6 nm thickness (Electron Microscopy Sciences).

ICP-OES was performed on a Thermo iCAP 7400 ICP-OES. Gold standards at 0 ppm (blank), 2 ppm, 5 ppm, 10 ppm, and 20 ppm were prepared using $HAuCl_4$ and ultrapure water. For sample preparation, 200 µL HGNs was added to 1800 µL blank to create a 1:10 dilution. Internal standardization was carried out with Sc and Y references. Two Au wavelengths (242.795 nm and 267.595 nm) and two Co wavelengths (238.892 nm and 237.862) were used

for analysis. For the samples containing cells, the ICP measurements were done after cell digestion. For digesting the cells, they were removed from the well plate using trypsin solution and then incubated with 100 μL of aqua regia and heated in a hot bath at 90 C for 1 hour. The digested cell solutions were further diluted with blank solution.

6.3.5 in vitro PTT

A-431 cells were cultured in HBSS according to previously published protocols and kept in a 37 °C, 5% CO_2 humidified incubator. Cells were grown in 96-well tissue culture plates overnight. After removing the growth media, 25 μL of the 4.0 OD HGNs-PEG-ab solutions were added to 75 μL HBSS and immediately transferred to the cells. After loading, the cells were incubated for 1 hour. For *in vitro* PTT treatment, the cells were exposed to a 795 nm NIR CW laser at 1.0 W/cm^2 for 5 minutes and then returned to the incubator. Cell viability was determined 24 hours after treatment using cell counting and propidium iodide markers for cell damage.

6.4 Results and Discussions

6.4.1 HGNs Characterization

To study the structural properties of the synthesized HGNs, they were characterized using SEM and UV_Vis spectroscopy. Fig. 3a shows the SEM image of HGNs, revealing the outer diameter to be 39 ± 5 nm, which is appropriate size for potential cell penetration. Also, in another study in our lab, we investigated the effect of nanoparticle size on the PTT efficiency and the preliminary results indicated that

HGNs in the size regime between 30-55 nm are most efficient. The HGNs in this size will maximize the absorption component and could therefore maximize heat generation. The findings also reveal that 50 nm HGNs generate ~2 times the heat per µg gold as their 70 nm counterparts and ~1.5 times the heat per µg gold as their 30 nm counterparts.

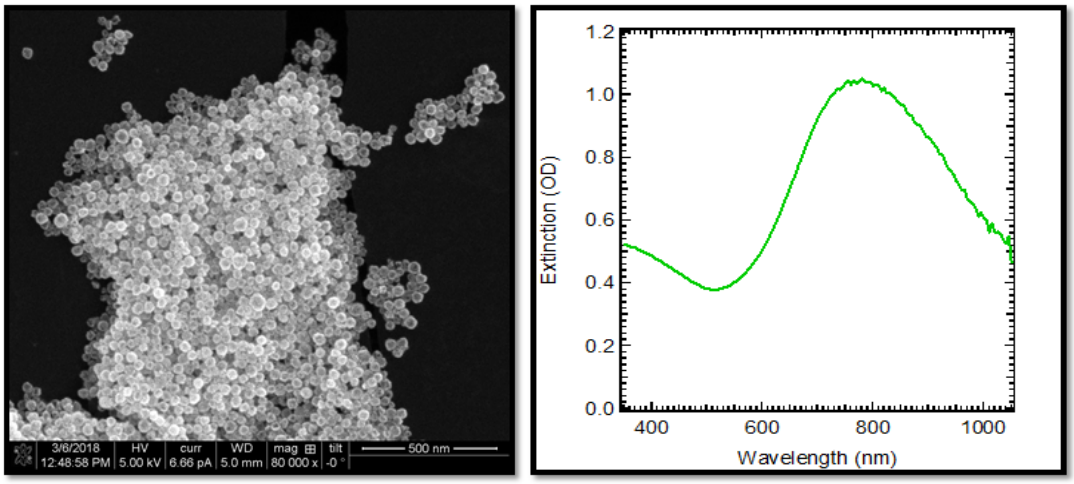

Figure 6-3- (a) SEM image of the HGNs, revealing an outer diameter of 39 nm with a shell (b) extinction spectra of the HGNs at 790 nm.

Fig. 3b represent the extinction spectra of synthesized HGNs which has a strong and symmetric peak at 790 nm. This symmetric peak shows uniformity of the particles and good size distribution. In addition, these HGNs fall into appropriate wavelength for biological applications which blood and tissue have minimum absorption.

6.4.2 Conjugation Characterization by UV- Vis

After characterizing the synthesized HGNs, they were concentrated to OD=4 for bioconjugation. As described in the experimental section, the concentrated HGNs

were incubated with 100 μL of Succinimidyl Valerate (SVA)_PEG_Orthopyridyldisulfate (OPSS) solution for PEGylation. The SVA-PEG_OPSS molecule was attached to the surface of HGNs via the gold-thiolate chemistry, resulting in amine-reactive succinimidyl ester-terminated PEGylated HGNs (SVA-PEG-HGNs).[81] It was previously reported that PEGylation of gold nanoparticles reduces nonspecific plasma protein binding and prolongs blood circulation time, which is a important for successful in vivo applications.[82,83] It is expected that the PEGylation of HGNs would improve their biocompatibility as well as their pharmacokinetic properties in vivo. The next step would be binding the PEGylated HGNs to the antibody or peptide through succinimidyl valerate terminus of PEG. HGNs-PEG conjugate was covalently bonded to EGF antibody and GE11peptide using through a reaction between SVA and amine groups in the sequence such as Lysin.[84] The bioconjugation of HGNs were confirmed by UV-Vis spectroscopy. As shown in Fig. 4, the absorption spectra of the HGNs broaden and redshifts. This shift in the absorption spectra while maintaining the overall shape and intensity of the spectra indicating successful conjugation of the antibody/peptide to the HGNs surface.

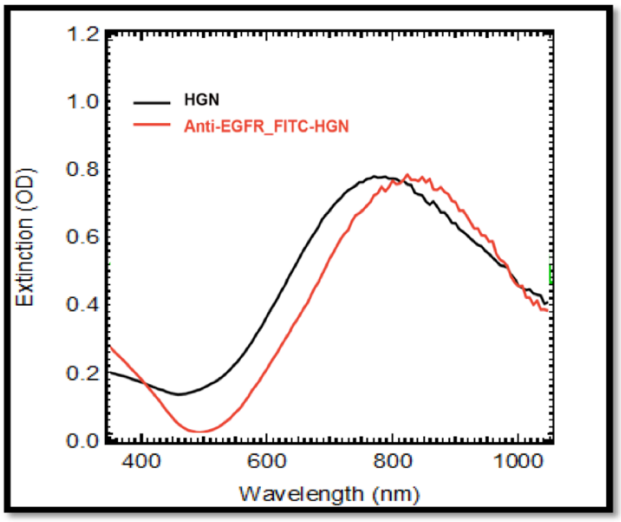

Figure 6-4- Extinction spectra of HGNs before (black) and after bioconjugation (red)

This observed spectral redshift after binding antibody/peptide to the surface is a result of an increase in the local refractive index at the gold nanoparticle surface.[85] This feature is also used in label free biosensing application.

6.4.3 Conjugation Characterization by PL

Since both antibody and peptide used in this study were tagged with fluorescein isothiocyanate (FITC) dye, we used fluorescence spectroscopy to further study the bioconjugation and quantify the amount of peptide/antibody on the HGNs surface. Fig. 5 shows the fluorescence intensity of different samples before and after conjugation with antibody. Here pure HGNs was used as control and the antibody conjugated HGNs are represented as HGN_antibody. The pure HGNs showed no PL and unwashed HGN_antibody solution showed PL intensity of about ~63000.

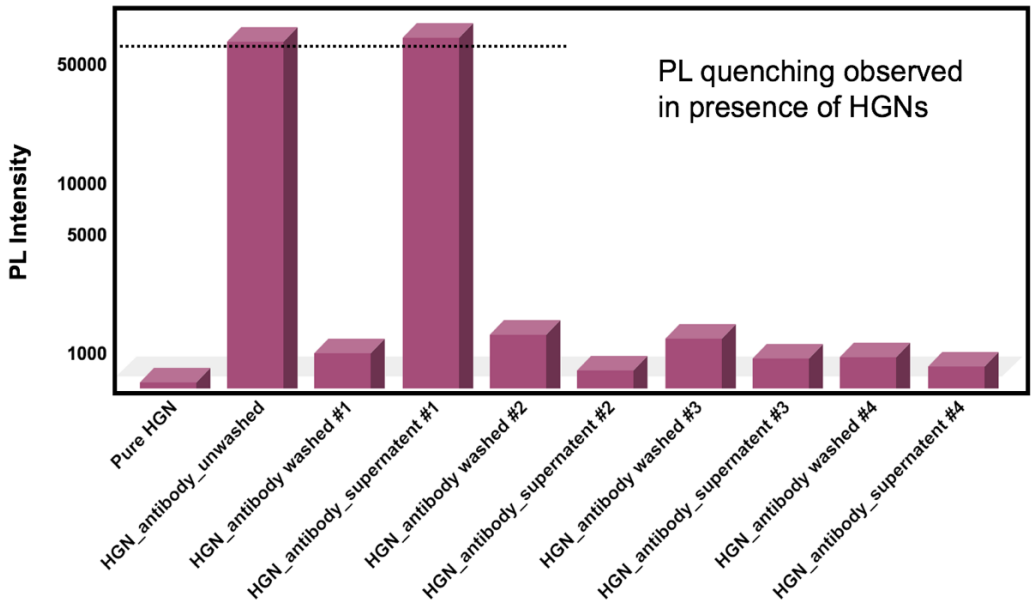

Figure 6-5- PL intensity of different samples, including pure HGNs, HGN_antibody conjugates, and supernatants after multiple washes. (#refers to number of washes)

After washing the HGN_antibody conjugates for the first time, PL of supernatant was measured as well as the washed particles. The PL intensity of the washed particles was higher than pure HGNs, which indicates presence of antibody molecules on the surface. However, the supernatant solution showed higher PL intensity compared to what was initially measured before wash. This result suggests quenching of fluorescence in presence of metal nanoparticles as reported previously.[86–88] The HGN_antibody conjugates were washed four times and Pl intensity of both washed particles and supernatant solution was measured. Even though, this measurement confirmed presence of FITC tagged antibodies on the HGNs surface after four washes, but due to this PL quenching, these results didn't help with quantifying the concentration of antibody/peptide on the particles.

6.4.4 Conjugation Characterization by BCA Assay

The bicinchoninic acid assay (BCA assay) was used to quantify the protein concentration in the solution. The total protein concentration is exhibited by a color change of the sample solution from green to purple in proportion to protein concentration, which can then be measured using colorimetric techniques. The BCA assay primarily relies on two reactions. First, the peptide bonds in protein reduce Cu^{2+} ions from the copper (II) sulfate to Cu^{+} (a temperature dependent reaction). The amount of Cu^{2+}reduced is proportional to the concentration of protein present in the solution. then, two molecules of bicinchoninic acid chelate with each Cu^{+} ion, forming a purple-colored complex that strongly absorbs light at a wavelength of 562 nm. these bicinchoninic acid Cu^{+} complex is formed by reacting with cysteine/cystine, tyrosine, and tryptophan side chains. At higher temperatures (37 to 60 °C), peptide bonds assist in the formation of the reaction complex.[89] The amount of protein present in a solution can be quantified by measuring the absorption spectra and comparing with protein solutions of known concentration. Fig. 6 shows the BCA assay of HGN_antibody conjugates.

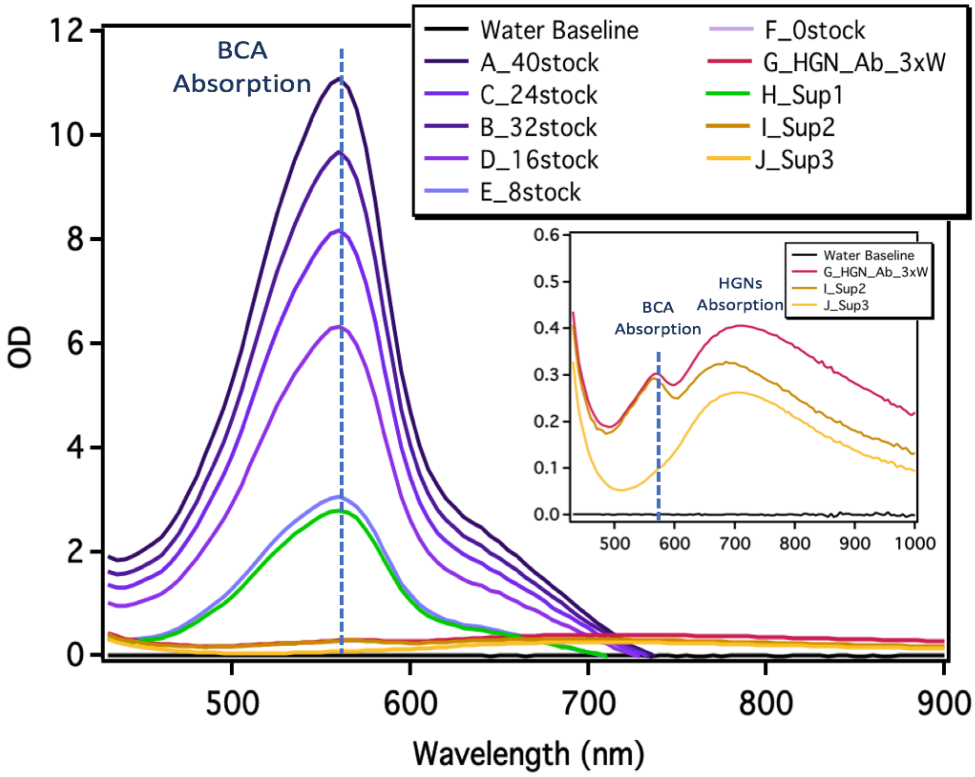

Figure 6-6- UV-Vis absorption spectra of standard BCA solutions and HGN-antibody conjugates in presence of BCA solution.

In this Assay, pure antibody stock solution with known concentration was used in presence of BCA solution to get the protein concentration calibration curve. The OD of each stock solution in the dilution series was measured at 562 nm and the extracted calibration curve is shown in Fig. 7. After making the calibration curve, the HGN_antibody conjugates after three washes and the supernatants after each wash were mixed with BCA solution and the absorption was measured at 562 nm. As it is shown in the inset of Fig. 6 the first supernatant has significant amount of protein in it. However, after each wash the absorption of the supernatant solution decreases significantly and finally after the 3rd wash no protein was observed in the supernatant.

On the other hand, noticeable amount of protein was measured in the HGN_antibody conjugates solution after three washes. These results indicate successful conjugation and strong binding of antibody on the HGNs surface after multiple washing. This also shows after three washes there are no free protein left in the solution.

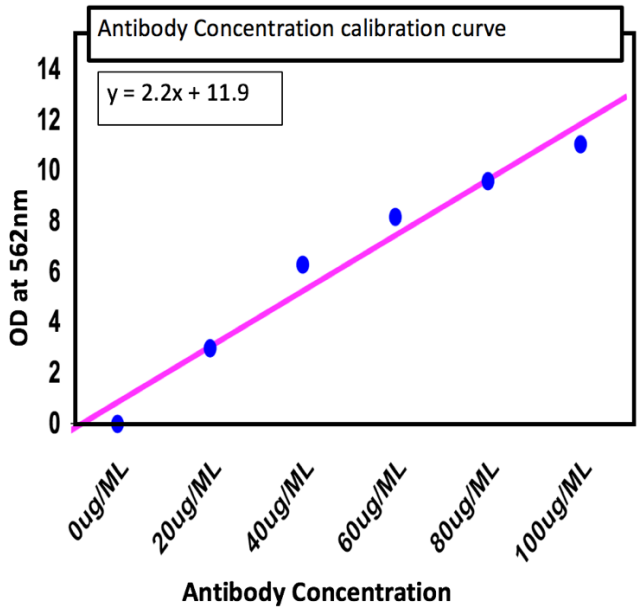

Figure 6-7- Antibody concentration calibration curve using BCA assay.

Using this calibration curve, we calculated the concentration of antibody left on the HGNs solution after three washes. Antibody Concentration on three times washed HGNs calculated to be 0.5 µg/ml. Considering the BCA results indicated all the protein left in the solution are bound to the HGN surface, we can quantify amount of antibody per HGN. This experiment was also performed with peptide conjugated HGNs and the results are shown in Fig. 8. However, the strong absorption of FITC shown in the UV_Vis spectra of the solution containing HGN_Peptide conjugates and BCA,

indicates dissociation of dye from the peptide. Therefore, this experiment should be repeated with fresh FITC labeled peptides for confident quantification of peptide concentration on HGNs.

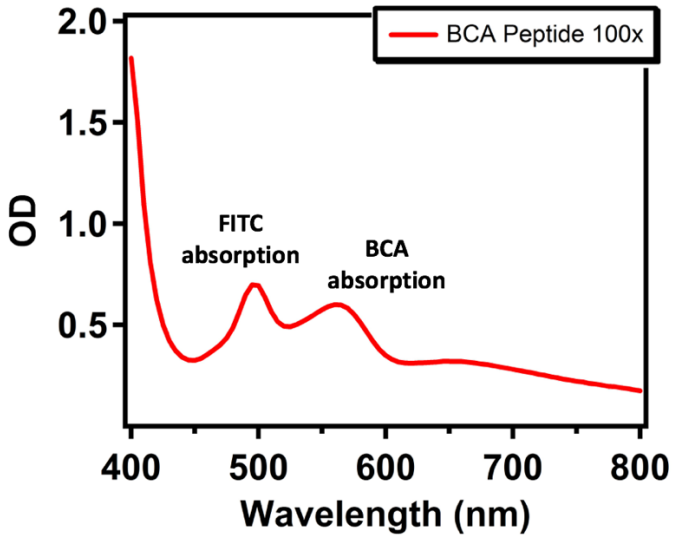

Figure 6-8- UV-Vis absorption spectra of standard BCA solutions and HGN-peptide conjugates in presence of BCA solution.

6.4.5 Cell Binding Assessment by Microscopy Imaging

The bioconjugated HGNs were incubated with oral squamous cell carcinoma (cell line A-431) to investigate the photothermal efficiency of these particles. Oral squamous cell carcinoma represents ~95% of all cases and is great candidate for PPT because it is a surface cancer and the oral cavity is easily accessible to incident laser light. Since the anti-EGFR antibody and GE-11 peptide used as targeting ligands for bioconjugation of HGNs, they can specifically target anti-epidermal growth factor receptor overexpressed on the surface of these cancer cells.[90] For the cell experiments,

HGNs-PEG-ab solutions were added to the cells cultured in a 96-well plate and incubated for 1 hour. After incubation, the cells were washed to remove free particles. The efficient targeting and delivery of these conjugates were investigated using confocal microscopy as shown in Fig. 9. The cell nuclei were stained with DAPI and represented as blue. Cell cytoskeletons are labeled with rhodamine phalloidin and shown in red and HGN_antibody conjugates are shown as green. Fig. 9a shows the oral squamous cells without particles and Fig. 9b shows the cells after incubation with HGN_antibody conjugates. The localization of the particles on the cells confirm successful targeting and delivery to the receptors.

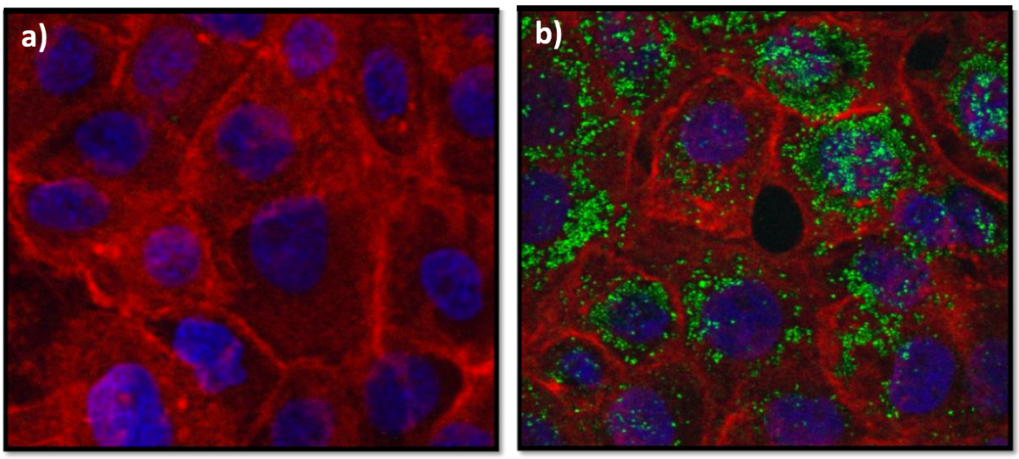

Figure 6-9- Confocal microscopy images of oral squamous cells (a) before and (b) after addition of HGN-PEG-ab. Cell nuclei are labeled with DAPI (shown in blue) and cell cytoskeleton is labeled with rhodamine-phalloidin (shown in red). The signal in green is associated with the presence of HGN_antibody conjugates.

Fluorescence microscopy is another technique we used to investigate particle delivery to the cells and efficient and specific targeting. In this imaging, the

fluorescence signal of FITC labels the location of HGNs and DAPI labels the cell nuclei. Fig. 10 shows cells stained with DAPI (red), FITC labeled antibody on HGN (pseudo-colored green), and the overlaid image. The resultant overlaid images show efficient binding of HGN_antibody to A431 cells which is represented by the strong fluorescence signal around the cell.

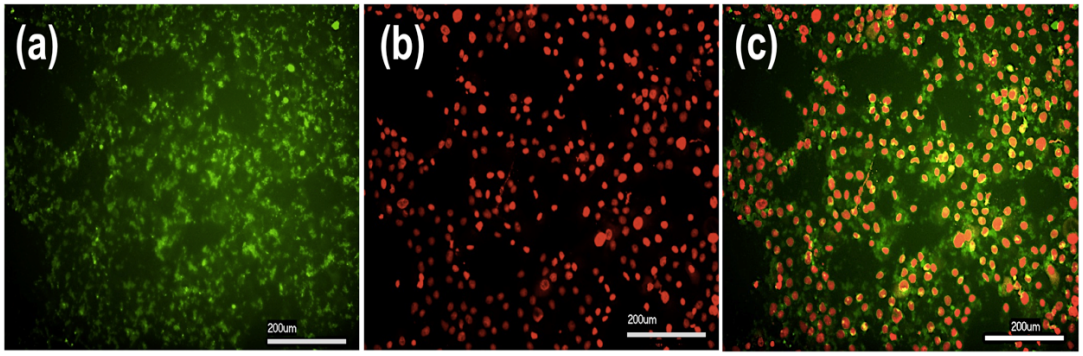

Figure 6-10- Fluorescence microscopy imaging of the HGN_antibody binding to A431 cells: (a) FITC labeled antibody on HGN (pseudo-colored green), (b)cells stained with DAPI (red), (c) overlaid image.

In order to investigate the specific binding of the particles to EGF receptors on the surface, the HGN_antibody conjugates were incubated with two different cell lines including healthy cells and breast cancer cells. Fig. 11 shows the fluorescence microscopy images of these particles.

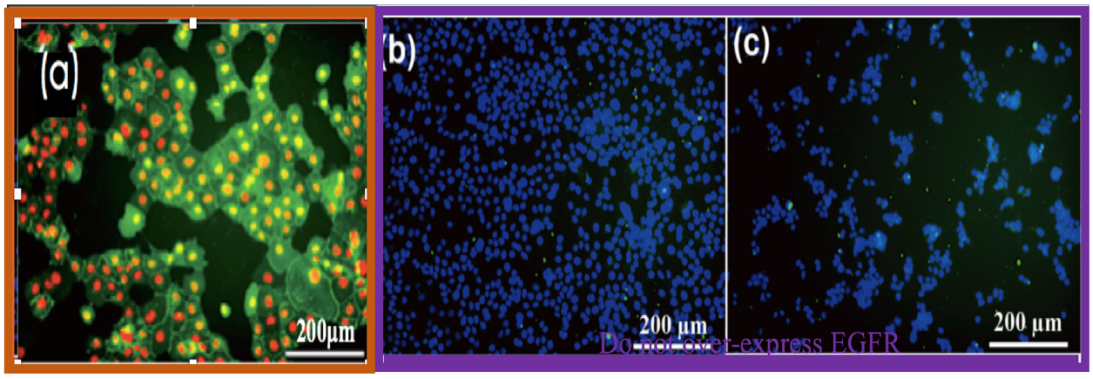

Figure 6-11- Fluorescence microscopy imaging of the HGN_antibody incubated with (a) A431 cells (b) Healthy HaCaT cells, and (c) MCF7 breast cancer cells.

As shown in Fig. 11, the HGN_antibody conjugates efficiently bound to the cells, while no particles were observed around the healthy HaCaT cells and MCF7 breast cancer cells since they don't overexpress specific EGF receptors. This result indicates specific binding and customized delivery of nanoparticles to the target cells. This is specifically important for cancer therapy without damaging healthy cells.

6.4.6 Binding Affinity Assessment by ICP-OES

One of the goals in this study is to compare the binding affinity of antibody conjugated HGNs to their smaller counterpart, peptide conjugated HGNs. The hypothesis is that because of smaller size of peptide, larger number of them can be fitted on the HGNs surface. This will eventually result in more efficient binding to the receptors. For this purpose, the amount of gold initially added to the cells was measured using ICP-OES. After 1-hour incubation, the cells were washed two times, leaving only bound HGNs on the cells. The solution containing the cells, bound particles and the

buffer was digested as described before. The digested cells and HGNs solutions were measured again by ICP_OES to quantify how much gold is bound to the particles. Fig. 12 shows calibration curve for standard concentration of gold prepared using the gold salt $HAuCl_4$. Using this calibration curve the concentration of left-over gold on the cells was measured. All the concentrations are reported in Table 1. The measured Au concentration in initial HGNs adjusted at OD=4 and added to the cells was measured to be 5.4 ppm. The concentration of gold left on the cells and the gold washed in the supernatant was also measured to be 1.14 ppm and 0.41 ppm, respectively. Even though these numbers don't add up the initial amount, it still shows higher concentration of gold on the cell compared to what was washed off. This might be due to losing some HGNs during the incubation and digestion process.

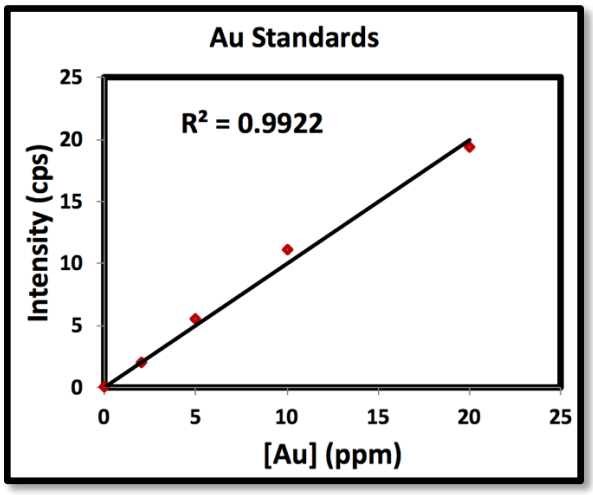

Figure 6-12- ICP-OES calibration curve for standard concentrations of Au.

Table 6-1- Au concentration in different HGNs samples measured by ICP-OES.

Sample	HBSS	HGN_ab added	HGN_ab on cells	HGN_ab in supernatant	HGN added	HGN On cells	HGN supernatant
[Au] ppm	0.05	5.4	1.14	0.41	3.5	0.23	1.29

As a control experiment we repeated this measurement using only pure HGNs and no targeting ligand. It was expected that particles wont bind to the cells and will mostly wash off. As expected, the concentration of gold in pure HGNs solution added to the cells was measured to be 3.5 ppm. However, only 0.23 ppm of it was left on the cells after washing and 1.29 ppm of it was removed in the supernatant solution. Similar measurements should be done using peptide conjugated HGNs in the future.

6.4.7 in vitro PTT

After delivering the conjugated particles to the cells, *in vitro* PTT was carried out for cells incubated with HGN_antibody and HGN_peptide conjugates. The PTT was performed using 795 nm laser light at 1.0 Wcm-2 directly applied to the cells for 5 min. The spot size was 7 mm in diameter to illuminate the entire well. The low laser power density and short treatment time was selected to avoid damage to the cells from the laser alone. Fluorescence microscopy was used before and after laser treatment for cell counting and determination of PTT efficacy. Fig. 13 shows the fluorescence microscopy images after treatment with laser. The cells were stained with propidium iodide (PI) (shown in pink), which is a DNA stain and is used to indicate cells that are dead or dying as it cannot pass the cell membrane of living cells.

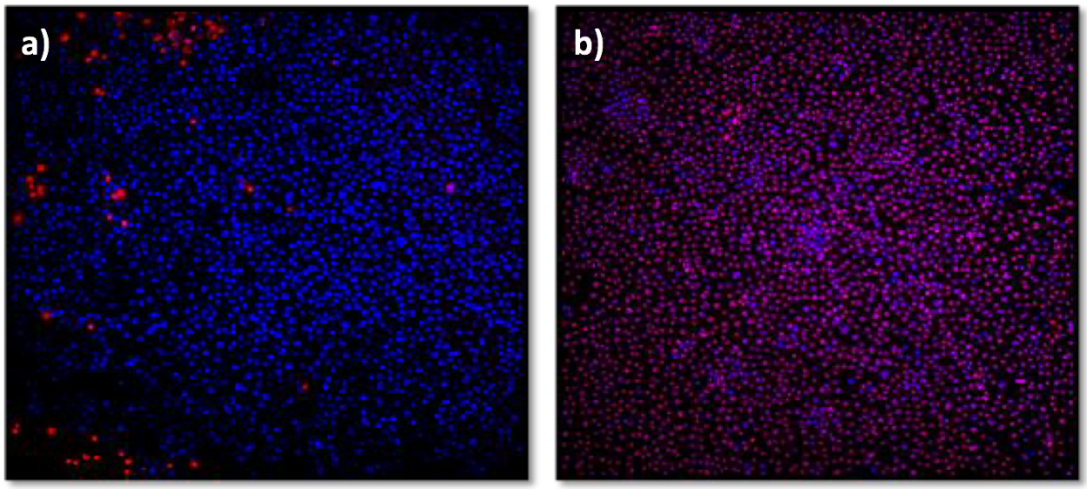

Figure 6-13- Fluorescence microscopy images of PTT efficacy (a) cell only controls, and (b) HGN_antibody after laser treatment. Cell nuclei are labeled with DAPI (shown in blue) and damaged cells are labeled with PI (shown in pink).

The significantly smaller number of PI markers in the cell only figure (Fig. 13a) clearly indicats that laser treatment alone is not harmful to the cells. The cell death happens only when combination of HGNs and laser treatment are applied. This experiment was repeated for peptide conjugated HGNs and results were significantly higher (91%) compared to HGN_antibody conjugates (54%). This dramatic difference might be due to multiple factors including closer proximity of HGNs to the cell surface, resulting in more efficient heat transfer and damage, consequently. More efficient targeting and possibility of particle internalization with the peptide targeting ligand is also considerable.

6.5 Conclusion and Future Work

In this work, the effect of targeting ligand on photothermal therapy (PTT) efficiency of hollow gold nanoparticles (HGNs) was investigated. The 40 nm HGNs were synthesized and bioconjugated to anti-EGF antibody and GE-11 peptide, which both target the epidermal growth factor receptors (EGFR) overexpressed on the surface of oral squamous cell carcinoma (cell line A-431). The structural and spectral properties of HGNs before and after conjugation was studied and the conjugation was confirmed using UV-Vis, PL spectroscopy and BCA assay. All these characterization techniques indicated proper surface modification and conjugation of HGNs. The conjugated HGNs were incubated with the cells and the specific binding and targeting of the cells was investigated by fluorescence and confocal microscopy. The binding affinity of the conjugated HGNs to the receptors was calculated by ICP-OES. Finally, the PTT efficacy of these particles was studied after laser treatment. The preliminary PTT results showed significantly higher cell death (91%) with peptide conjugated HGNs compared to HGN_antibody (54%). The possible explanations for this result were discussed including closer proximity to cell surface, internalization of the particles and more efficient binding to the receptors. Most of the work done in this project include design and development of protocols for surface modifications, bioconjugation, cell experiment, treatment parameters and characterization processes. These parts are mostly done with antibody and only some of them were reported for peptide. All these processes should be replicated and modified for peptide as well to provide further information to confirm proposed hypotheses. In addition, further

modifying the targeting ligand in order to efficiently target the receptors on the nuclei or in the cytoplasm may result in permanent damage of DNA and improved efficiency.

6.6 References

(1) Brongersma, M. L.; Halas, N. J.; Nordlander, P. Plasmon-Induced Hot Carrier Science and Technology. *Nat. Nanotechnol.* **2015**, *10* (1), 25–34.

(2) Wang, C.; Nie, X.-G.; Shi, Y.; Zhou, Y.; Xu, J.-J.; Xia, X.-H.; Chen, H.-Y. Direct Plasmon-Accelerated Electrochemical Reaction on Gold Nanoparticles. *ACS Nano* **2017**, *11* (6), 5897–5905.

(3) Spata, V. A.; Carter, E. A. Mechanistic Insights into Photocatalyzed Hydrogen Desorption from Palladium Surfaces Assisted by Localized Surface Plasmon Resonances. *ACS Nano* **2018**, *12* (4), 3512–3522.

(4) Yang, P.; Zheng, J.; Xu, Y.; Zhang, Q.; Jiang, L. Colloidal Synthesis and Applications of Plasmonic Metal Nanoparticles. *Adv. Mater.* **2016**, *28* (47), 10508–10517.

(5) Sheldon, M. T.; Groep, J. van de; Brown, A. M.; Polman, A.; Atwater, H. A. Plasmoelectric Potentials in Metal Nanostructures. *Science* **2014**, *346* (6211), 828–831.

(6) Choi, H.; Ko, S.-J.; Choi, Y.; Joo, P.; Kim, T.; Lee, B. R.; Jung, J.-W.; Choi, H. J.; Cha, M.; Jeong, J.-R.; et al. Versatile Surface Plasmon Resonance of Carbon-Dot-Supported Silver Nanoparticles in Polymer Optoelectronic Devices. *Nat. Photonics* **2013**, *7* (9), 732–738.

(7) Zhong, L.; Jiang, Y.; Liow, C.; Meng, F.; Sun, Y.; Chandran, B. K.; Liang, Z.; Jiang, L.; Li, S.; Chen, X. Highly Sensitive Electro-Plasmonic Switches Based on Fivefold Stellate Polyhedral Gold Nanoparticles. *Small* **2015**, *11* (40), 5395–5401.

(8) Meng, X.; Liu, L.; Ouyang, S.; Xu, H.; Wang, D.; Zhao, N.; Ye, J. Nanometals for Solar-to-Chemical Energy Conversion: From Semiconductor-Based Photocatalysis to Plasmon-Mediated Photocatalysis and Photo-Thermocatalysis. *Adv. Mater.* **2016**, *28* (32), 6781–6803.

(9) Christopher, P.; Xin, H.; Linic, S. Visible-Light-Enhanced Catalytic Oxidation Reactions on Plasmonic Silver Nanostructures. *Nat. Chem.* **2011**, *3* (6), 467–472.

(10) Langer, J.; Novikov, S. M.; Liz-Marzán, L. M. Sensing Using Plasmonic Nanostructures and Nanoparticles. *Nanotechnology* **2015**, *26* (32), 322001.

(11) Guerreiro, J. R. L.; Frederiksen, M.; Bochenkov, V. E.; De Freitas, V.; Ferreira Sales, M. G.; Sutherland, D. S. Multifunctional Biosensor Based on Localized Surface Plasmon Resonance for Monitoring Small Molecule–Protein Interaction. *ACS Nano* **2014**, *8* (8), 7958–7967.

(12) Li, M.; K. Cushing, S.; Wu, N. Plasmon-Enhanced Optical Sensors: A Review. *Analyst* **2015**, *140* (2), 386–406.

(13) You, J.; Zhang, G.; Li, C. Exceptionally High Payload of Doxorubicin in Hollow Gold Nanospheres for Near-Infrared Light-Triggered Drug Release. *ACS Nano* **2010**, *4* (2), 1033–1041.

(14) Vijayaraghavan, P.; Liu, C.-H.; Vankayala, R.; Chiang, C.-S.; Hwang, K. C. Designing Multi-Branched Gold Nanoechinus for NIR Light Activated Dual Modal

Photodynamic and Photothermal Therapy in the Second Biological Window. *Adv. Mater.* **2014**, *26* (39), 6689–6695.

(15) Xing, R.; Liu, K.; Jiao, T.; Zhang, N.; Ma, K.; Zhang, R.; Zou, Q.; Ma, G.; Yan, X. An Injectable Self-Assembling Collagen–Gold Hybrid Hydrogel for Combinatorial Antitumor Photothermal/Photodynamic Therapy. *Adv. Mater.* **2016**, *28* (19), 3669–3676.

(16) Link, S.; El-Sayed, M. A. Size and Temperature Dependence of the Plasmon Absorption of Colloidal Gold Nanoparticles. *J. Phys. Chem. B* **1999**, *103* (21), 4212–4217.

(17) Papavassiliou, G. C. Optical Properties of Small Inorganic and Organic Metal Particles. *Prog. Solid State Chem.* **1979**, *12* (3), 185–271.

(18) Alan Creighton, J.; G. Eadon, D. Ultraviolet–Visible Absorption Spectra of the Colloidal Metallic Elements. *J. Chem. Soc. Faraday Trans.* **1991**, *87* (24), 3881–3891.

(19) Kelly, K. L.; Coronado, E.; Zhao, L. L.; Schatz, G. C. The Optical Properties of Metal Nanoparticles: The Influence of Size, Shape, and Dielectric Environment. *J. Phys. Chem. B* **2003**, *107* (3), 668–677.

(20) Lee, K.-S.; El-Sayed, M. A. Dependence of the Enhanced Optical Scattering Efficiency Relative to That of Absorption for Gold Metal Nanorods on Aspect Ratio, Size, End-Cap Shape, and Medium Refractive Index. *J. Phys. Chem. B* **2005**, *109* (43), 20331–20338.

(21) Jain, P. K.; Lee, K. S.; El-Sayed, I. H.; El-Sayed, M. A. Calculated Absorption and Scattering Properties of Gold Nanoparticles of Different Size, Shape, and

Composition: Applications in Biological Imaging and Biomedicine. *J. Phys. Chem. B* **2006**, *110* (14), 7238–7248.

(22) Tcherniak, A.; Ha, J. W.; Dominguez-Medina, S.; Slaughter, L. S.; Link, S. Probing a Century Old Prediction One Plasmonic Particle at a Time. *Nano Lett.* **2010**, *10* (4), 1398–1404.

(23) J. Orendorff, C.; Gearheart, L.; R. Jana, N.; J. Murphy, C. Aspect Ratio Dependence on Surface Enhanced Raman Scattering Using Silver and Gold Nanorod Substrates. *Phys. Chem. Chem. Phys.* **2006**, *8* (1), 165–170.

(24) Wiley, B. J.; Chen, Y.; McLellan, J. M.; Xiong, Y.; Li, Z.-Y.; Ginger, D.; Xia, Y. Synthesis and Optical Properties of Silver Nanobars and Nanorice. *Nano Lett.* **2007**, *7* (4), 1032–1036.

(25) Young, J. K.; Figueroa, E. R.; Drezek, R. A. Tunable Nanostructures as Photothermal Theranostic Agents. *Ann. Biomed. Eng.* **2012**, *40* (2), 438–459.

(26) A. Sperling, R.; Gil, P. R.; Zhang, F.; Zanella, M.; J. Parak, W. Biological Applications of Gold Nanoparticles. *Chem. Soc. Rev.* **2008**, *37* (9), 1896–1908.

(27) Hirsch, L. R.; Stafford, R. J.; Bankson, J. A.; Sershen, S. R.; Rivera, B.; Price, R. E.; Hazle, J. D.; Halas, N. J.; West, J. L. Nanoshell-Mediated near-Infrared Thermal Therapy of Tumors under Magnetic Resonance Guidance. *Proc. Natl. Acad. Sci.* **2003**, *100* (23), 13549–13554.

(28) Hirsch, L. R.; Gobin, A. M.; Lowery, A. R.; Tam, F.; Drezek, R. A.; Halas, N. J.; West, J. L. Metal Nanoshells. *Ann. Biomed. Eng.* **2006**, *34* (1), 15–22.

(29) Lowery, A. R.; Gobin, A. M.; Day, E. S.; Halas, N. J.; West, J. L. Immunonanoshells for Targeted Photothermal Ablation of Tumor Cells. *Int. J. Nanomedicine* **2006**, *1* (2), 149–154.

(30) Goodrich, G. P.; Bao, L.; Gill-Sharp, K. L.; Sang, K. L.; Wang, J. C.; Payne, J. D. Photothermal Therapy in a Murine Colon Cancer Model Using Near-Infrared Absorbing Gold Nanorods. *J. Biomed. Opt.* **2010**, *15* (1), 018001.

(31) Schwartzberg, A. M.; Olson, T. Y.; Talley, C. E.; Zhang, J. Z. Synthesis, Characterization, and Tunable Optical Properties of Hollow Gold Nanospheres. *J. Phys. Chem. B* **2006**, *110* (40), 19935–19944.

(32) Skrabalak, S. E.; Chen, J.; Au, L.; Lu, X.; Li, X.; Xia, Y. Gold Nanocages for Biomedical Applications. *Adv. Mater.* **2007**, *19* (20), 3177–3184.

(33) Li, C.; Shuford, K. L.; Chen, M.; Lee, E. J.; Cho, S. O. A Facile Polyol Route to Uniform Gold Octahedra with Tailorable Size and Their Optical Properties. *ACS Nano* **2008**, *2* (9), 1760–1769.

(34) Kou, X.; Zhang, S.; Tsung, C.-K.; Yeung, M. H.; Shi, Q.; Stucky, G. D.; Sun, L.; Wang, J.; Yan, C. Growth of Gold Nanorods and Bipyramids Using CTEAB Surfactant. *J. Phys. Chem. B* **2006**, *110* (33), 16377–16383.

(35) Pérez-Juste, J.; Pastoriza-Santos, I.; Liz-Marzán, L. M.; Mulvaney, P. Gold Nanorods: Synthesis, Characterization and Applications. *Coord. Chem. Rev.* **2005**, *249* (17), 1870–1901.

(36) Alkilany, A. M.; Murphy, C. J. Toxicity and Cellular Uptake of Gold Nanoparticles: What We Have Learned so Far? *J. Nanoparticle Res.* **2010**, *12* (7), 2313–2333.

(37) Chithrani, B. D.; Ghazani, A. A.; Chan, W. C. W. Determining the Size and Shape Dependence of Gold Nanoparticle Uptake into Mammalian Cells. *Nano Lett.* **2006**, *6* (4), 662–668.

(38) El-Sayed, M. A. Small Is Different: Shape-, Size-, and Composition-Dependent Properties of Some Colloidal Semiconductor Nanocrystals. *Acc. Chem. Res.* **2004**, *37* (5), 326–333.

(39) Melancon, M. P.; Zhou, M.; Zhang, R.; Xiong, C.; Allen, P.; Wen, X.; Huang, Q.; Wallace, M.; Myers, J. N.; Stafford, R. J.; et al. Selective Uptake and Imaging of Aptamer- and Antibody-Conjugated Hollow Nanospheres Targeted to Epidermal Growth Factor Receptors Overexpressed in Head and Neck Cancer. *ACS Nano* **2014**, *8* (5), 4530–4538.

(40) Schwartzberg, A. M.; Zhang, J. Z. Novel Optical Properties and Emerging Applications of Metal Nanostructures. *J. Phys. Chem. C* **2008**, *112* (28), 10323–10337.

(41) Huang, X.; Jain, P. K.; El-Sayed, I. H.; El-Sayed, M. A. Plasmonic Photothermal Therapy (PPTT) Using Gold Nanoparticles. *Lasers Med. Sci.* **2007**, *23* (3), 217.

(42) Nam, J.; Won, N.; Jin, H.; Chung, H.; Kim, S. PH-Induced Aggregation of Gold Nanoparticles for Photothermal Cancer Therapy. *J. Am. Chem. Soc.* **2009**, *131* (38), 13639–13645.

(43) Zharov, V. P.; Galitovskaya, E. N.; Johnson, C.; Kelly, T. Synergistic Enhancement of Selective Nanophotothermolysis with Gold Nanoclusters: Potential for Cancer Therapy. *Lasers Surg. Med.* **2005**, *37* (3), 219–226.

(44) Adegboyega K. Oyelere, *; Po C. Chen, †; Xiaohua Huang, ‡; Ivan H. El-Sayed, § and; Mostafa A. El-Sayed*, ‡. Peptide-Conjugated Gold Nanorods for Nuclear Targeting https://pubs-acs-org.oca.ucsc.edu/doi/abs/10.1021/bc070132i (accessed Apr 24, 2019).

(45) Xiaohua Huang, †; Ivan H. El-Sayed, ‡; Wei Qian, † and; Mostafa A. El-Sayed*, †. Cancer Cells Assemble and Align Gold Nanorods Conjugated to Antibodies to Produce Highly Enhanced, Sharp, and Polarized Surface Raman Spectra: A Potential Cancer Diagnostic Marker https://pubs-acs-org.oca.ucsc.edu/doi/abs/10.1021/nl070472c (accessed Apr 24, 2019).

(46) André M. Gobin, †; Min Ho Lee, †; Naomi J. Halas, ‡; William D. James, §; Rebekah A. Drezek, † and; Jennifer L. West*, †. Near-Infrared Resonant Nanoshells for Combined Optical Imaging and Photothermal Cancer Therapy https://pubs-acs-org.oca.ucsc.edu/doi/abs/10.1021/nl070610y (accessed Apr 24, 2019).

(47) Christopher Loo, †; Amanda Lowery, †; Naomi Halas, §; Jennifer West, †; Rebekah Drezek*, †. Immunotargeted Nanoshells for Integrated Cancer Imaging and Therapy https://pubs-acs-org.oca.ucsc.edu/doi/abs/10.1021/nl050127s (accessed Apr 24, 2019).

(48) Gobin, A. M.; Watkins, E. M.; Quevedo, E.; Colvin, V. L.; West, J. L. Near-Infrared-Resonant Gold/Gold Sulfide Nanoparticles as a Photothermal Cancer Therapeutic Agent. *Small* **2010**, *6* (6), 745–752.

(49) Chen, Q.; Wang, X.; Wang, C.; Feng, L.; Li, Y.; Liu, Z. Drug-Induced Self-Assembly of Modified Albumins as Nano-Theranostics for Tumor-Targeted Combination Therapy. *ACS Nano* **2015**, *9* (5), 5223–5233.

(50) Xiaojun Ji, †; Ruping Shao, †; Andrew M. Elliott, ‡; R. Jason Stafford, ‡; Emilio Esparza-Coss, ‡; James A. Bankson, ‡; Gan Liang, §; Zhi-Ping Luo, ∥; Keeseong Park, ⊥; John T. Markert, ⊥ and; et al. Bifunctional Gold Nanoshells with a Superparamagnetic Iron Oxide−Silica Core Suitable for Both MR Imaging and Photothermal Therapy https://pubs-acs-org.oca.ucsc.edu/doi/abs/10.1021/jp0702245 (accessed Apr 24, 2019).

(51) Lindley, S. A.; Cooper, J. K.; Rojas-Andrade, M. D.; Fung, V.; Leahy, C. J.; Chen, S.; Zhang, J. Z. Highly Tunable Hollow Gold Nanospheres: Gaining Size Control and Uniform Galvanic Exchange of Sacrificial Cobalt Boride Scaffolds. *ACS Appl. Mater. Interfaces* **2018**.

(52) Dowgiallo, A.-M.; Schwartzberg, A. M.; Knappenberger, K. L. Structure-Dependent Coherent Acoustic Vibrations of Hollow Gold Nanospheres. *Nano Lett.* **2011**, *11* (8), 3258–3262.

(53) Dowgiallo, A.-M.; L. Knappenberger, K. Ultrafast Electron–Phonon Coupling in Hollow Gold Nanospheres. *Phys. Chem. Chem. Phys.* **2011**, *13* (48), 21585–21592.

(54) Chari, R. V. J.; Miller, M. L.; Widdison, W. C. Antibody–Drug Conjugates: An Emerging Concept in Cancer Therapy. *Angew. Chem. Int. Ed.* **2014**, *53* (15), 3796–3827.

(55) van der Meel, R.; Vehmeijer, L. J. C.; Kok, R. J.; Storm, G.; van Gaal, E. V. B. Ligand-Targeted Particulate Nanomedicines Undergoing Clinical Evaluation: Current Status. In *Intracellular Delivery III: Market Entry Barriers of Nanomedicines*; Prokop, A., Weissig, V., Eds.; Fundamental Biomedical Technologies; Springer International Publishing: Cham, 2016; pp 163–200.

(56) Zhang, X.; Zhang, J.; Ma, Y.; Pei, X.; Liu, Q.; Lu, B.; Jin, L.; Wang, J.; Liu, J. A Cell-Based Single-Stranded DNA Aptamer Specifically Targets Gastric Cancer. *Int. J. Biochem. Cell Biol.* **2014**, *46*, 1–8.

(57) Wang, A. Z.; Farokhzad, O. C. Current Progress of Aptamer-Based Molecular Imaging. *J. Nucl. Med.* **2014**, *55* (3), 353–356.

(58) Shahied, L. S.; Tang, Y.; Alpaugh, R. K.; Somer, R.; Greenspon, D.; Weiner, L. M. Bispecific Minibodies Targeting HER2/Neu and CD16 Exhibit Improved Tumor Lysis When Placed in a Divalent Tumor Antigen Binding Format. *J. Biol. Chem.* **2004**, *279* (52), 53907–53914.

(59) Rana, S.; Nissen, F.; Lindner, T.; Altmann, A.; Mier, W.; Debus, J.; Haberkorn, U.; Askoxylakis, V. Screening of a Novel Peptide Targeting the Proteoglycan-Like Region of Human Carbonic Anhydrase IX. *Mol. Imaging* **2013**, *12* (8), 7290.2013.00066.

(60) McGuire, M. J.; Gray, B. P.; Li, S.; Cupka, D.; Byers, L. A.; Wu, L.; Rezaie, S.; Liu, Y.-H.; Pattisapu, N.; Issac, J.; et al. Identification and Characterization of a Suite of Tumor Targeting Peptides for Non-Small Cell Lung Cancer. *Sci. Rep.* **2014**, *4*, 4480.

(61) Zhang, X.-X.; Eden, H. S.; Chen, X. Peptides in Cancer Nanomedicine: Drug Carriers, Targeting Ligands and Protease Substrates. *J. Controlled Release* **2012**, *159* (1), 2–13.

(62) Kurzrock, R.; Gabrail, N.; Chandhasin, C.; Moulder, S.; Smith, C.; Brenner, A.; Sankhala, K.; Mita, A.; Elian, K.; Bouchard, D.; et al. Safety, Pharmacokinetics, and Activity of GRN1005, a Novel Conjugate of Angiopep-2, a Peptide Facilitating Brain Penetration, and Paclitaxel, in Patients with Advanced Solid Tumors. *Mol. Cancer Ther.* **2012**, *11* (2), 308–316.

(63) Vaitilingam, B.; Chelvam, V.; Kularatne, S. A.; Poh, S.; Ayala-Lopez, W.; Low, P. S. A Folate Receptor-α–Specific Ligand That Targets Cancer Tissue and Not Sites of Inflammation. *J. Nucl. Med.* **2012**, *53* (7), 1127–1134.

(64) Xia, W.; Low, P. S. Folate-Targeted Therapies for Cancer. *J. Med. Chem.* **2010**, *53* (19), 6811–6824.

(65) Varghese, B.; Vlashi, E.; Xia, W.; Ayala Lopez, W.; Paulos, C. M.; Reddy, J.; Xu, L.-C.; Low, P. S. Folate Receptor-β in Activated Macrophages: Ligand Binding and Receptor Recycling Kinetics. *Mol. Pharm.* **2014**, *11* (10), 3609–3616.

(66) Shen, J.; Chelvam, V.; Cresswell, G.; Low, P. S. Use of Folate-Conjugated Imaging Agents To Target Alternatively Activated Macrophages in a Murine Model of Asthma. *Mol. Pharm.* **2013**, *10* (5), 1918–1927.

(67) Perini, G. F.; Pro, B. Brentuximab Vedotin in CD30+ Lymphomas. *Biol. Ther.* **2013**, *3* (1), 15–23.

(68) Liu, X.; Guo, J.; Han, S.; Yao, L.; Chen, A.; Yang, Q.; Bo, H.; Xu, P.; Yin, J.; Zhang, Z. Enhanced Immune Response Induced by a Potential Influenza A Vaccine Based on Branched M2e Polypeptides Linked to Tuftsin. *Vaccine* **2012**, *30* (46), 6527–6533.

(69) Adem, Y. T.; Schwarz, K. A.; Duenas, E.; Patapoff, T. W.; Galush, W. J.; Esue, O. Auristatin Antibody Drug Conjugate Physical Instability and the Role of Drug Payload. *Bioconjug. Chem.* **2014**, *25* (4), 656–664.

(70) Zimmerman, E. S.; Heibeck, T. H.; Gill, A.; Li, X.; Murray, C. J.; Madlansacay, M. R.; Tran, C.; Uter, N. T.; Yin, G.; Rivers, P. J.; et al. Production of Site-Specific Antibody–Drug Conjugates Using Optimized Non-Natural Amino Acids in a Cell-Free Expression System. *Bioconjug. Chem.* **2014**, *25* (2), 351–361.

(71) Behrens, C. R.; Liu, B. Methods for Site-Specific Drug Conjugation to Antibodies. *mAbs* **2014**, *6* (1), 46–53.

(72) Firer, M. A.; Gellerman, G. Targeted Drug Delivery for Cancer Therapy: The Other Side of Antibodies. *J. Hematol. Oncol.J Hematol Oncol* **2012**, *5* (1), 70.

(73) Juweid, M.; Neumann, R.; Paik, C.; Perez-Bacete, M. J.; Sato, J.; van Osdol, W.; Weinstein, J. N. Micropharmacology of Monoclonal Antibodies in Solid Tumors:

Direct Experimental Evidence for a Binding Site Barrier. *Cancer Res.* **1992**, *52* (19), 5144–5153.

(74) Kostarelos, K.; Emfietzoglou, D.; Papakostas, A.; Yang, W.-H.; Ballangrud, Å.; Sgouros, G. Binding and Interstitial Penetration of Liposomes within Avascular Tumor Spheroids. *Int. J. Cancer* **2004**, *112* (4), 713–721. h

(75) Lee, H.; Fonge, H.; Hoang, B.; Reilly, R. M.; Allen, C. The Effects of Particle Size and Molecular Targeting on the Intratumoral and Subcellular Distribution of Polymeric Nanoparticles. *Mol. Pharm.* **2010**, *7* (4), 1195–1208.

(76) van Osdol, W.; Fujimori, K.; Weinstein, J. N. An Analysis of Monoclonal Antibody Distribution in Microscopic Tumor Nodules: Consequences of a "Binding Site Barrier." *Cancer Res.* **1991**, *51* (18), 4776–4784.

(77) Weinstein, J. N.; van Osdol, W. Early Intervention in Cancer Using Monoclonal Antibodies and Other Biological Ligands: Micropharmacology and the "Binding Site Barrier." *Cancer Res.* **1992**, *52*, 2747s–2751s.

(78) Yuan, F.; Dellian, M.; Fukumura, D.; Leunig, M.; Berk, D. A.; Torchilin, V. P.; Jain, R. K. Vascular Permeability in a Human Tumor Xenograft: Molecular Size Dependence and Cutoff Size. *Cancer Res.* **1995**, *55* (17), 3752–3756.

(79) Jain, R. K.; Stylianopoulos, T. Delivering Nanomedicine to Solid Tumors. *Nat. Rev. Clin. Oncol.* **2010**, *7* (11), 653–664.

(80) Adams, S.; Thai, D.; Mascona, X.; Schwartzberg, A. M.; Zhang, J. Z. Key Factors Affecting the Reproducibility of Synthesis and Growth Mechanism of Near-

Infrared Absorbing Hollow Gold Nanospheres. *Chem. Mater.* **2014**, *26* (23), 6805–6810.

(81) Hong, E. J.; Kim, Y.-S.; Choi, D. G.; Shim, M. S. Cancer-Targeted Photothermal Therapy Using Aptamer-Conjugated Gold Nanoparticles. *J. Ind. Eng. Chem.* **2018**, *67*, 429–436.

(82) Shah, N. B.; Vercellotti, G. M.; White, J. G.; Fegan, A.; Wagner, C. R.; Bischof, J. C. Blood–Nanoparticle Interactions and in Vivo Biodistribution: Impact of Surface PEG and Ligand Properties. *Mol. Pharm.* **2012**, *9* (8), 2146–2155.

(83) Niidome, T.; Yamagata, M.; Okamoto, Y.; Akiyama, Y.; Takahashi, H.; Kawano, T.; Katayama, Y.; Niidome, Y. PEG-Modified Gold Nanorods with a Stealth Character for in Vivo Applications. *J. Controlled Release* **2006**, *114* (3), 343–347.

(84) Okur, A. C.; Erkoc, P.; Kizilel, S. Targeting Cancer Cells via Tumor-Homing Peptide CREKA Functional PEG Nanoparticles. *Colloids Surf. B Biointerfaces* **2016**, *147*, 191–200.

(85) Chen, Y.; Xianyu, Y.; Jiang, X. Surface Modification of Gold Nanoparticles with Small Molecules for Biochemical Analysis. *Acc. Chem. Res.* **2017**, *50* (2), 310–319.

(86) Dulkeith, E.; Ringler, M.; Klar, T. A.; Feldmann, J.; Muñoz Javier, A.; Parak, W. J. Gold Nanoparticles Quench Fluorescence by Phase Induced Radiative Rate Suppression. *Nano Lett.* **2005**, *5* (4), 585–589.

(87) Pons, T.; Medintz, I. L.; Sapsford, K. E.; Higashiya, S.; Grimes, A. F.; English, D. S.; Mattoussi, H. On the Quenching of Semiconductor Quantum Dot

Photoluminescence by Proximal Gold Nanoparticles. *Nano Lett.* **2007**, *7* (10), 3157–3164.

(88) Huang, C.-C.; Chiang, C.-K.; Lin, Z.-H.; Lee, K.-H.; Chang, H.-T. Bioconjugated Gold Nanodots and Nanoparticles for Protein Assays Based on Photoluminescence Quenching. *Anal. Chem.* **2008**, *80* (5), 1497–1504.

(89) Olson, B. J. S. C.; Markwell, J. Assays for Determination of Protein Concentration. *Curr. Protoc. Protein Sci.* **2007**, *48* (1), 3.4.1-3.4.29.

(90) Epidermal Growth Factor Receptor (EGFR) Biology and Human Oral Cancer. *Histol. Histopathol.* **1999**, No. 14, 491–500.